Technical Physics, Vol. 50, No. 10, 2005, pp. 1251–1254. Translated from Zhurnal Tekhnicheskoĭ Fiziki, Vol. 75, No. 10, 2005, pp. 1–4.

THEORETICAL AND MATHEMATICAL PHYSICS

Surrogate Navier–Stokes–Burgers Model for Simulation of Inhomogeneous Turbulence by Large-Scale Eddies

A. M. Balonishnikov

St. Petersburg State University of Economics and Engineering, St. Petersburg, 197002 Russia

e-mail: balonalex@yahoo.co.uk

Received November 16, 2004

Abstract—A model of parallel noninteracting cascades in the spectral space is suggested in terms of which the turbulent flow of an incompressible fluid subject to arbitrary large-scale velocity gradients is described. The linear parts of model equations for two polarization components of the velocity are derived from the Navier–Stokes equations, and their nonlinear parts correspond to the 1D Burgers model. Using the model suggested, explicit expressions for subgrid Reynolds stresses without empiric parameters are obtained. © *2005 Pleiades Publishing, Inc.*

INTRODUCTION

As is known, even simplified nonlinear equations for small-scale velocity components subject to arbitrary large-scale velocity gradients are very difficult, if possible at all, to solve analytically. With this in mind, researchers have recently developed synthetic (surrogate) models of turbulence, where the dynamics of small-scale eddies is simulated by some process that, while not rigorously following from equations for small-scale velocity, reproduces Reynolds stress spectra similar to those observed in experiment (see, e.g., [1]).

MODEL EQUATIONS

It is suggested that the exact equations for the modified polarization components of small-scale velocity [2] that are obtained by reducing the linear part of the system to the diagonal form be replaced by the simplified set of (1 + 1) integro-differential equations

$$(\partial_t + \nu k^2) v^1 = \lambda_1(\theta, \eta) v^1 - ik\Sigma_p v^1(p) v^1(k-p), \quad (1)$$

$$(\partial_t + \nu k^2) v^2 = \lambda_2(\theta, \eta) v^1 - ik\Sigma_p v^2(p) v^2(k-p), \quad (2)$$

where $\mathbf{u} = \mathbf{B}\mathbf{v}$ are standard polarization components and matrix $\mathbf{B}$ is specified by large-scale velocity gradients.

Note that nonlinearity set in such a form conserves the invariance of the system under proper Galilean transformations (the case of pure rotation, $\Omega \neq 0$ and $S = 0$, corresponds to purely imaginary $\lambda_{1,2}$; according to [3], the energy in this case is confined over large scales, the energy cascade does not occur, and turbulence can decay only in a viscous manner. This is consistent with our model, where subgrid Reynolds stresses are absent). In addition, with nonlinearity taken in such a form, the turbulence energy is also conserved. The above set consists of two uncoupled (1 + 1) integro-differential equations. The range of angles θ and η, which are the parameters of the equations, is such that λ_1 and λ_2 take positive values. In essence, these equations are the original Burgers equations [4] (the term *original* is borrowed from [5]), which have a finite number of analytical stationary solutions [4] at arbitrary grid Reynolds numbers (in terms of our approach). The number of these solutions increases in proportion to the square root of the grid Reynolds number, and their form simplifies greatly in the limit of large grid Re (as was noted by Burgers as early as in 1948 [4]). Here, the grid Re is defined as $\mathrm{Re}_{loc} = \lambda L^2/\nu$, where $\lambda = \lambda_1$ or λ_2 and L is the length of an edge of a cubic grid that separates small-scale and large-scale motions. The source (sink) and other terms in the above equations, except for nonlinear ones, are derived from the Navier–Stokes equations for an incompressible fluid, which allows us to speak of a surrogate Navier–Stokes–Burgers model. In this case, the complicated process of energy distribution over spectral components is replaced by a set of 1D cascade models where interaction between polarization velocity components v^1 and v^2, as well as between their spectral components variously oriented in the spectral space, is ignored.

It seems that all stationary solutions of the original Burgers equation are stable in both linear and nonlinear cases. Some reasoning behind their stability can be found elsewhere [5]. Since the highest amplitude solutions are major contributors to subgrid Reynolds stresses, it is reasonable to consider just these solutions, which can be selected from those obtained in the limit $\mathrm{Re}_{loc} \longrightarrow \infty$,

$$v_B = \frac{\lambda L}{2}\left(\frac{2\xi}{L} - 1 + \tanh[\lambda L(L-2\xi)/(8\nu)]\right). \quad (3)$$

1063-7842/05/5010-1251$26.00

Here, $\xi \in [0, L]$. This solution (antisymmetric about the midpoint of the segment) was constructed so as to satisfy the requirement imposed on velocity pulsations; namely, the space-averaged value of the velocity equals zero, $L^{-1}\int_0^L v_B\, d\xi = 0$. It varies linearly over the domain of definition, except for the neighborhood of the midpoint of the segment, where it varies significantly, producing two shock layers. It should be noted that the result discussed can be derived more rigorously than was done by Burgers in [4] and in his early works with the method of joining asymptotic expansions [6]. To proceed further and use this solution to construct 3D spectra of Reynolds stresses and energy of turbulence, we must find its Fourier components. Following Burgers, we expand this stationary solution into the Fourier series,

$$v_B(\xi) = \sum_{n=1}^{\infty} v_n \sin(\pi n\xi/L), \tag{4}$$

where

$$v_n = \frac{2}{L}\int_0^L v_B \sin(\pi n\xi/L)\, d\xi$$

or, in explicit form,

$$v_n = \lambda\int_0^L d\xi\{2\xi/L - 1 + \tanh[\lambda L(L-2\xi)/(8\nu)]\} \times \sin(\pi n\xi/L).$$

Changing of variables $z = 2\xi/L$ yields

$$v_n = \frac{\lambda L}{2}\int_0^2 dz[z - 1 + \tanh(\mathrm{Re}_{loc}(1-z)/16)] \times \sin(\pi nz/2), \tag{5}$$

where $\mathrm{Re}_{loc} = \lambda L^2/\nu$.

Halving the domain of integration, we obtain

$$v_n = \lambda L\int_0^2 dy[y - 1 + \tanh(\mathrm{Re}_{loc}(y-1)/16)] \times \sin(\pi ny/2). \tag{6}$$

The integral entering into (6) is other than zero for even $n = 2p$ ($p = 1, 2, 3, \ldots$) (this case will be considered below). To simplify (6), we take this integral by parts, representing *sin* as the derivative of *cos* with appropriate coefficients. Taking into account that $\tanh(x)' = \frac{1}{\cosh^2(x)}$, we arrive at

$$v_p = \lambda L\mathrm{Re}_{loc}/(8\pi p)\int_0^1 dy\cos(\pi py) \times \frac{1}{\cosh^2[\mathrm{Re}_{loc}(y-1)/16]}.$$

Putting $z = 1 - y$ and making straightforward simplifications, we eventually come to

$$v_p = \lambda L\mathrm{Re}_{loc}(-1)^p/(8\pi p)\int_0^1 \frac{dz\cos(\pi pz)}{\cosh^2(\mathrm{Re}_{loc}z/16)}. \tag{7}$$

At high Re_{loc} (as was assumed above), the hyperbolic cosine squared increases very rapidly; therefore, the unity in the upper limit of integration can be replaced by infinity,

$$v_p = \lambda L\mathrm{Re}_{loc}(-1)^p/(8\pi p)\int_0^\infty \frac{dz\cos(\pi pz)}{\cosh^2(\mathrm{Re}_{loc}z/16)}. \tag{8}$$

The resulting integral is a tabulated integral (it can be taken using the theory of residues) [7]; so,

$$\int_0^\infty \frac{\cos mx}{\cosh^2\alpha x}dx = \frac{\pi m}{2\alpha^2\sinh\dfrac{\pi m}{2\alpha}}. \tag{9}$$

In our case,

$$v(p) = \frac{16\pi\lambda L\mathrm{Re}_{loc}^{-1}(-1)^p}{\sinh\dfrac{8\pi^2 p}{\mathrm{Re}_{loc}}}. \tag{10}$$

Note that a similar formula was derived by Burgers in [4].

SPECTRA OF REYNOLDS STRESSES AND ENERGY OF TURBUILENCE

According to [8], Reynolds stresses $\langle u_i u_j\rangle$ are defined through their proper spectra Φ_{ij} as follows:

$$\langle u_i u_j\rangle = \int \Phi_{ij} d\mathbf{k}, \tag{11}$$

where

$$\langle u_i(\mathbf{k})u_j(-\mathbf{k})\rangle = \langle u_i(\mathbf{k})u_j^*(\mathbf{k})\rangle = \Phi_{ij}(-\mathbf{k}) = \Phi_{ij}^*(\mathbf{k}).$$

The energy of turbulence is given by

$$E_T = \frac{1}{2}\langle u_i u_i\rangle = \frac{1}{2}\int \Phi_{ii} d\mathbf{k}.$$

From the relationships between normal and polar-

ization spectral components, it follows that

$$\Phi_{ij} = \langle \varepsilon_i^\mu u^\mu \varepsilon_j^\gamma u^{*\gamma} \rangle. \quad (12)$$

Specifically,

$$\Phi_{ii} = \langle u^\mu u^{*\mu} \rangle; \quad (13)$$

whence,

$$E_T = \frac{1}{2}\int \langle u^\mu u^{*\mu} \rangle d\mathbf{k}.$$

According to Lee [9], passage from discrete Fourier harmonics to continuous ones and from sums to integrals in the 3D space involves the following substitutions:

$$\left(\frac{2\pi}{L}\right)^3 \Sigma \longrightarrow \int d^3\mathbf{k}. \quad (14)$$

Designate the normalizing factor as N,

$$N = \left(\frac{L}{2\pi}\right)^3. \quad (15)$$

One-dimensional energy spectrum $E(k)$ is given by [9]

$$E(k) = Nk^2 \int_0^{2\pi} d\theta \int_{-\pi/2}^{\pi/2} d\eta \cos\mu (u^1 u^{1*} + u^2 u^{2*}). \quad (16)$$

It will be recalled that, in the spherical coordinate system used by Lee [9], the elementary solid angle was $d\Omega = \cos\theta d\theta d\eta$. In terms of our approach, the 1D energy spectrum may be calculated by the same formula (see (16)) by taking into account that

$$\mathbf{u} = \mathbf{B}\mathbf{v},$$

where matrix $\mathbf{B}$ is specified by gradients of the large-scale velocity [2] and modified polarization vector $\mathbf{v}$ should be set equal to zero for those orientations of an object in the spectral space meeting positive proper values of λ (an energy source for a 1D cascade is absent).

SPECTRA OF REYNOLDS STRESSES AND ENERGY OF TURBUILENCE FOR UNDER UNIFORM SHEAR

Consider again uniform shear, in which case only component $\partial_2 U_1 = S$ of the large-scale velocity gradient is other than zero. Then,

$$\lambda_1 = 0.5S\sin(2\theta)\cos^2(\eta), \quad (17)$$

$$\lambda_2 = 0. \quad (18)$$

In terms of our surrogate model, solutions meeting the given situation have the form $v = (v_B, 0)$.

The second component of the velocity equals zero, since $\lambda_2 = 0$ for any orientation in the spectral space. Here, v_B is the expansion coefficient for the selected solution to the original Burgers equation. The coefficients of matrix $\mathbf{B}$ of transition from modified to normal polarization components have the form

$$b_{11} = 1, \quad b_{12} = \sin\eta\tan\theta,$$
$$b_{21} = \sin\eta\cos\theta, \quad b_{22} = 1.$$

Range D of angular variables for which $\lambda_1 > 0$ is given by

$$\theta \in [0, \pi/2] \cup [\pi, 3\pi/2], \quad \eta \in [-\pi/2, \pi/2].$$

Eventually, the energy spectrum is given by the following explicit expressions:

$$E(k) = Nk^2 \int_D d\theta d\eta \times \cos\eta[1 + \sin^2(\eta)\cos^2(\theta)] v_B^2(k, \theta, \eta), \quad (19)$$

where the continuous modulus of wavenumber k and the integer number p in the sine Fourier series are related as $k = 2\pi p/L$.

Consider uniform shear such that $\partial_1 u_2 = S$ and all other components of the large-scale velocity gradient are zero. Recall once again that polarization components v and u are related as

$$\mathbf{u} = \mathbf{B}\mathbf{v}.$$

For the 1D case at hand,

$$u^1 = v_B,$$

$$u^2 = v_B \sin\eta\cos\theta.$$

The 3D energy spectrum is then represented as

$$E(\mathbf{k}) = \frac{1}{2}(\Phi_{11} + \Phi_{22} + \Phi_{33})$$
$$= \frac{N}{2}[1 + \sin^2(\eta)\cos^2(\theta)] v_B^2.$$

The 1D spectra resulting upon integration over the spherical surface of radius k equal each other by definition (see, e.g., [8]),

$$\phi_{ij} = k^2 \iint \Phi_{ij}(\mathbf{k}, t) d\Omega, \quad (20)$$

where $d\Omega$ is an elementary solid angle.

Recall the relationships that will be used in subsequent considerations:

$$n = 2p \ (p = 1, 2, 3, \ldots);$$
$$k = \pi n/L,$$

where L is the scale separating large- and small-scale velocity fields; and

$$v_B = v(p) = \frac{16\pi\lambda L(-1)^p}{\mathrm{Re}_{loc}\sinh(8\pi^2 p/\mathrm{Re}_{loc})},$$

where v_B is the Fourier harmonic of the solution to the

original Burgers equation,

$$\mathrm{Re}_{\mathrm{loc}} = \lambda_1 L^2/\nu,$$

$$\lambda_1 = \frac{1}{2}S\sin(2\theta)\cos^2(\eta).$$

ASYMPTOTICS OF ONE-DIMENSIONAL REYNOLDS SPECTRA IN THE LIMIT OF LARGE WAVENUMBERS

Let

$$p \gg \mathrm{Re}_{\mathrm{loc\,max}}.$$

Then, the hyperbolic cosine may be replaced by an increasing exponential and the square of the Fourier component of the solution to the original Burgers equation can be written as

$$v^2(p) = 4(16\pi\lambda_1 L/\mathrm{Re}_{\mathrm{loc}})^2\exp(-16\pi^2 p/\mathrm{Re}_{\mathrm{loc}}), \quad (21)$$

where λ_1 and $\mathrm{Re}_{\mathrm{loc}}$ are known functions of the angular variables.

To find the spectra of 1D Reynolds stresses requires taking double integrals over the angular variables,

$$\phi = \int\int g_{ij}(\theta,\eta)\exp(hp)\cos\eta\, d\theta\, d\eta,$$

where

$$h = -16\pi^2/\mathrm{Re}_{\mathrm{loc}} = -\frac{64\pi^2\nu}{L^2 S\sin(2\theta)(1+\cos 2\eta)}$$

and

$$g_{ij} = k^2\Phi_{ij}\exp(-hp).$$

Applying the Laplace method [8] to calculate the asymptotics of the integrals, we obtain expressions for Reynolds stress spectra,

$$\phi_{11} = \frac{2L^2 k\nu S}{\pi}\exp(ph_{\max}), \quad (22)$$

$$\phi_{22} = \frac{2L^2 k\nu S}{\pi}\exp(ph_{\max}), \quad (23)$$

$$\phi_{12} = -\frac{2L^2 k\nu S}{\pi}\exp(ph_{\max}), \quad (24)$$

$$\phi_{33} = \frac{L^3 S^2}{8\pi^2}\exp(ph_{\max}), \quad (25)$$

$$\phi_{13} = -\frac{L^{5/2}k^{1/2}\nu^{1/2}S^{3/2}}{4\pi^2}\exp(ph_{\max}), \quad (26)$$

$$\phi_{23} = -\frac{L^{5/2}k^{1/2}\nu^{1/2}S^{3/2}}{8\pi^2}\exp(ph_{\max}), \quad (27)$$

$$E(k) = \frac{1}{2}(\phi_{11}+\phi_{22}+\phi_{33}) \approx \frac{2L^2 k\nu S}{\pi}\exp(ph_{\max}), \quad (28)$$

where

$$\exp(ph_{\max}) = \exp\left(-\frac{15\pi k\nu}{SL^2}\right).$$

It is known that both model and experimental data for turbulence show a rapid decay of the turbulence spectra at large wavenumbers, as also demonstrated by the spectra obtained. It is easy to check that, at intermediate wavenumbers, the 1D spectra are inversely proportional to wavenumber p squared, which is also in good agreement with experimental data and with Kolmogorov's minus five-thirds law [10]. This statement and the calculation of the spectra throughout the wavenumber range will be discussed at length in subsequent publications.

CONCLUSIONS

While the model ignores interaction between two polarization components (which makes turbulence isotropic), the descending character of the spectra and anisotropy persistence [11] even at very large Re numbers let us conclude that the model is of certain value.

REFERENCES

1. D. M. McDonough, S. A. Bible, and J. Scoville, J. Turbulence **4**, 1 (2003); http://jot.iop.org.
2. A. M. Balonishnikov, Zh. Tekh. Fiz. **73** (10), 36 (2003) [Tech. Phys. **48**, 1255 (2003)].
3. C. Cambon and J. Scott, Annu. Rev. Fluid Mech. **31**, 1 (1999).
4. J. M. Burgers, Adv. Appl. Mech. **1**, 171 (1948).
5. A. Eden, Nonlinearity **3**, 557 (1990).
6. A. H. Nayfeh, *Introduction to Perturbation Techniques* (Wiley, New York, 1981; Mir, Moscow, 1984).
7. A. P. Prudnikov, Yu. A. Brychkov, and O. I. Marichev, *Integrals and Series* (Nauka, Moscow, 1981; Gordon and Breach, New York, 1986), Vols. 1–3.
8. J. Mathieu and D. Jeandel, *Prediction Methods for Turbulent Flows*, Ed. by W. Kollmann (Hemisphere, New York, 1980; Mir, Moscow, 1984).
9. J. Lee, J. Math. Phys. **16**, 537 (1975).
10. J. C. R. Hunt and P. Carlotti, Flow, Turbul. Combust. **66**, 453 (2001).
11. X. Shen and Z. Warhaft, Phys. Fluids **12**, 2976 (2000).

Translated by V. Isaakyan

Technical Physics, Vol. 50, No. 10, 2005, pp. 1255–1258. Translated from Zhurnal Tekhnicheskoĭ Fiziki, Vol. 75, No. 10, 2005, pp. 5–8.

GASES AND LIQUIDS

Model of Pressure Variation in a Vacuum System for Volatile Liquid Evacuation

R. A. Nevshupa and L. S. Sinev

Bauman State Technical University, Vtoraya Baumanskaya ul. 5, Moscow, 105005 Russia

e-mail: nevshupa@bmstu.ru

Received February 8, 2005

Abstract—The behavior of the total and partial pressure in a vacuum system is studied for the case of volatile liquid evacuation. A mathematical model of the process is developed that is based on the joint solution of the balance equations for gas and vapor flows. The influence of the vacuum system parameters and liquid properties on the pressure variation is found. The equilibrium pressure and evacuation time are numerically calculated for different system's parameters. © *2005 Pleiades Publishing, Inc.*

INTRODUCTION

In a number of technological processes, there arises the need to evacuate a vacuum chamber containing a source of a volatile liquid. For example, in leak detection by means of the bubble method used for testing vacuum units or devices in the case where a high sensitivity is not a critical point, a test object is filled with air or a probe gas under an excess pressure and is immersed in a liquid. Bubbles emerging on the outer surface of the object indicate leakage. The gas flow is proportional to the number of bubbles per unit time and their volume, and the number of bubbles, in turn, is proportional to the difference between the pressures inside and outside the object. To improve the sensitivity of the method, the container with the liquid is evacuated to a pressure of $10^{3-5} \times 10^4$ Pa. The probe gas must have a low molar weight; the liquid (usually ethanol), a low surface tension coefficient. When designing vacuum systems using the bubble leak detection method, one must know the pressure variation in the vacuum system when vapors are evacuated from above the liquid surface. Since the evaporating liquid flux varies in time, the conventional approaches to designing vacuum systems fail [1]. In this work, we suggest a model that makes it possible to evaluate the residual pressure in a vacuum system and construct time curves of vapor evacuation from above the liquid phase surface with regard to evacuation of the residual atmosphere.

CONSTRUCTION OF THE MODEL AND PARAMETER ESTIMATION

Model. The model suggested is based on the balance equation for gas flows in an idealized vacuum chamber (Fig. 1) that has volume V and is pumped out with rate S. For the pressure interval 10^4–10^5 Pa and evacuation time 1–10 min, the time variation of gas desorption flux from the walls and gas evolution from the materials may be ignored and so the sum of these fluxes may be taken to be constant, Q_g = const. Other fluxes we deal with in this situation are flux Q_{ev} of evaporating molecules and flux Q_{con} of condensing molecules. For simplicity, we assume that, in a first approximation, adsorption of liquid molecules on and their desorption from the inner surfaces of the vacuum system can also be ignored.

The flux balance in the chamber can then be described by a set of two differential equations for liquid vapor flux balance and balance of other gas fluxes,

$$\frac{dp_c(t)}{dt}V = Q_{ev} - Q_{con} - p_c(t)S, \quad (1)$$

$$\frac{dp_s(t)}{dt}V = Q_g - p_s(t)S \quad (2)$$

(for notation, see Table 1).

The left-hand side of these equations is the rate of variation of the amount of gases or vapors in the vacuum chamber, and term pS on the right-hand side is the rate of evacuation (capacity of a pump). The fluxes of

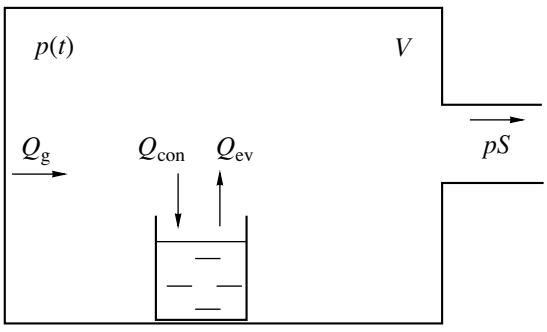

Fig. 1. Scheme of gas flows in the system.

1063-7842/05/5010-1255$26.00 © 2005 Pleiades Publishing, Inc.

Table 1

Notation	Meaning	Unit of measure
A	Surface area of liquid exposed to vacuum	m^2
E_d	Heat of vaporization	J/mol
M	Molar weight of liquid	kg/mol
n_m	Number of molecules per unit area in a layer	m^{-2}
p_c	Partial pressure of liquid vapor	Pa
p_{c0}	Partial vapor pressure of liquid at $t = 0$	Pa
p_s	Partial vapor pressure of other components	Pa
p_{s0}	Partial vapor pressure of other components at $t = 0$	Pa
p_{atm}	Atmospheric pressure	Pa
p_{sat}	Saturated vapor pressure of liquid	Pa
q_d	Specific desorption flux of liquid	$1/(cm^2\ s)$
q_a	Specific adsorption flux of liquid	$1/(cm^2\ s)$
Q_g	Gas liberation from chamber walls	$(m^3\ Pa)/s$
Q_{ev}	Evaporating liquid molecule flux	$(m^3\ Pa)/s$
Q_{con}	Condensing liquid molecule flux	$(m^3\ Pa)/s$
S	Effective rate of evacuation	m^3/s
t	Time	s
τ_0	Mean oscillation period of condensed molecule	s
T	Temperature	K
V	Chamber volume	m^3
k	Boltzmann constant	J/K
R	Gas constant	J/(mol K)
N_a	Avogadro number	mol^{-1}

Table 2. Parameters of the liquids and calculated consumption

Liquid	M, kg/mol [2]	E_d, kJ/mol [2]	Consumption, mg
Methanol (CH_3OH)	0.032	38.74	255
Ethanol (C_2H_5OH)	0.046	35.27	106
Propanol (C_3H_7OH)	0.06	40.48	77

evaporating and condensing liquid molecules are given by the formulas

$$Q_{ev} = q_d AkT, \tag{3}$$

$$Q_{con} = q_a AkT \tag{4}$$

(the Langmuir model); the specific desorption and adsorption fluxes of liquid molecules, by

$$q_d = n_m/\tau_0 \exp(-E_d/RT), \tag{5}$$

$$q_a = \frac{N_a p_c}{\sqrt{2\pi MRT}}. \tag{6}$$

The total molecular flux from the liquid surface, which is equal to the difference between the evaporating and condensing components, increases with decreasing pressure, since the evaporating component does not depend on the pressure and the condensing component is proportional to the vapor pressure.

Initial conditions. Since the system is evacuated starting from the atmospheric pressure, the initial condition for Eq. (2) (i.e., at the instant evacuation begins) is $p_{s0} = p_{atm} - p_{c0}$, where quantity p_{c0} depends on the rate of evaporation and the duration of stay of the liquid in the chamber before evacuation. To find p_{c0}, we assume that, prior to leak detection (i.e., prior to the container with the liquid being introduced into the chamber), the liquid vapor pressure equals zero. Then, at any time t after the chamber has been closed and the pump has been switched off, the vapor pressure is found from the balance between the fluxes of molecules being desorbed from and condensing on the liquid surface. The time dependence of the vapor pressure is given by

$$p_c(t) = \frac{1}{N_a} q_d AkT\sqrt{2\pi MRT} \times \left[1 - \exp\left(-\frac{N_a AkT}{V\sqrt{2\pi MRT}} t\right)\right]. \tag{7}$$

Calculation by (7) for ethanol at $T = 293$ K, $V = 4.33 \times 10^{-3}$ m^3, and $A = 30$ cm^2 (the values of other parameters are listed in Tables 2 and 3) showed that the saturated vapor pressure sets in (up to 0.1%) within 1.1 s. Therefore, for practical purposes, we may put

$$p_{c0} = p_{sat} = \frac{q_d\sqrt{2\pi MRT}}{N_a} \tag{8}$$

with a reasonable accuracy.

Then, in view of (8), the dependences $p_c(t)$ and $p_s(t)$ take the form

$$p_c(t) = \frac{q_d AkT\sqrt{2\pi MRT}}{N_a AkT + S\sqrt{2\pi MRT}} \times \left[1 - \exp\left(-\left[\frac{N_a AkT}{V\sqrt{2\pi MRT}} + \frac{S}{V}\right]t\right)\right] \tag{9}$$

Table 3. Parameters and constants used in calculation

Q_g	A	S	V	T	n_m	τ_0	k	R	N_a
1.37×10^{-4}	3×10^{-3}	4×10^{-4}	4.33×10^{-3}	293	3×10^{19}	2.76×10^{-14}	1.38×10^{-23}	8.31	6.02×10^{23}

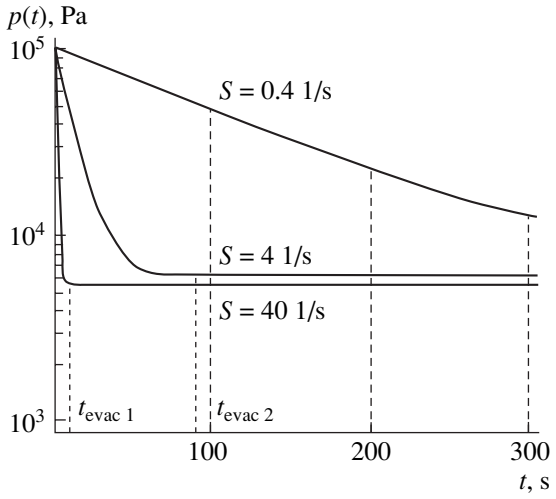

Fig. 2. Time variation of the total pressure in the vacuum chamber for different effective rates of evacuation S.

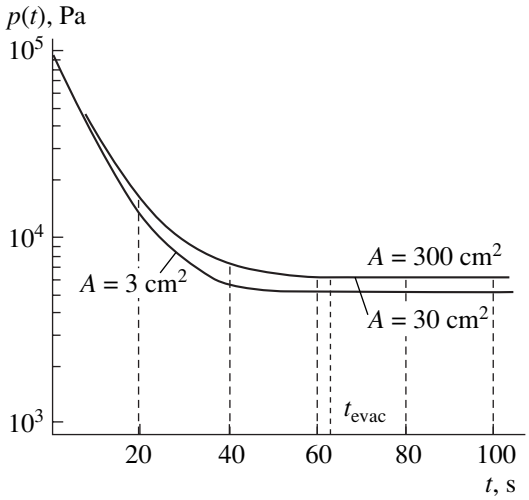

Fig. 3. Time variation of the total pressure in the vacuum chamber for different surface areas A of the liquid.

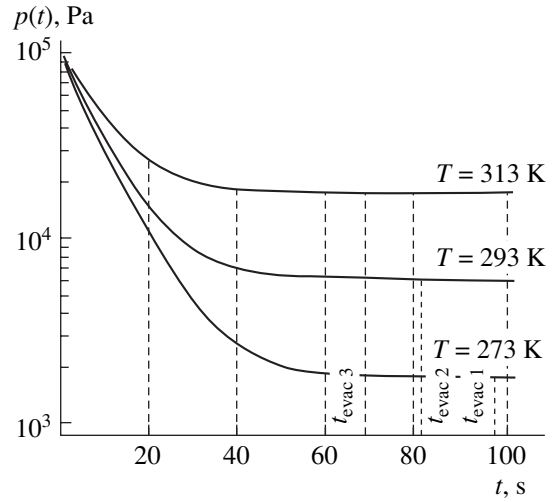

Fig. 4. Time variation of the total pressure in the vacuum chamber for different temperatures.

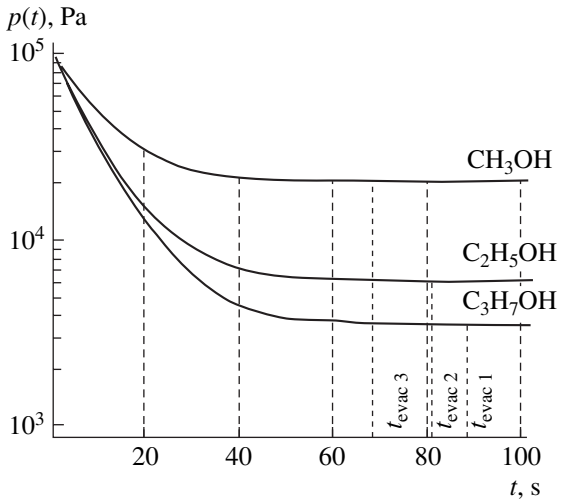

Fig. 5. Time variation of the total pressure in the vacuum chamber for different alcohols.

$$+ p_{c0}\exp\left(-\left[\frac{N_a AkT}{V\sqrt{2\pi MRT}} + \frac{S}{V}\right]t\right),$$

$$p_s(t) = \frac{Q_g}{S}\left[1 - \exp\left(-\frac{S}{V}t\right)\right] + p_{s0}\exp\left[1 - \exp\left(-\frac{S}{V}\right)t\right]. \quad (10)$$

The total instantaneous pressure in the vacuum chamber is the sum of p_c and p_s,

$$p(t) = \frac{q_d AkT\sqrt{2\pi MRT}}{N_a AkT + S\sqrt{2\pi MRT}} \times \left[1 - \exp\left(-\left[\frac{N_a AkT}{V\sqrt{2\pi MRT}} + \frac{S}{V}\right]t\right)\right] + p_{c0}\exp\left(-\left[\frac{N_a AkT}{V\sqrt{2\pi MRT}} + \frac{S}{V}\right]t\right) + \frac{Q_g}{S}\left(1 - \exp\left(-\frac{S}{V}t\right)\right) + p_{s0}\exp\left(-\frac{S}{V}t\right). \quad (11)$$

Calculation of the parameters and analysis of the dependences. Calculation by formula (11) was carried out for methanol, ethanol, and isopropanol using the values of the parameters and constants listed in Tables 2 and 3 (unless otherwise stated).

Consider how the parameters appearing in Eq. (11) influence the pressure in the chamber during evacua-

tion. Since the curve $p(t)$ asymptotically tends to equilibrium value p_∞, it is reasonable to take the evacuation duration in engineering calculations as the interval between the initial instant of evacuation (from the atmospheric pressure) and the time the pressure reaches given fraction α of the equilibrium pressure (say, $\alpha = 0.999$). The equilibrium pressure is determined from the formula

$$p_\infty = \frac{q_d AkT\sqrt{2\pi MRT}}{N_a AkT + S\sqrt{2\pi MRT}} + \frac{Q_g}{S}, \quad (12)$$

and evacuation time T_{evac} is found by solving the equation

$$p(t) = \alpha p_\infty. \quad (13)$$

Since Eq. (13) cannot be solved analytically, the evacuation time was determined numerically or graphically. Figure 2 shows the evacuation curves for different rates of evacuation S. It is distinctly seen that parameter S has a significant effect both on the equilibrium pressure value and on the time of evacuation. This is because this parameter enters into the exponent in formula (11). Under these conditions, the time of evacuation varies with frequency by a near-linear law.

Surface area A of the liquid affects the time of evacuation only slightly. Under the conditions corresponding to Tables 2 and 3, the residual pressure in the chamber decreases when A is below 30 cm^2, as follows from Fig. 3.

With an increase in alcohol temperature T, the residual pressure increases considerably. The time of evacuation also increases, though insignificantly, because of a rise in the alcohol saturated vapor pressure and rate of evaporation (Fig. 4). The sort of alcohol also markedly influences the residual pressure and time of evaporation (through parameters M and E_d), because the heat of vaporization grows and the saturated vapor pressure declines with increasing alcohol molar weight (Fig. 5).

The consumption of various liquids for the mean time of a test cycle, $t = 4$ min, is also of great practical importance. It is proportional to the integral of the partial vapor pressure over time of experiment and to the rate of evacuation. The corresponding results of calculation are summarized in Table 2.

CONCLUSIONS

In our work, we developed a mathematical model of pressure variation in a vacuum chamber containing a source of a volatile liquid. Unlike the conventional computational procedures, this model allows for the variation of gas liberation (including evaporation) with pressure and time. Analyzing the results obtained in this work, we found that the rate of evacuation, as well as the temperature and sort of liquid, are the key factors influencing the duration of evacuation and equilibrium pressure. At the same time, the surface area of the liquid exposed to a vacuum affects the rate of evacuation and equilibrium pressure insignificantly. The model makes it possible to control the leak detection process and substantially raises the accuracy of a quantitative estimate of the leakage. In addition, it allows engineers to optimize a vacuum system and technological process at the design stage.

ACKNOWLEDGMENTS

This work was supported by INTAS (grant no.YSF-2002-164D), a grant of the President of the Russian Federation in support of young Russian scientists (grant no. MK-763.2003.08), and a grant of the Ministry of Education and Science of the Russian Federation (the program “Advancement of Scientific Potential of Higher Schools” 2005).

REFERENCES

1. E. A. Deulin, *Design of Vacuum Equipment* (MGTU, Moscow, 2003) [in Russian].
2. *Handbook of Physical Quantities*, Ed. by I. S. Grigoriev and E. Z. Meilikhov (Énergoatomizdat, Moscow, 1991; CRC, Boca Raton, 1997).

Translated by V. Isaakyan

Technical Physics, Vol. 50, No. 10, 2005, pp. 1259–1267. Translated from Zhurnal Tekhnicheskoĭ Fiziki, Vol. 75, No. 10, 2005, pp. 9–17.

GASES AND LIQUIDS

Nonlinear Capillary–Gravitational Periodic Waves on the Charged Surface of a Finite-Thickness Viscous Liquid

A. V. Klimov, D. F. Belonozhko, and A. I. Grigor'ev

Demidov State University, Sovetskaya ul. 14, Yaroslavl, 150000 Russia

e-mail: grig@uniyar.ac.ru

Received February 16, 2005

Abstract—An analytical expression for the time evolution of the profile of a nonlinear periodic capillary–gravitational wave traveling over the charged surface of a viscous incompressible finite-thickness liquid is found. The calculation is carried out in the second order of smallness in wave amplitude. It is shown that the dependence of a nonlinear correction to a linear solution on the liquid viscosity and liquid layer thickness changes qualitatively in going from thick to thin liquid layers. *© 2005 Pleiades Publishing, Inc.*

(1) The nonlinear periodic capillary–gravitational wave flow of liquid is a wide-spread phenomenon in nature and technology and so is of both scientific and applied interest. A great variety of publications have been concerned with theoretical and experimental investigation of this phenomenon, starting from the latter half of the 19th century. Taking into consideration the viscosity of the liquid, presence of the surface charge, and finiteness (rather than smallness!) of the liquid layer thickness makes the problem still more challenging. A number of comprehensive studies devoted to nonlinear periodic waves on the charged free surface of an indefinitely deep ideal liquid [1–4] and on the charged free surface of a viscous liquid [5, 6] have recently been performed. Most of the studies dealing with nonlinear waves on a viscous liquid have been carried out in the shallow water approximation, when the ratio of the wavelength to the liquid film thickness is a small parameter of the problem (see, e.g., [7–10]). Such a simplification is sound but not universally true [11] and in most cases leads to mere derivation of nonlinear equations with soliton solutions [7–9].

The aim of this work is to (i) gain insight into nonlinear periodic capillary–gravitational waves on the surface of a viscous conducting liquid of finite thickness, (ii) find an analytical solution that is valid for layers of arbitrary thickness and allows for extrapolation to thin layers, and (iii) analyze the combined effect of viscosity and finite thickness on the nonlinear wave flow.

(2) Let a perfectly conducting incompressible liquid with density ρ, kinematic viscosity ν, and surface tension coefficient γ occupy an infinite (in the $x0y$ plane) layer $-d \le z \le 0$ in the gravitational field $\mathbf{g} \| -\mathbf{n}_z$. The origin of the Cartesian coordinate system (x, y, z) is on the undisturbed free surface of the liquid ($\mathbf{n}_z$ is the unit normal vector along the z axis), which is subjected to uniform electric field $\mathbf{E}_0$ pointing downward. A wave of amplitude α that is taken to be smaller than the wavelength and much smaller than capillary constant $a \equiv \sqrt{\gamma/\rho g}$ of the liquid propagates over the surface in the positive $0x$ direction. Ratio α/a defines a small parameter of the problem ε. Physical quantities ρ, ν, γ, g, d, E_0, α, and wavenumber k are assumed to be constant. Also, all the space-dependent variables are assumed to be y independent.

In view of the aforesaid, the nonlinear periodic capillary–wave flow on the uniformly charged surface of a viscous conducting liquid is mathematically described as follows:

$$
\begin{aligned}
&-d \le z \le \xi\colon \frac{\partial \mathbf{U}}{\partial t} + (\nabla \times \mathbf{U}) \times \mathbf{U} \\
&= -\nabla\left(\frac{1}{\rho}p + \frac{1}{2}U^2 + gz\right) + \nu\Delta\mathbf{U}; \quad \nabla \cdot \mathbf{U} = 0; \\
&z \ge \xi\colon \Delta\Phi = 0; \quad z \longrightarrow \infty\colon \nabla\Phi = -E_0 \cdot \mathbf{n}_z; \\
&z = \xi\colon \frac{\partial \xi}{\partial t} + u\frac{\partial \xi}{\partial x} = w; \\
&\boldsymbol{\tau} \cdot (\mathbf{n} \cdot \nabla)\mathbf{U} + \mathbf{n} \cdot (\boldsymbol{\tau} \cdot \nabla)\mathbf{U} = 0; \\
&p - 2\rho\nu\mathbf{n} \cdot (\mathbf{n} \cdot \nabla)\mathbf{U} + \frac{(\nabla\Phi)^2}{8\pi} \\
&= -\gamma\frac{\partial^2 \xi}{\partial x^2}\left(1 + \left(\frac{\partial \xi}{\partial x}\right)^2\right)^{-3/2}; \quad \Phi = 0; \\
&z = -d\colon u = 0; \quad w = 0.
\end{aligned}
\tag{1}
$$

Here, $\xi = \xi(x, t)$ is the deviation of the free surface from the equilibrium (flat) shape given by $z = 0$ due to the wave flow, $\mathbf{U} = (u, 0, w)$ is the velocity field of the liquid, $p(\mathbf{r}, t)$ is the hydrodynamic pressure inside the liquid, $\Phi(\mathbf{r}, t)$ is the electric field potential, $\mathbf{n}$ and $\boldsymbol{\tau}$ are the unit vectors that are normal and tangent to the free surface disturbed by the wave flow, and Δ is the Laplacian.

1063-7842/05/5010-1259$26.00

As is custom in calculations of the nonlinear periodic wave flow [3–6], initial conditions are selected such that a final solution has a form that is as simple as possible. For example, we may assume that, in the first approximation in small wave amplitude α, the disturbance of the free surface has the form of a harmonic wave traveling along the abscissa axis,

$$\xi(x, t) = 2\alpha\exp(St - ikx) + \text{c.c.} + o(\alpha), \qquad (1a)$$

where S is the complex frequency of the wave and c.c. is the complex conjugate.

Since the problem to be solved is extremely cumbersome, we will derive only an analytical expression for the profile of nonlinear waves on the liquid surface. Other desired quantities (the velocity field of the flow in the layer and the distributions of the pressure in and of the electric potential over the liquid) will be found during calculation (however, their final forms are too awkward and so will be omitted).

(3) In the zeroth approximation, the free surface is undisturbed, $\xi_0(x, t) = 0$. The velocity and pressure fields in the liquid, as well as the electric potential distribution over the liquid, are found from (1),

$$u_0 = w_0 = 0; \quad p_0 = -\frac{E_0^2}{8\pi} - \rho g z; \quad \Phi_0 = -E_0 z.$$

A solution to problem (1) will be sought as the expansions of the unknown components of free surface profile ξ, velocity field $(u, 0, w)$, pressure p, and electric potential Φ in powers of the small parameter,

$$\begin{gathered}\xi = \varepsilon\xi_1 + \varepsilon^2\xi_2 + O(\varepsilon^3); \quad u = \varepsilon u_1 + \varepsilon^2 u_2 + O(\varepsilon^3);\\ w = \varepsilon w_1 + \varepsilon^2 w_2 + O(\varepsilon^3);\\ p = p_0 + \varepsilon p_1 + \varepsilon^2 p_2 + O(\varepsilon^3);\\ \Phi = \Phi_0 + \varepsilon\Phi_1 + \varepsilon^2\Phi_2 + O(\varepsilon^3).\end{gathered} \qquad (2)$$

Now we substitute expressions (2) into (1) and partition the problem into subproblems of various orders of smallness.

(4a) In the first order of smallness, we obtain

$$\begin{gathered}-d \le z \le 0: \quad \frac{\partial \mathbf{U}_1}{\partial t} + \nabla\left(\frac{1}{\rho}p_1\right) - \nu\Delta\mathbf{U}_1 = 0;\\ \nabla\cdot\mathbf{U}_1 = 0;\\ z \ge 0: \Delta\Phi_1 = 0;\\ z \to \infty: |\nabla\Phi_1| \to 0; \quad \Phi_1 - E_0\xi_1 = 0;\\ z = 0: \frac{\partial\xi_1}{\partial t} - w_1 = 0; \quad \frac{\partial u_1}{\partial z} + \frac{\partial w_1}{\partial x} = 0;\\ -\rho g\xi_1 + p_1 - 2\rho\nu\frac{\partial w_1}{\partial z} - \frac{E_0}{4\pi}\frac{\partial\Phi_1}{\partial z} + \gamma\frac{\partial^2\xi_1}{\partial x^2} = 0;\\ z = -d: \quad u_1 = 0; \quad w_1 = 0,\end{gathered} \qquad (3)$$

where $\mathbf{U}_1$ is vector field $(u_1, 0, w_1)$.

(4b) It is easy to check that the continuity equations, Navier–Stokes equations, and pressure field can be expressed through velocity field potential φ_1 and stream function ψ_1 as follows:

$$\begin{gathered}\Delta\varphi_1 = 0; \quad \frac{\partial\psi_1}{\partial t} - \nu\Delta\psi_1 = 0; \quad u_1 = \frac{\partial\varphi_1}{\partial x} - \frac{\partial\psi_1}{\partial z};\\ w_1 = \frac{\partial\varphi_1}{\partial z} + \frac{\partial\psi_1}{\partial x}; \quad p_1 = -\rho\frac{\partial\varphi_1}{\partial t}.\end{gathered} \qquad (3a)$$

In the complex form, free surface profile ξ_1 is represented as a traveling wave,

$$\xi_1(x, t) = \zeta\exp(St - ikx), \qquad (4)$$

where amplitude factor ζ is expressed through amplitude α of the initial wave.

Eventually, the solution of the first-order subproblem is reduced to finding unknowns φ_1, ψ_1, Φ_1, and complex frequency S.

Expressions for velocity potential φ_1, stream function ψ_1, and electric potential Φ_1 will be sought in a form similar to the form of ξ_1,

$$\begin{aligned}\varphi_1(x, z, t) &= B(z)\exp(St - ikx);\\ \psi_1(x, z, t) &= C(z)\exp(St - ikx);\\ \Phi_1(x, z, t) &= A(z)\exp(St - ikx);\end{aligned} \qquad (5)$$

where A, B, and C are amplitudes to be found.

Substituting expressions (4) and (5) into (3) and (3a) yields desired electric potential Φ_1, pressure p_1, and velocity field components u_1 and w_1:

$$\begin{aligned}\Phi_1 &= E_0\zeta\exp(St - ikx - kz);\\ p_1 &= -\frac{i\rho S}{k}\zeta(\sigma_2 q\cosh(k(z + d))\\ &\quad + \sigma_1\sinh(k(z + d)))\exp(St - ikx);\\ u_1 &= \zeta(\sigma_2 q\cosh(k(z + d))\\ &\quad + \sigma_1 k\sinh(k(z + d)) - \sigma_2 q\cosh(q(z + d))\\ &\quad - \sigma_1 q\sinh(q(z + d)))\exp(St - ikx);\\ w_1 &= i\zeta(\sigma_1 k\cosh(k(z + d))\\ &\quad + \sigma_2 q\sinh k(z + d) - \sigma_1 k\cosh(q(z + d))\\ &\quad - \sigma_2 k\sinh(q(z + d)))\exp(St - ikx);\\ q &= \sqrt{k^2 + S/\nu}.\end{aligned} \qquad (6)$$

Frequency S can be determined from the dispersion relation [12]

$$\begin{gathered}\mathrm{Det}M = 0; \quad \omega_0^2 = gk\left(1 + \frac{\gamma}{\rho g}k^2 - \frac{E_0^2}{4\pi\rho g}k\right);\\ \beta \equiv kd; \quad \zeta \equiv qd;\end{gathered}$$

$$M = \begin{pmatrix} k & 0 & 0 & -q & 0 \\ 0 & 1 & -1 & 0 & 0 \\ -\sinh(\beta) & -\cosh(\beta) & \cosh(\xi) & \sinh(\xi) & S \\ (k^2+q^2)\cosh(\beta) & (k^2+q^2)\sinh(\beta) & -2kq\sinh(\zeta) & -2kq\cosh(\zeta) & \nu^{-1}\omega_0^2 \\ -2k^2\sinh(\beta) & -2k^2\cosh(\beta) & (k^2+q^2)\cosh(\zeta) & (k^2+q^2)\sinh(\zeta) & 0 \end{pmatrix},$$

and constants σ_1 and σ_2 have the form

$$\sigma_1 \equiv \frac{i\nu(2\zeta\sinh(\beta) - (k^2+q^2)\sinh(\zeta))}{q\cosh(\zeta)\sinh(\beta) - k\cosh(\beta)\sinh(\zeta)},$$

$$\sigma_2 \equiv \frac{i\nu(2k^2\cosh(\beta) - (k^2+q^2)\cosh(\zeta))}{q\cosh(\zeta)\sinh(\beta) - k\cosh(\xi)\sinh(\zeta)}.$$

Importantly, we have found the solution to the first-order subproblem in the complex form with initial condition (4). To reduce the solution to the real form of type (1a), it is necessary to complement found quantities (6) by their complex conjugates and put $\zeta = 2\alpha$.

(5) In the second-order of smallness, we obtain the subproblem stated as

$$-d \le z \le 0: \nabla \cdot \mathbf{U}_2 = 0; \tag{7}$$

$$\frac{\partial \mathbf{U}_2}{\partial t} + \nabla\left(\frac{1}{\rho}p_2\right) - \nu\Delta\mathbf{U}_2 = -\frac{1}{2}\nabla(U_1^2) - (\nabla\times\mathbf{U}_1)\times\mathbf{U}_1; \tag{8}$$

$$z \ge 0: \Delta\Phi_2 = 0; \tag{9}$$

$$z = 0: \frac{\partial\xi_2}{\partial t} - w_2 = \xi_1\frac{\partial w_1}{\partial z} - u_1\frac{\partial\xi_1}{\partial x}; \tag{10}$$

$$\Phi_2 - E_0\xi_2 = -\xi_1\frac{\partial\Phi_1}{\partial z}; \tag{11}$$

$$-\rho g\xi_2 + p_2 - 2\rho\nu\frac{\partial w_2}{\partial z} - \frac{E_0}{4\pi}\frac{\partial\Phi_2}{\partial z} + \gamma\frac{\partial^2\xi_2}{\partial x^2} = 2\rho\nu\xi_1\frac{\partial^2 w_1}{\partial z^2} - \xi_1\frac{\partial p_1}{\partial z} - \frac{1}{8\pi}\left(\left(\frac{\partial\Phi_1}{\partial x}\right)^2 + \left(\frac{\partial\Phi_1}{\partial z}\right)^2\right) \tag{12}$$

$$+\frac{E_0}{4\pi}\xi_1\frac{\partial^2\Phi_1}{\partial z^2} - 2\rho\nu\frac{\partial\xi_1}{\partial x}\frac{\partial u_1}{\partial z} - 2\rho\nu\frac{\partial\xi_1}{\partial x}\frac{\partial w_1}{\partial x};$$

$$\frac{\partial u_2}{\partial z} + \frac{\partial w_2}{\partial x} = 2\frac{\partial\xi_1}{\partial x}\frac{\partial u_1}{\partial x} - 2\frac{\partial\xi_1}{\partial x}\frac{\partial w_1}{\partial z} - \xi_1\frac{\partial^2 w_1}{\partial x\partial z} - \xi_1\frac{\partial^2 u_1}{\partial z^2}; \tag{13}$$

$$z = -d: u_2 = 0; \quad w_2 = 0; \tag{14}$$

$$z \to \infty: |\nabla\Phi_2| \to 0, \tag{15}$$

where $\mathbf{U}_2 = (u_2, 0, w_2)$.

(5a) The second-order subproblem represents a set of inhomogeneous linear partial differential equations. According to a rule common in perturbation techniques, when a problem is solved by the small parameter method, first a general solution to the first-order subproblem and then a partial solution to the second-order subproblem are found. It is known that a partial solution of a set of differential equations is found in the form similar to that of their right-hand sides (inhomogeneities). Therefore, it is necessary first to calculate the right-hand sides of expressions (7), (8), and (10)–(13). This is done by substituting expressions (8) into these expressions. In doing so, one should bear in mind that quantities Φ_1, p_1, u_1, w_1, and ξ_1 have complex conjugate terms.

The inhomogeneous set of Eqs. (7) and (8) is convenient to write in the matrix form, where the vector function of an inhomogeneity will have the form

$$F_j = \alpha^2\exp((S+\bar{S})t)\sum_{i=1}^{5}(A_{ji}\cosh(Q_i(d+z)) + H_{ji}\sinh(Q_i(d+z))) + \alpha^2\exp(2St - 2ikx) \times V_{j0} + \sum_{i=1}^{2}(Z_{ji}\cosh(Q_i(d+z)) + C_{ji}\sinh(Q_i(d+z))) + \text{c.c.}; \tag{16}$$

$$Q_1 = k+q; \quad Q_2 = k-q, \quad Q_3 = q+\bar{q}, \quad Q_4 = q-\bar{q}, \quad Q_5 = 2k.$$

Here, A_{ji}, H_{ji}, V_{ji}, and C_{ji} are 3×5 matrices with coefficients independent of time and spatial coordinates.

Their associated formulas are awkward and therefore omitted. However, their explicit form can easily be restored by substituting first-order solutions (6) into the right-hand sides of (7) and (8).

The vector function of inhomogeneity for set (10)–(13) has the form

$$\begin{aligned} G_j &= \alpha^2 \exp((S+\bar{S})t)(N_{j0} + N_{j1}\cosh(dk) \\ &+ U_{j1}\sinh(dk) + N_{j2}\cosh(dq) + U_{j2}\sinh(dq)) \\ &+ \alpha^2(\exp(2St - 2ikx)(M_{j0} + M_{j1}\cosh(dk) \\ &+ T_{j1}\sinh(dk) + M_{j2}\cosh(dq) + T_{j2}\sinh(dq))) + \text{c.c.}, \end{aligned} \tag{17}$$

where N_{ji}, U_{ji}, M_{ji}, and T_{ji} are 4×3 matrices.

Their associated formulas are awkward and therefore omitted. However, their explicit form can easily be restored by substituting first-order solutions (6) into the right-hand sides of Eqs. (10)–(13).

(5b) A solution to the second-order subproblem involves analytical expressions for unknowns Φ_2, p_2, u_2, w_2, and ξ_2. To proceed further, we will represent quantities u_2, w_2, and p_2 in the form of the sum

$$(u_2, v_2, p_2) = (u_2^+, w_2^+, p_2^+) + (u_2^*, w_2^*, p_2^*), \tag{18}$$

where the first term of this sum, (u_2^+, w_2^+, p_2^+), which will be hereafter called the "inflexible" part of the solution, is a partial solution to set (7)–(8) and the second term, (u_2^*, w_2^*, p_2^*), together with quantities Φ_2 and ξ_2, constitutes the so-called flexible part of the solution. This part is based on a solution to the homogeneous set that corresponds to inhomogeneous set (7)–(8) and contains two arbitrary constants, which are selected so that sum (18) satisfies boundary conditions (10)–(15).

First, we will determine the flexible part of the solution. In view of the form of inhomogeneity function F_{ji}, it should be sought in the form

$$\begin{aligned} (u_2^+, w_2^+, p_2^+) &= \alpha^2 \exp((S+\bar{S})t) \\ &\times \sum_{i=1}^{5} (a_{ji}\cosh(Q_i(d+z)) + h_{ji}\sinh(Q_i(d+z))) \\ &+ \alpha^2 \exp(2St - 2ikx)\left(g_{j0} + \sum_{i=1}^{2} (g_{ji}\cosh(Q_i(d+z)) \right. \\ &\left. + c_{ji}\sinh(Q_i(d+z)))\right) + \text{c.c.}, \end{aligned} \tag{19}$$

where a_{ji}, h_{ji}, g_{ji}, and c_{ji} are unknown 3×5 matrices with coefficients independent of time and spatial coordinates.

To find these matrices, it is necessary to substitute (19) into the set of Eqs. (7) and (8), the right-hand side of which has the form (16), and equate the coefficients multiplying identical expressions in the resulting system,

$$\exp(\Omega t - iKx)\cosh(Q(d+z));$$

$$\exp(\Omega t - iKx)\sinh(Q(d+z)),$$

to zero.

In this case, Eqs. (7) and (8) split into sets of simple algebraic equations from which the components of unknowns a_{ji}, h_{ji}, g_{ji}, and c_{ji} can be easily found.

In terms of linear transformations, these unknown matrices are found from matrices A_{ji}, H_{ji}, V_{ji}, and C_{ji} by applying a linear operator that is specified by matrices depending on parameters

$$L_1(K, Q, \Omega) = \frac{1}{(K^2 - Q^2)(\nu(K^2 - Q^2) + \Omega)}$$

$$\times \begin{pmatrix} -Q^2 & 0 & iK(\nu(K^2 - Q^2) + \Omega) \\ 0 & K^2 & 0 \\ i\rho K(\nu(K^2 - Q^2) + \Omega) & 0 & \rho(\nu(K^2 - Q^2) + \Omega^2) \end{pmatrix};$$

$$L_2(K, Q, \Omega) = \frac{Q}{(K^2 - Q^2)(\nu(K^2 - Q^2) + \Omega)}$$

$$\times \begin{pmatrix} 0 & iK & 0 \\ iK & 0 & \nu(K^2 - Q^2) + \Omega \\ 0 & \rho(\nu(K^2 - Q^2) + \Omega) & 0 \end{pmatrix}.$$

This linear transformation is stated as follows:

$$a_{ji} = L_1(0, Q_i, S + \bar{S})A_{ji} + L_2(0, Q_i, S + \bar{S})H_{ji},$$

$$h_{ji} = L_1(0, Q_i, S + \bar{S})H_{ji} + L_2(0, Q_i, S + \bar{S})A_{ji},$$

$$g_{ji} = L_1(2k, Q_i, 2S)V_{ji} + L_2(2k, Q_i, 2S)C_{ji},$$

$$c_{ji} = L_1(2k, Q_i, 2S)C_{ji} + L_2(2k, Q_i, 2S)V_{ji}.$$

These expressions should be substituted into (19) to find u_2^+, w_2^+, and p_2^+ in the final form.

The flexible part of the solution to the second-order subproblem is a solution to set (7)–(8) with the zero right-hand side. In such a representation, Eqs. (7) and (8) are equivalent to the following set of equations for the potentials and stream functions:

$$\begin{aligned} \Delta\varphi_2^* = 0; \quad \frac{\partial\psi_2^*}{\partial t} - \nu\Delta\psi_2^* = 0; \quad u_2^* = \frac{\partial\varphi_2^*}{\partial x} - \frac{\partial\psi_2^*}{\partial z}; \\ w_2^* = \frac{\partial\varphi_2^*}{\partial z} + \frac{\partial\psi_2^*}{\partial x}; \quad p_2^* = -\rho\frac{\partial\varphi_2^*}{\partial t}. \end{aligned} \tag{20}$$

Since the inhomogeneities of Eqs. (7) and (8), which are determined by equalities (16), are linear combinations of factors $\exp((S + \bar{S})t)$ and $\exp(2St - 2ikx)$, the

flexible part of the subproblem should be sought in the form

$$\begin{aligned}\xi_2 &= \alpha^2\exp((S+\bar{S})t)Z_0\\ &+\alpha^2\exp(2St-2ikx)Z_1+\text{c.c.};\\ (\varphi_2^*,\psi_2^*,\Phi_2) &= \alpha^2\exp((S+\bar{S})t)A_0(z)\\ &+\alpha^2\exp(2St-2ikx)A_1(z)+\text{c.c.},\end{aligned}\tag{21}$$

where Z_i are unknown constants and $A_i(z)$ are three-element columns of unknown constants.

Substitution of expressions (21) into relationships (7), (9), (15), and (20) makes it possible to refine the form of functions A_i and express u_2^*, w_2^*, and p_2^*,

$$\begin{aligned}\Phi_2 &= \alpha^2 a_0\exp((S+\bar{S})t)\\ &+\alpha^2 a_1\exp(2St-2ikx-2kz)+\text{c.c.};\\ (u_2^*,w_2^*,p_2^*)^T &= \alpha^2\exp((S+\bar{S})t)(b_{00}f_0+b_{10}j_0\\ &+b_{10}f_0(d+z)+c_{00}p_0\sinh(w_0(d+z))\\ &+c_{10}p_0\cosh(w_0(d+z)))+\alpha^2\exp(2St-2ikx)\\ &\times(b_{01}(f_1\cosh(2k(d+z))+h_1\sinh(2k(d+z)))\\ &+b_{11}(h_1\cosh(2k(d+z))+f_1h(2k(d+z)))\\ &+c_{01}(n_1\cosh(w_1(d+z))+p_1\sinh(w_1(d+z)))\\ &+c_{11}(p_1\cosh(w_1(d+z))+n_1\sinh(w_1(d+z)))+\text{c.c.}\end{aligned}\tag{22}$$

Here, a_0, a_1, b_{00}, b_{01}, b_{10}, b_{11}, c_{00}, c_{01}, c_{10}, and c_{11} are unknown constants that can be found from boundary conditions (10)–(15),

$$w_0=\sqrt{\frac{S+\bar{S}}{\nu}},\quad w_1=\sqrt{4k^2+\frac{2S}{\nu}},$$

$$f_0=\begin{pmatrix}0\\0\\-\rho(S+\bar{S})\end{pmatrix},\quad j_0=\begin{pmatrix}0\\1\\0\end{pmatrix},$$

$$p_0=\begin{pmatrix}-w_0\\0\\0\end{pmatrix},\quad f_1=\begin{pmatrix}-2ik\\0\\-2\rho S\end{pmatrix},\quad h_1=\begin{pmatrix}0\\2k\\0\end{pmatrix},$$

$$n_1=\begin{pmatrix}0\\-2ik\\0\end{pmatrix},\quad p_1=\begin{pmatrix}-w_0\\0\\0\end{pmatrix}.$$

(5c) To make the following mathematics more compact and illustrative, we represent boundary conditions (10)–(15) of the second second-order subproblem ($z = 0$) in the matrix form,

$$B(u_2,w_2,p_2,\Phi_2)+\Xi\xi_2=G_j;$$

$$B(u,w,p,\Phi)=\left(\begin{pmatrix}0&-1&0&0\\0&-2\rho\nu\dfrac{\partial}{\partial z}&1&\dfrac{-E_0}{4\pi}\dfrac{\partial}{\partial z}\\\dfrac{\partial}{\partial z}&\dfrac{\partial}{\partial x}&0&0\\0&0&0&1\end{pmatrix}\begin{pmatrix}u\\w\\p\\\Phi\end{pmatrix}\right)_{z=0};$$

$$\Xi=\begin{pmatrix}\dfrac{\partial}{\partial t}\\-\rho g+\gamma\dfrac{\partial^2}{\partial x^2}\\0\\-E_0\end{pmatrix}.$$

Here, B is the linear operator, Ξ is the vector-by-scalar multiplication operator, and G_j is defined by expression (17). Operator Ξ acts as follows:

$$\begin{aligned}\Xi\xi_2 &= \alpha^2\exp((S+\bar{S})t)Z_0Y_0\\ &+\alpha^2\exp(2St-2ikx)Z_1Y_1+\text{c.c.};\\ Y_0 &= (S+\bar{S},-\rho g,0,-E_0)^T;\\ Y_1 &= (2S,-\rho g-4\gamma k^2,0,-E_0)^T,\end{aligned}\tag{23}$$

where superscript T means matrix transposition.

The action of operator B on expressions of type

$$\begin{aligned}(u,w,p)^T &= \exp(\Omega t-iKx)\\ &\times(A_j\cosh(Q(d+z))+H_j\sinh(Q(d+z)));\\ \Phi &= \varphi\exp(\Omega t-iK(x-z)),\end{aligned}$$

where Ω, K, and Q are constants and A_j and H_j are three-element columns, has the form

$$\begin{aligned}B(u,w,p,\Phi) &= \exp(\Omega t-iKx)((B_1(K)A_j+B_2(Q)H_j)\\ &\times\cosh dQ+(B_1(K)H_j+B_2(Q)A_j)\sinh dQ+\varphi E(K));\end{aligned}$$

where

$$E(K)=\begin{pmatrix}0\\\dfrac{E_0K}{4\pi}\\0\\1\end{pmatrix},$$

$$B_1(K) = \begin{pmatrix} 0 & -1 & 0 \\ 0 & 0 & 1 \\ 0 & -iK & 0 \\ 0 & 0 & 0 \end{pmatrix}; \quad B_2(Q) = \begin{pmatrix} 0 & 0 & 0 \\ 0 & -2\nu\rho Q & 0 \\ Q & 0 & 0 \\ 0 & 0 & 0 \end{pmatrix}.$$

By virtue of equality (18), we have

$$B(u_2^*, w_2^*, p_2^*, \Phi_2) + \Xi\xi_2 = G_j - B(u_2^+, w_2^+, p_2^+, 0). \quad (24)$$

Taking into account the known expressions for the quantities appearing in the flexible part of the solution (see (21) and (22)) and (23), we can write the left of (24) as

$$\begin{aligned} &B(u_2^*, w_2^*, p_2^*, \Phi_2) + \Xi\xi_2 \\ &= \alpha^2 \exp((S+\bar{S})t)(B_1(0)((b_{00}+b_{10}d)f_0 + b_{10}j_0) \\ &+ b_{10}B_2(1)f_0 + (c_{10}B_1(0) + c_{00}B_2(w_0))p_0\cosh(dw_0) \\ &+ (c_{00}B_1(0) + c_{10}B_2(w_0))p_0\sinh(dw_0) + a_0E(0) \\ &+ Z_0Y_0) + \alpha^2\exp(2St - 2ikx)((B_1(2k)(b_{01}f_1 + b_{11}h_1) \\ &+ B_2(2k)(b_{01}h_1 + b_{11}f_1))\cosh(2dk) + (B_1(2k)(b_{01}h_1 \\ &+ b_{11}f_1) + B_2(2k)(b_{01}f_1 + b_{11}h_1))\sinh(2dk) \\ &+ (B_1(2k)(c_{01}n_1 + c_{11}p_1) + B_2(w_1)(c_{01}p_1 + c_{11}n_1)) \\ &\times\cosh(dw_1) + (B_1(2k)(c_{01}p_1 + c_{11}n_1) + B_2(w_1) \\ &\times(c_{01}n_1 + c_{11}p_1))\sinh(dw_1) + a_1E(2k) + Z_1Y_1) + \text{c.c.} \end{aligned} \quad (25)$$

Substituting (17) and (19) into the right of (24) yields

$$\begin{aligned} &G_j - B(u^+, w^+, p^+, 0) \\ &= \alpha^2\exp((S+\bar{S})t)(N_{j0} + N_{j1}\cosh(dk) + U_{j1}\sinh(dk) \\ &+ N_{j2}\cosh(dq) + U_{j2}\sinh(dq) - \sum_{i=1}^{5}((B_1(0)a_{ji} \\ &+ B_2(Q_i)h_{ji})\cosh(dQ_i) + (B_1(0)h_{ji} + B_2(Q_i)a_{ji}) \\ &\times\sinh(dQ_i))) + \alpha^2\exp(2St - 2ikx)(M_{j0} + M_{j1} \\ &\times\cosh(dk) + T_{j1}\sinh(dk) + M_{j2}\cosh d(q) \\ &+ T_{j2}\sinh(dq) - B_1(2k)g_{j0} - \sum_{i=1}^{2}((B_1(2k)g_{ji} + B_2(Q_i)c_{ji}) \\ &\times\cosh(dQ_i) + (B_1(2k)c_{ji} + B_2(Q_i)g_{ji})\sinh(dQ_i))) + \text{c.c.} \end{aligned} \quad (26)$$

(5d) Substituting (25) and (26) into (24), collecting the coefficients multiplying $\exp((S+\bar{S})t)$ and $\exp(2St - 2ikx)$, and equating them to zero, we arrive at equations for unknowns a_m, b_{mn}, c_{mn}, and Z_m. Complementing these equations by those resulting from substitution of (18) into boundary condition (14), we come to a set of algebraic equations from which constants a_m, b_{mn}, c_{mn}, and Z_m are uniquely found. Solving the resulting set by the Gauss method, we obtain expressions for Z_0 and Z_1,

$$\begin{aligned} &Z_0 = 0; \quad Z_1 = (2\pi k\nu\rho w_1(8k(S+4k^2\nu)R_{11} \\ &+ i(S+8k^2\nu)R_{13}) + 8\pi k^2\nu\rho w_1SR_{22}\cosh(2dk) \\ &+ 8\pi ik^2\nu\rho w_1SR_{21}\sinh(2dk) - 2\pi\rho w_1S(S+4k^2\nu) \\ &\times R_{22}\cosh(dw_1) - 4\pi ik\rho S(S+4k^2\nu)R_{21}\sinh(dw_1) \\ &- 2\pi\rho w_1((S^2+8k^2\nu S+32k^4\nu^2)R_{11} + ik\nu(S \\ &+ 8k^2\nu)R_{13})\cosh(2dk)\cosh(dw_1) + 4\pi k\rho((S^2 \\ &+ 16k^2\nu S + 32k^4\nu^2)R_{11} + ik\nu(3S+8k^2\nu)R_{13}) \\ &\times\sinh(2dk)\sinh(dw_1) - 2\pi k^2SR_{12}\cosh(2dk) \\ &\times\sinh(dw_1) + \pi kw_1SR_{12}\sinh(2dk)\cosh(dw_1))/\Delta_{Z_1}; \end{aligned}$$

$$\begin{aligned} \Delta_{Z_1} = \pi\rho S\Big(&32k^2\nu w_1(S+4k^2\nu) - 4w_1(S^2+8k^2S \\ &+ 32k^4\nu^2)\cosh(2dk)\cosh(dw_1) \\ &+ 8k(S^2+16k^2\nu S+32k^4\nu^2)\sinh(2dk)\sinh(dw_1) \\ &+ \left(2gk + 8\frac{k^3\gamma}{\rho} - \frac{E_0^2k^2}{\pi\rho}\right) \\ &\times(2k\cosh(2dk)\sinh(dw_1) - w_1\sinh(2dk)\cosh(dw_1))\Big); \end{aligned}$$

$$\begin{aligned} R_{11} = {} &\frac{ik^2}{2}\sigma_1\sinh(dk) - \frac{ikq}{2}\sigma_1\sinh(dq) \\ &+ \frac{ikq}{2}\sigma_2\cosh(dk) - \frac{ikq}{2}\sigma_2\cosh(dq) \\ &- \frac{kS^2\sigma_1\sigma_2\cosh(d(k+q))}{4\nu(S(S-4k^2\nu) - 8k^3\nu^2(k-q))} \\ &+ \frac{k(k-q)S(k\sigma_1^2 + q\sigma_2^2)\sinh(d(k+q))}{4(S(S-4k^2\nu) - 8k^3\nu^2(k-q))} \\ &+ \frac{kS^2\sigma_1\sigma_2\cosh d(k-d)}{4\nu(S(S-4k^2\nu) - 8k^3\nu^2(k+q))} \\ &+ \frac{k(k+q)S(k\sigma_1^2 - q\sigma_2^2)\sinh d(k-q)}{4(S(S-4k^2\nu) - 8k^3\nu^2(k+q))}; \end{aligned} \quad (27)$$

$$R_{12} = -\frac{E_0^2k^2}{8\pi} + \frac{i\rho}{2}(S+6k^2\nu)(q\sigma_2\sinh(dk)$$

$$+ k\sigma_1\cosh(dk)) - i\rho k(2S + 3k^2\nu)$$
$$\times(\sigma_1\cosh(dq) + \sigma_2\sinh(dq))$$
$$-\frac{\rho(S + 2k^2\nu)}{4\nu}\sigma_1^2 + \frac{\rho(S + k^2\nu)}{2\nu}\sigma_2^2$$
$$+\frac{k(3S + 2k(3k - q)\nu)\rho}{2\nu(3k - q)(S + 2k(k + q)\nu)}$$
$$\times(S\sigma_1\sigma_2\sinh(d(k - q)) + \nu(k + q)(k\sigma_1^2 - q\sigma_2^2))$$
$$\times\cosh(d(k - q))) - \frac{k(3S + 2k(3k + q)\nu)\rho}{2\nu(3k + q)(S + 2k(k - q)\nu)}$$
$$\times(S\sigma_1\sigma_2\sinh(d(k + q)) - \nu(k - q)$$
$$\times(k\sigma_1^2 + q\sigma_2^2)\cosh(d(k + q)));$$

$$R_{13} = -k^3\sigma_1\sinh(dk) + k^2q\sigma_1\sinh(dq)$$
$$-k^2q\sigma_2\cosh(dk) + k^2q\sigma_2\cosh(dq)$$
$$-\frac{iS(S + 2k(3k + q)\nu)}{8\nu^2(3k + q)(S + 2k(k - q)\nu)}$$
$$\times((k + q)\sigma_1\sigma_2\cosh(d(k + q)) + (k\sigma_1^2 + q\sigma_2^2)$$
$$\times\sinh(d(k + q))) + \frac{iS(S + 2k(3k - q)\nu)}{8\nu^2(3k - q)(S + 2k(k + q)\nu)}$$
$$\times((k - q)\sigma_1\sigma_2\cosh(d(k - q))$$
$$-(k\sigma_1^2 - q\sigma_2^2)\sinh(d(k - q)));$$

$$R_{21} = -\frac{ik(S(S - 4k^2\nu) - 8k^4\nu^2)}{4\nu S(S - 8k^2\nu)}\sigma_1^2$$
$$+\frac{2ik^3(S + k^2\nu)}{S(S - 8k^2\nu)}\sigma_2^2;$$

$$R_{22} = -\frac{4k^4\nu q}{S(S - 8k^2\nu)}\sigma_1\sigma_2.$$

Substituting expressions (27) into relationship (21) for ξ_2, we reduce it to the real form

$$\xi_2 = 2\alpha^2|Z_1|\exp(2\mathrm{Re}St)$$
$$\times\cos(2\mathrm{Im}St - 2kx + \mathrm{Arg}Z_1).$$

Eventually, for the profile of the nonlinear wave, we obtain the expression

$$\xi(x, t) = \alpha\exp(rt)\cos\theta$$
$$+ 2\alpha^2|Z_1|\exp(2rt)\cos(2\theta + \mathrm{Arg}Z_1); \qquad (28)$$
$$Q \equiv \mathrm{Im}St - kx; \quad r \equiv \mathrm{Re}S,$$

which is accurate up to quantities of the second order of smallness in wave amplitude.

(6) Amplitude factor Z_1 in the nonlinear correction to the wave profile is the most informative parameter of the solution obtained. This factor is complex: its real and imaginary parts depend on the physical parameters of the problem, including the thickness of the layer and viscosity of the liquid. Its absolute value, $|Z_1|$, characterizes the amount of internal nonlinear interaction between the term linear in amplitude α and the term quadratic in α (see expression (28) for the wave profile).

The profile of a traveling wave is frequently an object of interest in studies of nonlinear waves on the liquid surface. Specifically, its parameters, such as the sharpness and slope of the wave ridge, are estimated, which are also determined by factor Z_1. For example, $|Z_1|$ is a measure of skewness of the nonlinear wave profile relative to the strictly cosinusoidal shape. As $|Z_1|$ grows, blunted capillary waves become still more blunted, while gravitational waves, which have a sharper profile, become still sharper.

Ratio $\mathrm{Im}(Z_1)/\mathrm{Re}(Z_1)$, specifying the argument of complex quantity Z_1, also characterizes the skewness of the wave profile relative to the symmetric cosinusoidal shape: if $\mathrm{Im}(Z_1)/\mathrm{Re}(Z_1) < 0$, the profile is skewed in the direction of wave propagation; if $\mathrm{Im}(Z_1)/\mathrm{Re}(Z_1) > 0$, the profile is skewed in the opposite direction.

Figures 1–6 plot $|Z_1|$ and ratio $\mathrm{Im}(Z_1)/\mathrm{Re}(Z_1)$ versus dynamic viscosity η at $E_0 = 0$ for different thicknesses of the water layer ($\rho = 0.998$ g/cm^3, $\gamma = 72.8$ dyn/cm, $g = 981$ cm/s^2). It is known that capillary waves on the surface of a deep ideal liquid have blunted ridges. In the finite-thickness layer, the ridges of the waves sharpen with increasing viscosity, as follows from Fig. 1. Moreover, they become skewed in the direction opposite to the wave propagation, the skew growing with viscosity. As the layer gets thinner, the reverse effect is observed: the ridges become more blunt and the skew opposite to the direction of wave propagation disappears. The decrease in the layer thickness to 0.1λ, where λ is the wavelength, changes qualitatively the run of the curves. First, the radius of curvature of the ridges increases with the viscosity (Fig. 2) and, second, the waves become skewed in the direction of wave propagation. Moreover, in such a shallow liquid, the viscosity dependence of their skew becomes nonmonotonic, unlike in the deep liquid: as the viscosity grows, the skew initially increases and then starts declining and changes sign.

For short gravitational waves, these dependences are somewhat different: in thick ($d \gg 0.1\lambda$) and thin ($d \le 0.1\lambda$) liquid layers, they are qualitatively similar. However, the amount of nonlinear interaction in thick layers is 2–3 orders of magnitude lower than for capillary waves, while in thin layers, the amount of interaction is of the same order of magnitude as in capillary waves (Figs. 3–6).

The ridges of gravitational waves on the liquid layer with a depth on the order of wavelength are sharp and

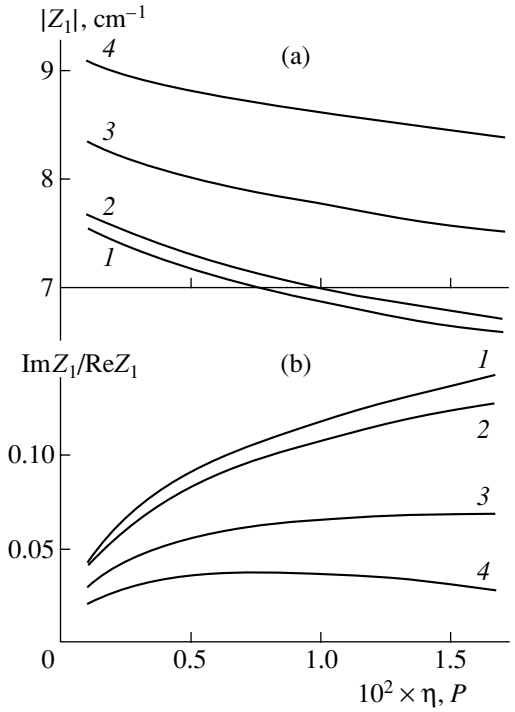

Fig. 1. (a) Absolute value of amplitude factor Z_1 appearing in the nonlinear correction to the wave profile and (b) the ratio between the imaginary and real parts of Z_1 vs. viscosity for short waves ($\lambda = 0.1$ cm) and thick layers. $d = (1)$ 4λ, (*2*) 0.4λ, (*3*) 0.25λ, and (*4*) 0.2λ.

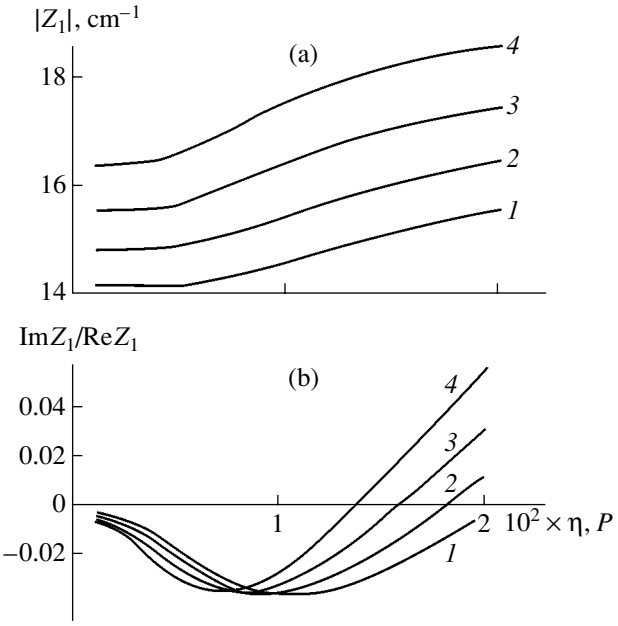

Fig. 2. (a) Absolute value of amplitude factor Z_1 and (b) the ratio between the imaginary and real parts of Z_1 vs. viscosity for short waves ($\lambda = 0.1$ cm) and shallow layers. $d = (1)$ 0.1λ, (*2*) 0.095λ, (*3*) 0.09λ, and (*4*) 0.085λ.

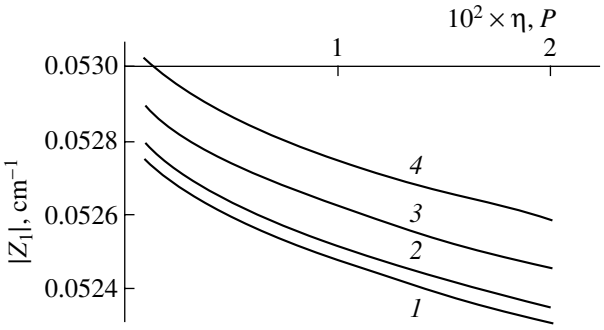

Fig. 3. Absolute value of amplitude factor Z_1 vs. viscosity for waves with $\lambda = 30$ cm and thick layers. $d = (1)$ 4λ, (*2*) 0.73λ, (*3*) 0.63λ, and (*4*) 0.58λ.

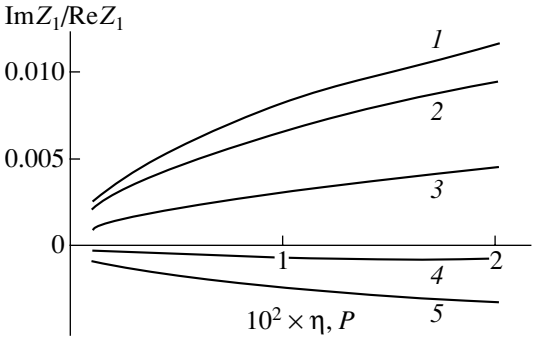

Fig. 4. Ratio between the imaginary and real parts of Z_1 vs. viscosity for waves with $\lambda = 30$ cm and thick layers. $d = (1)$ 4λ, (*2*) 0.33λ, (*3*) 0.23λ, (*4*) 0.19λ, and (*5*) 0.17λ.

slightly skewed in the direction of wave propagation. As the layer gets thinner, the ridges become still sharper and their skew decreases and changes sign at a thickness of ≈0.2λ. As the viscosity grows, the ridges become blunt and their skew increases. For very thin layers (≈0.05λ; Figs. 5 and 6), the run of the associated curves is basically similar: the only difference is that viscosity increases, rather than decreases, the sharpness of the ridges.

The effect of the electric charge on the wave flow on the surface of a viscous liquid was considered earlier for indefinitely deep liquids [5, 6]. It influences primarily the positions of internal nonlinear resonances (not considered here, although it is evident from expression (27) that resonant interaction of waves takes place and its amount will depend both on the viscosity of the liquid and on the thickness of the layer) and the curvature of the ridges. Basically, the effect of the charge on the wave flow of an indefinitely deep viscous liquid, which was discovered earlier, is the same as in finite-thickness layers. As for thin ($d \leq 0.1\lambda$) and thick ($d \gg 0.1\lambda$) layers, the effect of the electric charge calls for thorough analysis with inclusion of higher order corrections, which will be carried out later.

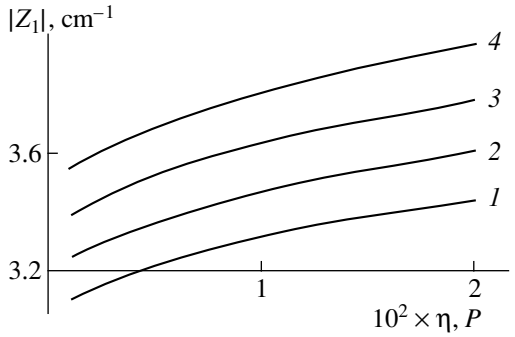

Fig. 5. Absolute value of amplitude factor Z_1 vs. viscosity for waves with $\lambda = 30$ cm and shallow layers. d = (*1*) $5 \times 10^{-2}\lambda$, (*2*) $4.93 \times 10^{-2}\lambda$, (*3*) $4.87 \times 10^{-2}\lambda$, and (*4*) $4.8 \times 10^{-2}\lambda$.

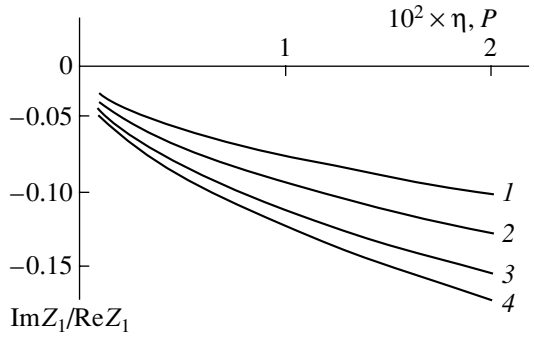

Fig. 6. Ratio between the imaginary and real parts of Z_1 vs. viscosity for waves with $\lambda = 30$ cm and shallow layers. d = (*1*) $5.67 \times 10^{-2}\lambda$, (*2*) $5.17 \times 10^{-2}\lambda$, (*3*) $4.83 \times 10^{-2}\lambda$, and (*4*) $4.67 \times 10^{-2}\lambda$.

In the approximation quadratic in wave amplitude, the damping of nonlinear capillary–gravitational waves in a viscous liquid of finite thickness is completely determined, according to (28), by the damping rate well known from the linear theory [13], which is described by real component $r = \mathrm{Re}S$ of complex frequency S. It is seen from (28) that the nonlinear (quadratic in wave amplitude) component of the total solution decreases with time with the double damping rate (unlike the linear part of the solution, which falls with the single damping rate). The dependence of the damping rate on the viscosity and liquid layer thickness was comprehensively studied in [12]. Specifically, it was found that the layer thickness has an effect on the damping rate only in shallow liquids with $d \le \lambda/\pi$. At $d \ge \lambda$, bottom damping influences the time evolution of the wave amplitude only slightly: the amplitude is totally specified by damping in the volume.

CONCLUSIONS

For both capillary and gravitational waves, the viscosity dependences of the curvature and skew of the wave ridges are different in thick ($d \gg 0.1\lambda$) and shallow ($d \le 0.1\lambda$) liquid layers. This indicates that the wave flow in shallow and thick liquids differ qualitatively and validates the popular opinion that long and short (compared with the layer thickness) waves on the viscous liquid surface should be studied by radically different methods.

ACKNOWLEDGMENTS

This work was supported by the Russian Foundation for Basic Research, grant no. 03-01-00760.

REFERENCES

1. N. M. Zubarev, Zh. Éksp. Teor. Fiz. **116**, 1990 (1999) [JETP **89**, 1078 (1999)].
2. N. M. Zubarev and O. V. Zubareva, Zh. Tekh. Fiz. **71** (7), 21 (2001) [Tech. Phys. **46**, 806 (2001)].
3. D. F. Belonozhko and A. I. Grigor'ev, Izv. Ross. Akad. Nauk, Mekh. Zhidk. Gaza, No. 6, 102 (2003).
4. A. V. Klimov, D. F. Belonozhko, and A. I. Grigor'ev, Zh. Tekh. Fiz. **74** (1), 32 (2004) [Tech. Phys. **49**, 30 (2004)].
5. D. F. Belonozhko and A. I. Grigor'ev, Zh. Tekh. Fiz. **73** (11), 37 (2003) [Tech. Phys. **48**, 1396 (2003)].
6. D. F. Belonozhko and A. I. Grigor'ev, Zh. Tekh. Fiz. **74** (3), 5 (2004) [Tech. Phys. **49**, 287 (2004)].
7. A. I. Zhakin, Izv. Akad. Nauk SSSR, Mekh. Zhidk. Gaza, No. 3, 94 (1984).
8. A. Gonzalez and A. Castellanos, Phys. Rev. E **49**, 2935 (1994).
9. A. Gonzalez and A. Castellanos, Phys. Rev. E **53**, 3573 (1996).
10. A. T. Il'ichev, Izv. Ross. Akad. Nauk, Mekh. Zhidk. Gaza, No. 2, 3 (2000).
11. V. S. Krylov, V. P. Vorotilin, and V. G. Levich, Teor. Osn. Khim. Tekhnol. **3**, 499 (1969).
12. A. I. Grigor'ev, S. O. Shiryaeva, V. A. Koromyslov, and D. F. Belonozhko, Zh. Tekh. Fiz. **67** (8), 27 (1997) [Tech. Phys. **42**, 877 (1997)].
13. V. G. Levich, *Physicochemical Hydrodynamics* (Fizmatgiz, Moscow, 1959; Prentice-Hall, Englewood Cliffs, 1962).

Translated by V. Isaakyan

Technical Physics, Vol. 50, No. 10, 2005, pp. 1268–1273. Translated from Zhurnal Tekhnicheskoĭ Fiziki, Vol. 75, No. 10, 2005, pp. 18–23.

GASES AND LIQUIDS

Approaches to Mathematical Design of Ballistic Experiment: Part I

S. V. Bobashev*, N. P. Mende*, A. B. Podlaskin*, V. A. Sakharov*, V. A. Berdnikov, V. A. Viktorov**, S. I. Oseeva**, and G. D. Sadchikov****

** Ioffe Physicotechnical Institute, Russian Academy of Sciences, Politekhnicheskaya ul. 26, St. Petersburg, 194021 Russia*

e-mail: s.bobashev@mail.ioffe.ru

*** All-Russia Research Institute of Experimental Physics, Russian Federal Nuclear Center, Sarov, Nizhegorodsk Oblast, 607190 Russia*

e-mail: berdnikov@dep16.vniief.ru

Received February 17, 2005

Abstract—Mathematical expedients used in designing ground tests of aerodynamic object models with the aim of finding experimental conditions optimal in terms of the body and accuracy of extracted information are described. In the first part of this paper, the method used in designing ballistic experiment is demonstrated with processing of single-experiment data. In the second part, the validity of the design approach is illustrated by simultaneously processing trajectory data obtained in several experiments. © *2005 Pleiades Publishing, Inc.*

INTRODUCTION

The ballistic experiment implies flight tests of models of aerodynamic objects under laboratory or natural conditions. Such tests are usually aimed at determining the force and moment characteristics of the object. We shall focus our attention on this problem.

The need for mathematical design of the ballistic experiment arises both at the stage of designing a new ballistic range and during investigation. In the latter case, the goal of experimental design is to find experimental conditions that are optimal in terms of the body and accuracy of extracted information. The approaches considered below allow one to solve both problems.

A ballistic range intended for determining the aerodynamic characteristics of an object from trajectory data comprises a launcher and a set of means (most frequently optical) for recording separate points of the trajectory. The number of these points may amount to several tens. By trajectory data are meant three linear coordinates of the center of mass of the object and three angular coordinates specifying the orientation of the object in space at certain time instants. The problem of finding the force characteristics from the trajectory data is reduced to solving the inverse problem of dynamics of a rigid body with the use of discrete trajectory data (points) involving measurement errors. It is obvious that such a problem, like any inverse problem, is ill-posed.

CONCISE DESCRIPTION OF THE MATHEMATICAL APPROACHES

The approaches to be discussed are based on nonlinear estimation of the system's parameters [1, 2] by fitting a mathematical model to numerical output data (the so-called responses) of the system. As far as we know, Chapman and Kirk [3] were the first to apply the approach used in this paper to the problem considered when analyzing the trajectory data of the Gemini lander. They named this approach "the method of differential correction." In the theory of nonlinear estimation, this approach is known as the Gauss–Newton method. The problem is solved by the least squares method with the aim to minimize the objective function, which is the residual sum of the squares of the deviations of the measured coordinates from the ones calculated using a chosen mathematical model and a certain approximation of desired parameters. The minimization is carried out by correcting the initial approximation of the parameters. However, analytical expressions for the objective function are impossible to derive, since analytical solutions to the set of nonlinear ordinary differential equations of motion are absent. The Gauss–Newton approach consists in representing unknown solutions in the form of linear parts of multivariate Taylor series in desired parameters. Following the authors of [3], we exemplify the aforesaid with a simple expression for the residual sum of squares in one coordinate,

$$\sum_{i=1}^{N}\varepsilon_i^2 = \sum_{i=1}^{N}\left[q_{\exp}(x_i) - q_{\mathrm{calc}}(x_i)_0 - \sum_{j=1}^{M}\left(\frac{\partial q}{\partial C_j}\right)_i \Delta C_j - \frac{\partial q}{\partial q_0}\Delta q_0 - \frac{\partial q}{\partial q_0'}\Delta q_0'\right]^2. \quad (1)$$

1063-7842/05/5010-1268$26.00 © 2005 Pleiades Publishing, Inc.

Here, ε_i are the deviations of coordinates $q_{\exp}(x_i)$ measured at N points x_i from values $q_{\text{calc}}(x_i)_0$ calculated using a chosen mathematical model, initial approximations of M desired parameters C_j, and two unknown initial conditions of motion q_0 and q_0'. Small increments of C_j, q_0, and q_0' (differentials ΔC_j, Δq_0, and $\Delta q_0'$, respectively) are expected to improve the approximation provided that the parenthesized first derivatives in expression (1) will be found and then these increments will be calculated from the minimum condition for the entire expression.

The first derivatives of the response function with respect to the desired parameters can be found as follows. The initial differential equation of motion for the response function (the coordinate of the object in the given case),

$$\frac{d^2q}{dx^2} + f\left(\frac{dq}{dx}, q\right) = 0,$$

is differentiated with respect to all desired parameters C_j in view of the initial conditions of motion, since function q depends on them too,

$$q = q(C_1, C_2, C_3, \ldots, C_m, q_0, q_x', x).$$

The independent variable is denoted as x arbitrarily: it may be the coordinate along the flight direction (as in [3]) or flight time. The sequence of differentiating function q with respect to the independent variable and desired parameters can be varied. This allows one to consider the derived equations as second-order linear differential equations with variable coefficients in the first partial derivatives of function q with respect to the desired parameters (including the initial conditions of motion). These equations are called the sensitivity equations. The initial conditions for the derivatives with respect to the aerodynamic coefficients that supplement the sensitivity equations are equal to zero and unity only for the derivatives with respect to the initial coordinate and initial rate of change of this coordinate. This is exemplified in detail in [3]. The coefficients of the sensitivity equations and their right-hand sides can be found by numerically integrating the initial equation of motion at a certain approximation of the desired parameters. Thus, by jointly numerically integrating the initial equation of motion and the sensitivity equations, one can find the partial derivatives of the response function with respect to the desired parameters at points x_i of the experimental design.

From the local minima of expression (1) in terms of the desired parameters, one finds $M + 2$ linear algebraic equations for corrections ΔC_j, Δq_0, and $\Delta q_0'$ and, accordingly, new approximations of these parameters, e.g., $C_j^{t+1} = C_j^t + \Delta C_j^t$, where superscript t is the serial number of the iteration. The iterative process converges very rapidly even if the initial approximations of the parameters are crude.

At the stage of solving the set of algebraic equations derived from the minimum condition for expression (1), it is reasonable to apply linear regression analysis [2, 4, 5] and, thereby, to statistically estimate the significance of the desired parameters in the course of construction of an adequate mathematical model of motion. The same approach allows one to evaluate the confidence intervals of the final parameters appearing in the dependences of the aerodynamic coefficients on the angle of attack and Mach number. In addition, it becomes possible to determine the confidence intervals for these functions themselves. To do this, the $N \times (M + 2)$ rectangular matrix of the coefficients of the algebraic equations obtained from the minima of expression (1) and the vector of residuals are multiplied from the left by the transposed matrix of the coefficients. The resulting square matrix is referred to as the information matrix. A solution to the matrix equation derived gives corrections to the desired coefficients. The inverse to the information matrix is the variance matrix. The elements of the variance matrix possess important properties. The diagonal elements of the variance matrix, being multiplied by the variance of measurements estimated from the root-mean-square residual give the variances of the desired coefficients. The off-diagonal elements, which are correlation coefficients for the model parameters, make it possible to evaluate the variances of the dependences of the aerodynamic coefficients on the angle of attack and Mach number. Based on the variances obtained, one can estimate, using the Student statistical distribution, the confidence intervals for the desired parameters at a given confidence probability at each step of the iteration process and judge the significance of the coefficients involved in the mathematical model. Thus, the construction of an adequate mathematical model through its successive complication at each step is controlled with the statistical tests.

An important property of the approach proposed in [3] is that it admits of simultaneous processing of trajectory data taken in several experiments with model objects of the same shape. The dimensions, weights, and moments of inertia of the objects, as well as the density of the gas in which the objects move, may vary from run to run. Naturally, the aerodynamic coefficients remain invariable in this case (if Reynolds numbers correspond to the same flow regime); only the initial conditions of motion may differ. This means that expression (1) written for each experiment must involve the partial derivatives with respect to the initial conditions of other experiments, which all will be identically equal to zero. Accordingly, the dimension of the information matrix including the results of all runs will increase by the double number of additional runs as compared with the matrix for a single test.

The possibility of jointly processing data collected in several runs is important not only because the num-

ber of points of the general experimental design increases, thereby increasing the number of degrees of freedom (i.e., the difference between the amount of measurements and the number of parameters to be evaluated). The fact is that, at a weak nonlinearity of the pitching moment, the oscillations are nearly sinusoidal (within the accuracy of measurement of the angular coordinates) [6]. Therefore, by analyzing the shape of oscillations alone, one cannot find nonlinear terms involved in the expression for the pitching moment. At the same time, the nonlinearity of the moment makes the oscillations asynchronous: their period (or wavelength) appreciably depends on the amplitude. In jointly processing the results of several runs with different peak-to-peak amplitudes, the moment as a function of the angle of attack is selected so as to fit all experimental results. (Chapman and Kirk [3] emphasized this merit of their approach.) Note also that simultaneous processing of data taken in several runs allows one, for example, to establish the Mach dependence of the moment even if the trajectory is short. For this purpose, it is sufficient that data for the same model object moving with different initial velocities be processed in order to cover the range where the Mach number has a tangible influence.

In mathematical design of the experiment, the direct problem of motion of a model object is solved as applied to a specific ballistic range (already existing or being designed). In this case, the residuals mentioned above are absent, since the trajectory is derived by numerically integrating the equation of motion. Residuals can be simulated by a random number generator with a given variance and mathematical expectation. However, there is no need to do this, because there exists the nondegenerate information matrix, and, consequently, its inverse, namely, the variance matrix with the remarkable properties discussed above. Therefore, it will suffice to set hypothetical variances of coordinate measurements in order to calculate expected variances and confidence intervals for the parameters to be evaluated.

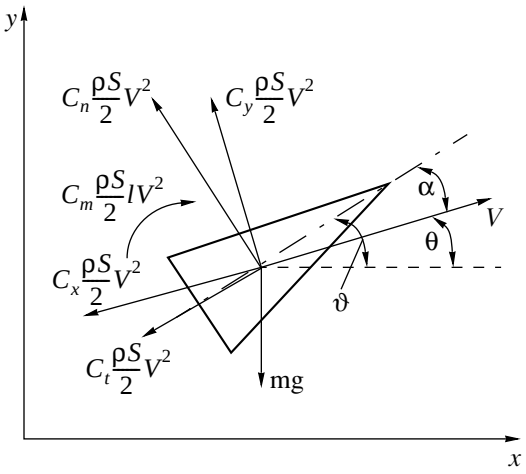

Fig. 1. Coordinate system, as well as the aerodynamic force components and aerodynamic moment acting on a flying body.

The goal of this paper is to exemplify the efficiency of mathematical design of the ballistic experiment. By multistage design, we mean successive refinement of optimal experimental conditions found from experimental data gained at the previous stages. We will synopsize the method used and cite the publications where the related approaches and algorithms are described in detail.

SIMULATION OF THE FREE FLIGHT OF AN AXISYMMETRIC OBJECT AIMED AT PROCESSING SINGLE-EXPERIMENT DATA

The parameters to be determined upon processing trajectory data (denoted above as C_j) are involved in the polynomial representations of the coefficients of drag, lift, and aerodynamic (pitching and damping) moments as functions of the angle of attack and Mach number. For even functions of angle of attack, such representations have the form $C_j = C_j^0 + C_j^{\alpha^2}\alpha^2 + C_j^{\alpha}\alpha^4 + \ldots$; for odd functions, the powers of angle of attack are odd. The dependence on the Mach number is given, in the general form, by a polynomial in $(M - M_0)$, where M_0 is chosen according to the specific form of the dependence.

We will consider the plane motion of an object oscillating in the vertical plane. The components of the aerodynamic force and moment are shown in Fig. 1. Let us write the equation of motion in the form [7]

$$t'' = kt'(C_x + C_y y')[1 + (y')^2]^{1/2}, \tag{2}$$

$$y'' = kC_y[1 + (y')^2]^{3/2} - (t')^2 g, \tag{3}$$

$$\vartheta'' = k(C_x + C_y y')[1 + (y')^2]^{1/2}\vartheta' + kr^{-2}lC_m[1 + (y')^2], \tag{4}$$

$$\vartheta = \alpha + \theta = \alpha + \arctan\left(\frac{dy}{dx}\right). \tag{5}$$

Here, t is the flight time, y is the vertical coordinate of the center of mass of the object, ϑ is the pitching angle, α is the angle of attack, and θ is the slope angle of the trajectory. The distance along the horizontal x coordinate is taken for an independent variable; the derivatives with respect to this coordinate are marked by the prime. The aerodynamic force is presented via its projections onto the wind coordinate axes. The aerodynamic coefficients have the form

$$C_x = C_x(\alpha, M), \tag{6}$$

$$C_y = C_y^{\alpha}(\alpha, M)\alpha + C_y^{\bar{\omega}}(\alpha, M)[1 + (y')^2]^{-1/2}l\vartheta', \tag{7}$$

$$C_m = C_m^{\alpha}(\alpha, M)\alpha + C_m^{\varpi}(\alpha, M)[1 + (y')^2]^{-1/2} l\vartheta', \quad (8)$$

where

$$\varpi = \frac{d\vartheta}{dt}\frac{l}{V} = [1 + (y')^2]^{-1/2}\vartheta' l.$$

For illustration, we take a model object in the form of a body of revolution with a length of 0.1 m, diameter of 0.045 m, and weight of 0.2 kg. The principal moment of inertia about the transverse axis is 5×10^{-5} kg m^2. The working medium is air under the normal conditions with a density of 1.25 kg/m^3. It is assumed that the model executes a plane motion, because it is clear from general considerations that the effect of nonlinearity of the aerodynamic characteristics shows up most vividly in this case (at regular precession, for example, the angle of attack has a value equal to the angle of nutation and so the nonlinear dependences of the coefficients on the angle of attack remain latent).

The aerodynamic characteristics are taken from the range typical of bodies of revolution with the given aspect ratio. They are assigned nonlinearities in such a way that the coefficients multiplying the angle of attack in the second power on, when determined from trajectory data at a given measurement error, are close to their limiting significance. The coefficients thus chosen are listed in Table 1 together with their confidence half-intervals at a confidence probability of 0.95. In Table 1, subscripts *x*, *y*, and *m* refer, respectively, to the parameters of expansion of the drag coefficient, parameters of expansion of the lift, and parameters of the pitching moment coefficient; the superscripts relate the coefficients to the corresponding powers of the angle of attack; and C_y^{ϖ} and C_m^{ϖ} are the constant coefficients of the damping lift and damping moment, respectively. The angle of attack is taken in radians; so, all the coefficients are dimensionless.

The confidence half-intervals listed in Table 1 are calculated under the following conditions. The trajectory data were obtained at twenty points equally spaced over a trajectory length of 60 m. The mean measurement errors are 0.25 mm for the linear coordinates, 0.2° for the angular ones, and 0.5 μs for the flight time. The initial velocity of the model is 1000 m/s; a decline of the velocity, 5.7%; and the average Mach number, 2.82. The trajectory segment being considered accommodates 4.14 oscillation wavelengths. The initial amplitude variation of the angle of attack is 20°.

Figure 2 is a graphical representation of the aerodynamic coefficients, and Fig. 3 shows the variation of the pitching angle and vertical coordinate of the center of mass of the object along the trajectory.

From Table 1, it follows that the accuracy of determining the nonlinear components of the aerodynamic force and moment is poor, as was expected. The accuracy of determining the damping and nonlinear components of the lift should also be raised. The reason for the poor accuracy may be a high oscillation frequency of the object, that is, a short time within which the lift is of constant sign. As a result, the oscillation amplitude of the center of mass in the vertical direction reaches 7 mm. To decrease the error involved in the lift coefficient, it is necessary to extend the time of action of the lift, in other words, to increase the oscillation period or wavelength. The question arises of how this can be done.

Table 1

Coefficient	Dimensionless value	Error, %
C_x^0	0.2	1.4
$C_x^{\alpha^2}$	0.1	87.7
C_y^{ϖ}	2.0	27.9
C_y^{α}	1.0	6.8
$C_y^{\alpha^3}$	–2.0	53.9
C_m^{ϖ}	−0.1	4.8
C_m^{α}	−0.1	1.4
$C_m^{\alpha^3}$	0.02	131.9

Let us consider the motion of the object in a linear approximation when the lift and moment are linear

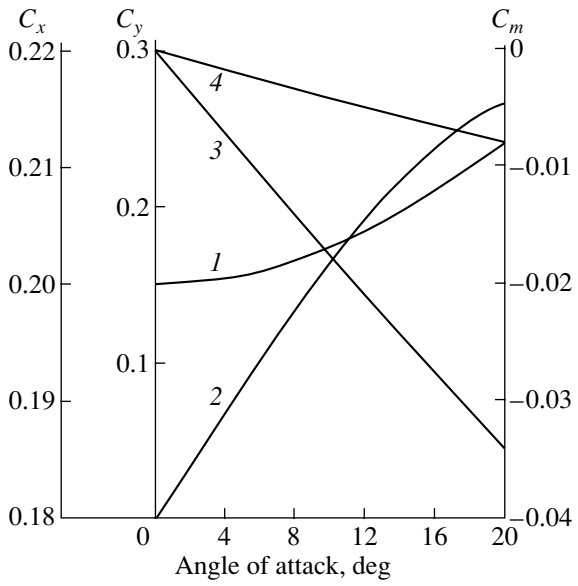

Fig. 2. Aerodynamic coefficients of the hypothetical model vs. angle of attack α (*1*) $C_x = 0.2 + 0.1\alpha^2$, (*2*) $C_y = 1.0\alpha - 2.0\alpha^3$, (*3*) $C_m = -0.1\alpha + 0.02\alpha^3$, and (*4*) $C_m = -0.025\alpha + 0.02\alpha^3$.

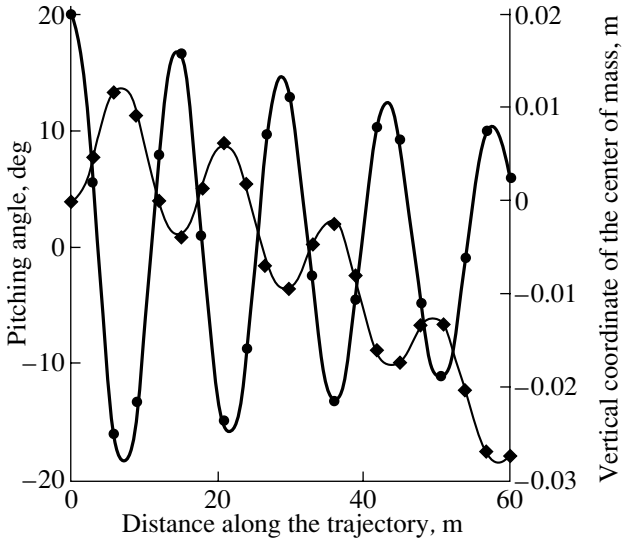

Fig. 3. Variation of the pitching angle (circles) and vertical coordinate of the center of mass along the trajectory (rhombs). The circles and rhombs correspond to the locations of trajectory recording stations.

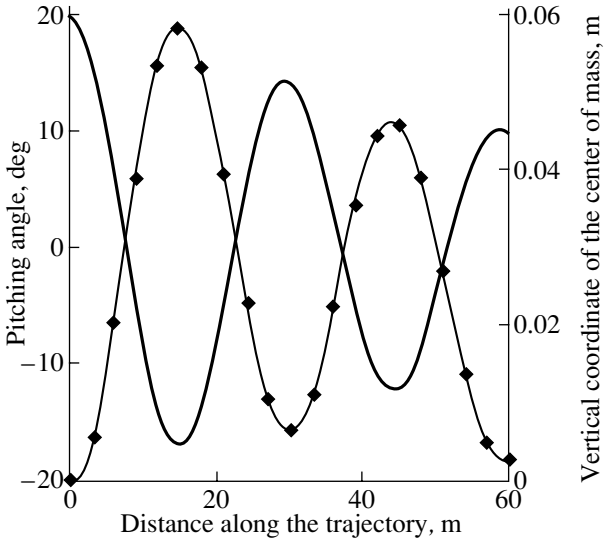

Fig. 4. Variation of the pitching angle and vertical coordinate of the center of mass for the model with the reduced pitching moment. For the circles and rhombs, see Fig. 3.

functions of the angle of attack and are independent of the Mach number in the absence of damping. Taking distance x along the trajectory as an independent variable [7] and setting the pitching angle equal to the angle of attack (the oscillations are weak, and the trajectory is near-horizontal), we can write the equation of oscillation in the form

$$\frac{d^2\alpha}{dx^2} = C_m^\alpha \frac{\rho_g S}{2I_z} l\alpha. \tag{9}$$

Here, α is the angle of attack, C_m^α is the derivative of the moment coefficient with respect to the angle of attack, ρ_g is the gas density, S is the midsectional area of the object, I_z is the principal central moment of inertia about to the transverse axis, and l is the characteristic length of the object. The squared velocity entering into the expression for the dynamic head disappeared when the longitudinal coordinate was taken as an independent variable instead of time. It is obvious that the solution to Eq. (9) is

$$\alpha = \alpha_m \sin\left(\frac{2\pi}{L}x + \varphi_0\right), \tag{10}$$

where

$$\frac{2\pi}{L} = \sqrt{C_m^\alpha \frac{\rho_g S}{2I_z}}\, l,$$

α_m is the oscillation amplitude, and φ_0 is the initial phase.

The equation of motion of the center of mass in the vertical plane has the form [7]

$$\frac{d^2y}{dx^2} = C_y^\alpha \frac{\rho_g S}{2m}\alpha - (t')^2 g, \tag{11}$$

where C_y^α is the derivative of the lift coefficient with respect to the angle of attack, m is the weight of the object, and g is the acceleration of gravity.

Double integration of the first term on the right of (11) with regard to (10) yields

$$y = -C_y^\alpha \frac{\rho_g S}{2m}\alpha_m \left(\frac{2\pi}{L}\right)^{-2} \sin\left(\frac{2\pi}{L}x + \varphi_0\right). \tag{12}$$

The factor multiplying the sine in (12) is oscillation amplitude y_m of the center of mass in the vertical plane. This quantity is proportional (see (10)) to the following parameters:

$$y_m \approx \frac{C_y^\alpha}{C_m^\alpha}\frac{\rho_g S}{2m}\frac{2I_z}{\rho_g S l} \approx \frac{C_y^\alpha}{C_m^\alpha} l, \tag{13}$$

since the weight and moment of inertia vary as the third and fifth power of the object's linear size, respectively.

From (13), it follows that, to increase the oscillation amplitude of the center of mass of a model, one should increase its linear size. However, such a possibility in experimental ballistics is only speculative: it is limited by the diameter of the bore of a launcher.

However, expression (13) involves one more parameter that can be varied: the derivative of the pitching moment. This parameter decreases when the center of mass shifts toward the center of pressure, thereby

Table 2

Coefficient	Dimensionless value	Error, %
C_x^0	0.2	1.4
$C_x^{\alpha^2}$	0.1	88.3
$C_y^{\bar{\omega}}$	2.0	15.5
C_y^{α}	1.0	1.7
$C_y^{\alpha^3}$	–2.0	14.6
$C_m^{\bar{\omega}}$	–0.1	4.6
C_m^{α}	–0.25	3.1
$C_m^{\alpha^3}$	0.02	77.7

diminishing the static stability margin of the body. In so doing, the transverse moment of inertia may change insignificantly. Therefore, we assume that, when the position of the center of mass changes due to the mass redistribution over the volume of the model, the transverse moment of inertia remains unchanged. This assumption will be used in the following consideration. Thus, a change in the pitching moment turns out to be the decisive factor. Naturally, either the pitching moment found in such experiments should then be reduced to the given center of mass or special experiments should be carried out to determine the initial values of the pitching and damping moments.

To simulate such an approach, we decrease the derivative of the pitching moment at the zero angle of attack (Table 1) by a factor of 4 (Fig. 2) with the moment of inertia and other parameters of expansions of the aerodynamic coefficients remaining unchanged (in this case, the oscillation wavelength increases approximately twofold). Figure 4 demonstrates the variation of the pitching angle and vertical coordinate of the center of mass of the new model along the trajectory. Now the trajectory accommodates two oscillation wavelengths.

It is seen from Fig. 4 that the oscillation amplitude of the center of mass of the model has increased several times up to 30 mm. Accordingly, the accuracy of determining the components of the lift coefficient has improved (Table 2). The errors involved in the moment and drag coefficients have changed insignificantly, whereas the lift coefficients have been determined much more accurately. This example illustrates the efficiency and necessity of multistage design of the ballistic experiment. In Part II of this paper, we perform simulation using the parameters from Table 2 to demonstrate the efficiency of simultaneously processing data obtained in several experiments with models of the same shape.

REFERENCES

1. Y. Bard, *Nonlinear Parameter Estimation* (Academic, New York, 1974; Statistika, Moscow, 1979).
2. K. Hartmann, E. Lezki, W. Schäfer, *et al.*, in *Design of Experiments in Process Research (Statistische Versuchsplanung und Auswertung in der Stoffwitschaft)* (VEB Deutscher Verlag für Grundstoffindustrie, 1974; Mir, Moscow, 1977) [translated from German].
3. G. T. Chapman and D. B. Kirk, AIAA J. **8**, 753 (1970); Raketnaya Tekh. Kosmonavtika **8**, 182 (1970).
4. S. I. Ermakov and A. A. Zhiglyavskiĭ, *Mathematical Theory of Optimal Experiment* (Nauka, Moscow, 1987) [in Russian].
5. N. P. Mende, Preprint No. 1326, FTI im. A. F. Ioffe (Ioffe Physicotechnical Institute, AN SSSR, Leningrad, 1989); N. P. Mende, in *Gas Dynamics*, Ed. by Yu. I. Koptev (Nova Science, New York, 1992), pp. 325–356.
6. N. Kryloff and N. Bogoliuboff, *Introduction to Non-Linear Mechanics* (Izd. Ukr. Akad. Nauk, Kiev, 1937; Princeton Univ. Press, Princeton, 1943).
7. N. P. Mende, in *Physical Gasdynamic Ballistic Investigations*, Ed. by G. I. Mishin (Nauka, Leningrad, 1980), pp. 200–224 [in Russian].

Translated by N. Mende

Technical Physics, Vol. 50, No. 10, 2005, pp. 1274–1278. Translated from Zhurnal Tekhnicheskoĭ Fiziki, Vol. 75, No. 10, 2005, pp. 24–28.

GASES AND LIQUIDS

Approaches to Mathematical Design of Ballistic Experiment: Part II

S. V. Bobashev*, N. P. Mende*, A. B. Podlaskin*, V. A. Sakharov*, V. A. Berdnikov, V. A. Viktorov**, S. I. Oseeva**, and G. D. Sadchikov****

** Ioffe Physicotechnical Institute, Russian Academy of Sciences, Politekhnicheskaya ul. 26, St. Petersburg, 194021 Russia*

e-mail: s.bobashev@mail.ioffe.ru

*** All-Russia Research Institute of Experimental Physics, Russian Federal Nuclear Center, Sarov, Nizhegorodsk Oblast, 607190 Russia*

e-mail: berdnikov@dep16.vniief.ru

Received February 17, 2005

Abstract—Mathematical expedients used in designing ground tests of aerodynamic object models with the aim of finding experimental conditions optimal in terms of the body and accuracy of extracted information are described. In the first part of this paper, the method used in designing the ballistic experiment is demonstrated with processing of single-experiment data. In the second part, the validity of the design approach is illustrated by simultaneously processing trajectory data obtained in several experiments. © *2005 Pleiades Publishing, Inc.*

SIMULATION OF THE FREE FLIGHT OF AN AXISYMMETRIC OBJECT: SIMULTANEOUS PROCESSING OF DATA OF SEVERAL EXPERIMENTS

In Part I of this paper, we considered the flight of an axisymmetric aerodynamic object in air. It will be remembered that the object has a length of 0.1 m, diameter of 0.045 m, and mass of 0.2 kg. Its principal moment of inertia about the transverse axis equals 5×10^{-5} kg m^2. The air density was taken to be equal to 1.25 kg/m^3. The 60-m-long trajectory is provided with 20 stations for recording trajectory data with an accuracy of 0.25 mm for the linear coordinates of the center of mass, 0.2° for the angular coordinates, and 0.5 μs for time. The initial velocity of the body amounts to 1000 m/s, and the initial angle of attack is 20°. The aerodynamic object is assigned aerodynamic characteristics that are specified by the initial coefficients of their expansions into power series in the angle of attack. These are drag coefficient $C_x = C_x^0 + C_x^{\alpha^2}$, damping lift coefficient $C_y^{\bar{\omega}} = \text{const}$, lift coefficient $C_y = C_y^{\alpha}\alpha + C_y^{\alpha^3}\alpha^3$, damping moment coefficient $C_m^{\bar{\omega}} = \text{const}$, and static pitching moment coefficient $C_m = C_m^{\alpha}\alpha + C_m^{\alpha^3}\alpha^3$. The equations of motion are given in Part I.

The coefficients of the polynomial representations of the aerodynamic characteristics are listed in Table 1 together with the confidence half-intervals for their estimates based on single-experiment data obtained under the experimental conditions mentioned above.

From Table 1, it follows that the accuracy in determining the nonlinear (in angle of attack) components of the drag and pitching moment coefficients is very low. The reason for a low accuracy was discussed in Part I. To decrease the errors, we simultaneously process data of four model experiments with initial angles of attack of 5°, –10°, 15°, and 20°. The associated confidence half-intervals are presented in Table 2.

It is seen that the accuracy of determining the expansion coefficients has noticeably increased compared with the data in Table 1. For the errors involved in the higher expansion coefficients to decline further, it is

Table 1

Coefficient	Dimensionless value	Error, %
C_x^0	0.2	1.4
$C_x^{\alpha^2}$	0.1	88.3
$C_y^{\bar{\omega}}$	2.0	15.5
C_y^{α}	1.0	1.7
$C_y^{\alpha^3}$	–2.0	14.6
$C_m^{\bar{\omega}}$	–0.1	4.6
C_m^{α}	–0.25	3.1
$C_m^{\alpha^3}$	0.02	77.7

1063-7842/05/5010-1274$26.00 © 2005 Pleiades Publishing, Inc.

necessary either to measure the coordinates and time with a higher accuracy, which seems unrealistic, or process a larger body of experimental data, including those obtained at different oscillation amplitudes.

Importantly, the errors in the nonlinear components of the aerodynamic coefficients, which may be as high as 20–30%, affect the calculated dependences of the coefficients on the angle of attack insignificantly. This is because these components correlate with each other (the correlation results from their linear interrelation, which, in turn, reflects the fact that the components are related by linear algebraic equations [1–3]). By way of illustration, Table 3 lists the aerodynamic coefficients and their confidence half-intervals as functions of the angle of attack that were calculated using the data from Table 2 with regard to the coefficients of correlation between the parameters of expansions of the coefficients. The coefficients of correlation, which are the off-diagonal elements of the variance matrix, are omitted here.

From Table 3, it follows that the confidence intervals for the functions describing the variation of the aerodynamic coefficients increase noticeably near the upper limit of the angle-of-attack range. However, this increase is not too strong, as might be expected based on 20–30% confidence half-intervals for the higher coefficients in the expansions of these functions (Table 2).

Table 2

Coefficient	Dimensionless value	Error, %
C_x^0	0.2	0.14
$C_x^{\alpha^2}$	0.1	14.5
$C_y^{\bar{\omega}}$	2.0	11.5
C_y^{α}	1.0	0.9
$C_y^{\alpha^3}$	–2.0	9.4
$C_m^{\bar{\omega}}$	−0.1	3.3
C_m^{α}	−0.25	0.9
$C_m^{\alpha^3}$	0.02	27.9

INFLUENCE OF THE NUMBER AND LOCATION OF TRAJECTORY RECORDING STATIONS

Now consider how the number of recording stations uniformly located along a 60-m-long flight path influences the accuracy of finding the aerodynamic coefficients when the data of four experiments are processed simultaneously (the problem of designing a new ballistic range). The associated results are shown in Figs. 1 and 2. It is seen that the confidence intervals for the linear components and damping moment are one order of magnitude smaller than those for the nonlinear components and damping lift. Recall that the latter components were deliberately chosen near their significance limit in processing single-experiment data. Simultaneous processing of data taken in four experiments has allowed us to decrease the errors involved in these coefficients by three times on average. As was expected, the errors in determination of the aerodynamic coefficients decrease with increasing number of recording stations; however, these dependences smooth out in this case. Since the errors in the aerodynamic coefficients can be diminished by increasing the number of experiments processed simultaneously, it seems reasonable to limit the number of the stations over a flight path of 60 m to twenty or thirty. In this case, the spacing between regularly arranged recording stations (approximately 2 m) is sufficient for placing processing equipment and auxiliary facilities. However, the descending curves in Figs. 1 and 2 mean increased costs of construction and maintenance of a range; therefore, the optimal number of recording stations depends on many, including subjective, factors.

It can be shown by simulation that whether recording stations are arranged regularly or not is of minor significance. When, say, ten stations are placed over the first 20 m of the trajectory and other ten over the remaining 40 m, the errors change by fractions of percent in Fig. 1 and by 1–2% in Fig. 2. Then, it follows that it is reasonable to arrange the stations nonuniformly in order to use, if necessary, only the initial part of the trajectory and still have an acceptable number of points in the experimental design.

ON THE INFLUENCE OF THE WORKING GAS PRESSURE

If a ballistic range is equipped with a measuring pressure chamber allowing one to control the parameters of the gas medium where an object flies, additional possibilities appear for choosing a relationship between the wavelength of object's oscillations and the length of the trajectory being recorded. The oscillation wavelength can be extended up to the entire length of the pressure chamber by reducing the gas pressure inside the chamber. Figure 3 demonstrates the variation of the pitching angle and vertical coordinate of the center of mass of the object along the 60-m trajectory when the air pressure is reduced to 10^{-4} Pa. Table 4 lists errors expected when the data of four experiments at the reduced pressure were processed simultaneously. From this table, it follows that, at the pressure equal to one-tenth of the atmospheric value, it is necessary to extend the trajectory length in order to determine the nonlinear components of the aerodynamic coefficients, because even simultaneous processing of several tests does not help (cf. Table 1). With the trajectory length extended

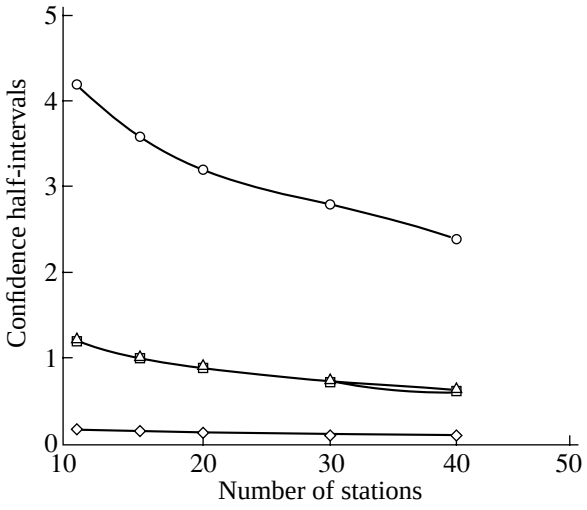

Fig. 1. Confidence half-intervals for the (○) damping moment and linear components of the aerodynamic coefficients: (△) pitching moment, (□) lift, and (◇) drag vs. the number of recording stations when simultaneously processing data of four experiments over a trajectory of length 60 m. The confidence probability is 0.95.

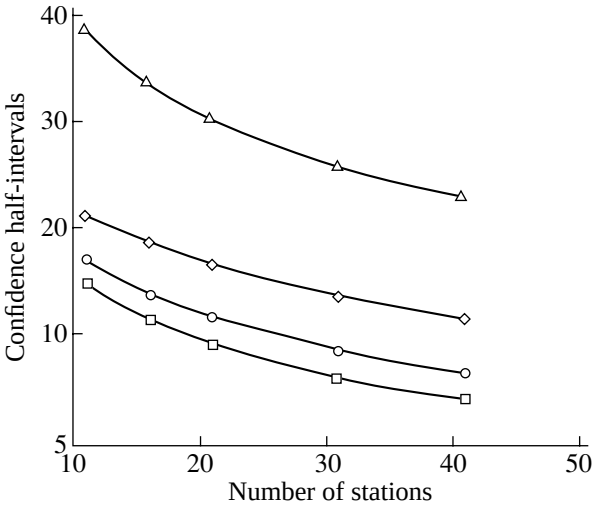

Fig. 2. Same as in Fig. 1 for the (o) damping lift component and nonlinear components of the static aerodynamic coefficients: (△) pitching moment, (□) lift, and (◇) drag.

three times (180 m), the errors diminish appreciably (Table 5).

INFLUENCE OF THE OBJECT'S INITIAL VELOCITY

The influence of the initial velocity of the object on errors in determination of the aerodynamic coefficients from the trajectory data can be clarified without resort to numerical simulation. Paper [4] gives equations of plane motion of an object in a gas in the linear approximation. Ignoring the terms of little significance in these equations yields

$$t'' = kt'C_x, \tag{1}$$

$$y'' = kC_y - (t')^2 g, \tag{2}$$

$$\vartheta'' = -kr_z^{-2} lC_m, \tag{3}$$

where the primes denote derivatives of time t, coordinate y, and pitching angle ϑ with respect to longitudinal coordinate x [5, 6]); $k = \rho S/2m$; ρ is the gas density; S is the mid-sectional area of the object; m and l are the mass and length of the object, respectively; r_z is the radius of inertia about the transverse axis; C_x, C_y, and C_m are the coefficients of drag, lift, and total aerody-

Table 3

Angle of attack, deg	Drag coefficient		Lift coefficient		Pitching moment coefficient	
	dimensionless value	confidence half-interval, %	dimensionless value	confidence half-interval, %	dimensionless value	confidence half-interval, %
0	0.2000	0.14	0.0000		0.0000	
2.00	0.2001	0.13	0.0348	0.86	−0.0009	0.88
4.00	0.2005	0.11	0.0691	0.81	−0.0017	0.81
6.00	0.2011	0.09	0.1024	0.72	−0.0026	0.69
8.00	0.2019	0.09	0.1342	0.61	−0.0034	0.54
10.00	0.2030	0.14	0.1639	0.51	−0.0043	0.41
12.00	0.2044	0.22	0.1911	0.48	−0.0051	0.41
14.00	0.2060	0.33	0.2152	0.64	−0.0058	0.66
16.00	0.2078	0.45	0.2357	0.98	−0.0065	1.05
18.00	0.2099	0.58	0.2521	1.46	−0.0072	1.55
20.00	0.2122	0.73	0.2965	2.10	−0.0079	2.14

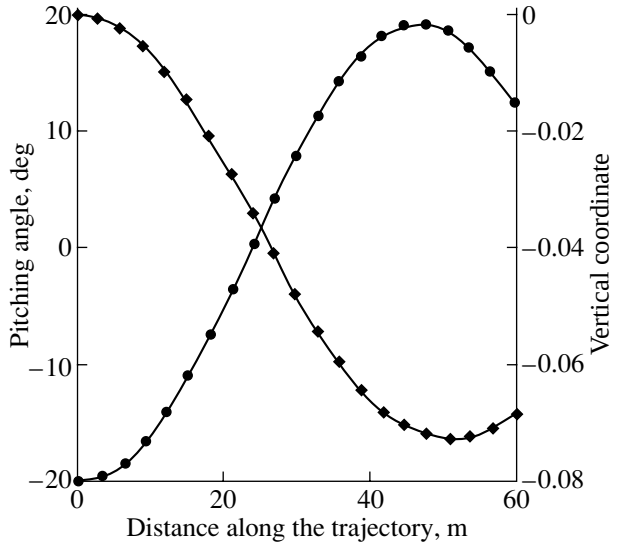

Fig. 3. Variation of the (●) pitching angle and (◆) vertical coordinate of the center of mass of the object along the trajectory. The air pressure is one-tenth of the atmospheric value.

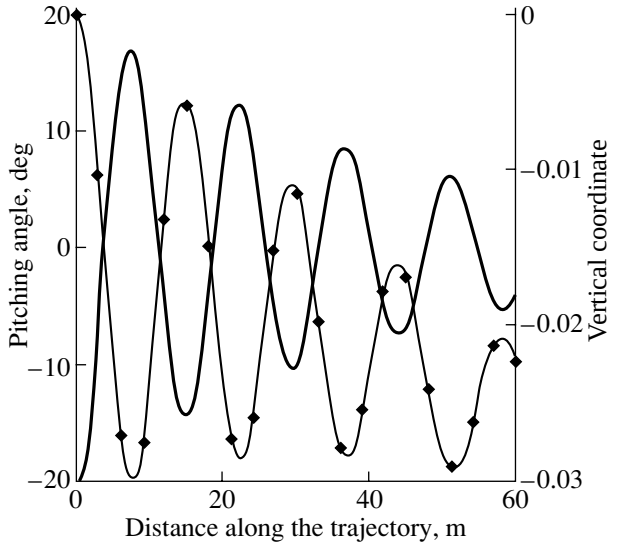

Fig. 4. Variation of the pitching angle (curve without symbols) and (◆) vertical coordinate of the center of mass along the trajectory for the model half as large as that in Fig. 1 with the same mass distribution over the volume. The initial flight velocity is 2.5 km/s.

namic moment (including damping), respectively; and g is the gravitational acceleration.

Omitting the second term on the right of (2) (the free fall of the model may be approximately taken into account by neglecting a small vertical component of the drag through addition of $gt^2/2$ to the corresponding y coordinate), one can see that neither time nor the flight velocity enter into Eqs. (2) and (3) explicitly (the velocity dependences of coefficients C_y and C_m can be neglected over a short part of the trajectory). Thus, both quantities do not influence the estimates of the lift and aerodynamic moment.

Not so with Eq. (1). Here, the response function (the flight time) itself directly depends on the flight velocity, growing monotonically: the higher the velocity, the slower the growth ($t' \sim V^{-1}$, where V is the model instantaneous velocity). However, we are interested in the contribution to the response function from the wind resistance rather than in the whole response function.

At constant C_x, the second integral of Eq. (1) has the form

$$t = t_0 + \frac{t_0'}{kC_x}(\exp(kC_x x) - 1). \qquad (4)$$

Lets us expand expression (4) into a power series in x,

$$t = t_0 + t_0' x + t_0'\left(kC_x\frac{x^2}{2!} + k^2C_x^2\frac{x^3}{3!} + \ldots\right). \qquad (5)$$

The first two terms on the right of (5) correspond to uniform motion (without drag). The expression in parentheses describes the contribution due to a velocity decrease, which is velocity-independent (if one neglects the dependence of the drag on the Mach number; however, this effect is of the second order of smallness in this case). The factor multiplying the parenthesis is the reciprocal of the model's initial velocity. Thus, the higher the initial velocity, the smaller the absolute contribution of the wind resistance to the response function (flight time); that is, the quantity of interest varies inversely with the velocity. It is natural to suppose that the relative error of estimation of the drag over a fixed part of the trajectory will grow nearly proportionally to an increase in the initial velocity if the

Table 4

Coefficient	Dimensionless value	Error, %
C_x^0	0.2	1.4
$C_x^{\alpha^2}$	0.1	92.0
$C_y^{\bar{\omega}}$	2.0	291.0
C_y^{α}	1.0	3.5
$C_y^{\alpha^3}$	–2.0	25.2
$C_m^{\bar{\omega}}$	−0.1	179.3
C_m^{α}	−0.25	4.1
$C_m^{\alpha^3}$	0.02	72.6

Table 5

Coefficient	Dimensionless value	Error, %
C_x^0	0.2	0.16
$C_x^{\alpha^2}$	0.1	10.5
$C_y^{\bar{\omega}}$	2.0	27.1
C_y^{α}	1.0	0.9
$C_y^{\alpha^3}$	–2.0	7.1
$C_m^{\bar{\omega}}$	–0.1	9.0
C_m^{α}	–0.25	0.8
$C_m^{\alpha^3}$	0.02	16.0

Table 6

Coefficient	Dimensionless value	Error, %
C_x^0	0.2	0.15
$C_x^{\alpha^2}$	0.1	27.2
$C_y^{\bar{\omega}}$	2.0	26.0
C_y^{α}	1.0	1.8
$C_y^{\alpha^3}$	–2.0	19.9
$C_m^{\bar{\omega}}$	–0.1	2.4
C_m^{α}	–0.25	0.5
$C_m^{\alpha^3}$	0.02	22.1

errors involved in the time and flight path remain constant. Numerical simulation completely confirms this supposition. Thus, to maintain the error in determination of the drag coefficient from trajectory data at an accepted level when the initial velocity increases, it is necessary, as in the case of decreasing pressure of the working gas, to extend the recorded part of the flight path. In this case, the extension of the flight path should be roughly proportional to the increase in the initial velocity.

ON THE CHOICE OF THE DIMENSIONS AND INERTIAL CHARACTERISTICS OF THE OBJECT

The experimental conditions may also be optimized by properly choosing the dimensions of the model (with its shape remaining invariable) and its inertial characteristics. The former and the latter can be done independently; however, change of the dimensions seems to be more promising and logical (to change the density of the model material is a much more difficult task than to change the dimensions of a model). Let us simulate the four previous atmospheric-pressure experiments having cut the dimensions of the model by half. Its mass and moment of inertia then decrease eightfold and 32-fold, respectively. The angular oscillations and transverse displacement of the center of mass of the model observed in one of the experiments are shown in Fig. 4, and the related errors are given in Table 6.

Under the given conditions, as the oscillation frequency grows (because of decreasing the moment of inertia), the error involved in the lift coefficient components increases, as follows from Fig. 4 and Table 6. However, this does not mean that variation of the dimensions and inertial characteristics of a model cannot provide good results.

CONCLUSIONS

The algorithm for numerically simulating the plane motion of an axisymmetric object in a gas medium elaborating upon the approaches proposed by other authors to identifying the aerodynamic characteristics of the object from the trajectory data is helpful in for multistage design of the ballistic experiment. These approaches are supplemented by the procedures used in statistic estimation of expected identification errors for given errors of measurement of the trajectory data. Mathematical design of the ballistic experiment is aimed at optimizing experimental conditions to improve the measurement accuracy.

ACKNOWLEDGMENTS

The authors are grateful to V.O. Afanas'ev for cooperation.

REFERENCES

1. Y. Bard, *Nonlinear Parameter Estimation* (Academic, New York, 1974; Statistika, Moscow, 1979).
2. K. Hartmann, E. Lezki, W. Schäfer, *et al.*, in *Design of Experiments in Process Research (Statistische Versuchsplanung und Auswertung in der Stoffwitschaft)* (VEB Deutscher Verlag für Grundstoffindustrie, 1974; Mir, Moscow, 1977) [translated from German].
3. S. M. Ermakov and A. A. Zhiglyavskiĭ, *Mathematical Theory of Optimal Experiment* (Nauka, Moscow, 1987) [in Russian].
4. N. P. Mende, in *Physical Gasdynamic Ballistic Investigations*, Ed. by G. I. Mishin (Nauka, Leningrad, 1980), pp. 200–224.
5. G. T. Chapman and D. B. Kirk, AIAA J. **8**, 753 (1970); Raketnaya Tekh. Kosmonavtika **8**, 182 (1970).
6. N. P. Mende, Preprint No. 1326, FTI im. A. F. Ioffe (Ioffe Physicotechnical Institute, AN SSSR, Leningrad, 1989); N. P. Mende, in *Gas Dynamics*, Ed. by Yu. I. Koptev (Nova Science, New York, 1992), pp. 325–356.

Translated by N. Mende

Technical Physics, Vol. 50, No. 10, 2005, pp. 1279–1283. Translated from Zhurnal Tekhnicheskoĭ Fiziki, Vol. 75, No. 10, 2005, pp. 29–33.

GAS DISCHARGES, PLASMA

Properties of Nickel Oxide Nanopowders Prepared by Electrical Explosion of a Wire

Yu. A. Kotov, A. V. Bagazeyev, I. V. Beketov, A. M. Murzakaev, O. M. Samatov, A. I. Medvedev, N. I. Moskalenko, O. R. Timoshenkova, T. M. Demina, and A. K. Shtolts

Institute of Electrophysics, Ural Division, Russian Academy of Sciences, ul. Amundsena 106, Yekaterinburg, 620016 Russia

e-mail: kotov@iep.uran.ru

Received January 21, 2005

Abstract—The properties of NiO nanopowders prepared by electrical explosion of a wire in an oxygen-containing atmosphere are presented. Most of the NiO nanopowders are found to be oxygen-enriched, the excess of oxygen depending mainly on the nickel vapor concentration. The dependences of the powder particle size on the oxygen concentration and overheating of the exploding metal are discussed. The powder nanoparticles are both single-crystal and polycrystalline with a rhombohedral lattice and have different shapes (from cubic to spherical). There typical sizes range from 15 to 50 nm, depending on the explosion conditions. © *2005 Pleiades Publishing, Inc.*

INTRODUCTION

NiO powders were prepared by electrical explosion of a wire with the aim of studying their activity in various solid-phase reactions and producing a conducting phase in the anodes of fuel elements.

When producing powders consisting of oxides of Al [1, 2], as well as Zr and Ti [3], i.e., of metals whose heat of oxidation is substantially higher than their energy of sublimation (by a factor of 2.6, 2.2, and 1.3 for Al, Ti, and Zr, respectively), we noticed that a decrease in the overheating of the metal makes it possible to diminish the particle size through a decrease in the concentration of suspended burning liquid metal droplets (metal vapor). For the same reason (a reduction of the vapor concentration), the particles shrink with decreasing diameter of the exploding wire, all other things being equal. It was also found that the particle size can be decreased further by extending the combustion time via reduction of the oxygen concentration [4].

It is of interest to verify these dependences with nickel oxide powders, since the energy of oxidation of Ni is as low as 0.66 of its energy of sublimation.

EXPERIMENTAL

The powders were prepared from two pieces of NP2 nickel wire (99.5% Ni) with diameter d = 0.3 and 0.5 mm and length l = 227 and 150 mm long. The discharge circuit had an inductance of 0.5 μH and a total capacitance of a capacitor bank of 3.1 μF. The charging voltage was varied from 10 to 33 kV, which provided overheat factor $K = W/W_s$ (W is the energy applied to the wire, and W_s is the energy of sublimation of the metal) ranging from 0.4 to 1.3. The wire was exploded under normal pressure in a $N_2 + O_2$ mixture, where the O_2 concentration, k_{O_2}, was varied from 8 to 30 vol%.

Combustion produces a mixture of nanopowders containing nonevaporated drops whose size may reach several tens of microns. Therefore, the flue gas path was equipped with a set of devices for particle separation [5], namely, a screw separator connected to the explosion chamber, the first cyclone 40 mm in diameter, the second cyclone 40 mm in diameter, an electric filter, and a fabric filter. Such an experimental scheme was applied earlier in production of Al, Zr, Ti, etc., oxides. The cross section of the pipeline and screw separator was 690 mm^2. We analyzed only the powders collected in the electric filter.

The powders were sorted in accordance with their specific surface area S by argon sorption on/desorption from an argon–helium mixture with a GKh-1 device. The content of volatiles in the powders was determined with a Q-1500 derivatograph. In addition, the phase composition of the powders (DRON-4 diffractometer) and their elemental composition (Jobin Yvon 48 spectrometer) were analyzed. The powders were also examined by transmission electron microscopy and electron diffraction (JEM-200 microscope), as well as by scanning electron microscopy (LEO-982 microscope).

RESULTS AND DISCUSSION

The results obtained indicate that, as for the metals studied earlier, combustion makes it possible to decrease the particle size roughly by 3.5 times with the overheat decreasing from 1.3 to 0.45–0.40 (Fig. 1).

The powder yield in the electric filter is ~8%. However, we failed to reliably establish the dependence of

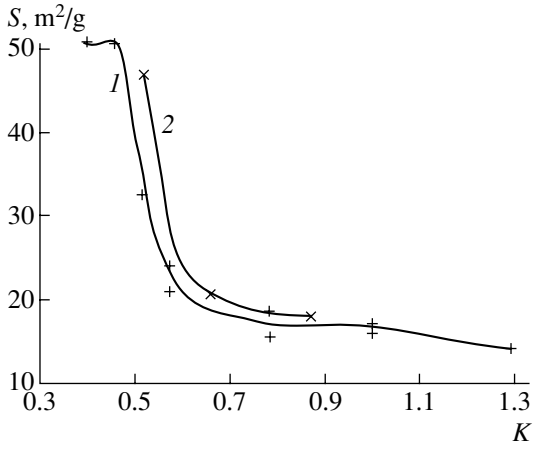

Fig. 1. Overheat dependence of the specific surface area of the NiO powder in the electric filter at k_{O_2} = 21 vol%. (*1*) l = 227 mm, d = 0.3 mm and (*2*) l = 150 mm, d = 0.5 mm.

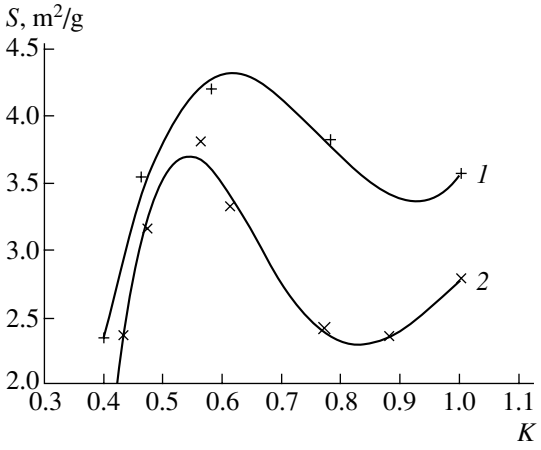

Fig. 2. Overheat dependence of the total specific surface area of the NiO powder at k_{O_2} = 21 vol%. (*1*) l = 227 mm, d = 0.3 mm and (*2*) l = 150 mm, d = 0.5 mm.

the yield on the overheat in small lots of samples because of strong adhesion of the fine fraction to the walls of the flue gas path. A major portion of the powder (up to 80% of the wire weight) settles in the primary separators (traps, screws, and the first cyclone) and in the chamber; thereby, the nanofraction is partly lost. To determine the total yield of fractions with a particle size of less than 200 nm, we performed sedimentation analysis of the powders collected from all relevant sites and measured the weight of the collections. It was found that the real content of nanoparticles in the powder varies from 15 to 30 wt% as the overheat increases from 0.5 to 1.0.

In an effort to reduce adhesion to the interior of the flue gas path and improve the yield at sites of collection, we diminished the particle concentration in the flow. To this end, we increased the cross section of the gas tubes fivefold and the diameter of the first cyclone by a factor of 7.5.

As follows from the experimental data, the use of wider tubes allowed us to decrease the amount of the powder remaining in the flue gas path by one order of magnitude. The increased heat-exchange surface and decreased particle concentration in the flow provided more rapid cooling of the particles and, hence, lowered adhesion losses.

As follows from Fig. 1, the specific surface area of the powder from the electric filter after explosion of the wire with d = 0.5 mm is larger than that of the powder produced from the wire with d = 0.3 mm under similar conditions. This seems contrary to the dependence of the specific surface area on the wire diameter found in [2]: S increases with decreasing wire diameter, all things being equal. However, in [2] and other studies, the specific surface areas of the powders collected without separation (i.e., the total amount of the powder produced by explosion and collected in the explosion chamber) were compared. Therefore, we carried out special experiments and, as in [2], collected the whole powder in the explosion chamber. The results (Fig. 2) demonstrated that the dependence of the total specific surface area on the wire diameter remains the same.

Unlike the metals studied earlier, a rise in the oxygen concentration increases, rather than decreases, the specific surface area, all other things being equal (Fig. 3). In the oxygen concentration range from 8 to 30 vol %, the increase amounts to 25%. However, as the nickel overheats more and more, an increase in the oxygen concentration gives a smaller increase in S, and the specific surface area even decreases at $K \geq 1$.

Such behavior can qualitatively be explained as follows. The rate of a chemical reaction is known to be controlled by the concentrations of reagents. Under the conditions of wire explosion, this means that the higher the oxygen concentration in the vapor, the more intense combustion and evaporation of drops. Accordingly, the vapor concentration grows and the vapor may become supersaturated with subsequent condensation on appropriate nuclei. The higher the supersaturation, the higher the particle growth rate and, hence, the coarser the particles. Such a scenario was observed in production of powder oxides of chemically active metals (Al, Ti, Zr, and $MgAl_2O_x$) [1–4]. Therefore, in the works cited, the oxygen concentration was lowered in order to decrease the particle size; as a result, the combustion rate and vapor concentration declined.

Since the heat of oxidation of nickel is low, nickel drops evaporate with a much lower rate. Therefore, one can safely raise the oxygen concentration to a certain value without supersaturating the vapor. Higher rates of oxidation and evaporation increase the amount of the vapor phase and its temperature, thereby extending the condensation range because of later cooling and, eventually, decreasing the particle size. As the overheating

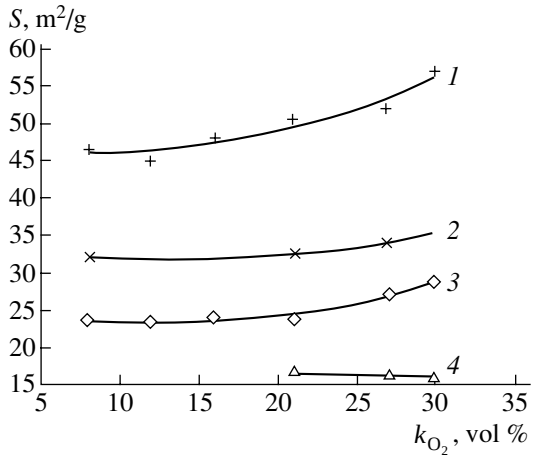

Fig. 3. Dependence of the specific surface area of NiO in the electric filter on the oxygen concentration at l = 227 mm and d = 0.3 mm. K = (*1*) 0.46, (*2*) 0.52, (*3*) 0.58, and (*4*) 1.

grows, so does the vapor phase concentration, and an increase in the O_2 concentration in the working gas has no longer a significant influence. At K = 1, the vapor seems to be supersaturated even at the very beginning of expansion: the particle size grows, and the specific surface area of the powder declines (Fig. 3).

To determine the oxygen content, we proceeded as follows. The nickel content was determined by elemental analysis using an inductively coupled plasma (ICP), and the Ni and NiO contents in the powder were found by X-ray diffraction (XRD). The Ni content determined by the ICP analysis was corrected for the content of volatiles that was obtained by thermogravimetric analysis (TGA). From the resulting value, the nickel content calculated from the XRD data was subtracted. Then, the oxygen content was calculated. The tabulated data show that the powders free of metallic nickel are both stoichiometric in oxygen content (lot NiO-56) and oxygen-enriched to 9%. The oxygen content in the lots with metallic Ni (NiO-9 and others) was calculated approximately, since the Q-1500 derivatograph failed in correctly measuring the content of volatiles in the neutral gas. The TGA data represent the sum of desorption from and oxidation of metallic nickel. Analyzing the explosion conditions and oxygen content, we found that the latter grows with decreasing nickel vapor concentration. The oxygen content in the powders prepared by explosion of the thinner wire is higher, all other things being equal.

There is evidence that higher nickel oxides (Ni_2O_3) exist [6]. This suggests that the excessive oxygen observed in the nickel oxide nanopowders enters into Ni_2O_3 present in NiO in the form of a solid solution. However, the existence of Ni_2O_3 is not yet a well-documented fact [6].

After sedimentation under the conditions described, the powders contain particles up to 300 nm in size and

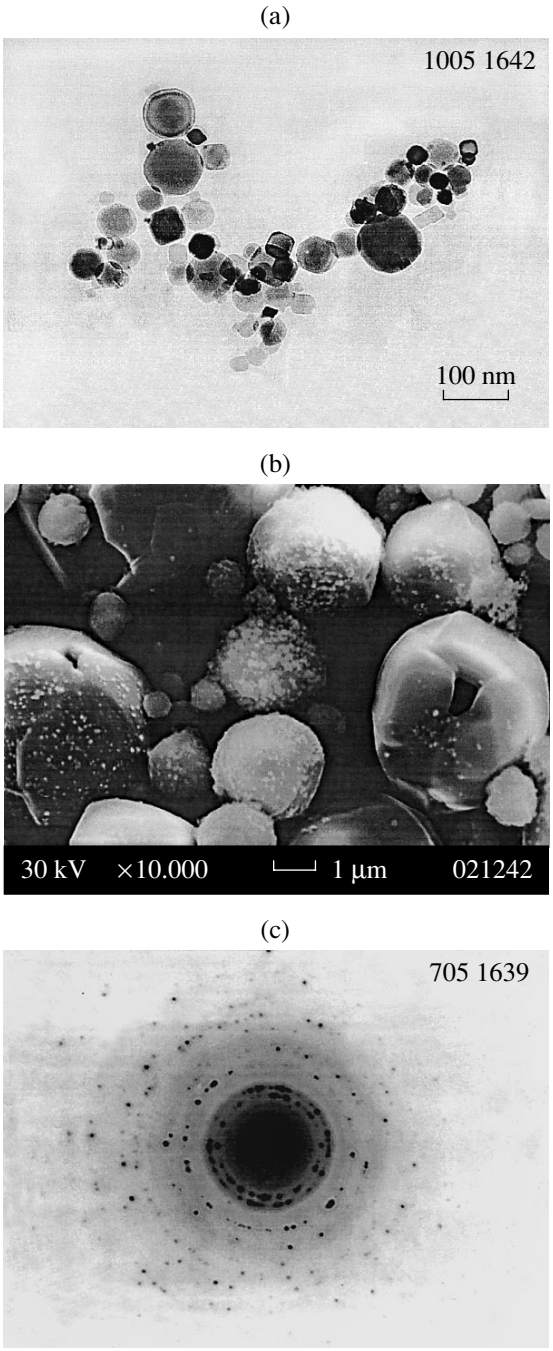

Fig. 4. Typical micrographs of the (a) nanoparticles and (b) sediments and (c) the electron diffraction pattern of the nanoparticles.

are free of metallic nickel (see the XRD data in table); therefore, we may conclude that Ni is present in particles whose size exceeds 300 nm.

From micrographs (Fig. 4a) and electron diffraction patterns (Fig. 4c) taken of the powder particles, it follows that they have different shapes (from cubic to spherical) and a crystal structure where the basic phase is rhombohedral NiO. The latter fact is supported by the

Table

Lot no.	S, m^2/g	Ni content (ICP analysis), wt %	Content of volatiles (TGA), wt %	Metallic Ni content (XRD), wt %	Ni content in NiO, wt %	Oxygen content in oxide
NiO-6*ns*	36	75.9	2.75	0	78.05	$NiO_{1.033}$
NiO-7*ns*	54	74.4	3.5	0	77.1	$NiO_{1.09}$
NiO-9*ns*	30	76.05	1.94	0	77.6	$NiO_{1.06}$
NiO-10*ns*	45	75.4	3.3	0	78.0	$NiO_{1.04}$
NiO-9	24	77.4	1.48	3.7	74.9	$NiO_{1.23}$
NiO-13	21	76.8	1.73	1.3	76.8	$NiO_{1.11}$
NiO-50	47	75.8	2.82	1.0	77.0	$NiO_{1.096}$
NiO-52	27	75.1	2.71	<0.5	76.7	$NiO_{1.11}$
NiO-56	57	75.5	4.0	0	78.6	$NiO_{1.0}$
NiO-61	16	77.2	1.77	<0.5	78.1	$NiO_{1.029}$

Notes: The error in the Ni content determined by both methods is ±0.3%. The stoichiometric Ni content in the NiO oxide is 78.58 wt %. Letters *ns* in the batch number indicate that the powder was subjected to sedimentation in isopropyl alcohol and does not contain particles coarser than 300 nm.

XRD data. The lattice parameters along the hexagonal axes are a = 0.2952 nm and c = 0.7237 nm. Comparing the grain sizes determined by XRD (34–49 nm) with the mean of the bulk and surface particle diameters (d_{BET} = 15–50 nm) from lot to lot shows that these values may both coincide and differ by roughly twofold. This suggests that the NiO particles are in both the single-crystal and polycrystalline states. We failed to establish any correlation between the grain size and explosion conditions.

The micrographs of the powder sediments (Fig. 4b) exhibit particles that are likely to form when the liquid metal splashes out through the solidifying surface layer (the melting point of nickel is lower than that of its oxide) because of heating the particles by the energy of oxidation. This finding confirms our concepts of the particle formation mechanism.

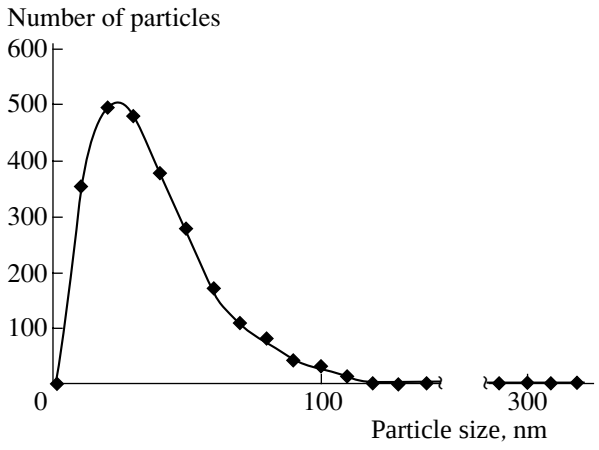

Fig. 5. Particle size distribution in the powder from lot 10 ns.

The particle size distribution in the powder sediment (Fig. 5, a total of 2448 particles included) turns out to be close to the logarithmically normal distribution with average geometric diameter d_g = 24.4 nm and standard deviation σ_g = 2.3. Here, 28 particles have a diameter falling into the range 100–200 nm and four particles have a diameter of >200 nm (the largest one had a diameter of 317 nm). The calculation based on this distribution demonstrates that the weight of particles smaller than 100 nm across accounts for 58% of the total weight and the percentage of these particles is more than 98%.

CONCLUSIONS

The conditions for production of nickel oxide nanopowders by electrical explosion of a wire were studied. A decrease in the overheat and an increase in the oxygen concentration favor the preparation of the powders with a nanoparticle size of ≈15 nm by explosion in a gaseous atmosphere under normal pressure.

The yield of the powder fraction with a particle size of less than 100 nm accounts for about 15% of the weight of the wire for low-overheat explosions and increases to 30% at K = 1.

A decrease in the particle concentration in the flow through an increase in the cross section of the gas tubes and in the diameter of the cyclones substantially improves powder separation and increases the weight of the nanofraction.

The particles have various shapes and may be both single-crystal and polycrystalline.

The nickel oxide prepared under our conditions is oxygen-enriched to 9% relative to its stoichiometric composition.

ACKNOWLEDGMENTS

We are grateful to T.M. Demina and V.M. Tel'nova for assistance and also to E.I. Azarkevich for valuable discussion.

This work was supported by the program "Fundamental Problems in the Physics and Chemistry of Nanosystems and Nanomaterials" at the Russian Academy of Sciences.

REFERENCES

1. Yu. A. Kotov and O. M. Samatov, Poverkhnost, Nos. 10–11, 90 (1994).
2. Yu. A. Kotov, E. I. Azarkevich, I. V. Beketov, *et al.*, Key Eng. Mater. **132–136**, 173 (1997).
3. E. I. Azarkevich, I. V. Beketov, Yu. A. Kotov, *et al.*, in *Proceedings of the 5th All-Russia Conference on Physical Chemistry of Ultradisperse Systems, Yekaterinburg, 2000* (Inst. Fiz. Met., Ural. Otd. Ross. Akad. Nauk, Yekaterinburg, 2001), Part 1, pp. 104–108.
4. Yu. A. Kotov, I. V. Beketov, E. I. Azarkevich, *et al.*, in *Proceedings of the 9th CIMTEC – World Ceramics Congress and Forum on New Materials, Florence, 1999*, Ed. by P. Vincenzin (Techna, Faenza, 1999), pp. 277–284.
5. Yu. A. Kotov, E. I. Azarkevich, I. V. Beketov, *et al.*, in *Structure, Phase Transformations and Properties of Nanocrystalline Alloys* (UrO RAN, Yekaterinburg, 1997), pp. 28–36.
6. N. A. Toropov, V. P. Barzakovskiĭ, I. A. Bondar', and Yu. P. Udalov, *A Handbook: State Diagrams of Silicate Systems*, Issue 2: *Metal-Oxide Compounds of Silicate Systems* (Nauka, Leningrad, 1970) [in Russian].

Translated by K. Shakhlevich

Technical Physics, Vol. 50, No. 10, 2005, pp. 1284–1294. Translated from Zhurnal Tekhnicheskoĭ Fiziki, Vol. 75, No. 10, 2005, pp. 34–43.

GAS DISCHARGES, PLASMA

Low-Frequency Dielectric-Barrier Discharge in the Townsend Mode

D. S. Nikandrov and L. D. Tsendin

St. Petersburg State Polytechnical University, ul. Politekhnicheskaya 29, St. Petersburg, 195251 Russia

Received February 10, 2005

Abstract—An analytic model is proposed of a dielectric-barrier discharge in the Townsend mode, in which the space charge is small compared to the charge accumulated on the dielectric surface. The discharge mode depends substantially on the ratio between the frequency of the external voltage and the ion drift time through the gap. A low-frequency case is investigated, in which the space charge can be ignored. The analytic expressions obtained agree well with experiments and numerical simulations. The physical mechanism for the onset of relaxation oscillations in the Townsend mode is revealed. The time behavior of a dielectric-barrier discharge is qualitatively described, and its basic scaling parameters are determined. © *2005 Pleiades Publishing, Inc.*

INTRODUCTION

The dielectric-barrier discharge (DBD) is a gas discharge operating between electrodes one (or both) of which is covered with a dielectric (see Fig. 1). DBDs were first utilized to produce ozone [1, 2]. Nowadays, they are widely used for the sterilization of medical instrumentation [3], in plasma panels [4], and in excimer lamps [5]. When an ac voltage is applied to the electrodes, the electric field in the gap is determined by the applied voltage and the charge accumulated on the dielectric surface. The discharge occurs when the field strength exceeds the breakdown level. DBD experiments were carried out over a wide range of the discharge parameters: the pressure was varied from a few Torr to several hundred Torr [6, 7], and the frequency of the applied voltage was varied from a few kHz to several hundred kHz [7, 8]. The electrode gap length was usually on the order of several millimeters.

Three fundamentally different DBD modes can be distinguished: the Townsend mode, the uniform glow mode, and the filamentary mode. The simplest is the Townsend mode, in which the electric field is not disturbed by the space charge and no plasma is produced. In the glow discharge mode, which is often observed at high frequencies of the external voltage, the field is strongly disturbed by the space charge and most of the discharge volume is occupied by the plasma. A filamentary discharge is an ensemble of thin conducting plasma channels (filaments) growing chaotically between the electrodes.

In spite of significant progress in numerical simulations (see, e.g., [5, 9]), it is desirable to obtain a qualitative analytic picture of such discharges. In this study, we consider the basic scaling laws that allow one to predict the time dependences of the DBD current and electric field in the Townsend mode. The physical mechanism for the onset of oscillations of the current and electric field in a DBD discharge is revealed, and simple analytic expressions describing such oscillations are obtained.

Here, we consider the case where the frequency of the applied voltage ω is much lower than the inverse ion drift time through the discharge gap, τ^{-1}. If the ion motion is governed by the ion mobility, then we have

$$\tau = \frac{L}{E_{\rm br} b_i} \ll \frac{2\pi}{\omega}, \qquad (1)$$

where $E_{\rm br}$ is the breakdown electric field and b_i is the ion mobility. In Section 1, we present the basic equations of the problem. If there are no charged particles in the gap (passive phase II), then the surface charge is constant and the electric field in the gap follows the applied voltage $U(t)$. Active phase I is accompanied by oscillations of the discharge current, the electric field in the gap, and the surface charge. A relation between the applied voltage $U(t)$, the electric field in the gap, and the surface charge density is obtained. In Section 2, the equation for the conduction current is derived. Oscilla-

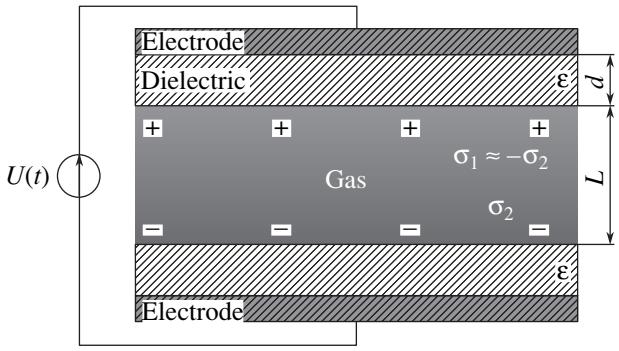

Fig. 1. Scheme of a discharge cell.

1063-7842/05/5010-1284$26.00 © 2005 Pleiades Publishing, Inc.

tion mode I is investigated in Section 3. The oscillation mode that occurs when the applied voltage $U(t)$ varies gradually over time is investigated in Sections 4 and 5. It is shown that, when $U(t)$ varies abruptly (a meandering voltage), no oscillations are excited. In Section 6, the calculated results are compared to experiments and numerical simulations. The distortion of the electric field in the gap by the space charge is considered in the Appendix.

1. BASIC EQUATIONS AND SIMPLE ESTIMATES

The current in the dielectric is entirely carried by the displacement current, whereas, in the discharge gap, it is carried by both the displacement and conduction currents. The charges produced in the gap are rapidly (over a time of about τ) carried away from the gap to the dielectric surface and accumulate on it over a time on the order of ω^{-1}. Therefore, when inequality (1) is satisfied, the space charge is small compared to the surface charge and the charge densities on the electrodes differ only in their signs,

$$\sigma_1(t) \approx -\sigma_2(t). \tag{2}$$

In this case, the electric field in the gap is determined by the applied voltage and the surface charges. The field produced by the surface charges can partially neutralize the applied voltage; therefore, in the case of high overvoltages, the net field in the gap is the difference of the two large terms. The condition under which the distortion of the field in the gap by the space charge is small in comparison to the breakdown field is found in the Appendix.

In order to solve the problem, it is necessary to express the field in the gap through the applied voltage $U(t)$ and the charge density on the dielectric surface, $\sigma(t) = |\sigma_1(t)|$. According to the Gauss theorem, we have

$$E = U\frac{1}{L + \frac{2d}{\varepsilon}} + \sigma\frac{8\pi}{L + \frac{2d}{\varepsilon}}\frac{d}{\varepsilon}. \tag{3}$$

As soon as the field in the gap exceeds E_{br}, the current begins to grow rapidly. The discharge current as a function of the electric field is determined by the exponential dependence of the first Townsend ionization coefficient α on the electric field. In turn, the ratio M of the electron flux onto the anode to that onto the cathode depends exponentially on α. The current through the gap increases by a factor of $M - 1$ over a time on the order of τ. Therefore, the current grows over time by a nearly exponential law with the power index $\int^t \frac{M-1}{\tau}\,dt$. According to the Le Chatelier principle, such a rapidly growing current keeps the electric field at a level close to E_{br}. Therefore, when developing a simplified model, we can assume that the electric field in a Townsend discharge does not exceed the breakdown field, $|E(t)| \le E_{br}$. The discharge operation over the entire period of the applied voltage can be separated into two phases. During active phase I ($t^* < t < \pi/2\omega$), the conduction current flowing through the gap changes the surface charge density and maintains the electric field at the level $E \approx E_{br}$. According to Eq. (3), the surface charge density varies in proportion to $-U(t)$. During phase II,

$$\frac{\pi}{2\omega} < t < \frac{\pi}{\omega} + t^*,$$

the electric field in the gap is lower than E_{br}. At the very beginning of this phase, all the charged particles are carried away from the gap to the dielectric surface. After this, the conduction current is zero and the surface charge density is constant. According to Eq. (3), a change in the applied voltage leads only to a change in the electric field in the gap. The beginning of active phase I is uniquely determined by the formula

$$t^* = U^{-1}\left(2E_{br}\left(L + \frac{2d}{\varepsilon}\right) - U\Big|_{t=\frac{\pi}{2\omega}}\right). \tag{4}$$

When phase I changes into phase II, the electric field in the gap varies continuously,

$$E(t) = \begin{cases} \dfrac{U(t) + U\big|_{t=\frac{\pi}{2\omega}}}{L + \dfrac{2d}{\varepsilon}} - E_{br}, & -\dfrac{\pi}{2\omega} < t < t^* \\ E_{br}, \quad t^* < t < \dfrac{\pi}{2\omega}. \end{cases} \tag{5}$$

The time evolution of the electric field, the surface charge density, and the current in the case of a sinusoidal voltage is shown in Fig. 2.

When the overvoltage is low,

$$U_{max} < 2L\left(1 + \frac{2d}{L\varepsilon}\right)E_{br}, \tag{6}$$

breakdown occurs after $U(t)$ changes its sign. Conversely, in the case of high overvoltages,

$$U_{max} > 2L\left(1 + \frac{2d}{L\varepsilon}\right)E_{br},$$

breakdown occurs before $U(t)$ changes its sign. It can be seen that the durations of phases I and II depend on the amplitude of the applied voltage. The overall pattern of the time evolution of the electric field is illustrated in Fig. 3.

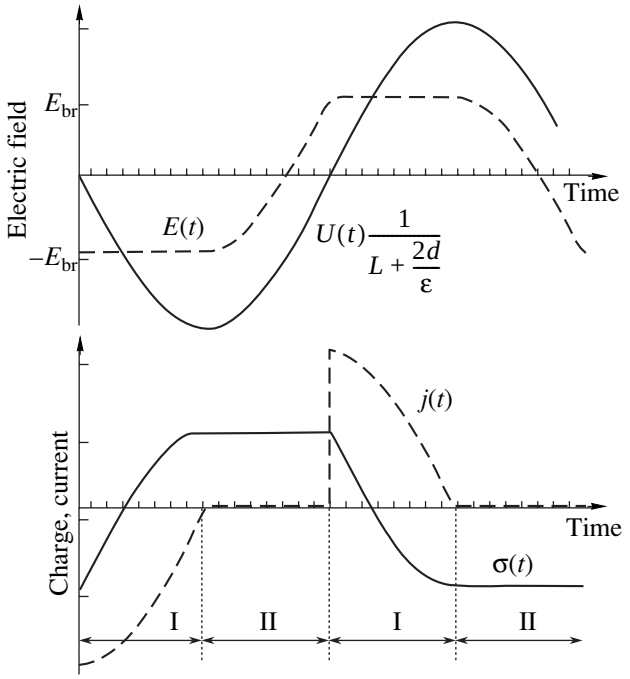

Fig. 2. Time evolution of the current, the surface charge, and the electric field in the gap. In phase I, the current maintains the electric field at a level of $E \approx E_{br}$. In phase II, the conduction current is absent.

From Eq. (3), we obtain the expression for the conduction current that is necessary to limit the electric field:

$$j = \frac{d\sigma}{dt} = \begin{cases} \dfrac{dU}{dt}\dfrac{\varepsilon}{8\pi d}, & t \in \text{I} \\ 0, & t \in \text{II}. \end{cases} \tag{7}$$

In fact, the current during phase II is very low. It cannot increase instantaneously to the value prescribed by Eq. (7). Therefore, the current is delayed relative to the applied voltage; this circumstance is not accounted for in our simplified model. When the electric field reaches E_{br}, the current is still very low and the surface charge density is essentially constant. Since the voltage $U(t)$ varies with time, while the surface charge density remains constant, the electric field in the gap continues to grow (see Eq. (3)) and exceeds E_{br}. This process continues until the current becomes high enough for the surface charge density to vary significantly; as a result, the electric field begins to decrease. The current increases until $E(t)$ becomes lower than E_{br}. Such behavior corresponds to relaxation oscillations. To describe these oscillations quantitatively, it is necessary to determine the functional dependence between the electric field and the current. Below, we will derive a closed equation describing oscillation phase I.

2. CURRENT EVOLUTION

We restrict ourselves to a simple Townsend model in which the electrons in the gap are multiplied mostly via the impact ionization of neutral atoms. This process is determined by the electric field alone. The secondary electrons are emitted from the cathode due to its bombardment by ions. The duration of the electron multiplication cycle in a Townsend discharge is determined by the characteristic drift time τ of an ion from the place of its origin to the cathode surface (the cathode and the anode are defined in relation to the electric field in the gap). Let us first consider the case of local ionization. In this case, the current varies according to the formula [10]

$$j(t) = j_{ext}(t) + \int_0^L j\left(t - \frac{x}{u}\right)\gamma\alpha\left(t - \frac{x}{u}\right) \times \exp\left[x\alpha\left(t - \frac{x}{u}\right)\right]dx. \tag{8}$$

Here, $j(t)$ is the conduction current at the cathode, $j_{ext}(t)$ the ion-induced electron emission (the external ionizer current), and u is the ion drift velocity. Note that, knowing solution (8) with $j_{ext}(t) \propto \delta(t - t')$, we can find the solution for an arbitrary time dependence of $j_{ext}(t)$:

$$j(t) = \frac{u}{L}\int_{-\infty}^{t} j_{ext}(t')i(t, t')dt',$$

$$i(t, t') = \frac{L}{u}\delta(t - t') + \int_0^L i\left(t - \frac{x}{u}\right)\gamma\alpha\left(t - \frac{x}{u}\right)\exp\left[x\alpha\left(t - \frac{x}{u}\right)\right]dx. \tag{9}$$

Therefore, the solution $i = i(t, t')$ is a kind of Green's function for our problem. Since we describe variations in the electric field during phase I, we have $\gamma(e^{\alpha(t)L} - 1) \approx 1$. In case of a constant overvoltage, the current grows exponentially, $i = i_0\exp(\beta(t - t'))$. Indeed, such a time dependence is a solution to Eq. (9). The coefficient β satisfies the transcendent equation

$$\left[1 + \gamma - \frac{\beta}{u\alpha}\right]\frac{1}{\gamma e^{\alpha L}} = \exp\left(-\frac{\beta L}{u}\right), \tag{10}$$

which always has a solution. For example, when $\gamma \ll 1$, we have

$$\beta = \frac{u\ln(\gamma(e^{\alpha(t)L} - 1))}{L}.$$

If β changes only slightly over the time τ, then we can use an approach similar to the WKB approxima-

tion; i.e., we can assume

$$i = i_0 \exp\left(\int_{t'}^{t} \beta\right), \tag{11}$$

where β depends explicitly on time,

$$\left[1 + \gamma - \frac{\beta}{u\alpha(t)}\right]\frac{1}{\gamma e^{\alpha(t)L}} = \exp\left(-\frac{\beta L}{u}\right). \tag{12}$$

It follows from Eqs. (9) and (11) that, in the case of local ionization, the current varies as

$$j(t) = \int_{-\infty}^{t} \frac{j_{\text{ext}}(t')}{\tau} \exp\left(\int_{t'}^{t} \frac{\ln[\gamma(e^{\alpha(t'')L} - 1)]}{\tau} dt''\right) dt'. \tag{13}$$

The results obtained can be generalized to the case of nonlocal ionization. Thus, solution (8) can be rewritten as

$$j(t) = j_{\text{ext}}(t) + \int_0^L j\left(t - \frac{x}{u}\right)\frac{\partial M}{\partial x}\bigg|_{t-\frac{x}{u}} dx, \tag{14}$$

where $M(x, E)$ is the coefficient of electron multiplication.

This coefficient is equal to the number of secondary electrons generated by one primary electron as it travels a distance x from the cathode. In the case of local ionization, we have

$$M(x, E) = \gamma(e^{\alpha(E)x} - 1). \tag{15}$$

Therefore, the only characteristic of the ionization process is the coefficient $M(x, E)$. A conventionally used multiplication coefficient is equal to $M(E(t)) = M(L, E(t))$. Hence, solution (14) can be rewritten as

$$j(t) = \int_{-\infty}^{t} \frac{j_{\text{ext}}(t')}{\tau} \exp\left(\int_{t'}^{t} \frac{\ln M(E(t''))}{\tau} dt''\right) dt'. \tag{16}$$

Expression (16) has a clear physical meaning. The current at the time t is determined by the values of the external ionizer current and the electric field at the previous times. The ionizer currents generated at the previous times are amplified by a factor of $M^{t/\tau}$ and are added together. It can be seen that the current does not change instantaneously, as was assumed in the above simplified model (see Fig. 2).

The lower integration limit in Eq. (16) corresponds to phase II, in which $M \ll 1$. The conduction current at the instant of breakdown is determined by the expression

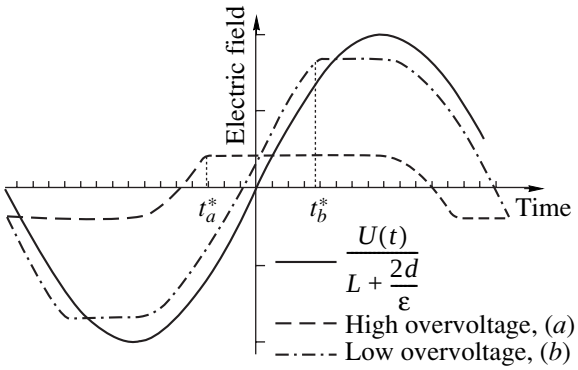

Fig. 3. The effect of the overvoltage on the electric field in the gap.

$$\begin{aligned} j(t^*) &= \int_{-\infty}^{t^*} \frac{j_{\text{ext}}(t')}{\tau} \exp\left(\int_{t'}^{t^*} \frac{\ln M(t'')}{\tau} dt''\right) dt' \\ &\approx j_{\text{ext}}(t^*) \sqrt{\frac{\pi}{2\tau \dfrac{d[M(E(t))]}{dt}\bigg|_{t=t^*}}}. \end{aligned} \tag{17}$$

For the sake of convenience, we will further assume that $t^* = 0$ (see Fig. 3).

3. OSCILLATORY DISCHARGE MODE

Expression (16) is a solution to the differential equation

$$\tau \frac{dj}{dt} = j \ln M(E) + j_{\text{ext}}. \tag{18}$$

By differentiating Eq. (3) over time, we obtain an additional equation for the electric field in the gap,

$$\frac{dE}{dt} = \frac{dU}{dt}\frac{1}{L + \frac{2d}{\varepsilon}} - j\frac{8\pi}{L + \frac{2d}{\varepsilon}}\frac{d}{\varepsilon}. \tag{19}$$

Combining Eqs. (18) and (19), we obtain a closed differential equation for the electric field in phase I,

$$\begin{aligned} \frac{d^2E}{dt^2} &= \frac{d^2U}{dt^2}\frac{1}{L\left(1 + \dfrac{2d}{\varepsilon L}\right)} \\ &+ \frac{\ln M(E)}{\tau}\left(\frac{dE}{dt} - \frac{dU}{dt}\frac{1}{L\left(1 + \dfrac{2d}{\varepsilon L}\right)}\right) - \frac{8d\pi}{\varepsilon L + 2d}\frac{j_{\text{ext}}(t)}{\tau}. \end{aligned} \tag{20}$$

To analyze this equation, we introduce the following dimensionless variables: the time $\theta = t/\tau$, the electric

field $E = E/E_{br}$, the external voltage

$$\Phi = \frac{U}{1 + \frac{2d}{\varepsilon L}} \frac{1}{E_{br} L},$$

and the ionizer current $\iota = j_{ext}/j|_{t=0}$. We also introduce the dimensionless coefficient

$$\kappa = \frac{8\pi d}{(\varepsilon L + 2d)} \frac{j|_{t=0}}{E_{br}} \tau. \quad (21)$$

The current at the instant of breakdown, $j|_{t=0}$, is proportional to the ionizer current and is defined by Eq. (17). Hence, Eq. (20) can be rewritten as

$$\begin{cases} \dfrac{d^2\mathrm{E}}{d\theta^2} - \dfrac{d^2\Phi}{d\theta^2} - \ln(M(\mathrm{E}))\left(\dfrac{d\mathrm{E}}{d\theta} - \dfrac{d\Phi}{d\theta}\right) = -\iota\kappa \\ E|_{\theta=0} = 1, \quad \left.\dfrac{d\mathrm{E}}{d\theta}\right|_{\theta=0} = \left.\dfrac{d\Phi}{d\theta}\right|_{\theta=0} - \kappa. \end{cases} \quad (22)$$

In the case of local ionization, the coefficient $M(\mathrm{E})$ is determined by Eq. (15). The ionization coefficient α is related to the electric field and gas pressure as $\alpha/p = f(E/p)$ and is usually written as

$$\alpha/p = A\exp\left(-\frac{B}{E/p}\right).$$

It is worth noting that the above equations remain valid for any other dependence of the multiplication coefficient on the electric field.

Equation (22) describes relaxation oscillations of the electric field. If the frequency of these oscillations is much higher than ω, which takes place when expression (1) is satisfied with a large margin, then the oscillation characteristics adiabatically follow $d\Phi/d\theta$. This was proved experimentally for the first time in [11]. The value of $d^2\Phi/d\theta^2$ does not influence the solution because, as follows from condition (1),

$$\frac{d\Phi}{d\theta} \gg \frac{d^2\Phi}{d\theta^2}.$$

An exception is the case where $\Phi(\theta)$ varies abruptly. We will consider this case using a meandering $\Phi(\theta)$ as an example.

4. THE CASE OF A GRADUALLY VARYING EXTERNAL VOLTAGE

In the case of a gradually varying external voltage, Eq. (22) can be rewritten as

$$\begin{cases} \dfrac{d^2\mathrm{E}}{d\theta^2} - \ln(M(\mathrm{E}))\left(\dfrac{d\mathrm{E}}{d\theta} - \Phi'\right) = -\iota\kappa \\ \mathrm{E}|_{\theta=0} = 1, \quad \left.\dfrac{d\mathrm{E}}{d\theta}\right|_{\theta=0} = \Phi' - \kappa, \quad \Phi' = \dfrac{d\Phi}{d\theta} = \text{const}. \end{cases} \quad (23)$$

Note that there is a small parameter κ in both Eq. (23) and the initial condition for the time derivative. The smallness of the parameter κ follows from its proportionality to the external ionizer current. Omitting this parameter in the equation is equivalent to the switching-off of the ionizer at the time $\theta = 0$. The multiplication of electrons in the growing electric field $\mathrm{E}(\theta) > 1$ is always very intense; hence, taking into account the ionizer current against this background leads only to small corrections that decrease with decreasing κ, as will be shown below. Ignoring these corrections, we obtain

$$\frac{d^2\mathrm{E}}{d\theta^2} - \ln(M(\mathrm{E}))\left(\frac{d\mathrm{E}}{d\theta} - \Phi'\right) = 0. \quad (24)$$

This equation describes the motion of a particle in a system with a driving force and alternating friction. The driving force and friction change their signs at $\mathrm{E} = 1$. Homogeneous equation (24) has a strictly periodic solution. The electric field $\mathrm{E}(\theta)$ oscillates from $\mathrm{E}_{max} = \max_\theta(\mathrm{E})$ to $\mathrm{E}_{min} = \min_\theta(\mathrm{E})$, so that

$$\begin{gathered} \int_1^{E_{max}} \ln M d\mathrm{E} = \kappa + \Phi'\left(\ln\frac{\Phi'}{\kappa} - 1\right), \\ \int_{E_{min}}^{E_{max}} \ln M d\mathrm{E} = 0. \end{gathered} \quad (25)$$

Let us consider the case of small-amplitude oscillations. In this case, we have $M(\mathrm{E}) = 1 + M'(\mathrm{E} - 1)$. It can be seen from Eq. (25) that this equality is equivalent to the condition

$$\mathrm{E}_{max} - 1 \approx 1 - \mathrm{E}_{min}. \quad (26)$$

The phase portrait of the solution in this case,

$$\begin{cases} p + \ln|p-1| = z^2 - X \\ p = \dfrac{d\mathrm{E}}{d\theta}\dfrac{1}{\Phi'}, \quad Z = \left(\dfrac{M'}{2\Phi'}\right)^{1/2}(\mathrm{E}-1); \quad X = \ln\dfrac{\Phi'}{\kappa} - 1 \end{cases} \quad (27)$$

is shown in Fig. 4.

At large values of the parameter X (starting from $X \approx 1$), the phase trajectory in the region of a decreasing electric field can be approximated by $p = z^2 - X$. This allows us to determine both the law according to which the electric filed decreases and the oscillation period Θ,

$$\begin{gathered} \mathrm{E} = 1 - \sqrt{\frac{2\Phi' X}{M'}}\tanh\left(\left(\theta - \frac{\Theta}{2}\right)\sqrt{\frac{M'\Phi' X}{2}}\right) \\ \approx 1 - \Phi' X\left(\theta - \frac{\Theta}{2}\right), \end{gathered} \quad (28)$$

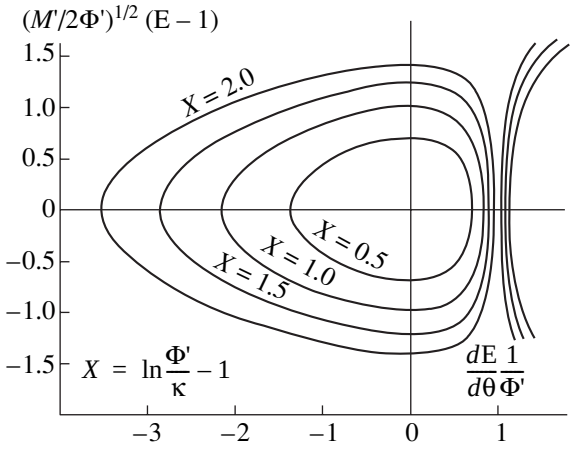

Fig. 4. Phase trajectories of the electric field in a DBD discharge (the case of small-amplitude oscillations).

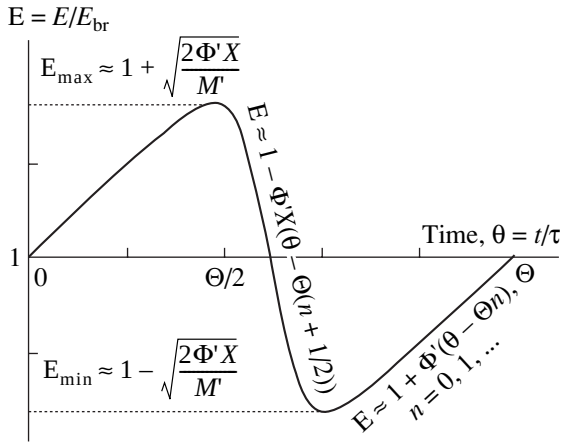

Fig. 5. Small-amplitude oscillations of the electric field in the gap for $X = 4$.

$$\Theta \approx \frac{1+X}{\Phi' X}(E_{max} - E_{min}) \approx (1+X)\sqrt{\frac{8}{\Phi' X M'}}. \quad (29)$$

A strictly periodic solution (see Fig. 5) can be obtained only when the external ionizer is completely switched off at the time θ = 0. Taking into consideration the ionizer current at a constant Φ' results in a gradual decrease in the oscillation amplitude with time. In this case, the field approaches a limiting value E_{lim}, satisfying the equation

$$M(E_{lim}) = \exp\left(-\frac{\iota\kappa}{\Phi'}\right). \quad (30)$$

In the case of $E_{lim} \approx 1$, Eq. (30) has the solution

$$E_{lim} = 1 - \frac{\iota\kappa}{M'\Phi'}.$$

The characteristic decay time of the electric-field oscillations can easily be estimated. Defining E as a solution to Eq. (24) and E + δE as a solution to Eq. (23), we can expand δE in a series up to the first nonvanishing term,

$$\delta E \approx -\frac{\iota\kappa}{2}\theta^2.$$

This allows us to estimate the correction to the electric field over a time interval during which the field increases, i.e., up to

$$\theta = \frac{(E_{max} - 1)}{\Phi'}.$$

A small inhomogeneity of Eq. (23) affects the solution only in the phase in which the electric field grows with time and the difference $\left(\frac{dE}{d\theta} - \Phi'\right)$ is small. Over one oscillation period, the oscillation amplitude decreases by

$$\delta E \approx \frac{\iota\kappa}{2}\left[\frac{(E_{max} - 1)}{\Phi'}\right]^2.$$

As a result, we find that the characteristic time of the oscillation damping due to the action of the external ionizer is equal to

$$\frac{\Phi'(1+X)}{\iota\kappa X}. \quad (31)$$

If time (31) is much longer than the time during which $d\Phi/d\theta$ = const, then the electric field decreases insignificantly. The condition

$$\frac{\Phi'(1+X)}{\iota\kappa X} \gg \Theta. \quad (32)$$

which follows from expression (31), can serve as a criterion of the applicability of Eq. (24) instead of Eq. (23).

This condition is satisfied at sufficiently small values of κ. When this condition is not satisfied, electric-field oscillations are almost absent, $E(\theta) = E_{lim}$ (see Fig. 3). Expressions (27), (29), and (31) determine the basic scaling parameters in the case of a gradually varying external voltage.

5. THE CASE OF A MEANDERING EXTERNAL VOLTAGE

The problem is significantly simplified in the case of a step external voltage. The main simplification is the absence of phase II (see Fig. 2), because the electric field in the gap is always on the order of the breakdown field. Equation (22) for the electric field in the gap takes

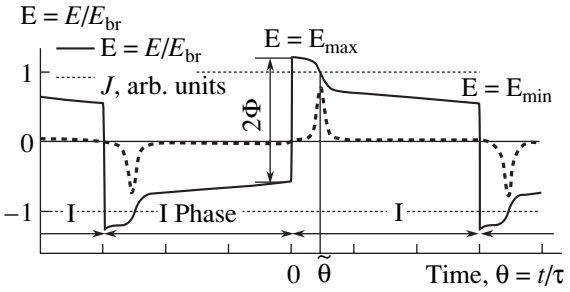

Fig. 6. Time evolution of the electric field and conduction current in the gap in the case of a meandering external voltage.

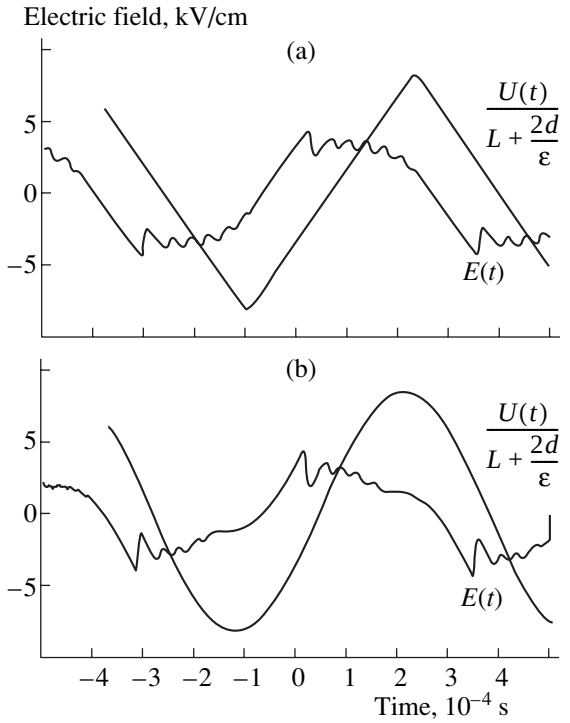

Fig. 7. Time evolution of the electric field and external voltage in a DBD [11].

the form

$$\begin{cases} \dfrac{d^2\mathrm{E}}{d\theta^2} - \ln(M(\mathrm{E}))\dfrac{d\mathrm{E}}{d\theta} = -\iota\kappa \\ \mathrm{E}|_{\theta=0} = \mathrm{E}_{\max}, \quad \left.\dfrac{d\mathrm{E}}{d\theta}\right|_{\theta=0} = -\kappa. \end{cases} \tag{33}$$

Like in the case of a gradually varying external voltage, we consider a homogeneous equation, keeping a small parameter in the initial condition,

$$\frac{d^2\mathrm{E}}{d\theta^2} - \ln(M(\mathrm{E}))\frac{d\mathrm{E}}{d\theta} = 0. \tag{34}$$

Solution to Eq. (34) can be written in quadratures,

$$\theta(\mathrm{E}) = \int_{\mathrm{E}}^{\mathrm{E}_{\max}} \frac{dx}{\kappa + \int_{x}^{\mathrm{E}_{\max}} \ln(M)}. \tag{35}$$

It can be seen from Eq. (35) that the electric field is a monotonically decreasing function that asymptotically approaches the value $\mathrm{E}_{\min}$, defined by the condition

$$\mathrm{E}_{\min}\colon \int_{\mathrm{E}_{\min}}^{\mathrm{E}_{\max}} \ln M dE = -\kappa. \tag{36}$$

To investigate solution (35) qualitatively, we write down the expressions for the time dependences of the electric field and current in the case of low overvoltages (this is equivalent to the expansion of the multiplication coefficient into a series $M(\mathrm{E}) = 1 + M'(\mathrm{E} - 1)$),

$$\begin{aligned} \mathrm{E} &= C_1 \tanh\left(C_2 - \frac{C_1 M'}{2}\theta\right) + 1, \\ J &= \frac{C_1^2 M'}{2\kappa \cosh^2\left(C_2 - \frac{C_1 M'}{2}\theta\right)}, \\ C_1 &= \sqrt{(\mathrm{E}_{\max} - 1)^2 + \frac{2\kappa}{M'}} \approx \mathrm{E}_{\max} - 1, \\ C_2 &= \operatorname{arcsinh}\left(\frac{\mathrm{E}_{\max} - 1}{\sqrt{\frac{2\kappa}{M'}}}\right). \end{aligned} \tag{37}$$

It can be seen that the current pulse is delayed relative to the $\Phi(\theta)$ and reaches its maximum at the time

$$\tilde{\theta} = \frac{2C_2}{C_1 M'} \approx \frac{2C_2}{(\mathrm{E}_{\max} - 1)M'}.$$

The maximum current is proportional to the overvoltage squared, $J(\tilde{\theta}) \sim (\mathrm{E}_{\max} - 1)^2$. It can also be seen that, at low overvoltages, we have $\mathrm{E}_{\max} - 1 \approx 1 - \mathrm{E}_{\min}$.

If the duration of phase I (see Fig. 6) is much longer than $2\tilde{\theta}$, i.e., if $\tilde{\theta} \ll \pi/2\omega\tau$, then it is necessary to consider corrections associated with the external ionizer current (i.e., to take into account the inhomogeneity of Eq. (33)),

$$\mathrm{E}(\theta) = \mathrm{E}_{\min} - \kappa \int_0^{\theta} e^{(\theta - \theta')\ln M(\mathrm{E}_{\min})} \left(\int_0^{\theta'} t(\theta'')d\theta''\right) d\theta', \tag{38}$$
$$\theta \gg \tilde{\theta}.$$

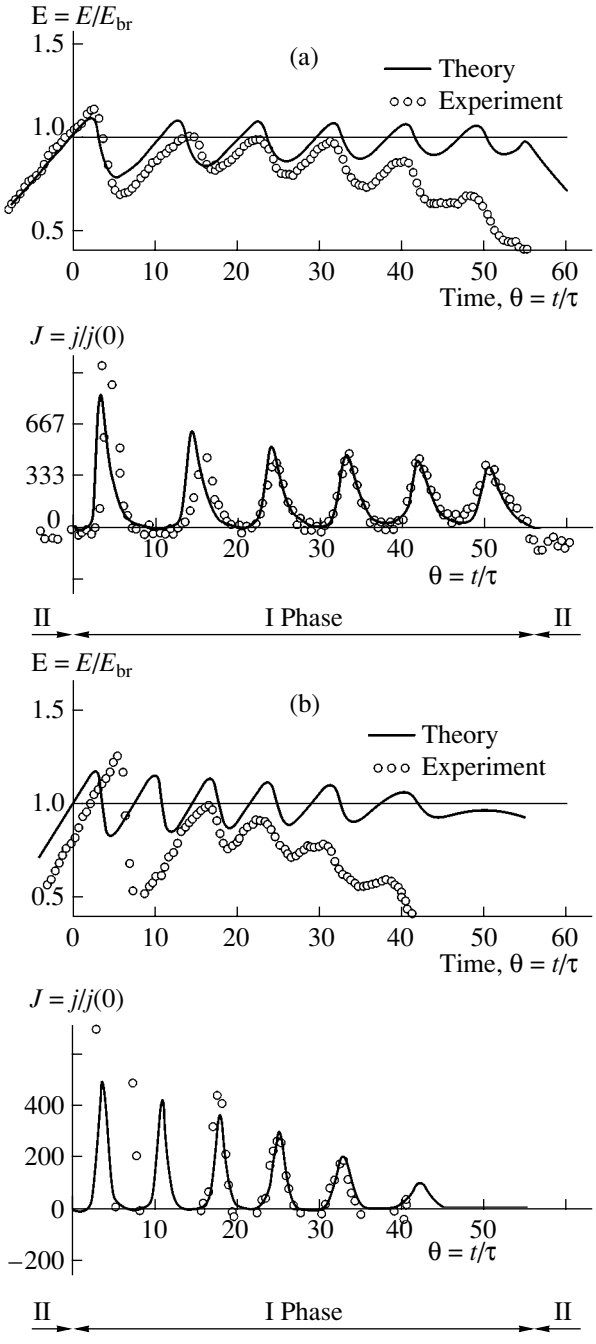

Fig. 8. Measured [11] and calculated time dependences of the electric field and current for (a) a linearly varying and (b) a sinusoidal external voltages.

Solutions (37) were found earlier in [10]. However, an important advantage of the present approach is the possibility of analyzing the case of high overvoltages and determining E_{max}. The condition of the discharge periodicity and the parity of the electrodes allows us to write the equation

$$E_{max} = 2\Phi - E\left(\frac{\pi}{\varpi\tau}\right) \approx 2\Phi - E_{min}.$$

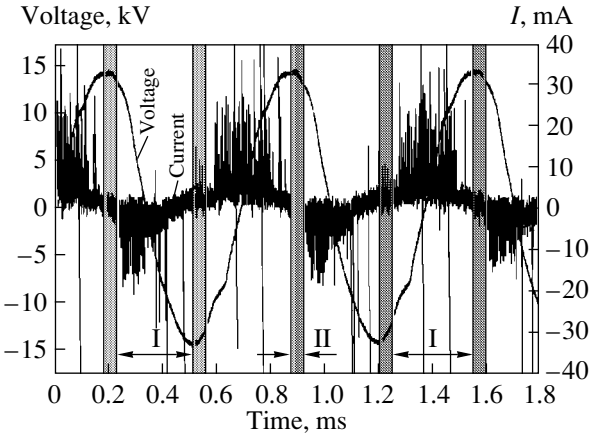

Fig. 9. Time evolution of the current and the external voltage [6]: the separation of the discharge into two phases.

Taking into consideration condition (36), we obtain the equation for E_{max},

$$\int_{2\Phi - E_{max}}^{E_{max}} \ln(M)dE = -\kappa. \quad (39)$$

In formula (39), correction (38) can also be taken into account.

6. COMPARISON WITH EXPERIMENT

The above model agrees surprisingly well with existing experimental and simulation results [6, 8, 11, 12]. The observed time evolution of the discharge parameters is analogous to those described by Eq. (5). Figure 7 illustrates the time evolution of the electric field in a discharge operating in a helium flow at a pressure of 730 Torr [11]. The frequency of the external voltage (sawtooth in case (a) and sinusoidal in case (b)) was 1.5 kHz, the other parameters being $L = 0.2$ cm, $d = 0.23$ cm, and $\varepsilon = 5$. Relaxation oscillations are clearly seen. The amplitude value of $U(t)/(L + 2d/\varepsilon)$ was close to $2E_{br}$; therefore, in accordance with Eqs. (4) and (6), phase I began just after $U(t)$ changed its sign. In accordance with simplified model (5), the oscillations terminated when the voltage reached its maximum. Note that, in the case of a sawtooth voltage, the oscillations (except for the first one) were almost periodic. Since the surface charge was constant during passive phase II, the curve $E(t)$ in this phase almost exactly followed $U(t)/L + 2d/\varepsilon$ (see Eq. (5)). The parameter pL corresponded to the right branch of the Paschen curve. When comparing the results of calculations by using Eq. (22) to the experiment, we used the Townsend approximation,

$$\alpha = Ap\exp\left(-\frac{B}{E/p}\right),$$

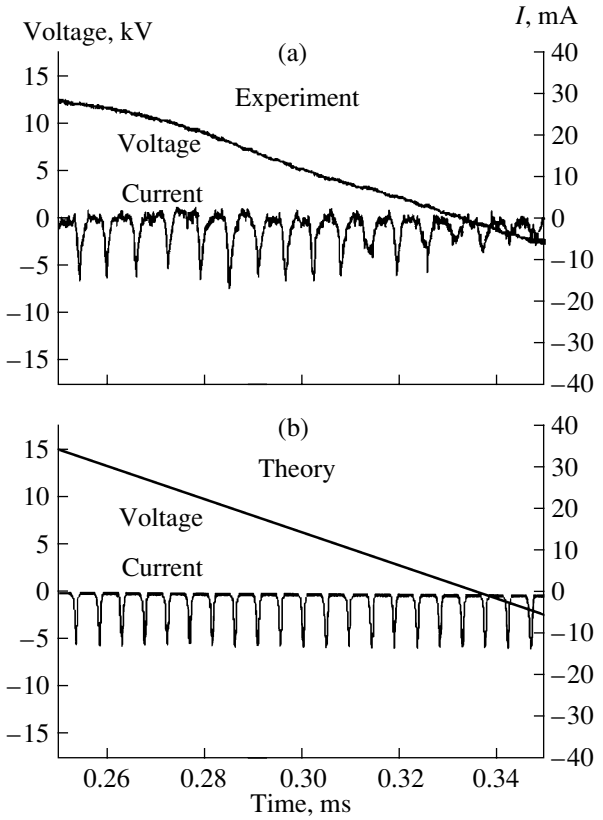

Fig. 10. Current oscillations in a DBD [6].

where $A = 3$ (cm Torr)$^{-1}$ and $B = 25$ V/(cm Torr) [13].

Such a comparison allows us to estimate the current density of the external ionizer in the range from 10^{-4} to 10^{-5} mA/cm^2. The simulation results are presented in Fig. 8. The only adjustable parameter in these calculations was the value of j_{ext}. For linearly varying and a sinusoidal external voltages, this parameter was set at 10^{-4} and 3×10^{-4} mA/cm^2, respectively. It should be noted that the results are almost insensitive to j_{ext}. Thus, in order to adequately describe the first current pulse, which differs from the others by a factor of about 2, it would necessary to assume $j_{ext} \approx 10^{-6}$ mA/cm^2.

As was mentioned above, the expressions obtained depend only on the multiplication coefficient, so they are applicable both to the right branch of the Paschen curve, when the ionization can be considered local, and to its left branch, when the ionization is nonlocal and approximation (15) is inapplicable (see [14]). Such a situation took place, e.g., in [6], where a discharge in methane at a pressure of 0.75 Torr was investigated, the other parameters being $L = 0.5$ cm, $d = 0.5$ cm, and $f = 1.4$ kHz. The separation of the discharge into two phases in accordance with our simplified model is illustrated in Fig. 9. The breakdown time determined by formula (4) is in good agreement with the experiment, in particular, at negative currents.

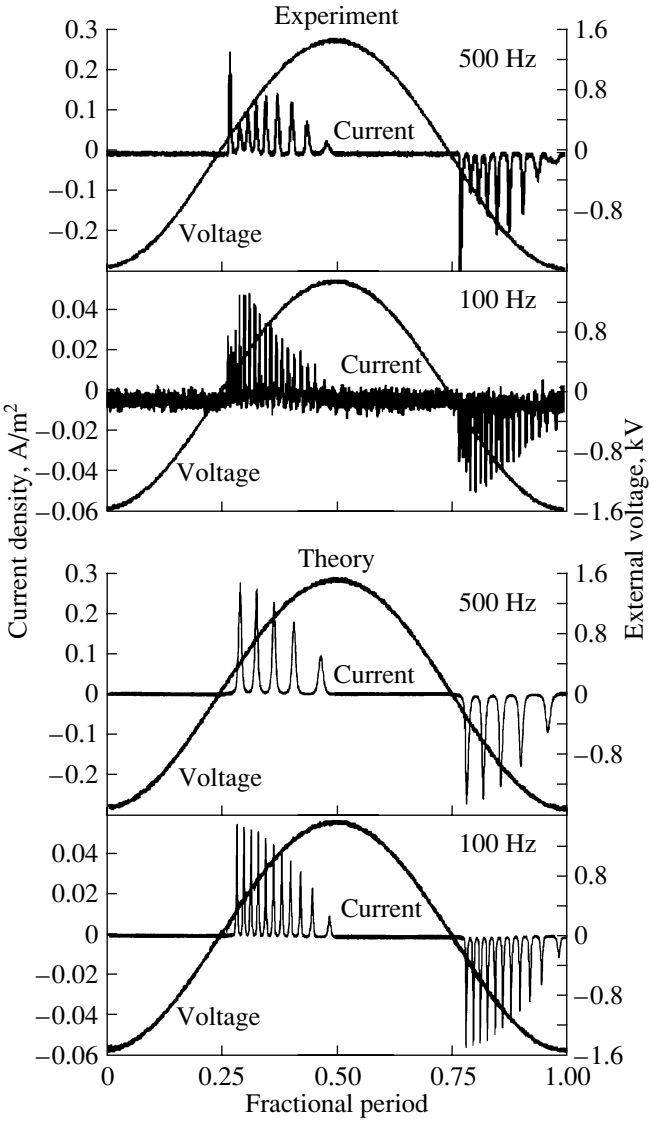

Fig. 11. Measured [8] and modeled time dependences of the current in a DBD.

From the Paschen curve presented in [6], the local values of the coefficients in the Townsend approximation were found to be $A = 12$ (cm Torr)$^{-1}$ and $B = 800$ V/(cm Torr). The time τ was estimated from the characteristic cross sections for ion–molecular collisions, and it was assumed that $j_{ext} \approx 10^{-4}$ mA/cm^2. The experimental data and theoretical results are presented in Fig. 10.

In [8], a discharge in helium at atmospheric pressure was investigated. An advantage of those experiments was that they were conducted within a wide frequency range (from 100 Hz to 10 kHz) satisfying condition (1). When comparing the results of calculations by using Eq. (24) to the experiment (see Fig. 11), we used the

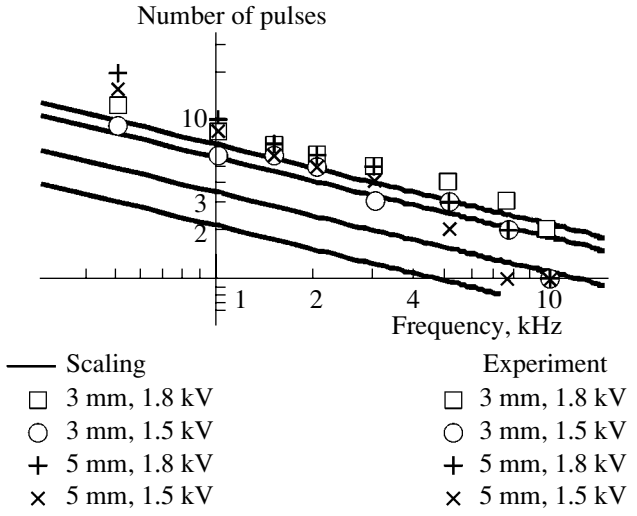

Fig. 12. The number of current pulses vs. frequency [8] and its scaling.

approximation

$$\alpha = Cp\exp\left(-D\sqrt{\frac{p}{E}}\right),$$

where $C = 44$ (cm Torr)$^{-1}$, $D = 14$ V$^{1/2}$/(cm Torr)$^{1/2}$, $L = 0.3$ cm, $d = 0.23$ cm, $\varepsilon = 7.63$, and $\gamma = 0.01$ (see [8]).

It can be seen from Fig. 11 that the theoretical results are in good agreement with the experimental data. In calculations, it was assumed that $j_{ext} \approx 5 \times 10^{-4}$ mA/cm^2 for $f = 500$ Hz and $j_{ext} = 10^{-4}$ mA/cm^2 for $f = 100$ Hz. These values of j_{ext} are in agreement with the assumption that the external ionizer current is caused by the interaction of metastable atoms with the cathode surface. However, the calculated value of the oscillation period was found to be half again the observed one. We failed to achieve better agreement in the period and shape of oscillations by varying the j_{ext} value.

The scaling of the oscillation period (see Eq. (29)) allows us to determine the number of current pulses during active phase I (Fig. 12). An approximately twofold decrease in the duration of phase I and a twofold increase in τ when passing from $L = 0.3$ to 0.5 cm should lead to a fourfold decrease in the number of current pulses. In the experiment, however, the number of current pulses did not change as compared to the case of $L = 0.3$ cm. This is presumably associated with the influence of the space charge (see Eq. (42)). Indeed, at the same frequency and waveform of the applied voltage, the space charge in the case of $L = 0.5$ cm is approximately twice as large as that in the case of $L = 0.3$ cm. It can be seen from Eq. (29) that the oscillation period is proportional to $\omega^{1/2}$. The duration of phase I is proportional to ω^{-1} and, at a given frequency, is only determined by the overvoltage (see Fig. 3). Therefore,

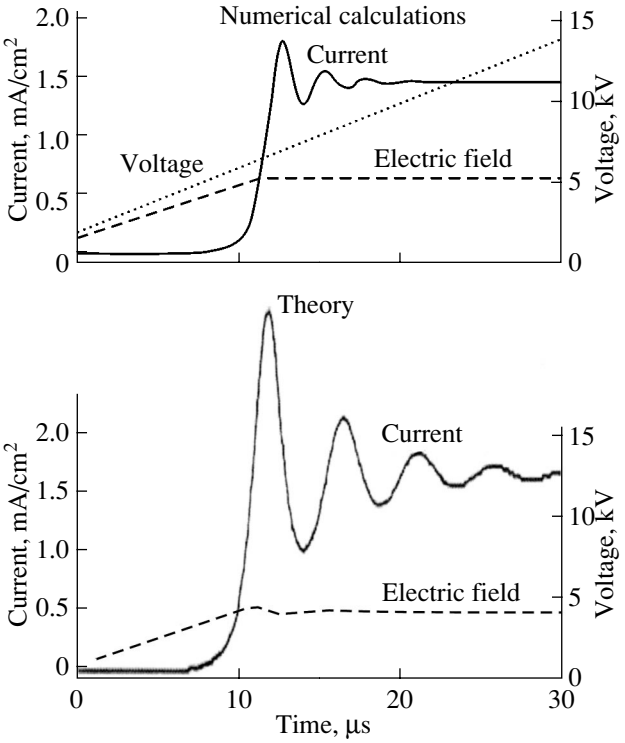

Fig. 13. Results of numerical calculations [12] and our theoretical model.

the number of current pulses is proportional to $\omega^{-1/2}$, which agrees with the experiment over the entire frequency range. Our model is also in good agreement with numerical simulations, e.g., with the results of [12], where a uniform Townsend DBD was simulated. A specific feature of those simulations was the presence of a strong external ionizer (the desorption of electrons from the cathode). As was noted above, the presence of a sufficiently strong ionizer results in the decay of relaxation oscillations (see Eq. (31)) even in the case of a linearly growing voltage. The numerical simulations carried out in [12] corresponded to a discharge in nitrogen at a pressure of 760 Torr, the other parameters being $L = 0.1$ cm, $d = 0.01$ cm, and $\varepsilon = 1$. The voltage grew linearly with $dU/dt = 4 \times 10^8$ V/s. The coefficients in the Townsend approximation were assumed to be $A = 8.8$ (cm Torr)$^{-1}$ and $B = 275$ V/(cm Torr) [13]. The simulation results [12] and the results of calculations of the electric field and current by using Eq. (22) and formula (16) are presented in Fig. 13.

CONCLUSIONS

An analytic model of a uniform DBD has been proposed. It is shown that, when the frequency of the external voltage is low as compared to the ion drift time through the gap, the discharge operates in the Townsend mode. The analytic expressions obtained are in good agreement with experimental results. The phys-

ical mechanism for the onset of relaxation oscillations in the Townsend DBD is revealed. The time behavior of a DBD is qualitatively described, and its basic scaling parameters are determined.

APPENDIX

Disturbance of the Electric Field by the Space Charge

In a Townsend discharge, the electric field is only slightly disturbed by the space charge. Let us estimate the space charge and find the disturbed electric field. We represent the electric field in the gap as a sum of two components: $E(t) = \mathrm{E}E_{\mathrm{br}} + \delta E$, where $E_{\mathrm{br}} \gg \delta E$, E is a solution to Eq. (22) and $\delta E(x, t)$ is a correction associated with the space charge. The correction δE satisfies the equation

$$\frac{d(\delta E)}{dx} = -4\pi n_{\mathrm{ion}} e, \tag{40}$$

where

$$n_{\mathrm{ion}}(x, t) = \frac{j_{\mathrm{ion}}(x, t)}{ebE_{\mathrm{br}}} \approx \frac{M\left(t - \dfrac{L-x}{bE_{\mathrm{br}}}\right) j\left(L, t - \dfrac{L-x}{bE_{\mathrm{br}}}\right)}{ebE_{\mathrm{br}}}.$$

The factor M appears due to the noncoincidence of the cathode and anode currents. Therefore, we have

$$\delta E(x, t) \approx 4\pi \int_{\left(1-\frac{x}{L}\right)\tau}^{\tau} M(t-t')\, j(t-t')\, dt'. \tag{41}$$

A discharge operates in the Townsend mode only when the inequality

$$\frac{(\delta E)_{\max}}{E_{\mathrm{br}}} \ll 1$$

is satisfied.

Let us estimate $(\delta E)_{\max}/E_{\mathrm{br}}$ for the case of a gradually varying external voltage. Using Eqs. (19) and (28), the maximum current can be estimated at

$$\frac{\Phi' \varepsilon E_{\mathrm{br}} (1 + X)\left(L + \dfrac{2d}{\varepsilon}\right)}{8\pi d\tau}.$$

Substituting this current into Eq. (41), we obtain

$$\frac{(\delta E)_{\max}}{E_{\mathrm{br}}} \approx \tau\omega \frac{U_{\max}}{LE_{\mathrm{br}}} \frac{M\varepsilon L(1 + X)}{\pi d}. \tag{42}$$

It is also easy to estimate $(\delta E)_{\max}/E_{\mathrm{br}}$ for the case of a meandering external voltage. Using Eq. (37), the maximum current can be estimated at

$$\frac{M' j|_{t=0} (\mathrm{E}_{\max} - 1)^2}{2\kappa}.$$

Then, we have

$$\frac{(\delta E)_{\max}}{E_{\mathrm{br}}} \approx \left(1 + \frac{\varepsilon L}{2d}\right) \frac{MM' (\mathrm{E}_{\max} - 1)^2}{2}. \tag{43}$$

When condition (1) is satisfied and ratio (42) or (43) is small, the discharge operates in the Townsend mode.

ACKNOWLEDGMENTS

This work was supported in part by the Russian Foundation for Basic Research (project no. 04-02-16483) and the US Civilian and Research Development Foundation (grant no. RP1-567-ST-03).

REFERENCES

1. U. Kogelschatz, Plasma Chem. Plasma Process **23**, 1 (2003).
2. G. M. Kogoma and S. Okazaki, J. Phys. D **24**, 1985 (1994).
3. M. Laroussi, G. S. Sayler, B. B. Glascock, *et al.*, IEEE Trans. Plasma Sci. **27**, 34 (1999).
4. Th. Callegari, R. Ganter, and J. Boeuf, J. Appl. Phys. **88**, 3905 (2000).
5. Akinori Oda, Yosuke Sakai, and Akashi Haruaki Sugawara, J. Phys. D **32**, 2726 (1999).
6. Liu Dongping, Ma Tengcai, Yu, Shiji, *et al.*, J. Phys. D **34**, 1651 (2001).
7. F. Massines, A. Rabehi, Ph. Decomps, *et al.*, J. Appl. Phys. **83**, 2950 (1998).
8. Jichul Shin and Laxminarayan L. Raja, J. Appl. Phys. **94**, 7408 (2003).
9. Yu. B. Golubosckii, V. A. Maiorov, J. Behnke, and J. F. Behnke, J. Phys. D **36**, 39 (2003).
10. V. P. Nagorny, P. J. Drallos, and W. Williamson, J. Appl. Phys. **77**, 3645 (1995).
11. G. Visentin, L. Mangolini, K. Orlov, U. Kortshagen, and J. Heberlein, in *Proceedings of the 15th International Symposium on Plasma Chemistry, Orleans, 2001*, Vol. 8, pp. 3251–3256.
12. Yu. B. Golubovskii, V. A. Maiorov, J. Behnke, and J. F. Behnke, J. Phys. D **36**, 975 (2003).
13. Yu. Yu. Protasov and S. N. Chuvashev, in *Encyclopedia of Low-Temperature Plasma*, Ed. by V. E. Fortov (Nauka, Moscow, 2000), Vol. 4, pp. 180–204 [in Russian].
14. L. D. Tsendin, in *Encyclopedia of Low-Temperature Plasma*, Ed. by V. E. Fortov (Nauka, Moscow, 2000), Vol. 4, pp. 5–16 [in Russian].

Translated by B. Chernyavskiĭ

Technical Physics, Vol. 50, No. 10, 2005, pp. 1295–1300. Translated from Zhurnal Tekhnicheskoĭ Fiziki, Vol. 75, No. 10, 2005, pp. 44–50.

SOLIDS

Effect of the Surface Crystallographic Orientation and Thickness of Fe–3 wt%Si Single Crystals on Magnetic Losses in Rotating Magnetic Fields

V. F. Tiunov and B. N. Filippov

Institute of Metal Physics, Ural Division, Russian Academy of Sciences, ul. S. Kovalevskoĭ 18, Yekaterinburg, 620219 Russia

e-mail: filbor@imp.uran.ru

Received December 15, 2004

Abstract—The response of magnetic losses to rotation-induced magnetization reversal in single-crystal Fe–3 wt%Si disks is studied as a function of the disk thickness and magnetic induction. It is shown that the loss power varies nonmonotonically with disk thickness d, exhibiting a minimum at $d = 0.15$ mm. The crystallographic orientation of the disk surface significantly influences the amount of the losses. The variation of the losses is discussed with regard to the effect a rotating magnetic field has on the domain structure. © *2005 Pleiades Publishing, Inc.*

INTRODUCTION

A challenging problem, which is associated with using silicon steels in the electric engineering industry, consists in decreasing energy losses due to magnetization reversal in magnetic circuits subjected to variable linearly polarized (hereafter alternating) and rotating magnetic fields. Alternating fields and their related alternating magnetic fluxes are commonly encountered in the magnetic circuits of transformers. Great advances have been achieved in developing steels featuring low losses in harmonically varying magnetic fields (see, e.g., [1]). These are (110)[001] textured steels with a high level of perfection (the [001] axis is one of the easy magnetic axes), where (110) plane deviates from the plane of the sheet by small angle β (several degrees).

Efficient ways of improving the quality of electrical steels (reducing specific magnetic losses) are thinning of the sheet and proper orientation of the surface of crystallites relative to the plane of the textured sheet (i.e., the proper choice of β). The effect of these factors on magnetic losses has been carefully studied on Fe–3 wt%Si specimens magnetically switched in alternating magnetic fields [2–6]. It has been shown, in particular, that, as thickness d of steel sheets decreases, magnetic loss power P varies nonmonotonically for a given harmonically varied magnetic induction. Initially, P declines, reaching a minimal value at certain $d = d_0$, and then rises. It has been found [4] that the value of d_0 depends on the hysteresis component of the total electromagnetic losses.

The effect of the grain surface orientation in textured Fe–3 wt%Si sheets placed in sinusoidal magnetic fields on the amount of electromagnetic losses has been studied at length in [5]. The total losses have been shown to be the lowest when the plane of the sheet deviates from the (110) plane by $\beta \approx 3°$, rather than when these two planes totally coincide ($\beta = 0$). Minimization of the losses at $\beta \neq 0$ was related to a smaller domain width (L) in this case compared with the case $\beta = 0$. Accordingly, the loss component due to eddy currents diminishes. Similar data for single-crystal Fe–3 wt%Si specimens have been obtained in [6], where the losses have been shown to be minimal at a certain (optimal) orientation of the specimen surface about the (110) crystal axis.

At the same time, the effect of specimen thickness and orientation on magnetic losses at rotation-induced magnetization reversal is scantily known. However, the problem of loss minimization in this case is of no less importance than in the case of alternating fields. This issue is of both scientific and applied value, since rotational magnetization reversal is typical of magnetic circuits in a variety of motors and generators.

Sparse investigations into the problem of loss minimization at rotational magnetic reversal are explained primarily by the lack of a reliable commonly accepted magnetic loss measuring technique. Treating of experimental data is also a bottleneck. It will be remembered that some insights into the nature of losses under the action of alternating fields have been gained after the role of the domain structure (DS) dynamics in occurrence of eddy current losses was clarified [1, 7–10] (largely owing to experimental studies of DS dynamic reconfiguration taking place when the specimens are magnetically switched in alternating magnetic fields [4, 11–13]). Works [4, 11–13] pioneered investigation into the DS dynamics under rotational magnetization reversal. Specifically, losses due to rotational magneti-

1063-7842/05/5010-1295$26.00 © 2005 Pleiades Publishing, Inc.

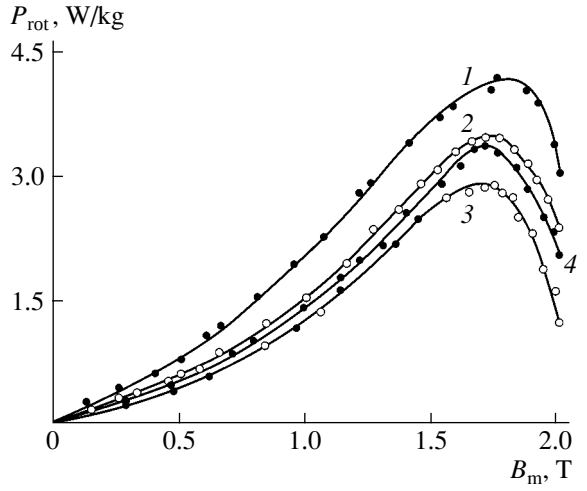

Fig. 1. RMR loss power P_{rot} vs. induction amplitude B_m for specimen thicknesses d = (*1*) 0.4, (*2*) 0.25, (*3*) 0.18, and (*4*) 0.08 mm. $\beta = 1.5°$.

zation reversal (RMR) versus specimen thickness d were examined in [11, 14]. Unfortunately, the authors of [14] restricted the analysis to the hysteresis component. Yet, the important result was obtained that, under RMR, the hysteresis losses grow as the specimen gets thinner, as in the case of magnetization reversal in linearly polarized fields [4]. An attempt to take the d dependence of total losses P was undertaken in [11]. It was established that P decreases with decreasing the specimen thickness. However, the range of d studied was narrow (0.25–0.40 mm) because of a poor sensitivity of the instrument.

In this work, we show that the P versus d behavior in a wider range of d is nonmonotonic and akin to that for magnetization reversal in linearly polarized fields.

The effect of grain axis misorientation relative to the plane of Fe–3 wt%Si sheets on losses under RMR is yet to be understood. The fact is that RMR losses have been studied either on polycrystals [14], where such a correlation is basically impossible to establish, or on single crystals whose surface coincided with the (100), (110), or (111) planes [15]. However, one may expect that the losses considerably depend on β not only under reversal in alternating fields but also under RMR, which the similar DS dynamics in both cases [12] indicates.

Thus, the aim of this work is to comprehensively examine the effect of specimen thickness and small deviation of the sheet plane from the (110) plane on total losses under RMR.

EXPERIMENTAL

We prepared two groups of single-crystal Fe–3 wt%Si disks of diameter 18 mm and thickness ranging from 0.08 to 0.40 mm. The disks were cut by means of an electric arc from two thick crystals of textured electrical steel. The surface of group-I specimens coincided with the (110) plane. In group-II specimens, the [001] easy magnetic axis made angle $\beta = 1.5°$ with the surface. The thickness of the specimens was varied by grinding with abrasive powders followed by polishing with diamond paste. Then, the single-crystal disks were annealed under a pressure of 10^{-6} mm Hg for 1 h to relieve mechanical stresses.

Magnetization curves $B_m(H)$ were taken from the specimens by the technique described in [13] (here, B_m is the maximal (amplitude) value of the induction and H is the external magnetic field strength). RMR losses $P_{rot}(H)$ were determined from the twist of the suspended disk rotating in the field of an electromagnet with a rate of 50 Hz (for details, see [16]). The refinement of this measuring technique has made it possible to raise the sensitivity of the instrument and, thereby, measure losses in thin ($d < 0.1$ mm) specimens. The measurement error did not exceed 8%. Based on the curves $B_m(H)$ and $P_{rot}(H)$, we constructed curves $P_{rot}(B_m)$ for each thickness.

RESULTS AND DISCUSSION

Figure 1 plots the RMR losses versus induction amplitude B_m for a number of single crystals of different thickness with $\beta = 1.5°$. The losses are seen to vary nonmonotonically with B_m for all the specimens. At low inductions, the losses grow, reaching a maximum at $B_m = 1.7$–1.8 T, and then decline. Such behavior has been observed previously; importantly, however, it is characteristic of all the specimens studied, irrespective of their thickness. This allowed us to discover a new effect: the loss minimum shifts toward lower inductions as the specimen gets thinner.

From Fig. 1, it also follows that the thickness dependence of the losses is nonmonotonic at any B_m in the thickness range used in the experiment. Let us try to explain the findings.

First of all, it should be noted that, in some cases (for example, under magnetization reversal along the [001] axis), magnetic losses observed in an alternating field are much lower than rotational hysteresis losses [4–6]. If an alternating field is aligned with the [111] direction, RMR losses become as high as those in a rotating magnetic field. It will be shown here that, on average, there is no discrepancy between the losses in one or another direction and that both the amount and behavior of the losses as a function of crystal parameters can be explained in the same way in both cases. Work [9] is worth noting in this respect, where it was demonstrated that both the total and eddy-current losses in a (110) single-crystal sheet depend on angle α nonmonotonically (α is the angle between a linearly polarized field and the [001] axis lying in the plane of the sheet). For α near 55°, total losses P reach a maximum and, significantly, the maximal losses are roughly three times higher (at $B_m = 0.75$ T, $d = 0.25$ mm) than P at $\alpha = 0$.

Let us average losses obtained in [9] over angle α as follows:

$$\bar{P} = \frac{2}{\pi}\int_0^{\pi/2} P(\alpha)d\alpha.$$

Averaging is carried out numerically based on experimental data [9] for $P(\alpha)$. For the 0.25-mm-thick specimens at $B_m = 0.75$ T and f = 60 Hz, we obtain $\bar{P} = 0.92$ W/kg, $\bar{P}_e = 0.7$ W/kg, and $\bar{P}_h = 0.219$ W/kg. Here, $\bar{P}_e$ and $\bar{P}_h$ are the eddy-current and hysteresis losses, respectively, found in the same way as $\bar{P}$. The total RMR losses obtained in this work equal 0.96 W/kg, i.e., agree well with the above value of $\bar{P}$.

Two conclusions can be drawn from this comparison. First, RMR losses are in good agreement with losses due to magnetization reversal in a linearly polarized field. RMR losses turn out to be high, since their components at any α add up, including α close to 55°, at which even magnetization reversal losses in an alternating field are very high.

The second conclusion is that the eddy current component is the major contributor to the total losses measured. Moreover, according to [12], where RMR-induced changes in the domain structure were revealed, one can assume that, at least up to $B_m = 1$ T, RMR losses have the same origin as magnetization reversal losses in an alternating field ($\alpha \neq 0$); i.e., they are related to the DS dynamic reconfiguration. By way of example, Fig. 2 demonstrates the DS reconfiguration in a quasistatic magnetic field applied to the specimens studied. In the demagnetized state (Fig. 2a), the DS of the single-crystal disks consists of large strip domains separated by 180° walls. Even in a weak field directed at an angle to the [001] axis, the disks are magnetized owing to a closure DS propagating from their edges (Fig. 2b) and consisting of a set of fine domains making an angle of 55°–60° with the strip domains. The closure DS, compensating for stray magnetic fields at the edges of the disk, is not continuous: it consists of a variety of inner and surface domains (for more details, see [9]).

As the field grows further (Fig. 2c), so does the specimen area occupied by the closure DS, which eventually covers the initial strip DS. The dynamics of the strip and closure DSs in single-crystal Fe–3 wt%Si disks subjected to rotating magnetic fields was studied at length in [11, 12].

Let us concentrate now on the nonmonotonic induction dependence of the losses. Such a dependence seems surprising, since, according to the electromagnetic field theory, the losses must be proportional to the time-averaged variation of the induction, $\overline{(dB/dt)^2} \sim B_m^2$, provided that the permeability has a moderate and constant value. Actually, however, nothing of this sort is

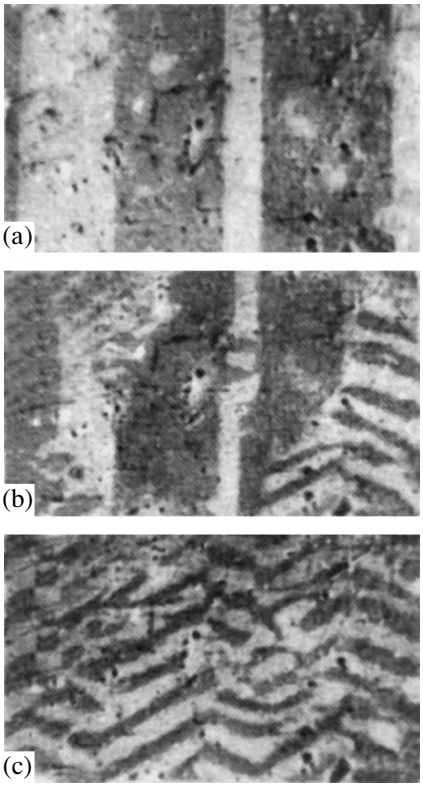

Fig. 2. Domain structure of the 0.3-mm-thick disk magnetized at an angle of 90° to the [001] axis: (a) demagnetized state, (b) state with $B_m = 0.66$ T, and (c) state with $B_m = 1.02$ T.

observed. This means that (see, e.g., [1, 10]) the electrodynamics of ferromagnets must take into account the DS dynamics in variable magnetic fields. It is because of this dynamics that the dependence $P(B_m)$ becomes more complicated than linear. The decrease in the losses after a maximum in the curve $P(B_m)$ may be related to the fact [12] that the wall motion takes place only in part of the crystal at a high induction. Regions appear where magnetization reversal is observed. The specific (and hence, integral) contribution from these regions to the total losses is much smaller than the contribution from the regions with DS reconstruction. It is natural to assume that the higher B_m, the larger the volume of magnetization reversal regions, and so the losses will decrease with increasing B_m. Nevertheless, the DS dynamics goes on contributing significantly to the losses even at $B_m = 2$ T. As follows from Fig. 1, $P = 2.25$ W/kg (for $d = 0.25$ mm) in this case. If, however, the DS dynamics is not included explicitly, the well-known formula [17]

$$P = \frac{1}{6}\frac{(\pi d f B_m)^2}{\rho \rho_E c^2}$$

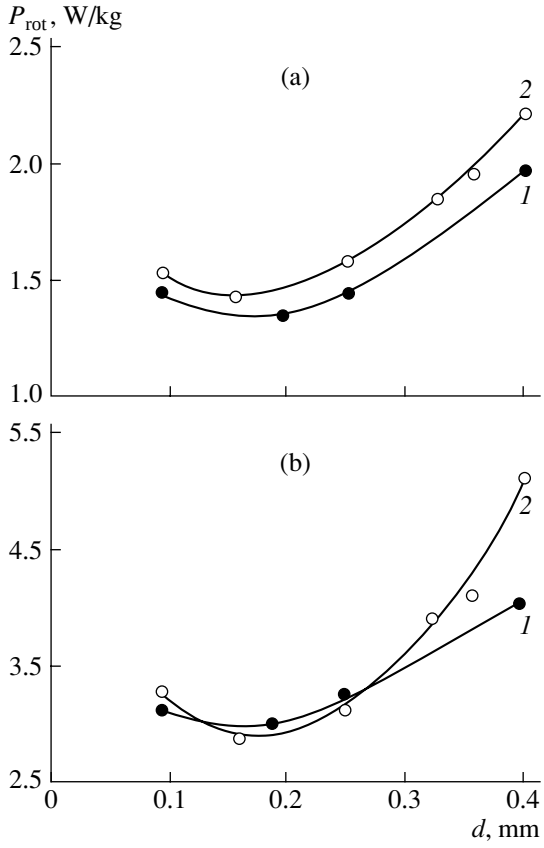

Fig. 3. RMR losses P_{rot} vs. specimen thickness d for B_m = (a) 1.0 and (b) 1.7 T and β = (*1*) 1.5° and (*2*) 0.

(where ρ is the density of the material, ρ_E is the resistivity, and c is the speed of light) yields $P = 0.48$ W/kg, all other specimen parameters being the same.

Such a discrepancy is impossible to explain even if the hysteresis losses estimated above are taken into account.

Let us enlarge upon the shift of the maximum in the $P(B_m)$ dependence as the specimen gets thinner. It will be remembered first of all that, as the crystal gets thinner, the hysteresis component of magnetic losses grows [14]. This means that thinning of the crystal places obstacles in the motion of domain walls and in reconfiguration of the DS as a whole. Therefore, for the induction in the specimen to reach a certain level with a fixed magnetic field, an additional magnetization reversal mechanism must come into play. Such may be the process of magnetization rotation. Thus, the thinner the specimen, the earlier the rotation process has an effect, indicating (see above) that the induction at which the losses are minimal shifts toward lower values. One more important point needs to be made. We assume that the difficulties associated with DS reconfiguration are related not to defects but to internal factors, i.e., specific domain structures that may reconfigure only by overcoming an energy barrier.

Now let us trace how magnetic losses in the single crystals vary with thickness. Figure 3a plots these dependences for a moderate induction, $B_m = 1.0$ T. As the specimens from both groups get thinner, the losses first decrease monotonically, reaching a minimum at thicknesses of 0.15–0.18 mm, and then grow. It is easy to see that the losses in the specimens with β = 0 exceed those in the specimens with β = 1.5° throughout the thickness range.

At $B_m = 1.7$ T (Fig. 3b), the run of the loss curves is in many ways similar to the case $B_m = 0.1$ T. As above, the losses in the specimens of both groups first decrease, become minimal near 0.15 mm, and then grow. However, unlike Fig. 3a, the losses differ not throughout the thickness range but only at the initial thickness. In fact, at $d = 0.4$ mm, the difference is the greatest, 25–30%. As d decreases, the curves approach together and, at $d = 0.30$ mm, the losses in the specimens of both groups coincide (within the measurement error).

Interestingly, the thickness of the single crystals at which the losses in rotating fields are minimal is 1.5–2.0 times larger than that when the Fe–3 wt% Si single crystals are switched by an alternating field. Such a difference in the specimen thickness seems to be the result of different hysteresis losses when magnetization reversal takes place in linearly polarized and rotating magnetic fields. It was shown, in particular [4], that, when magnetization reversal occurs in a linearly polarized field, the thickness corresponding to minimal magnetic losses increases (decreases) with increasing (decreasing) hysteresis component. With this in mind and also taking into account that hysteresis losses observed when the specimens is magnetically switched in rotating fields are higher than those in alternating fields [18], one can assume that the difference between the minimal-loss thicknesses is really associated with the difference in hysteresis losses.

Thus, as the Fe–3 wt%Si specimens get thinner, the d dependence of the losses in rotating, as well as in alternating, magnetic fields is nonmonotone: the curves first decrease, reaching a minimum at $d = 0.15$ mm, and then grow. Even a slight misorientation of the specimen plane about the [001] axis changes the d dependence of magnetic losses.

Let us discuss the thickness dependence of the losses (Fig. 3). It is known [14] that thinning of Fe–3 wt%Si specimens is accompanied by a rise in the hysteresis component of RMR losses. Then, one can argue (Fig. 3) that the total losses in the thickness range 0.15–0.40 mm decline owing to a decrease in the eddy current component alone. The decrease in this component is likely to be associated with the specific behavior of the domain structure in the specimens. Its dynamics in rotating magnetic fields was studied in [11, 19]. For example, it was demonstrated [19] that, when the induction is not too high ($B < 1.2$ T), magnetization reversal in Fe–3 wt%Si specimens proceeds largely

through the motion of 180° domain walls in the strip DS, the number of the wall remaining constant during a magnetization reversal cycle. In this case, the contribution from the closure DS to the magnetization is insignificant.

Based on the aforesaid, let us estimate the eddy current losses at $B_m = 1.0$ T. Assuming that magnetization reversal at such B_m is accomplished by uniform displacement of flat 180° walls, we find, according to [7], that eddy current losses P_e are proportional to $LdB_m^2 f^2$, where L is the width of basic domains. In our case, of importance is the fact that losses P_e are proportional to the thickness of the specimen. According to [7], L may also depend on d. However, in the crystallites under study, this dependence is very weak and can be ignored. Therefore, the amount of eddy current losses is bound to vary in proportion to d. Unfortunately, our loss-measuring technique cannot discriminate between eddy-current and hysteresis loss components. As for the total losses, it follows from Fig. 1 that, when the crystal thickness decreases from 0.4 and 0.2 mm (i.e., twofold), the total RMR losses measured change by a factor of 1.5. It then becomes clear that, up to the minimum, the eddy current component prevails in the d dependence of the RMR losses. The observed deviation of this dependence from linearity can be explained by a contribution from the hysteresis component, which is known [11] to grow as the specimen gets thinner. This growth may explain the increase in the total losses in the specimens less than 0.15 mm thick.

Note that, in [19], the motion velocities of 180° domain walls in Fe–3 wt%Si single crystals during magnetization reversal cycles in rotating fields were measured. From these velocities, the induction dependence of the eddy current component was estimated in the range 0.5–1.2 T. The estimated and measured induction dependences turned out to be in satisfactory quantitative agreement. This corroborates the earlier supposition that the displacement of 180° domain walls in the strip DS is the major source of magnetic losses in rotating fields at moderate induction values (1.0–1.2 T or lower).

To reveal specific features of the DS dynamics that are responsible for a reduction of the losses with decreasing specimen thickness at high induction amplitudes (Fig. 2b) is a much more challenging task. This is because magnetization reversal in rotating fields at such amplitudes proceeds solely through the displacement of the walls of the closure DS [12]. Strip domains do not emerge on the specimen surface throughout a reversal cycle. In addition, the sizes of domains in the closure DS vary considerably at different sites of the specimen because of the nonuniformity of their internal fields. In light of this, the contribution of the closure DS to magnetic losses can be estimated by visualizing its dynamics on the entire specimen surface. In our case, this seems infeasible in view of the large dimensions of the specimens studied.

Yet, based on the results obtained in [20], let us try to explain the variation of the magnetic losses that is demonstrated in Fig. 3b. Theoretical analysis performed in [20] showed that, as Fe–3 wt%Si specimens with the [001] axis lying in the specimen plane get thinner, the domains forming the fine structure of the closure regions narrow. This causes the closure domains, as well as their related sizes of the basic strip structure, to diminish. Therefore, the reduction of magnetic losses at high inductions may be associated with a decrease in the mean size of the domains in the closure DS when the specimens become thinner. The subsequent growth of the losses is due, as before, to a rise in the hysteresis component, which accounts for more than half of the total losses at thicknesses below 0.15 mm. Finally, let us see why the losses differ in the specimens with different orientations of the [001] axis. As is known [6], the misorientation of the magnetization relative to the specimen plane by small angle β causes a large number of droplike domains to emerge on the surface. Upon magnetization reversal, some of them penetrate into new strip domains and decrease the mean width of the already existing strip domain structure. This, in turn, diminishes the eddy current component and, accordingly, the total magnetic losses in the specimen. Using the same line of reasoning, we can also explain why the losses in the specimens with $\beta = 1.5°$ are higher than in those with $\beta = 0$ (Fig. 3a). A similar relationship between the loss components in specimens comparable in size is observed when the induction is high (Fig. 3b). In this case, as was noted above, magnetization reversal is associated only with the displacement of the walls of the closure DS. One may therefore suppose that misorientation of the magnetization ([001] axis) relative to the specimen surface shrinks not only strip domains but also domains in the closure DS.

It has been already noted that the difference between magnetic losses in the specimens with the variously oriented [001] axis decreases as the specimens become thinner. A reason may be a nontrivial variation of the domain width when the specimens with $\beta = 1.5°$ are thinned. In experiments [3] with single crystals with $\beta > 0$, it was conjectured that, as the thickness of the crystal drops to a value less than the strip domain width, the domain width is governed by magnetostatic poles on opposite faces of the specimen rather than by magnetoelastic interaction at the end faces that are normal to the magnetization projections onto the specimen surface. In this case, the basic strip DS naturally shrinks. Such a variation of the DS sizes was observed in [4] during dynamic magnetization reversal in Fe–3 wt%Si with $\beta = 1°$. The aforesaid leads us to conclude that, as the specimens in Fig. 3 become thinner, the difference between magnetic losses diminishes because of a decrease in the DS "dispersion" (and, hence, in the eddy-current losses) in the specimen with $\beta = 1.5°$.

CONCLUSIONS

Thus, we have ascertained how RMR losses depend on the thickness of the Fe–3 wt%Si specimen, misorientation of its surface relative to the (110) plane, and induction amplitude. It has been found that total losses P depend on induction amplitude B_m nonmonotonically in a wide specimen thickness range (0.08–0.40 mm) and that the minimum of the curve $P(B_m)$ shifts toward lower B_m as the specimens are thinned. Specifically, as they become thinner, RMR losses first decline, reaching a minimum at 0.15 mm, and then grow. In the minimum, the total losses are, on average, 30–50% lower than at the initial thickness. The minimal-loss thickness under RMR is 1.5–2.0 times larger than the corresponding value under magnetization reversal in a linearly polarized field.

A small deviation of the crystal surface relative to the (110) plane (β is roughly equal to 1.5°) results in a substantial decrease in the magnetic losses compared with the losses in the specimens with $\beta = 0$. The amount of decrease is the most significant (by about 25%) in the thickest specimens and monotonically declines with decreasing specimen thickness.

It has been demonstrated that the data on RMR losses can be explained by considering the DS dynamics.

ACKNOWLEDGMENTS

This work was partially supported by the Department of Physical Sciences, Russian Academy of Sciences, and the Russian Foundation for Basic Research (grant no. 02-02-16443).

REFERENCES

1. V. A. Zaĭkova, I. E. Startseva, and B. N. Filippov, *Domain Structure and Magnetic Properties of Electrical Steels* (Nauka, Moscow, 1992) [in Russian].
2. S. D. Washko and R. F. Miller, J. Magn. Magn. Mater. **19**, 361 (1980).
3. T. Yamaguchi and K. Takeda, IEEE Trans. Magn. **20**, 41 (1984).
4. V. F. Tiunov, Fiz. Met. Metalloved., No. 7, 67 (1990).
5. Yu. N. Dragoshanskiĭ, V. A. Zaĭkova, and E. B. Khan, in *Proceedings of the International Conference on Magnetism (MKM-73), Moscow, 1973* (Nauka, Moscow, 1974), Vol. 4, pp. 518–520.
6. Yu. N. Dragoshanskiĭ, N. K. Esina, and V. A. Zaĭkova, Fiz. Met. Metalloved. **45**, 723 (1978).
7. R. H. Pry and C. P. Bean, J. Appl. Phys. **29**, 532 (1958).
8. L. E. L. Bishop, Phys. Status Solidi A **7**, 117 (1971).
9. B. N. Filippov, V. A. Zaĭkova, S. V. Zhakov, and Yu. N. Dragoshanskiĭi, Izv. Akad. Nauk SSSR, Ser. Fiz. **42**, 1744 (1978).
10. B. N. Filippov and A. P. Tankeev, *Dynamic Effects in Ferromagnets with Domain Structure* (Nauka, Moscow, 1987) [in Russian].
11. V. F. Tiunov and G. S. Korzunin, Fiz. Met. Metalloved. **91** (2), 41 (2001).
12. V. F. Tiunov, Fiz. Met. Metalloved. **98** (2), 35 (2004).
13. V. F. Tiunov and G. S. Korzunin, Defektoskopiya, No. 11, 37 (2002).
14. W. F. Archenhold, H. F. Sandham, and J. E. Thompson, J. Appl. Phys. **11**, 46 (1960).
15. S. R. Boon and J. E. Thompson, Proc. IEEE **111**, 605 (1964).
16. A. D. Abramov, G. S. Korzunin, L. A. Inisheva, and G. I. Tkachenko, USSR Inventor's Certificate No. 954908, Byull. Izobret., No. 32 (1982).
17. R. M. Bozorth, *Ferromagnetism* (Van Nostrand, New York, 1951; Inostrannaya Literatura, Moscow, 1956).
18. F. Fiorillo and A. M. Rietto, J. Magn. Magn. Mater. **83**, 402 (1990).
19. V. F. Tiunov, Fiz. Met. Metalloved. **92**, 20 (2001).
20. B. N. Filippov, S. V. Zhakov, Yu. N. Dragoshanskiĭ, *et al.*, Fiz. Met. Metalloved. **42**, 260 (1976).

Translated by V. Isaakyan

Technical Physics, Vol. 50, No. 10, 2005, pp. 1301–1304. Translated from Zhurnal Tekhnicheskoĭ Fiziki, Vol. 75, No. 10, 2005, pp. 51–54.

SOLID-STATE ELECTRONICS

Composition of Higher Fullerenes Obtained by Laser Ablation of Carboniferous Materials

M. A. Khodorkovskii*, T. O. Artamonova*, S. V. Murashov*, A. L. Shakhmin*, A. A. Belyaeva*, L. P. Rakcheeva, I. M. Fonseca**, and S. B. Ljubčik****

** Prikladnaya Khimiya Russian Research Center, St. Petersburg, 197198 Russia*

e-mail: mkhodorkovskii@rscac.spb.ru

*** New University of Lisbon, Monte Caparica, 2825 Portugal*

Received September 22, 2004; in final form, January 27, 2005

Abstract—The compositions of higher fullerenes produced by ablation of various carboniferous materials are experimentally studied. The yield of fullerenes versus the type of carboniferous materials and laser radiation parameters is found. *© 2005 Pleiades Publishing, Inc.*

INTRODUCTION

The production of pure fullerenes is known to be based on their extraction with organic solvents from fullerene soot prepared by laser ablation [1] or using an electric arc [2]. According to the publications, the yield of the most abundant fullerenes (C_{60} and C_{70}) from fullerene soot is less than 15% and the yield of heavier fullerenes up to C_{84} does not exceed a few fractions of a percent.

The low yield of higher fullerenes makes them extremely expensive, which to a great extent prevents insight into the properties of these molecules. However, interest in these materials is continuously growing, especially in light of their potential use in large endocomplexes. Such complexes are expected to contain not only individual atoms but also molecules inside the cavities of higher fullerenes, which will substantially extend the application of fullerenes in various fields of science and technology.

An important factor that is responsible for such a low yield of higher fullerenes is their content in fullerene soot. In this work, we study the formation of higher and giant fullerenes by laser ablation versus the parameters of laser radiation and the type of carboniferous materials.

EXPERIMENTAL

We developed a technique based on detection of positive ions that form during the laser ablation of carboniferous materials by time-of-flight (TOF) mass spectrometry. The experimental setup consisted of a TOF mass spectrometer with an ion source generating a laser plasma. As a radiation source, we used a tunable dye laser pumped by a pulsed excimer laser. Two wavelength ranges, 480–520 and 240–260 nm, were used. The laser pulse duration was 15 ns, and the pulse repetition rate was 1 Hz. The radiation was focused on the sample placed at the axis of the mass spectrometer. The diameter of a laser spot on the sample was 0.1 mm, and the radiation power density was 10^5–10^7 W/cm^2. The samples were prepared from powdered carboniferous materials by their sedimentation in an alcohol solution onto a metallic substrate. They were first degassed in a low-pressure chamber and then placed in an ultrahigh-vacuum chamber by means of a manipulator. The number of laser pulses depended on the signal-to-noise ratio. A pulsed voltage injected ionic ablation products into the drift chamber of the mass spectrometer, whose resolution allowed us to reliably record neighboring fullerene ions (C_{2N}, $C_{2(N+1)}$).

Along with routine recording of the mass spectra of ablation products, we used the TOF technique to analyze the ionic composition of the ablation products at each stage of laser plasma formation. This technique consists in recording laser plasma ions within short time intervals delayed relative to a laser pulse. By varying the delay time and recording time interval, one can obtain additional information on the ion formation process. As applied to materials that initially contain carbon aggregates, this technique is of special importance, since it can detect those fullerene ions in the mass spectrum forming during clustering of ions from initial molecules and/or their fragments.

RESULTS AND DISCUSSION

As noted above, from the mass spectra of positive ions that appear as a result of the laser ablation of carboniferous materials, one can reveal the dependence of the fullerene composition on the type of the material. In this work, we studied various types of graphites; carbon and fullerene soots; carbon sorbents; and nanoporous carbon materials produced from boron, silicon, or titanium carbides.

1063-7842/05/5010-1301$26.00

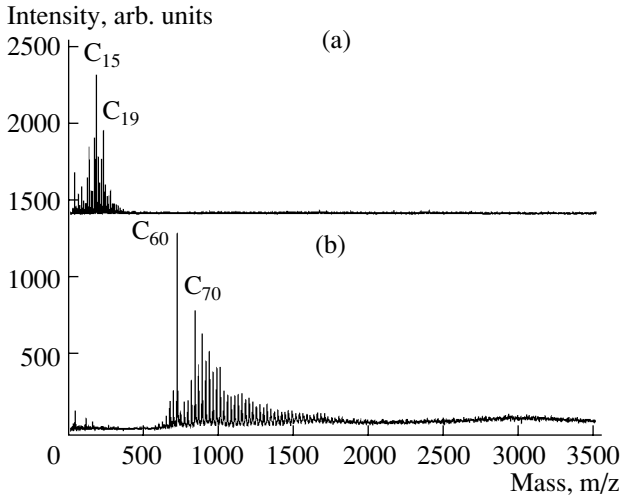

Fig. 1. Mass spectra of (a) graphite and (b) fullerene soot.

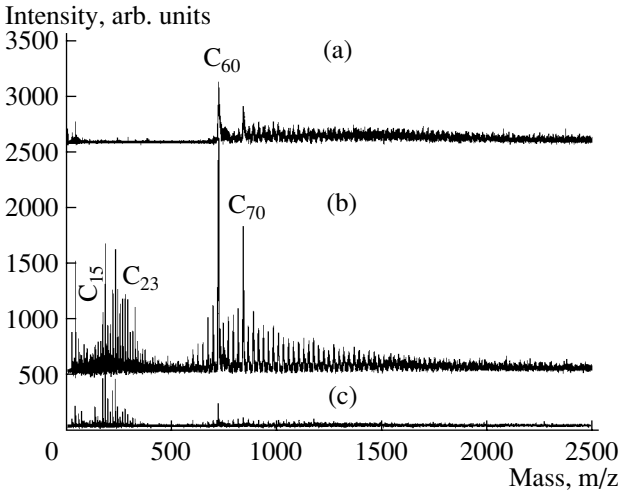

Fig. 2. Mass spectra of fullerene soot after (a) the first 5 laser shots, (b) 50 shots, and (c) 70 shots.

The results indicate that higher fullerenes are difficult to prepare from these materials, except for fullerene soot; in some cases, we could obtain the most abundant C_{60} and C_{70} fullerenes and a minor amount of fullerenes having a mass of C_{180} or less. The carboniferous material most promising for preparing higher fullerenes turned out to be fullerene soot, whose ablation products contained higher fullerenes with up to 500 carbon atoms. To compare the yield of higher fullerenes from different materials, Fig. 1 shows the mass spectra of graphite and fullerene soot taken at the same parameters of laser radiation. The graphite spectrum exhibits only small C_3–C_{27} carbon clusters, the structures of which do not correspond to fullerene ions. At the same time, the ionic composition of the laser plasma of the fullerene soot consists mainly of fullerene ions with the characteristic distribution including giant fullerenes. It is interesting that, as the number of laser pulses per irradiation area increases, heavy ions gradually disappear from the spectrum of fullerene soot and the mass spectrum becomes similar to that of the graphite sample (Fig. 2). In other words, increasing the number of laser actions on the fullerene soot causes its graphitization. The yield of higher fullerenes from the soot indicates that the initial product contains carbon compounds, which transform readily into higher fullerenes during radiation.

It was shown [3, 4] that initially fullerene soot exhibits a variety of carbon structures: from small carbon flakes to giant carbon clusters. Attempts to separate these clusters with active solvents revealed the fullerene nature of their crystal structure. In [4], separated clusters were analyzed by mass spectrometry with laser desorption and ionization and the extraction products were found to contain a wide spectrum of fullerene molecules from C_{60} to C_{418}. However, the interpretation of these data seems to be doubtful, because molecular ions of higher fullerenes might be synthesized during the laser ablation of the extraction products.

Our next goal was to clarify the dependence of the ablation product composition on the type of fullerene soot. Figures 3 and 4 show that the mass spectra of the fullerene soots produced by combustion of various graphite electrodes (Fig. 3) at different buffer gas pressures in a synthesis chamber (Fig. 4). All the curves exhibit a wide ion distribution up to C_{400}–C_{500}. It should be noted that the recorded ions belong to fullerene compounds, since the difference between neighboring peaks is equal to 24 m/z. This difference, being a characteristic sign of fullerene mass spectra, corresponds to complex C_2 (the main building block of fullerenes), which is lost upon treatment [5–7]. The extents and forms of the distributions shown in Figs. 3 and 4 indicate that, first, the synthesis conditions influence the soot composition and, second, some types of soot are more favorable for producing higher fullerenes by laser ablation.

To additionally support the efficiency of fullerene soot as a starting material to form fullerenes in a laser plasma, we analyzed the dependence of the fullerene yield on the number of laser pulses. The results demonstrate that ablation leads to deposition of the laser plasma products on the sample surface, and so the fullerene ions result from interaction of laser radiation with the surface covered by carbon compounds (deposited previously) rather than with the initial surface [1]. This situation shows up most vividly in ablation of graphite, where higher fullerenes cannot be produced by a single laser shot. These data confirm the efficiency of using fullerene soot, whose nature is similar to that of deposits due to graphite ablation [1, 8–10].

Thus, our results demonstrate that the carboniferous material most promising for the production of higher fullerenes is fullerene soot, whose ablation products

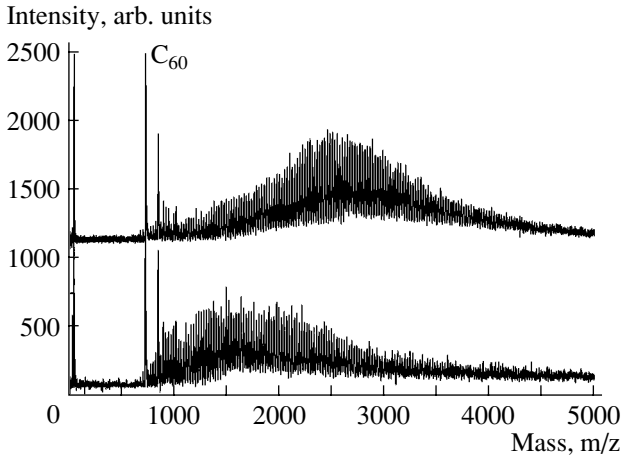

Fig. 3. Mass spectra of fullerene soot for various graphites.

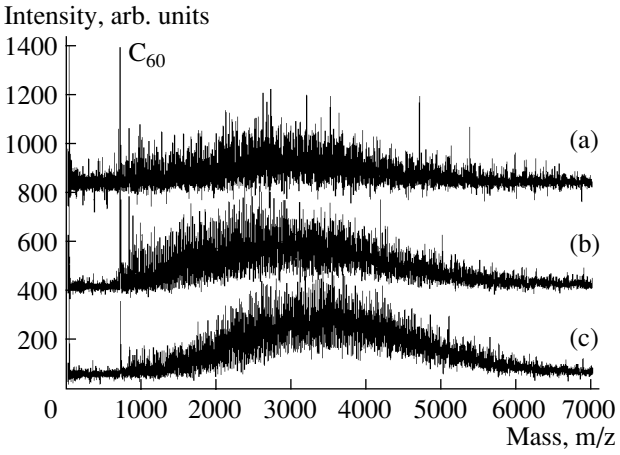

Fig. 4. Mass spectra of fullerene soot at a helium pressure of (a) 100, (b) 400, and (c) 500 Torr.

contain higher fullerenes consisting of up to 500 carbon atoms. In the other products, higher fullerenes were extremely difficult to detect; in some cases, we managed to obtain ordinary C_{60} and C_{70} fullerenes and a small amount of fullerenes having a mass of C_{180} at most.

When studying the formation efficiency of positive ions of higher fullerenes, we used the fullerene soots providing a maximum yield of higher fullerenes. To find the dependence of the formation efficiency of these compounds on the irradiation conditions, we varied the radiation wavelength and power and studied the ionic composition at different stages of laser plasma development.

Since the dye laser could operate in two wavelength ranges (240–260 and 480–520 nm), we analyzed the spectral dependence of the fullerene yield in the near ultraviolet and visible ranges by varying the power density of the radiation from 10^5 to 10^7 W/cm^2.

Our results show that coalescence, which is responsible for the formation of higher fullerenes, goes in parallel with fragmentation, which results in degradation of fullerene compounds and increases the fraction of small carbon clusters. The same dependence is also observed for a radiation power density higher than 10^6 W/cm^2 irrespective of the wavelength. Such behavior indicates that, as the laser plasma temperature exceeds a certain threshold, the initial carbon compounds decompose into atoms and tiny clusters, which form linear or planar configurations rather than bulk fullerene compounds upon subsequent coalescence. It should be noted that a plasma overheat due to visible radiation is likely to be due to radiation absorption in the surface layer of the sample, where the concentration of evaporated carbon particles, which are responsible for the formation of higher fullerenes, is maximum.

To see how the plasma temperature influences the yield of fullerene ions, we studied the mass spectrum of the fullerene soot at each stage of laser plasma development. Figure 5 shows the evolution of the mass spectrum of ions coming to the detector at different time instants after the laser pulse is incident on the fullerene soot. As is seen, the distribution substantially depends on the stage of plasma development. At the early stage, characterized by the fastest ions, it consists of two broad components with greatly differing masses. As the plasma develops, these distribution components first broaden and shift toward higher masses and then the double-humped distribution changes to one broad distribution.

Such an evolution of the mass spectrum can be explained by clustering of fullerene ions early in plasma development, when the concentration of initial ions (region *A*) still suffices to form heavier fullerene ions (region *B*). The same velocities of particles greatly differing in mass can be explained only by clustering and gasdynamic acceleration of the clusters; otherwise,

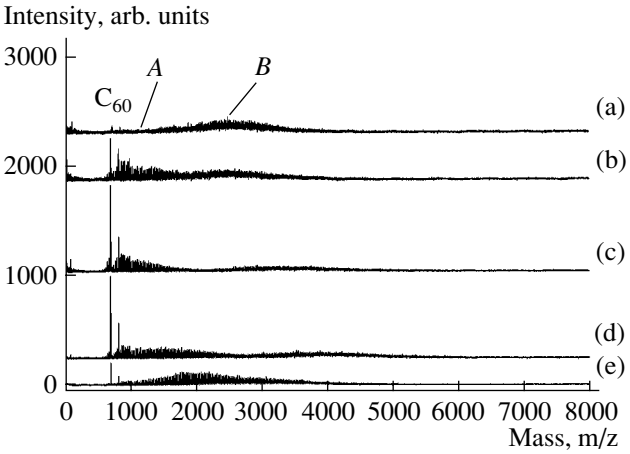

Fig. 5. Mass spectra of fullerene soot as a function of the delay time between the laser pulse and injection voltage: (a) 5, (b) 10, (c) 15, (d) 20, and (e) 40 μs.

the particles would have velocities inversely proportional to the square root of their masses [11]. A similar explanation for the formation of giant fullerene ions is given in [12], where these ions were the products of graphite ablation.

However, the origin of the fullerene ions with smaller masses (region *A*) remains unclear. They may be formed by laser ionization of the corresponding molecules if they are present in the fullerene soot or through clustering of still lighter ions appearing when graphite flakes in the soot vaporize.

CONCLUSIONS

The material most promising for the formation of higher fullerenes by pulsed laser ablation seems to be fullerene soot. The maximal effect is reached when ultraviolet radiation of power less than 10^6 W/cm^2 is used. It should be emphasized that, with graphite used as a starting material at the same ultraviolet radiation power, the mass spectra contain only small C_3–C_{27} carbon clusters. The yield of fullerene compounds depends on the stage of laser plasma development. The processes responsible for coalescence and fragmentation are qualitatively outlined.

Our data make it possible to find laser radiation parameters providing a maximal yield of higher fullerenes.

ACKNOWLEDGMENTS

This work was supported by the Russian Foundation for Basic Research (project no. 04-03-32249), the state research program "Fullerenes and Atomic Clusters," the NATO program "Science for Peace" (project no. 977984), and the program "SERH/BPD/7150/2001."

REFERENCES

1. H. W. Kroto, J. R. Hearth, R. E. Smalley, *et al.*, Nature **318**, 152 (1985).
2. W. Kraetschmer, L. D. Lamb, K. Fostirovios, *et al.*, Nature **347**, 354 (1990).
3. D. H. Parker, P. Wurz, K. Chatterjee, *et al.*, J. Am. Chem. Soc. **113**, 7499 (1991).
4. F. Beer, A. Gugel, K. Maratin, *et al.*, J. Mater. Chem. **7**, 1327 (1997).
5. S. C. O'Brien, J. R. Heart, R. F. Curl, *et al.*, J. Chem. Phys. **88**, 220 (1988).
6. J. Laskin, C. Weickhardt, and C. Lifshitz, Int. J. Mass Spectrom. Ion Processes **161**, L.7 (1997).
7. H. Hohmann, C. Callegari, S. Furrer, *et al.*, Phys. Rev. Lett. **73**, 1919 (1994).
8. C. H. Becker and J. B. Palix, J. Appl. Phys. **64**, 5152 (1988).
9. K. Kaizu, M. Kohno, S. Sizuki, *et al.*, J. Chem. Phys. **106**, 9954 (1997).
10. B. N. Kozlov, S. N. Kirillov, and B. A. Mamyrin, Proc. SPIE **3093**, 233 (1997).
11. E. E. B. Campbell, G. Ulmer, H.-G. Busmann, *et al.*, Chem. Phys. Lett. **175**, 505 (1990).
12. T. Moriwaki, K. Kobayashi, M. Osaka, *et al.*, J. Chem. Phys. **107**, 8927 (1997).

Translated by K. Shakhlevich

Technical Physics, Vol. 50, No. 10, 2005, pp. 1305–1310. Translated from Zhurnal Tekhnicheskoĭ Fiziki, Vol. 75, No. 10, 2005, pp. 55–60.

SOLID-STATE ELECTRONICS

Magnetization Switching in Single-Domain Particles and a Response to a Field Pulse

L. N. Kotov and L. S. Nosov

Syktyvkar State University, Syktyvkar, 167001 Komi Republic, Russia

e-mail: kotov@syktsu.ru

Received May 14, 2004

Abstract—An equation in the Gilbert form that describes the motion of the magnetization vector in intense high-frequency magnetic fields is solved numerically. The solution obtained is used to study switching of the magnetization of a single-domain ferromagnetic particle that has the shape of an ellipsoid of revolution and possesses cubic anisotropy from the position parallel to an easy axis to the position normal to this axis. The ranges of amplitudes and frequencies of the magnetic field where magnetization switching is observed are determined. An expression for the response of an ensemble of variously oriented particles is derived. It is shown that a particle ensemble generated by an rf field may serve as a data carrier on which information is written and read out by means of nonlinear and linear ferromagnetic resonances. © *2005 Pleiades Publishing, Inc.*

INTRODUCTION

An ensemble of unrelated oriented single-domain ferromagnetic particles can be viewed as an alternative medium for nonvolatile storage devices [1–3]. Data readout from such an ensemble implies its excitation by a low-power pulse of a variable magnetic field at the ferromagnetic resonance (FMR) frequency. Information is read out by scanning the variable field frequency: a response at a certain frequency corresponds to logic unity; its absence, to logic zero [4, 5]. For data writing using a pulsed high-frequency field, the magnetization vector in the particle must be switched from the position parallel to an easy axis to the position normal to this axis [2, 3].

To date, the problem of switching at resonant frequencies has been poorly explored experimentally; so, the only way to tackle this problem today is theoretical analysis and numerical simulation of the magnetization behavior in a single-domain particle placed in various fields. In our previous work [2], a solution method for this problem in the case of spherical particles was outlined. In this work, the problem of magnetization switching in single-domain particles is extended to the case of particles in the form of an ellipsoid of revolution subjected to an intense pulsed high-frequency field and an expression for the electromagnetic response from an ensemble of variously oriented particles is derived.

EQUATION OF MOTION OF MAGNETIZATION VECTOR

Consider the behavior of magnetization vector **M** of one particle. We assume that the particles are independent (uncoupled) and have the form of an oblate ellipsoid of revolution whose axis coincides with one of crystallographic axes. The magnetic energy density of the particle is represented as a sum of the cubic anisotropy energy density, demagnetizing field energy density, and Zeeman energy density (the energy density of the magnetic moment of the particle in a variable magnetic field) [6],

$$U(\mathbf{m}) = K_1(m_x^2m_y^2 + m_y^2m_z^2 + m_x^2m_z^2) + K_2m_x^2m_y^2m_z^2 + 2\pi\mathbf{M}\hat{N}\mathbf{M} - \mathbf{M}\cdot\mathbf{H}_{\sim}. \quad (1)$$

Here, $K_1 > 0$ and $K_2 < 0$ are the first and second constants of cubic anisotropy, respectively; $\mathbf{H}_{\sim} = \mathbf{h}\sin(\omega t)$ is the external magnetic field with frequency ω; $\mathbf{m} = \mathbf{M}/M_0$ is the direction cosine vector of magnetization M, $M_0 = |\mathbf{M}|$; and $\hat{N} = \mathrm{diag}(N_x, N_y, N_z)$ is the diagonal tensor of demagnetizing factors of the ellipsoid, where $N_x = N_y \le N_z$. Coordinate axes *Ox*, *Oy*, and *Oz* are directed along the crystallographic axes [100], [010], and [001] of the particle.

In the absence of an external field, the magnetization vector is in either of two stable positions, which correspond to a minimum of energy: it runs parallel to either axis *Ox* or *Oy*. Upon change of variables, the equation of motion of magnetization vector in the Gilbert form can be recast as [2]

$$\frac{d\mathbf{m}}{dt^*} = -[\mathbf{m}\times\mathbf{H}_{\mathrm{eff}}^*] + \alpha\left[\mathbf{m}\times\frac{d\mathbf{m}}{dt^*}\right], \quad (2)$$

where α is a dimensionless damping parameter; $\mathbf{H}_{\mathrm{eff}}^* = -\delta U^*/\delta\mathbf{m}$ is the reduced effective magnetic field acting on the magnetic moment ($U^*(\mathbf{m}) = U(\mathbf{m})/2K_1$ is the reduced free energy density); $t^* = t^2 2\gamma K_1/M_0$ is the reduced time; $\omega^* = \omega M_0/2\gamma K_1$ is the reduced frequency;

1063-7842/05/5010-1305$26.00

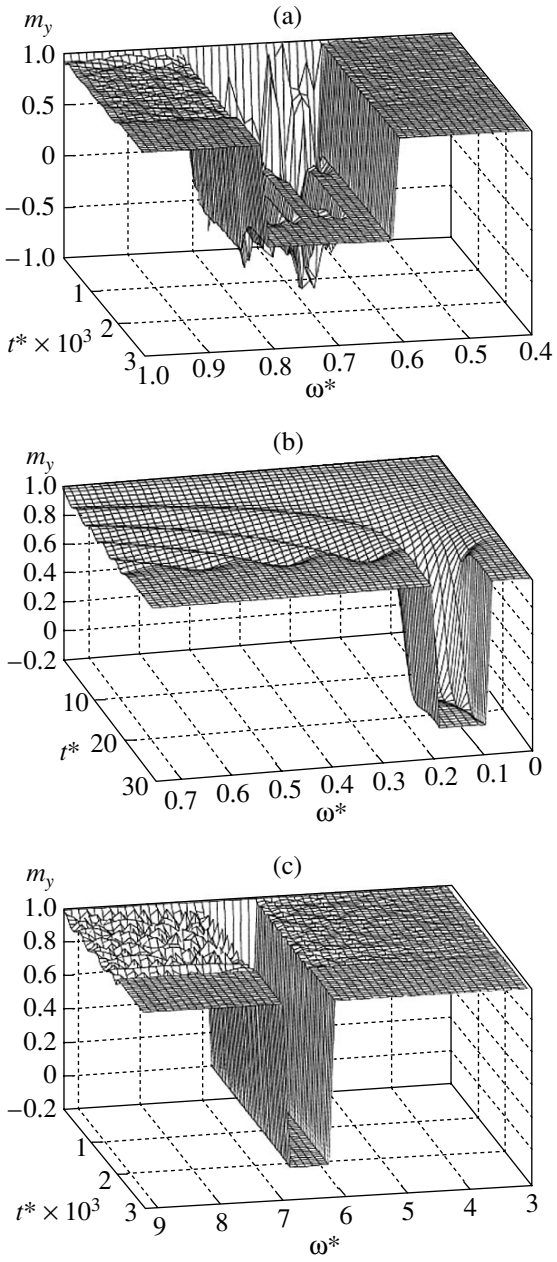

Fig. 1. Component m_y vs. reduced time t^* and variable field frequency ω*: (a) spherical particle at $\alpha = 0.01$, $\omega^*_{res} = 0.9999$, and $h^* = 0.09$; (b) spherical particle at $\alpha = 1$, $\omega^*_{res} = 0.5$, and $h^* = 0.33$; and (c) disk-shaped particle at $\alpha = 0.01$, $\omega^*_{res} = 6.35$, and $h^* = 0.1$.

$\mathbf{h}^* = \mathbf{h}M_0/2K_1$ and h^* are, respectively, the reduced vector and magnitude of the variable magnetic field; and γ is the gyromagnetic ratio.

In the spherical coordinate system such that the azimuth axis is aligned with axis *Oz* and the polar axis is aligned with axis *Ox*, Eq. (2) takes the form

$$\begin{cases} \dfrac{d\theta}{dt^*} = -\dfrac{1}{\sin\theta(\alpha^2+1)}\dfrac{\partial U^*}{\partial\varphi} - \dfrac{\alpha}{\alpha^2+1}\dfrac{\partial U^*}{\partial\theta} \\ \dfrac{d\varphi}{dt^*} = \dfrac{1}{\sin\theta(\alpha^2+1)}\dfrac{\partial U^*}{\partial\theta} - \dfrac{\alpha}{\sin^2\theta(\alpha^2+1)}\dfrac{\partial U^*}{\partial\varphi}, \end{cases} \quad (3)$$

where θ and φ are the azimuth and polar angles.

NUMERICAL ANALYSIS AND DISCUSSION OF RESULTS

We assume that, prior to switching of a variable magnetic field aligned with the *Ox* axis, magnetization vector **M** is directed along the *Oy* axis. Equation (3) was solved by the Runge–Kutta methods of orders four and five [7]. In calculation, the time of action of the variable field and the observation time were taken to be (in terms of the reduced time) $\tau^* = 20/\alpha$ and $\Delta t^* = 1.5\tau^*$, respectively. Also, we put $K_2/K_1 = -0.16$ and $M_0^2/K_1 = 6.25$. The numerical solution of set (3) shows (Fig. 1) that, as amplitude h^* of the variable field grows, oscillating magnetization vector **M** deviates from the stable equilibrium position, passes through the unstable equilibrium position, and switches to another stable equilibrium position that is normal to the initial stable position. Such behavior is of resonant character. The magnetization vector switches in a certain band of reduced frequencies Δω*, which we call the switching band. The extent of this band depends on reduced variable field amplitude h^*, dimensionless damping parameter α, and shape of the particle. If a minimal value of h^* (with a field frequency fixed), h^*_{min}, at which **M** rotates by π/2 is taken for the switching threshold, then resonant switching at h^*_{min} takes place at frequencies close to reduced FMR frequency ω^*_{res} of an oblate ellipsoid of revolution,

$$\omega^*_{res} = \sqrt{(\omega^*_0)^2 - (\omega^*_r)^2}, \quad (4)$$

$$\omega^*_0 = \sqrt{\frac{\left(1 + 2\pi\frac{M_0^2}{K_1}(N_z - N_y)\right)}{1+\alpha^2}}, \qquad \omega^*_r = -\frac{\alpha\left(1 + 2\pi\frac{M_0^2}{K_1}\frac{N_z - N_y}{2}\right)}{1+\alpha^2}, \quad (5)$$

where ω^*_0 is the reduced precession eigenfrequency (or Kittel frequency) of the ellipsoid and ω^*_r is the reduced relaxation frequency [3].

For spherical particles, the switching band always lies below the reduced FMR frequency, the separation

increasing with damping parameter (Figs. 1a and 1b). For disk-shaped particles, the switching band includes the reduced frequency of linear FMR at the same reduced field amplitude (Fig. 1c). This is because the demagnetizing field in our system is several times higher than the anisotropy field, and so the first harmonic, which is embodied in linear FMR in isotropic disks (uniform precession in the plane of the disk under a low anisotropy field) prevails in magnetization vector oscillation. The higher h^*, the wider the switching band for spherical particles and the larger damping parameter α, the narrower the switching band at a fixed variable field amplitude. Also, with increasing damping parameter, the switching band shifts toward lower frequencies, moving away from the linear FMR frequency (Fig. 2). When the variable field amplitude is very high ($h^* \gg h^*_{\min}$), magnetization vector **M** behaves in a random manner. In this case, the variable field causes the magnetization to switch in the directions normal, antiparallel, and parallel to its initial position. The run of the frequency dependence of the switching threshold is the same for all oblate ellipsoids of revolution: the curve "expands" as the semiaxis of revolution decreases (Fig. 3).

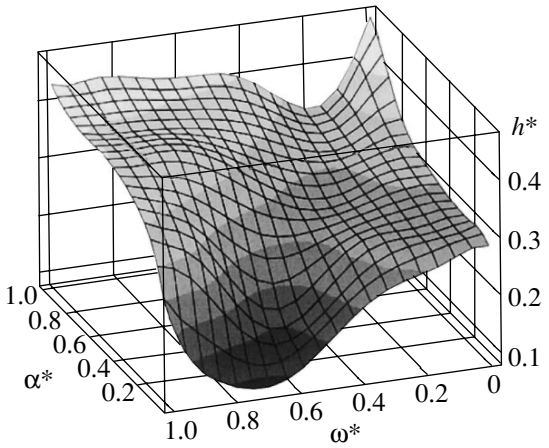

Fig. 2. Switching threshold vs. frequency and damping parameter for spherical particles.

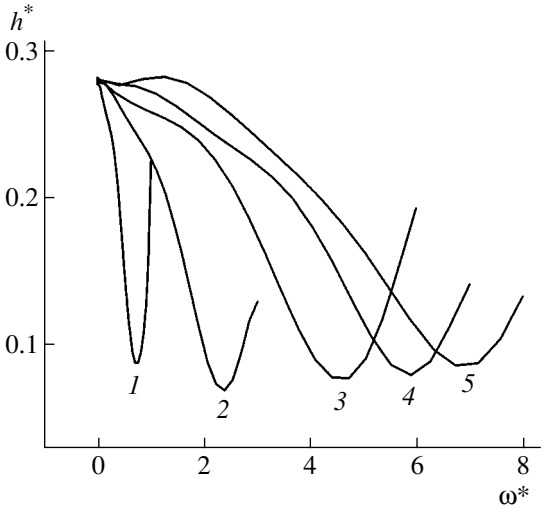

Fig. 3. Switching threshold vs. reduced frequency at α = 0.01 and demagnetizing factor N equal to (*1*) 1/3, (*2*) 0.3, (*3*) 0.2, (*4*) 0.1, and (*5*) 0.

ELECTROMAGNETIC RESPONSE FROM A SINGLE-DOMAIN FERROMAGNETIC PARTICLE

The response will be described using modified Gilbert equation (2) as the equation of motion. Let a particle be subjected to alternating magnetic field $\mathbf{H}^*_{\sim}(t^*) = \mathbf{h}^*\exp(i\omega^* t^*)$. For $h^* \ll H^*_{\text{eff}}$, a solution to (2) will be sought in the form

$$\mathbf{m}(t^*) = \mathbf{m}_0 + \mathbf{m}_1\exp(i\omega^* t^*) + \mathbf{m}_2\exp((\omega^*_r + i\omega^*_{\text{res}})t^*), \quad (6)$$

where $\mathbf{m}_0$ is the component of vector **m** in the stable equilibrium position in the absence of the magnetic field (in the presence of the field, $\mathbf{m}_0 \parallel \mathbf{H}^*_{\text{eff}}(\mathbf{m}_0)$).

Let the magnetic field be aligned with the *Ox* axis and the orientations of the particle magnetization along the *Ox* and *Oy* axes be designated as positions *a* and *b*. Then, for position *a*, $\mathbf{h}^* \parallel \mathbf{m}_0$, $\mathbf{m}_0 \times \mathbf{h}^* = 0$, and the solution to Eq. (2) is $\mathbf{m} = \mathbf{m}_0$. For position *b*, the sets of equations for the components of vectors $\mathbf{m}_1$ ($m_{1y} = 0$) and $\mathbf{m}_2$ ($m_{2y} = 0$) have the form (accurate to the second order of smallness in $\mathbf{m}_1$ and $\mathbf{m}_2$)

$$\begin{cases} i\omega^* m_{1x} - \left(1 + 4\pi\dfrac{M_0^2}{2K_1}(N_z - N_y) + i\omega^*\alpha\right)m_{1z} = 0 \\ (1 + i\omega^*\alpha)m_{1x} + i\omega^* m_{1z} = h^*, \end{cases} \quad (7)$$

$$\begin{cases} (\omega^*_r + i\omega^*_{\text{res}})m_{2x} - \left(1 + 4\pi\dfrac{M_0^2}{2K_1}(N_z - N_y)\right. \\ \left. + (\omega^*_r + i\omega^*_{\text{res}})\alpha\right)m_{2z} = 0, \\ (1 + \alpha(\omega^*_r + i\omega^*_{\text{res}}))m_{2x} + (\omega^*_r + i\omega^*_{\text{res}})m_{2z} = 0. \end{cases} \quad (8)$$

From set (8), one can find the resonant and relaxation frequencies appearing in (6). A solution to set (7) can be represented in the form

$$\begin{cases} m_{1x} = h^*\dfrac{1 + (\omega^*_0)^2(1 + \alpha^2) + i\omega^*\alpha}{(1 + \alpha^2)((\omega^*_0)^2 - (\omega^*)^2 + 2i\omega^*_r\omega^*)} \\ m_{1z} = h^*\dfrac{i\omega^*}{(1 + \alpha^2)((\omega^*_0)^2 - (\omega^*)^2 + 2i\omega^*_r\omega^*)}. \end{cases} \quad (9)$$

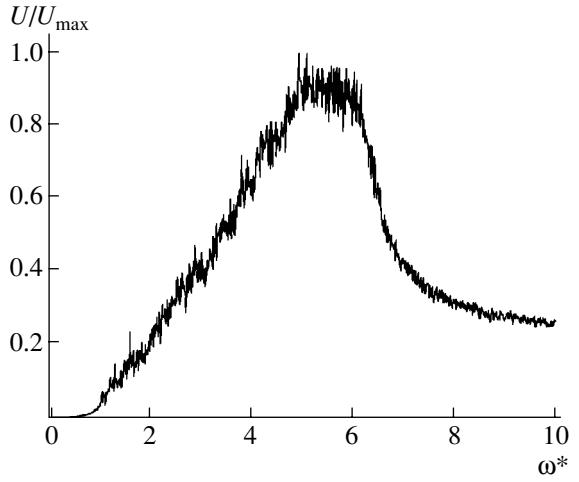

Fig. 4. Frequency dependence of the relative amplitude of the response from 1000 particles half of which are in state *a* and the other half, in state *b*. $\alpha = 0.01$.

Response E (in volts) from one particle, which is proportional to the rate of change of the magnetic moment, is sensed by an induction coil whose axis is directed along the Oz axis of the laboratory frame of reference [4],

$$E = -\mu_0 M_0 \frac{dm_z}{dt} Vn, \tag{10}$$

where $\mu_0 = 4\pi \times 10^{-7}$ H/m is the magnetic constant, V is the particle volume, and n is the number of turns per unit length.

From solution (9), one can obtain the steady-state response amplitude per particle as a function of the reduced frequency,

$$U(\omega^*) = \frac{1}{1+\alpha^2} \times \frac{\mu_0 M_0 h^* Vn\omega^*}{\sqrt{((\omega_0^*)^2 - (\omega^*)^2)^2 + 4(\omega_r^*\omega^*)^2}}. \tag{11}$$

As follows from (6), the relaxation time of the particle magnetization, $\tau_r = 2\pi/\omega_r \sim 1/\alpha$ (which coincides with the time of excitation of particle magnetization oscillation), depends on damping parameter α. From (11), we see that the response of the particle is maximal at reduced FMR frequency ω_{res}^* and is $\Delta\omega^* \sim \omega_r^*$ wide.

RESPONSE OF A PARTICLE ENSEMBLE TO A FIELD PULSE

Consider now the response from a particle ensemble excited by a variable field. We assume that the basic crystallographic axes are parallel to and the axes of revolution of all particles are directed along the Oz axis of the laboratory frame of reference. Then, we have the unique coordinate system for all the particles. Let the magnetizations of the particles be aligned with the Oy axis and $\mathbf{h} \parallel Ox$ Then, after the ensemble has been exposed to an intense pulsed high-frequency field, some of the particles whose switching bands contain the variable field frequency switch to the position parallel to the Ox axis (write event). Switching of magnetization $\mathbf{M}$ can be detected from a change in the electromagnetic response of the particles exposed to a small-amplitude variable field with a frequency close to the write frequency. Response E from the entire ensemble of independent particles, which is detected by the coil, equals the sum of partial responses E_k (see (10)) [1, 8],

$$E = \sum_k E_k. \tag{12}$$

For fine particles, a spread in sizes (volumes) is considered to be Gaussian in accordance with experimental data [4, 8]. We also assume that the particle shape distribution provides the uniform distribution of the demagnetizing factor along the axis of revolution in the interval $N_z \in [1/3, 1]$. When the particles in the ensemble are oriented randomly, i.e., when the number of particles in states *a* and *b* is the same, the response from the ensemble will show several discrete peaks against the diffuse background, the density of the peaks depending on the number of particles in the ensemble (Fig. 4). If all particles the resonant frequencies of which fall into a certain interval are in state *a*, while the remaining ones are in state *b*, the spectrum will exhibit a dip near this frequency interval and the depth of this dip will depend on damping parameter α (Figs. 5a and 5b). Hence, the dip will characterize the amount of particles with a definite direction of the magnetization vector. Its presence may be used for reading-out of information written by intense pulses of the variable field.

FMR-BASED WRITING/READING FEASIBILITY

As was already noted, when the magnetization of the particles is aligned with or normal to the variable field, the response is, respectively, high and low. Accordingly, from the amount of response, one can judge the particle magnetization orientation distribution. The data currently available suggest the feasibility of a data carrier based on the frequency writing/reading mechanism [1, 4, 5, 9]. Unlike the mechanism proposed in [4, 5, 9], where information is written by means of two rf pulses, here one pulse is used, which cuts the write time by more than one order of magnitude. Information is stored by some of the particles whose magnetization is parallel to the field and whose resonant frequencies are close to each other. If the response amplitude at a given frequency is below a certain level, one can assume that the logic zero is written at this frequency. In other words, this means that the magnetizations of most of the particles with closely spaced resonant frequencies are collinear with a scanning weakly

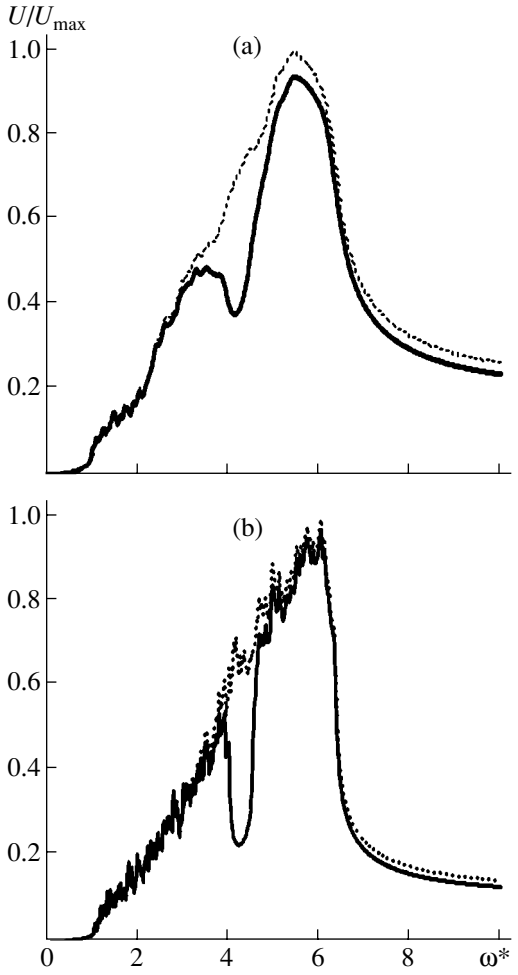

Fig. 5. Frequency dependence of the relative amplitude of the response from 1000 particles for α = (a) 0.01 and (b) 0.001. The dotted lines depict the response from all the particles whose magnetization runs normally to the variable field.

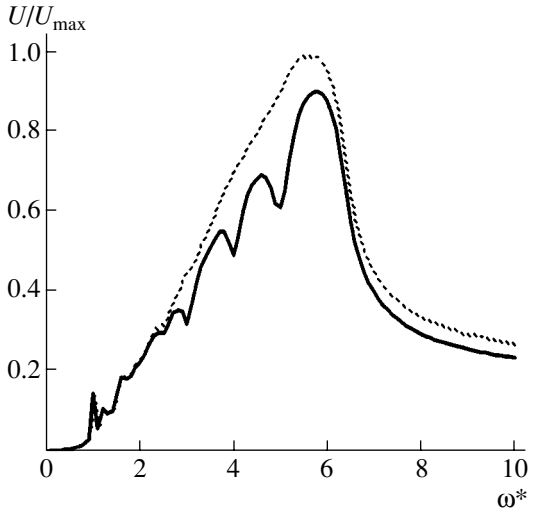

Fig. 6. Frequency dependence of the relative amplitude of the response from 1000 particles some of which are in state *a* and the rest of them are in state *b* (near reduced frequencies of 3, 4, and 5) for α = 0.01. The dotted line depicts the response from all the particles whose magnetization runs normally to the variable field.

varying magnetic field (Fig. 6). Otherwise (the response exceeds a certain level at a given frequency), one can assume that the logic unity is written. In the simplest case of highly anisotropic particles, the writing density depends on relaxation frequency $\omega_r^* \approx -\alpha\omega_{res}^*$ or damping parameter α. The smaller the damping parameter, the higher the frequency writing density and vice versa.

The condition of particle independence can be written in the form of the inequality $H_{dd} \ll H_{an}$, where $H_{dd} \approx VM_0/d^3$ is the field of dipole–dipole interaction between two particles d distant from each other and $H_{an} = 2K_1/M_0$ is the anisotropy field. Hence, the mean distance between the particles must obey the relationship $d \gg (VM_0^2/2K_1)^{1/3}$. In our system, $M_0^2/K_1 = 6.25$ and the particles are 10–100 nm across (as follows from the fact that they are single-domain [8]); therefore, $d = 10^{-5}$–10^{-4} m. Accordingly, the particle concentration is 10^8–10^9 cm^{-3} and the writing density is 10^8–10^9 bit/cm^3 (two to three particles per bit). As the amount of anisotropy rises, the writing density is bound to grow as $(H_{an})^{1/3}$. Thus, nonlinear and linear FMRs can be used for data writing/reading in an ensemble of fine single-domain particles.

CONCLUSIONS

We considered the linear and nonlinear dynamics of magnetization in an ensemble of independent single-domain particles subjected to high-frequency electromagnetic field pulses. At certain values of the pulse amplitude and frequency, the magnetization vector of one particle resonantly switches to the position perpendicular to its initial orientation. This phenomenon is akin to the occurrence of nonuniform nonlinear FMR, since the frequency dependence of the switching threshold is similar to the frequency dependence of the nonlinear FMR excitation threshold [10].

If the field amplitude is small, the oscillations of magnetization vector **M** are based on nonlinear FMR. In this case, the response both from one particle, if its size exceeds a certain value [11], and from a particle ensemble can be detected. The amount of the electromagnetic response is related to the particle shape, since its spectrum depends on the particle distribution over resonant frequencies, which, in turn, depend on the particle shape distribution. The spectrum of the response is also affected by the orientation of the magnetization vector in the particles relative to a given axis. Numerical analysis of the solution to the equation of motion of

magnetization vector convincingly suggests that an ensemble of single-domain particles excited by an rf field may be used as an information carrier where data writing/reading is based on nonlinear/linear FMR.

REFERENCES

1. L. N. Kotov, Fanur F. Asadullin, and Farit F. Asadullin, in *Proceedings of the International Forum on Wave Electronics and Its Applications, St. Petersburg, 2000*, pp. 196–198.
2. L. N. Kotov and L. S. Nosov, Pis'ma Zh. Tekh. Fiz. **29** (20), 38 (2003) [Tech. Phys. Lett. **29**, 853 (2003)].
3. L. N. Kotov and L. S. Nosov, in *Proceedings of the 18th International Seminar "New Magnetic Materials for Microelectronics" (NMMM), Moscow, 2002*, pp. 734–736.
4. B. A. Goldin, L. N. Kotov, L. K. Zarembo, and S. N. Karpachev, *Spin–Phonon Interactions in Crystal Ferrites* (Nauka, Leningrad, 1991) [in Russian].
5. V. A. Shutilov, I. E. Adzhikovich, L. N. Kotov, and V. L. Komashnya, USSR Inventor's Certificate No. 1332379, Byull. Izobret., No. 31 (1987).
6. A. G. Gurevich, *Magnetic Resonance in Ferrites and Antiferromagnets* (Nauka, Moscow, 1973) [in Russian].
7. S. I. Khudyaev, *Approximate Methods of Mathematical Physics: A School Book* (Syktyvkar Univ., Syktyvkar, 1998) [in Russian].
8. Yu. I. Petrov, *Clusters and Fine Particles* (Nauka, Moscow, 1986) [in Russian].
9. L. N. Kotov and V. N. Shaporov, Pis'ma Zh. Tekh. Fiz. **24** (19), 76 (1998) [Tech. Phys. Lett. **24**, 780 (1998)].
10. Ya. A. Monosov, *Nonlinear Ferromagnetic Resonance* (Nauka, Moscow, 1971) [in Russian].
11. S. Zhang, S. A. Oliver, N. E. Israeloff, and C. Vittoria, Appl. Phys. Lett. **70**, 2756 (1997).

Translated by V. Isaakyan

Technical Physics, Vol. 50, No. 10, 2005, pp. 1311–1315. Translated from Zhurnal Tekhnicheskoĭ Fiziki, Vol. 75, No. 10, 2005, pp. 61–65.

SOLID-STATE ELECTRONICS

Structure and Magnetic Properties of Iron- and Cobalt-Based Amorphous Alloys Versus Nanocrystallization Conditions

N. I. Noskova, V. V. Shulika, A. G. Lavrent'ev, A. P. Potapov, and G. S. Korzunin

Institute of Metal Physics, Ural Division, Russian Academy of Sciences, ul. S. Kovalevskoĭ 18, Yekaterinburg, 620219 Russia

e-mail: phisica@imp.uran.ru

Received January 12, 2005

Abstract—The effect of the structural state of $Fe_5Co_{70}Si_{15}B_{10}$, $Fe_{60}Co_{20}Si_5B_{15}$, and $Co_{81.5}Mo_{9.5}Zr_9$ amorphous alloys on their magnetic properties is studied under different nanocrystallization conditions. A permanent magnetic field applied during thermomagnetic treatment is found to affect structuring in the amorphous alloys at the initial stage of devitrification. The fine structure of the devitrified amorphous alloys is shown to correlate with the field shifting the hysteresis loop. A mechanism accounting for a hysteresis loop shift in amorphous alloys is discussed. © *2005 Pleiades Publishing, Inc.*

INTRODUCTION

The magnetic properties of soft magnetic materials depend on their structure, the structures of domain walls, and the domain wall stability. By modifying the structure of ferromagnets, one can control their magnetic properties. Electron microscopy is widely applied to study the structural state of amorphous and nanocrystalline alloys. Additional information on the structure of the alloys can be extracted from the key parameters involved in the Barkhausen effect [1, 2].

In this work, we studied the effect of the structural state of Fe- and Co-based amorphous alloys on their magnetic properties and parameters of the Barkhausen effect under various conditions of heat treatment and thermomagnetic treatment (TMT). Specifically, we revealed how the annealing temperature, cooling rate, and magnetic field frequency influence the magnetic properties of the heat-treated alloys and found a relationship between the structure of the amorphous alloys (disperse phase precipitation) and field ΔH shifting a hysteresis loop (ΔH is the field between the center of the loop and the origin).

The chemical compositions of the disperse phases were determined. Concepts concerning a mechanism accounting for a hysteresis loop shift in the amorphous alloys are presented.

RESULTS AND DISCUSSION

Amorphous ribbons 20–25 μm thick and 5 mm wide were produced by quenching from the melt on a rotating copper wheel. The samples had the shape of strips and toroids. The amorphous samples had different values of magnetostriction λ_s: $\sim 30 \times 10^{-6}$ for $Fe_{60}Co_{20}Si_5B_{15}$ and $\sim 0.5 \times 10^{-6}$ for $Fe_5Co_{70}Si_{15}B_{10}$. For $Co_{81.5}Mo_{9.5}Zr_9$, λ_s was close to zero.

To relieve quenching-induced stresses, the samples were vacuum-annealed at temperatures varying from 300 to 450°C. Then, they were subjected to longitudinal magnetic fields of different frequencies (namely, in a permanent field, in an ac field with f = 50 Hz, and in a high-frequency field with f = 80 kHz). Some of the samples were subjected to complex thermomagnetic treatment: they were annealed in a certain temperature range and simultaneously exposed to a constant or high-frequency magnetic field. Some of the samples were water-quenched in an ac magnetic field starting from the Curie temperature (the cooling rate was 50 K/min).

The structure of the amorphous ribbons was studied under a JEM-200KX transmission electron microscope. For electron microscopic analysis, the ribbons were electrolytically thinned to foils having regions as thin as 200–300 nm.

As a key (information-carrying) parameter of the Barkhausen effect, we chose electromotive force ε of the flux of magnetization (Barkhausen) jumps averaged over the magnetization reversal period. The flux of magnetization jumps (MJs) was displayed on an oscilloscope screen, and ε was measured on the strip samples by an add-on transducer [3, 4]. The toroidal samples were used to measure static hysteresis loops, initial permeability μ_0, and magnetic losses $P_{0.2/20000}$. The magnetic losses measured at a frequency of 20 kHz and an induction of 0.2 T were calculated from the area of stroboscopically recorded dynamic hysteresis loops. The initial permeability was determined at a frequency of 80 Hz in a field of 0.05 A/m. From the strip samples, we also took static hysteresis loops.

The basic parameters of the alloys, namely, Curie temperature T_C and crystallization temperature T_{cr}, are given in Table 1. Table 2 lists the magnetic properties of

1063-7842/05/5010-1311$26.00

Table 1. Values of T_C and T_{cr} for the amorphous alloys

Alloy	T_C, °C	T_{cr}, °C
$Fe_5Co_{70}Si_{15}B_{10}$	380	480
$Fe_{60}Co_{20}Si_5B_{15}$	550	490
$Co_{81.5}Mo_{9.5}Zr_9$	462	540

the $Fe_{60}Co_{20}Si_5B_{15}$, $Fe_5Co_{70}Si_{15}B_{10}$, and $Co_{81.5}Mo_{9.5}Zr_9$ alloys after the heat and thermomechanical treatments. Here, μ_0 is the initial permeability, H_c is the coercive force, $P_{0.2/20000}$ is the magnetic losses, and B_r/B_m is the squareness ratio of a hysteresis loop.

Figure 1 shows the hysteresis loops for different states of the $Fe_5Co_{70}Si_{15}B_{10}$ alloy: after annealing in the absence of the magnetic field, after TMT in the permanent magnetic field, and after TMT in the high-frequency magnetic field (f = 80 kHz). After rapid quenching from the melt on the rotating wheel, the sample has a rounded symmetrical hysteresis loop. After no-field annealing, the hysteresis loop has inflections (Fig. 1a). After TMT in the permanent magnetic field, the loop becomes rectangular and shifts along the field axis (Fig. 1b). TMT in the 80-kHz field leads to a symmetric rounded hysteresis loop with a minimum coercive force (Fig. 1c). In the last case, the effect is similar to that of TMT in a rotating magnetic field. Note that water quenching of the $Fe_5Co_{70}Si_{15}B_{10}$ alloy from the Curie temperature and TMT in the high-frequency magnetic field give the same result.

Figure 2 plots shift field ΔH against the temperature of TMT in the permanent field for the $Fe_5Co_{70}Si_{15}B_{10}$ alloy. The annealing time was 1 h for all the samples.

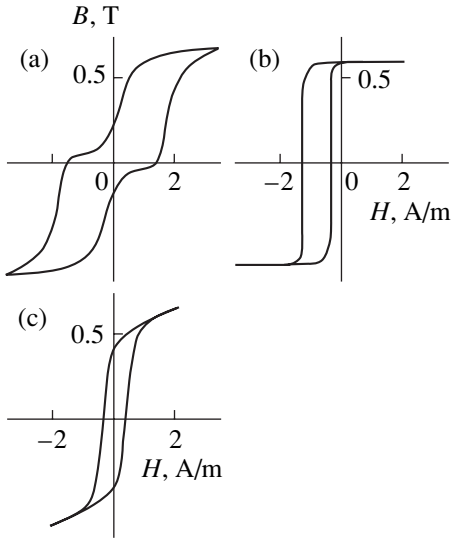

Fig. 1. Hysteresis loops in the $Fe_5Co_{70}Si_{15}B_{10}$ amorphous alloy after (a) annealing in the absence of the magnetic field, (b) TMT in the permanent magnetic field, and (c) TMT in the high-frequency magnetic field.

It is seen that TMT at temperatures to 250°C does not shift the hysteresis loop. The treatment in the temperature range 250–350°C slightly shifts the loop (by about 1–2 H_c). At higher TMT temperatures, the shift of the hysteresis loop increases sharply, reaching 10–15 H_c.

Similar results were obtained for the $Fe_{60}Co_{20}Si_5B_{15}$ and $Co_{81.5}Mo_{9.5}Zr_9$ alloys. The experimental data indicate that the shape of the hysteresis loop, magnetic losses, and permeability of the samples depend on the treatment conditions.

The Fe- and Co-based amorphous alloys annealed in the absence of the field exhibit hysteresis loops of the Perminvar type. Hysteresis loops with inflections are associated with the stabilizing domain structure: domain walls tend to return to their initial positions as the applied magnetic field decreases to zero. The presence of the stabilized domain structure in the samples annealed without the magnetic field can be judged from elevated magnetic losses and low initial permeabilities.

During TMT in the 80-kHz field, magnetization reversal in the amorphous ribbons occurs via magnetization rotation. When the sample is annealed in this field, induced anisotropy does not arise because of the absence of a preferred orientation. The destabilization of the domain structure that occurs at TMT in the high-frequency field results in rounded symmetric hysteresis loops, low magnetic losses, a low coercive force, and a high permeability.

The rectangular hysteresis loops shifted along the field axis that are observed after TMT in the constant

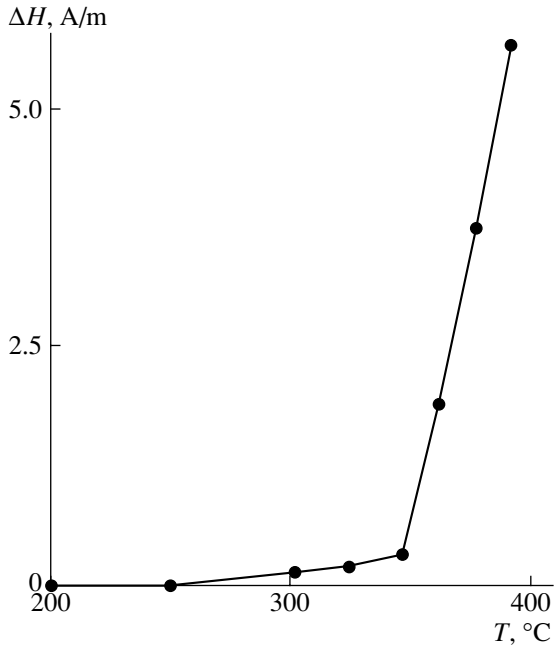

Fig. 2. Field shifting the hysteresis loop vs. the temperature of TMT in the permanent magnetic field for $Fe_5Co_{70}Si_{15}B_{10}$.

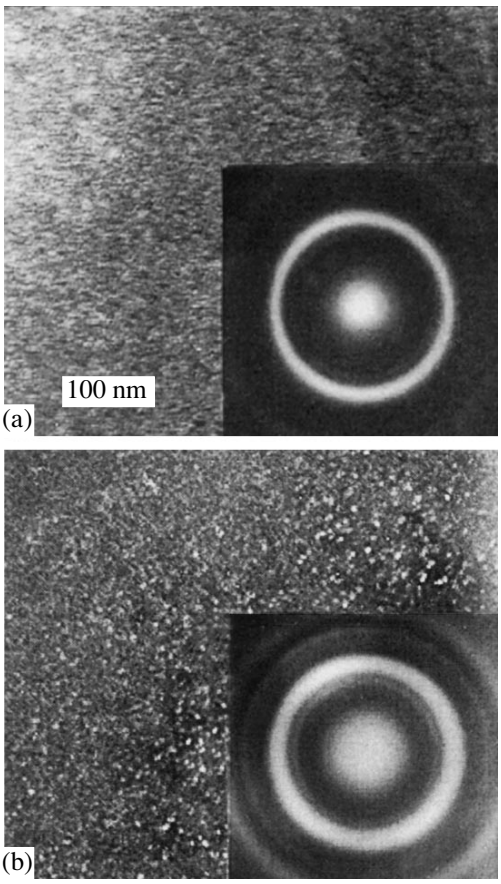

Fig. 3. Electron micrographs taken of amorphous $Fe_5Co_{70}Si_{15}B_{10}$ and the corresponding electron diffraction patterns taken after TMT in the permanent field at (a) 280 and (b) 380°C.

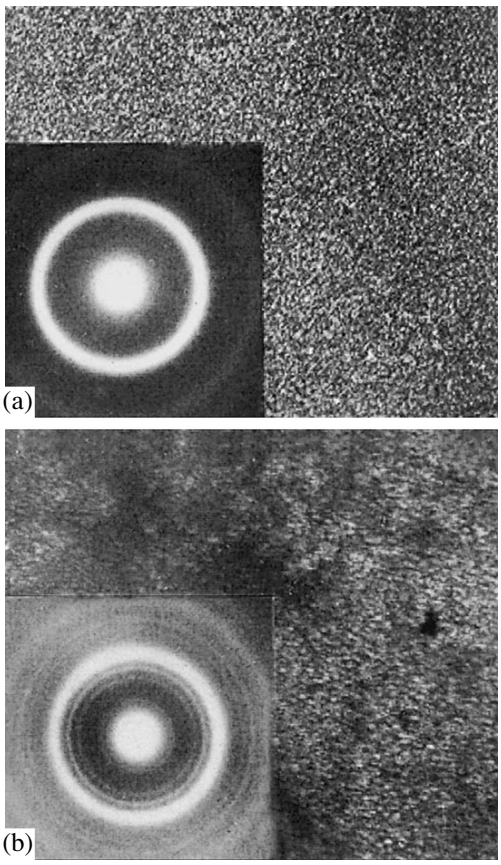

Fig. 4. Electron micrographs taken of amorphous $Co_{81.5}Mo_{9.5}Zr_9$ and the corresponding electron diffraction patterns after (a) heat treatment at 300°C for 2 h and (b) TMT in the permanent field at 450°C for 1 h.

magnetic field are likely to be related to microcrystalline high-coercivity precipitates in the amorphous matrix with their magnetization directions specified by the direction of the magnetic field during TMT. The results of structure analysis that follow confirm this assumption.

For the $Fe_5Co_{70}Si_{15}B_{10}$ amorphous alloy, it turned out that, after TMT in the constant magnetic field at 280°C (ΔH is at most 1–2 H_c), its matrix contains disperse α-Co clusters. In dark-field images of the alloy after this treatment, these clusters appear as diffuse and clear-cut spots and the inner ring in the electron diffraction pattern is smeared (Fig. 3a). After TMT in the constant magnetic field at 380°C, ΔH equals 10–15 H_c. The alloy contains disperse precipitates (<5 nm across) of the Co_2Si and Fe_3Si phases (Fig. 3b), which are not observed after annealing at a lower temperature (280°C). Remarkably, these phases (disperse precipitates) are arranged into chains.

The structure analysis suggests that the small shift of the hysteresis loop in the case of the $Fe_5Co_{70}Si_{15}B_{10}$ amorphous alloy subjected to TMT in the temperature range 250–350°C is related mainly to the formation of α-Co clusters, which stabilize the domain structure. The shift of the hysteresis loops in the samples annealed at higher temperatures is likely to be caused by the precipitation of disperse phases with a higher coercive force and the magnetization direction specified by the direction of the magnetic field in the course of TMT.

After TMT in the constant magnetic field at 400°C, the $Fe_{60}Co_{20}Si_5B_{15}$ alloy also contains disperse (<5-nm) Co_2Si and Fe_3Si precipitates. The magnetization direction in them depends on the direction of the magnetic field in the course of treatment. Note that such a treatment causes a significant shift of the hysteresis loop (ΔH = 10–15 H_c).

Figure 4 shows the electron micrographs taken of the $Co_{81.5}Mo_{9.5}Zr_9$ alloy after heat treatment at 300°C for 2 h (Fig. 4a) and after TMT in the constant magnetic field at 450°C for 1 h (Fig. 4b).

It is seen that the matrix of the alloy annealed at 300°C for 2 h remains amorphous. However, along with the first and second diffuse halos, the electron diffraction pattern contains diffraction spots and rings, the lat-

Table 2. Magnetic properties of the amorphous alloys after different treatments

Alloy	Treatment	μ_0	H_c, A/m	$P_{0.2/20000}$, W/kg	B_r/B_m
$Fe_5Co_{70}Si_{15}B_{10}$	Annealing	4500	1.3	30	0.3
	TMT in permanent field	5200	0.6	37	0.97
	Rapid cooling in ac field	45 000	0.4	5	0.96
$Fe_{60}Co_{20}Si_5B_{15}$	Annealing	1050	2.5	55	0.3
	TMT in permanent field	1200	2.5	60	0.97
	Complex TMT	7500	1.0	7	0.97
$Co_{81.5}Mo_{9.5}Zr_9$	Annealing	1200	1.5	35	0.4
	TMT in permanent field	3500	0.8	40	0.97
	Rapid cooling in ac field	50 000	0.3	5	0.96

ter consisting of small reflections. The dark-field image of the alloy demonstrates crystalline phases; by interplanar spacings, these can be identified as α-Co and β-Co precipitates less than 2 nm across.

Although the alloy annealed in the constant magnetic field at 450°C contains the α-Co, β-Co, and Co_2(Mo,Zr) disperse phases, its alloy structure still remains largely amorphous. The effect of a constant magnetic field on structuring early in devitrification of the amorphous alloy during heat treatment is of particular interest. The constant magnetic field seems to favor the growth of α-Co clusters and their aggregation into linear (inside the ribbon) or 3D arrays, which originate at the ribbon surface.

Figure 5 shows the oscillograms of the envelopes of the MJ flux amplitudes in the metalloid-free $Co_{81.5}Mo_{9.5}Zr_9$ amorphous alloy subjected to heat treatment at 300°C for 2 h (curve *1*) and to TMT in the constant magnetic field at 450°C for 1 h (curve *2*). Comparing these oscillograms with the electron micrographs taken of the $Co_{81.5}Mo_{9.5}Zr_9$ alloy (Fig. 4) indicates a correlation between the alloy structure and the chosen information-carrying parameter of the Barkhausen effect. Specifically, the field distribution of MJs in the Gaussian form (Fig. 5, curve *1*) corresponds to the amorphous structure, while intervals of critical start fields in the oscillogram are assigned to precipitation in the amorphous matrix (Fig. 5, curve *2*).

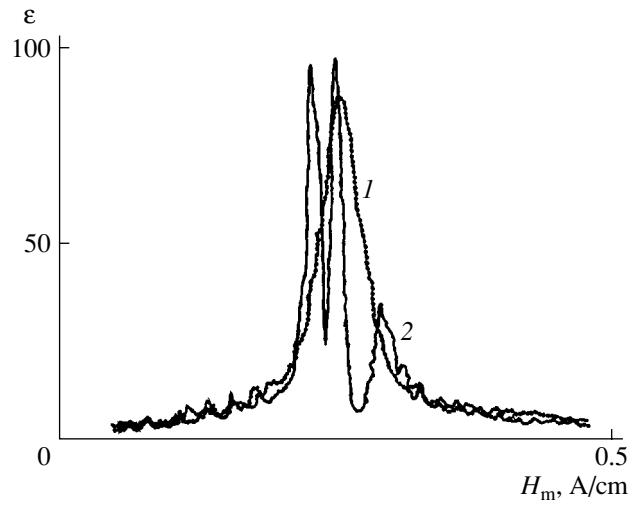

Fig. 5. Oscillograms of the MJ flux amplitude envelopes for $Co_{81.5}Mo_{9.5}Zr_9$ after (*1*) heat treatment at 300°C for 2 h and (*2*) TMT in the permanent magnetic field at 450°C for 1 h.

After TMT in the constant magnetic field, the oscillogram of the MJ flux amplitude envelope shifts along the field axis, in accordance with the shift of the hysteresis loop. The oscillogram exhibits several intervals of critical start fields. The α-Co, β-Co, and Co_2(Mo,Zr) disperse phases (with their magnetization directions specified by the direction of the constant magnetic field during TMT) precipitating in this alloy result in an increase in the MJ flux amplitude and simultaneously narrow the intervals of critical start fields.

CONCLUSIONS

A constant magnetic field applied during thermomagnetic treatment has been found to affect structuring at the initial stage of devitrification of the amorphous alloys. The fine structure of the devitrified amorphous alloys correlates with the field shifting the hysteresis loop. The parameters of the Barkhausen effect are shown to correlate with the fine structure of the devitrified amorphous alloys.

It is shown that magnetization reversal in the samples subjected to thermomagnetic treatment in a constant magnetic field is accomplished via a set of magnetization jumps in start fields close to each other, which results in an increase in the magnetic losses.

Methods that could prevent a shift of the hysteresis loop and significantly improve the magnetic properties of amorphous soft magnetic materials are (i) complex

thermomagnetic treatment (the simultaneous action of high-frequency and permanent magnetic fields) and (ii) rapid cooling starting from a temperature above the Curie temperature at a rate of 50 K/min in an ac magnetic field. Changes in the magnetic properties of the alloys after such treatments are due to the occurrence of uniaxial magnetic anisotropy and the destabilization of domain walls.

ACKNOWLEDGMENTS

This work was supported by the project "Integration" in cooperation with the Siberian Division, Russian Academy of Sciences.

REFERENCES

1. É. S. Gorkunov, Yu. N. Dragoshanskiĭ, and M. Micovsky, Defektoskopiya, No. 6, 3 (2000).
2. É. S. Gorkunov, V. V. Shulika, A. G. Lavrent'ev, *et al.*, Dokl. Akad. Nauk **386**, 468 (2002) [Dokl. Phys. **47**, 728 (2002)].
3. G. S. Korzunin and A. G. Lavrent'ev, Defektoskopiya, No. 6, 24 (1999).
4. A. A. Glazer, V. V. Shulika, and A. P. Potapov, Dokl. Akad. Nauk SSSR **324**, 1191 (1992) [Sov. Phys. Dokl. **37**, 314 (1992)].

Translated by K. Shakhlevich

Technical Physics, Vol. 50, No. 10, 2005, pp. 1316–1318. Translated from Zhurnal Tekhnicheskoĭ Fiziki, Vol. 75, No. 10, 2005, pp. 66–68.

OPTICS, QUANTUM ELECTRONICS

Computerized Setup for Double-Monochromator Photoreflectance Spectroscopy

L. P. Avakyants, P. Yu. Bokov, and A. V. Chervyakov

Moscow State University, Vorob'evy Gory, Moscow, 119992 Russia

e-mail: avakants@genphys.phys.msu.ru

Received December 3, 2004

Abstract—An experimental setup for studying semiconductor structures by photoreflectance spectroscopy is designed. The double-monochromator-based optical scheme of the setup makes it possible to depress uncontrolled heating of the sample and diminishes a bending of the energy bands due to charge carrier photogeneration. Accordingly, the photoreflectance spectra are detected with a minimal influence of the modulating and probe radiations on the sample. With this setup, the room-temperature photoreflectance spectra from GaAs/GaAsP superlattices are taken and the interband transition energies, as well as a potential step in the conduction band of these superlattices, are measured. © *2005 Pleiades Publishing, Inc.*

The techniques of modulation spectroscopy are being widely used in studying semiconductor structures, such as quantum wells and superlattices. The most popular are the photoreflectance and electroreflectance methods [1], which measure the variation of reflectance R of the sample in the presence of an electric field. In the case of photoreflectance (PR), R is modulated by the electric field varying in the space charge region when electron–hole pairs are generated by a modulating laser radiation. Although the relative variation of the reflectance under the action of the modulating radiation is small, $\Delta R/R \sim 10^{-5}$, it can be recorded using synchronous detection. The PR method is contactless and offers a high spatial locality.

PR spectra can be recorded with a monochromator placed in front of the object (Fig. 1a) [2] or behind it (Fig. 1b) [3]. In the former case, the radiation from spectrometer lamp *1* (probe radiation shown with the dashed line) passes through monochromator *2* and is incident on the sample. The reflected beam strikes photodetector *4* [2]. Modulating beam *5* is incident on the same place on the sample as the probe radiation. In such a configuration, the photodetector receives both the desired PR signal and the modulating radiation scattered by the surface roughness. Therefore, the signal to be measured may fall outside the dynamic range of measurements in the case of synchronous detection.

In the latter case (Fig. 1b), the total radiation from spectrometer lamp *1* and modulating radiation *5* are incident on the sample, reflect from it, and enter the entrance slit of monochromator *2*. The monochromator transmits only the probe radiation (dashed line), which is then recorded by photodetector *4*. In this case, the monochromator filters out the modulating radiation scattered by the surface roughness. However, the sample is constantly irradiated by the entire spectrum of the intense lamp. This leads to local heating of the sample, photoexcitation of carriers, and, eventually, an uncontrolled bending of the energy bands.

To get rid of the disadvantages inherent in the above schemes, we developed a setup for recording PR spectra that is based on a double monochromator (Fig. 1c). Here, the radiation from spectrometer lamp *1* passes through first monochromator *2* and is incident on sample *3*. The modulating radiation strikes the sample at the same place. The reflected radiation passes through second monochromator *2* and arrives at photodetector *4*. Such a scheme prevents sample heating, and the scattered modulating radiation is filtered out by the second monochromator. Figure 2 shows the block diagram of the experimental setup for PR spectroscopy equipped with an MDR-6 double monochromator (the focal length 30 cm, the aperture ratio 1 : 6). Additional entrance slit *A* is mounted in the second stage of the monochromator instead of the middle slit.

The radiation from 30-W spectrometer lamp *1* is focused by optical system *2* on the entrance slit of first monochromator *3*(I), passes through it, and is directed to sample *5* by means of optical system *4*. The radiation of He–Ne laser *10* modulated with mechanical chopper *11* is incident at the same point of the sample. The modulation frequency can be varied from 50 to 1500 Hz. The probe radiation reflected from the sample (the dashed line in Fig. 2) is focused by objective *6* on entrance slit *A* of second monochromator *3*(II) interfaced with low-noise photoamplifier *7*. An FDK-263 silicon photodiode connected by the zero-bias scheme serves as the sensor of the photoamplifier. The frequency response of the amplifier is optimized for the frequency band 50–1500 Hz. The output signal of the amplifier is applied to lock-in detector *8* of a Unipan-232B selective nanovoltmeter. The signal from photo-

1063-7842/05/5010-1316$26.00

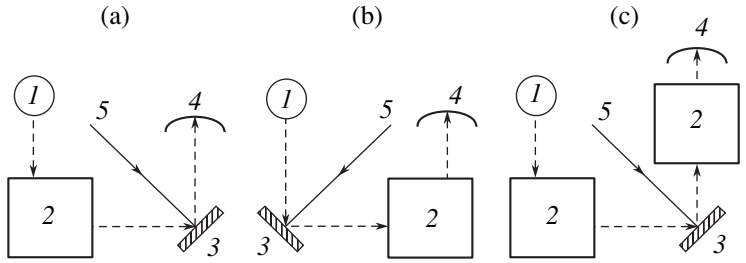

Fig. 1. Recording of PR spectra with (a, b) one and (c) two monochromators: (*1*) spectrometer lamp, (*2*) monochromator, (*3*) sample, (*4*) photodetector, and (*5*) modulating radiation.

diode *13* serves as a reference voltage for the lock-in detector. Photodiode *13* detects the modulating radiation from laser *10*, which reflects from the sample (the dotted line in Fig. 2). Thus, the output voltage of the lock-in detector is proportional to the variation of reflectance R at the modulation frequency. The apertures of optical systems *2*, *4*, and *6* are matched with the aperture of the monochromator. To control the positions of the monochromator gratings and to measure the PR signal, we used PC *9* with an RS-232 interface and an original interface unit [4] based on an Amtel 89c51 microcontroller. The spectral width of the monochromator's instrument function was 1 meV. The PR spectra were recorded at room temperature.

Figures 3a and 3b show the PR spectra of a GaAs/GaAsP superlattice that were taken using a single (Fig. 1a) and double (Fig. 1b) monochromator, respectively. The spectral lines at 1.459 and 1.903 eV correspond to basic transitions in the strained GaAs and $GaAs_{0.6}P_{0.4}$ layers, respectively. The lines in the range 1.459–1.903 eV are assigned to interband transitions in the superlattice. It is seen that the PR spectra differ in signal-to-noise ratio and shape because of a reduced effect of the probe radiation on the sample in Fig. 3b.

To find the energies of the interband transitions, the experimental spectra were fitted to the Aspnes low-field model [5],

$$\frac{\Delta R}{R}(E) = \mathrm{Re}[Ae^{i\varphi}(E - E_i + \Gamma)^{-m}]. \qquad (1)$$

Here, A and φ are the amplitude and phase parameters, E is the probe radiation energy, E_i is the position of an ith spectral feature, Γ is a phenomenological broadening parameter, and m is a parameter depending on the type of the critical point and on the order of the derivative of permittivity $\varepsilon(E)$ with respect to energy.

In the case under consideration, $m = 2$ [5]. The arrows in Fig. 3b indicate the energies of interband transitions in the superlattice calculated from the experimental spectrum. Based on the simulation results for the GaAs/GaAsP band structure and the experimental data obtained from the PR spectra, we estimate a band discontinuity at the heterojunction, $\Delta E_c/\Delta E_g = 0.15$ [6]. Here, ΔE_g is the difference between the energy gaps of

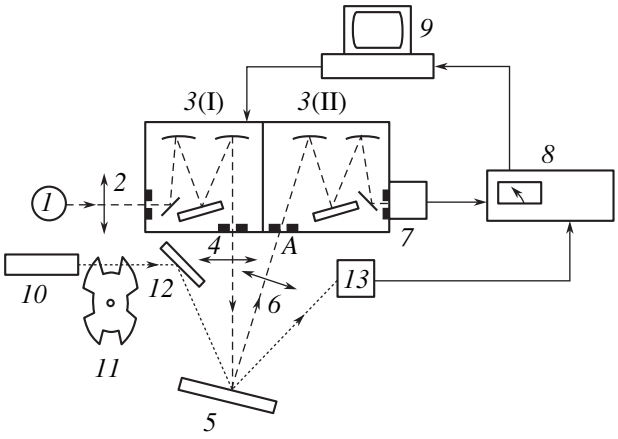

Fig. 2. Block diagram of the experimental setup for PR spectroscopy: (*1*) spectrometer lamp, (*2*, *4*, *6*) objectives, (*3*) MDR-6 double monochromator, (*5*) sample, (*7*) photodetector with low-noise amplifier, (*8*) Unipan-232B selective nanovoltmeter, (*9*) PC with microprocessor-based interface unit, (*10*) He–Ne laser, (*11*) chopper, (*12*) deflecting mirror, and (*13*) reference signal photodetector.

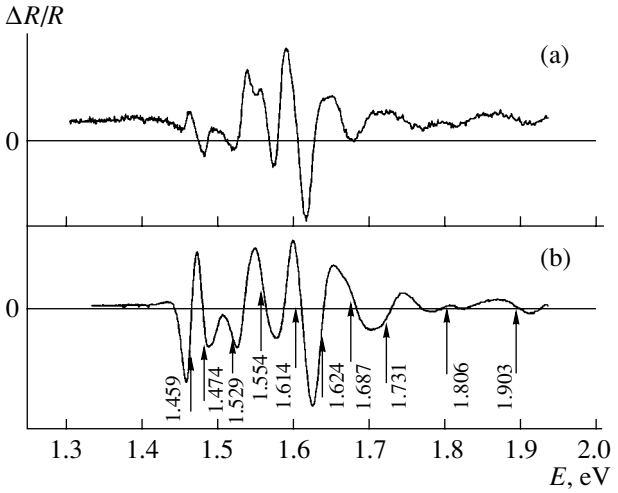

Fig. 3. PR spectra from the GaAs/GaAsP superlattice taken (a) single and (b) double monochromator. The arrows indicate the interband transition energies in the superlattice that were determined by fitting sum (1) of Aspnes expressions to the spectra.

the barrier and well and ΔE_c is the conduction band discontinuity at the heterojunction.

Thus, we developed a computerized setup for PR spectroscopy of semiconductor compounds. Our approach makes it possible to suppress probe-radiation-induced perturbing effects and, thereby, to avoid uncontrolled heating of the sample and bending of energy bands due to photogeneration of carriers. The room-temperature experiments carried out with this setup allowed us to estimate the interband transition energies in the strained GaAs/GaAsP superlattice and a potential step at the heterojunction.

REFERENCES

1. F. H. Pollak, Proc. SPIE **3944**, 408 (2000).
2. P. J. Hughes, B. L. Weiss, and T. J. S. Hosea, J. Appl. Phys. **77**, 6472 (1995).
3. L. P. Avakyants, P. Yu. Bokov, I. P. Kazakov, *et al.*, Vestn. Mosk. Univ., Ser. 3: Fiz., Astron. **32** (4), 48 (2002).
4. P. Yu. Bokov, A. A. Ivantsov, I. V. Mitin, *et al.*, in *Proceedings of the Conference "Modern Student Training in Physics," St. Petersburg, 2002*, p. 34.
5. D. E. Aspnes, Surf. Sci. **37**, 418 (1973).
6. L. P. Avakyants, P. Yu. Bokov, T. P. Kolmakova, and A. V. Chervyakov, Fiz. Tekh. Poluprovodn. (St. Petersburg) **38**, 1439 (2004) [Semiconductors **38**, 1384 (2004)].

Translated by A. Chikishev

Technical Physics, Vol. 50, No. 10, 2005, pp. 1319–1322. Translated from Zhurnal Tekhnicheskoĭ Fiziki, Vol. 75, No. 10, 2005, pp. 69–72.

**OPTICS,
QUANTUM ELECTRONICS**

Double-Pass Copper-Vapor Laser Amplifier with a High Peak Power

V. T. Karpukhin and M. M. Malikov

Institute for High Temperatures Scientific Association (IVTAN), Russian Academy of Sciences, Izhorskaya ul. 13/19, Moscow, 125412 Russia

e-mail: mmalikov@oivtran.iitp.ru

Received January 12, 2005

Abstract—New findings concerning a double-pass amplifier of original design allowing for a significant increase in the peak power of laser pulses without changing the lasing mean power and pump power are presented. A peak power of 305 kW is demonstrated at a lasing mean power of about 25 W. The physics of such an amplifier and prospects for its application are discussed. © *2005 Pleiades Publishing, Inc.*

INTRODUCTION

The creation of self-terminating laser systems with a relatively high peak power is a topical problem for a number of applications, such as laser frequency conversion with nonlinear crystals, dye laser pumping, microprocessing of materials, etc. Earlier [1, 2], we proposed a scheme of a multipass amplifier in order to increase the peak power of a copper-vapor laser. The specific design of this amplifier makes it possible to increase the peak power severalfold without changing the way and amount of energy deposition into the active medium.

The effect is reached by the multiple passage of a sharp short laser pulse generated by a master oscillator (MO) through the active medium of the amplifier. Duration τ_{0s} of this pulse must be substantially shorter than inversion lifetime τ_{inv} in the active medium of the amplifier stage. It has been experimentally demonstrated [3] that the energy taken from the active medium by and accumulated in a short input pulse is nearly equal to the energy acquired by a long input pulse, $\tau_{0s} \geq \tau_{inv}$, in a one-pass scheme, the lasing volume being equal. Therefore, the amplitude of the short pulse is higher than that of the long pulse by a factor of τ_{inv}/τ_{0s}. Using qualitative expressions derived in [3], one can find optimal relationships between τ_{0s}, τ_{inv}, length L_{amp} of the active medium of the amplifier, and delay time τ_{del} of the beam-turning unit of a copper-vapor multipass amplifier. In this work, we perform experimental verification of these expressions and refine the optical scheme of a copper-vapor multipass amplifier with the aim of improving the parameters of radiation.

EXPERIMENTAL

In experiments, we employed a simple (double-pass) copper-vapor laser amplifier with counterpropagating and polarization-decoupled beams (Fig. 1). The system consists of MO *1*; collimator *2*; polarization beamsplitter (Glan prism) *3*; amplifier stage *4*; and beam-turning unit *5*, containing quarter-wave plate *6* and plane mirror *7*.

MO *1* (LT-1Cu commercial laser tube [4]) equipped with an unstable resonator (mirrors *8* and *9*) with magnification $M = 5$ and polarizer *11* (Glan prism) generates pulses with wavelengths of 0.51 and 0.578 μm at a repetition rate of 10 kHz. The radiation is polarized horizontally, so that electric vector $E_{\|}$ lies in the plane of Fig. 1. Telescopic collimator *2* consisting of two concave spherical mirrors *8* and *9* magnifies the diameter of the MO beam to 20 mm and partly suppresses its superluminescent background, separating out (through pinhole *10*) the central part of the beam with divergence φ_{in}, which is approximately five times greater than the diffraction-limited divergence. The (input) MO radia-

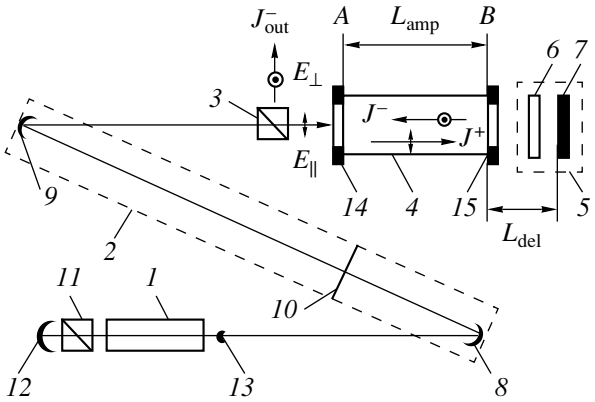

Fig. 1. Experimental scheme: (*1*) MO, (*2*) collimator, (*3*) polarization beamsplitter, (*4*) amplifier stage, (*5*) beam-turning unit, (*6*) quarter-wave phase plate, (*7*) plane mirror, (*8*, *9*) mirrors, (*10*) collimator pinhole, (*11*) MO polarizer, (*12*, *13*) mirrors of MO resonator, and (*14*, *15*) mirrors of amplifier stage.

1063-7842/05/5010-1319$26.00 © 2005 Pleiades Publishing, Inc.

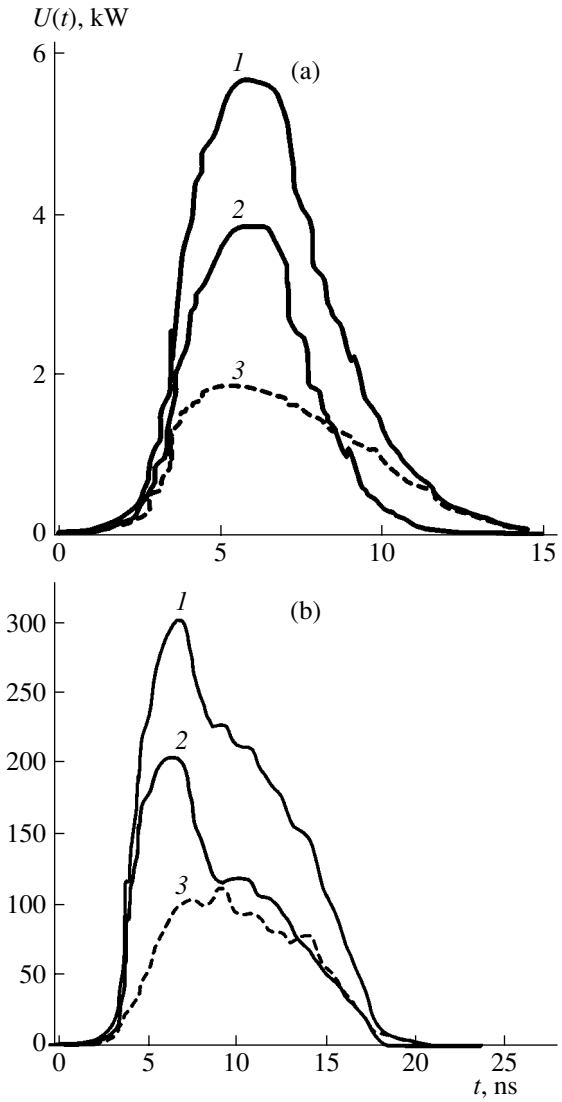

Fig. 2. (a) Pulses from the MO built around the LT-1Cu tube at the entrance to the amplifier (W_{in} = 0.3 W) and (b) the corresponding output pulses of the amplifier: (*1*) total power, (*2*) power at a wavelength of 0.51 μm, and (*3*) power at a wavelength of 0.578 μm.

tion power at the entrance to the amplifier stage is W_{in} = 0.3 W, and the width of the pulse base is τ_{0s} = 12–13 ns. In several experiments, an LT-3Cu higher power commercial laser tube [4] was used, which raised W_{in} to 0.7–0.9 W at M = 230. In this case, duration τ_{0s} was about 17 ns and φ_{in} was three times as large as the diffraction-limited divergence.

The application of the unstable resonator incorporated into the MO, mirror collimator with spatial filtering, and high-quality optical windows and mirrors, along with the upgraded MO pump source, made it possible to decrease the divergence and increase the power of the beam at the entrance to the amplifier stage compared with early values [3] of these parameters. The chromatic aberrations and beam astigmatism at the entrance to and exit from the amplifier stage were also reduced.

Amplifier stage *4* contains a GL-201 tube with working chamber length L_{amp} = 80 cm and a diameter of 20 mm. The inversion lifetime (measured at the base) is $\tau_{inv} \approx 35$ ns at a typical pump power of 3.0–3.2 kW and a pulse repetition rate of 10 kHz. Horizontally polarized beam J^+ enters the active medium of amplifier stage *4* through section *A* and falls on turning unit *5*. Beam J^- propagating in the opposite direction acquires orthogonal polarization ($E_\perp$). Therefore, it does not interfere with beam J^+ and is removed from the system by means of polarization beamsplitter *3*.

Delay time τ_{del} and its corresponding distance L_{del} from section *B* of the discharge chamber containing the active medium of the amplifier stage to mirror *7* were taken so as to satisfy the relationships derived in [3] for a double-pass system at given τ_{0s}. In the experiments, ratio τ_{inv}/τ_{0s} was varied from 2 to 3.

Repetition-rate-averaged input power W_{in} of amplifier stage *4* and average amplified power W_{out} at the output of this stage were measure with an IMO-4S calorimeter. Corresponding waveforms $U_{in}(t)$ and $U_{out}(t)$ were detected using FÉK-22spu phototubes and a sampling oscilloscope with a bandwidth of 3.7 GHz. The waveforms were related to the time axis with regard to the delays in the optical measuring paths. For the double-pass configuration, waveforms $U_{in}(t)$ and $U_{out}(t)$ in section *A* are shown.

The results were compared with those obtained in [3, 5] for a single-pass amplifier with the same amplifier stage and pump power. In [3, 5], the MO generated pulses of duration equal to the inversion lifetime in the amplifier stage (about 35 ns). For the single-pass amplifier, the maximal powers were W_{out} = 23 W and U_{out} = 136 kW.

RESULTS AND DISCUSSION

Figures 2 and 3 show waveforms $U_{in}(t)$ (panels (a)) of pulses from the MO and waveforms $U_{out}(t)$ (panels (b)) of pulses from the double-pass amplifier for the MOs based on the LT-1Cu and LT-3Cu tubes, respectively. Either version had its own optimal length L_{del} corresponding to τ_{del}. It is seen from Fig. 3a that the input pulse generated by the LT-3Cu-based MO is not smooth, exhibiting three humps (τ_{0s} is about 17 ns). In both cases, the output pulse of the double-pass amplifier is 2–3 ns longer than the input pulse. The increase in the peak power is the highest for a short smooth pulse with $\tau_{0s} \approx 12.5$ ns. It is seen from Fig. 2b that the total (for two wavelengths) output peak power (curve *1*) amounts to 305 kW at a mean power of 25 W (curves *2* and *3* correspond to green and yellow lines, respectively). When the input pulse is generated using the LT-3Cu tube, the maximum output peak power of the dou-

ble-pass amplifier is 210 kW (Fig. 3b). This value is lower than that obtained in [3] (240 kW) for a smooth input pulse with the same duration of 17 ns. This indicates that the shape and steepness of the input (MO) pulse have a significant effect on the peak power.

Note that, in both cases, the peak power of the double-pass amplifier built around the scheme from [2] is 1.5–2.2 times higher than the peak power (136 kW) of the conventional single-pass amplifier with the mean radiation powers, pump powers, and lasing volumes being equal.

It follows from the results presented that the energies extracted from the active medium in the single- and double-pass amplifiers are virtually equal to each other. The pulse duration at the entrance to the double-pass amplifier remains approximately equal to the input pulse duration and is twice as short as the superluminescence pulse duration.

Figure 4 demonstrates the peak power of the double-pass amplifier optimized in this parameter versus delay time τ_{del} and pulse duration τ_{0s} with the amplifier excitation mode remaining unchanged (τ_{inv} = 35–40 ns). It is seen that each τ_{0s} can be assigned optimal τ_{del}. Comparison of curves *1* and *2* obtained for the smooth MO pulses with durations of 12.5 and 17 ns, respectively, shows that such a dependence complies with the optimization relationships derived in [3]. For a double-pass amplifier, these relationships are written as

$$\tau_{0s} \approx \tau_{inv} - \frac{2L_{amp}}{c} - \tau_{del}, \quad (1)$$

$$\tau_{0s} \geq \left(\frac{2L_{amp}}{c} + \tau_{del}\right). \quad (2)$$

Expression (1) was obtained under the assumption that two passes of a single MO pulse cover the inversion time in the amplifier stage. Expression (2) implies that an MO pulse completely fills the volume of the amplifying medium for the inversion lifetime. For τ_{0s} and τ_{del} much shorter than those satisfying the above formulas, an MO pulse covers the inversion time incompletely and cannot totally fill the working volume of the amplifier. Accordingly, part of the excitation energy remains unutilized. If τ_{del} is much greater than the optimal value, the trailing edge of the pulse has no time to leave the channel before the inversion is terminated and the pulse energy is partially absorbed. In both cases, the amplitude of the power pulse at the exit of the double-pass amplifier decreases. The maxima in the curves depicted in Fig. 4 correspond to an optimal value of τ_{del}. On the other hand, when the MO generates shorter pulses, we, in accordance to expression (2), need to decrease an optimal value of τ_{del}, as demonstrated in the experiment: the maxima in the curves in Fig. 4 shift leftward.

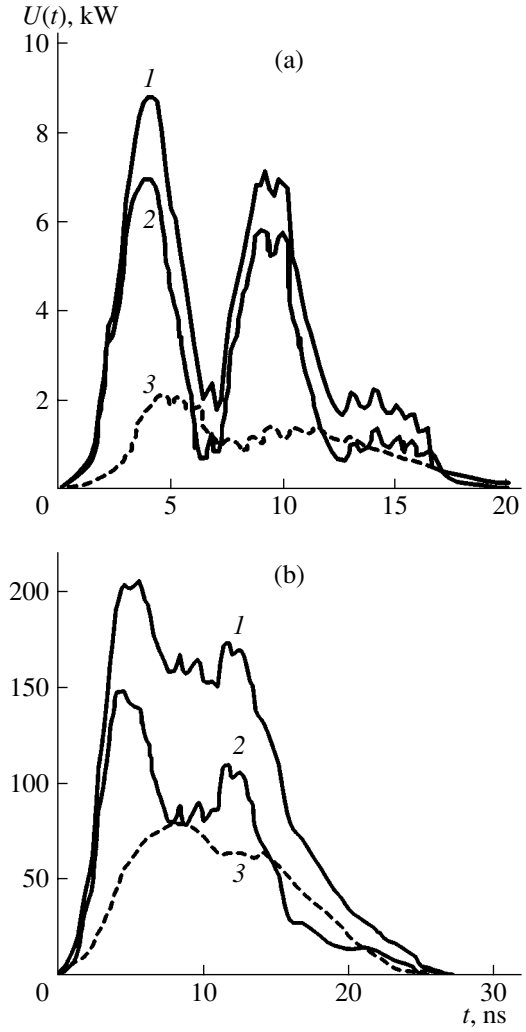

Fig. 3. (a) Pulses from the MO built around the LT-3Cu tube at the entrance to the amplifier (W_{in} = 0.7 W) and (b) the corresponding output pulses of the amplifier: (*1*) total power, (*2*) power at a wavelength of 0.51 μm, and (*3*) power at a wavelength of 0.578 μm.

Note that the value of τ_{inv} in expression (1) is to a great extent uncertain, since this quantity depends on the amplification dynamics and laser energy density in the active medium of self-terminating lasers. In addition, expressions (1) and (2) ignore an increase in the pulse duration at the exit from the amplifier. The superluminescence lifetime (35–40 ns for the system under study) may apparently be taken as the maximum value of τ_{inv}. For developed stimulated emission with an energy density higher by one order of magnitude, one should keep in mind more the pulse duration for a plane-resonator laser (25–30 ns for the given experimental conditions). Figure 4 supports the above statement. Specifically, substituting optimal delays $\tau_{del} \approx$ 8 ns (curve *1*) and $\tau_{del} \approx$ 14 ns (curve *3*) into expression (1), we obtain $\tau_{inv} \approx$ 26 and ≈36 ns, respectively. Estimation of the electromagnetic field energy density

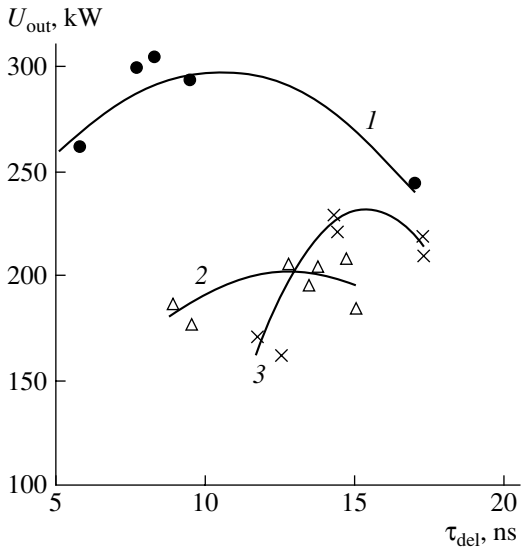

Fig. 4. Peak power of the amplified pulses vs. delay time τ_{del} at (*1*) $\tau_{0s} \approx 12.5$ ns and $U_{0s} = 5.7$ kW, (*2*) $\tau_{0s} \approx 17.5$ ns and $U_{0s} = 6$–9 kW, and (*3*) $\tau_{0s} \approx 17$ ns and $U_{0s} = 3$ kW [3].

averaged over the laser pulse duration yields 5 and ≈ 3.4 μJ/cm^3: i.e., the higher the peak power of the amplifier, the shorter the inversion lifetime. A more rigorous analysis of the multipass amplifier considered requires the self-consistent solution of the kinetic equations for populations, equation of the energy balance in a plasma, and transfer equations for amplified radiation.

CONCLUSIONS

Upgrading of a copper-vapor double-pass amplifier and the application of an MO pulse shorter than in the previous work [3] made it possible to raise the peak power of the output pulse to 305 kW. This value is 2.2 times higher than that of a single-pass amplifier with the mean output power (23–25 W), pump power, and lasing medium of the amplifiers being equal. The results obtained support the validity of the qualitative physical model that explains the method [1] of increasing the pulse amplitude without significantly changing the specific mean power. Note that single-pass amplifiers using MO pulses shorter than the inversion lifetime in the amplifier stage also offer a high output power. However, the mean power here decreases, because the inversion energy is utilized incompletely. In particular, using tubes with a volume two to four times greater, Evtushenko *et al.* [6] obtained a peak power of 600 kW at a specific mean power seven to eight times lower than the mean power in this work.

To clarify the prospects of our approach, additional calculations and experiments (in particular, with a larger number of passes in the amplifier stage) are needed. Such amplifiers would make it possible to effectively employ small and, hence, cheap lasing elements [4] with a mean radiation power of 10–20 W instead of expensive devices with a mean output of tens or hundreds of watts in technological equipment requiring high-peak-power radiation pulses.

ACKNOWLEDGMENTS

We are grateful to N.A. Lyabin, A.D. Chursin, and S.A. Ugol'nikov for the assistance in fabricating the developmental version of a copper-vapor laser amplifier.

REFERENCES

1. V. T. Karpukhin and M. M. Malikov, RF Inventor's Certificate No. 2,197,042 (2001), Byull. Izobret., No. 2 (2003).
2. V. T. Karpukhin and M. M. Malikov, RF Inventor's Certificate No. 19,612, Byull. Izobret., No. 25 (2001).
3. V. T. Karpukhin and M. M. Malikov, Kvantovaya Élektron. (Moscow) **33**, 411 (2003).
4. N. A. Lyabin, A. D. Chursin, S. A. Ugol'nikov, *et al.*, Kvantovaya Élektron. (Moscow) **31**, 191 (2001).
5. V. T. Karpukhin, Yu. B. Konev, and M. M. Malikov, Izv. Ross. Akad. Nauk, Ser. Fiz. **66**, 934 (2002).
6. G. S. Evtushenko, A. E. Kirillov, V. L. Kruglyakov, *et al.*, Zh. Prikl. Spektrosk. **49**, 745 (1988).

Translated by A. Chikishev

Technical Physics, Vol. 50, No. 10, 2005, pp. 1323–1327. Translated from Zhurnal Tekhnicheskoĭ Fiziki, Vol. 75, No. 10, 2005, pp. 73–77.

OPTICS, QUANTUM ELECTRONICS

Generation of Fast Protons in the Interaction of Relativistic Laser Pulses with a Thin Foil

I. N. Kosarev

Russian Federal Nuclear Center All-Russia Research Institute of Experimental Physics, Sarov, Nizhegorodsk Oblast, 607190 Russia

e-mail: kosarev@vniief.ru

Received October 19, 2004

Abstract—The interaction of a powerful femtosecond laser pulse with a thin aluminum foil containing a hydrogen admixture is investigated. The calculations in question are performed for actual ion charges and at a solid-state density. The investigation is carried out with the aid of the previously developed theory of interaction of powerful short laser pulses with plasmas. This theory is based on constructing propagators for plasma-particle distributions. The calculated fast-proton distributions are in good agreement with experimental data. © *2005 Pleiades Publishing, Inc.*

INTRODUCTION

Present-day lasers of power in the multitera- and petawatt ranges make it possible to obtain high-intensity femtosecond pulses (see, for example, [1]). In such cases, the intensity may range between 10^{18} and 10^{20} W/cm^2 at the focus of a laser pulse. At intensities as high as this, the oscillatory motion of an electron in the field of a wave becomes relativistic (at a wavelength of about 1 μm). An intensity of 8×10^{18} W/cm^2 can also be obtained by means of a portable laser as well [2]. A great number of experiments [3–16] and a numerical simulation by the "particles in a cell" method [17–27] showed that the interaction of such intense laser pulses with a thin target (or a thick target in the presence of a weak prepulse) may produce intense fast-proton beams, which can be used for a fast ignition of a thermonuclear target [28, 29], diagnostics of fast processes in plasmas [30], and isochoric heating of a solid body with the aim of obtaining high pressures [31], as well as in neutron sources [3].

The mechanism of proton acceleration in the interaction of an intense femtosecond laser pulse with a thin target is as follows. The ponderomotive force accelerates electrons, with the result that there arises charge separation. This generates an ambipolar electric field, and it is this field that accelerates ions in the target plasma. An additional acceleration may be due to the Coulomb explosion of ions [17] and a vortex electric field [18]. There is also a stochastic mechanism of electron acceleration [32], in which case the conditions for proton acceleration are optimal [26]. Ions may be accelerated both near the forward boundary of a thin target [3, 14, 20, 21] and near its rear boundary [6, 8, 13, 17, 18, 22]. In the calculations reported in [27], the accelerating ambipolar field was distributed over a wide region. In the case where a laser pulse is incident to a thick target, ions are also accelerated owing to the emergence of an ambipolar field [1]. It should be emphasized that the energy distribution of accelerated ions depends on the distribution of displaced electrons. For the case of a free plasma expansion into a vacuum, this was proven in [33].

BASIC RELATIONS

Plasma dynamics is studied here within the theory developed previously in [34] to describe the interaction of powerful short laser pulses with plasma. This theory is based on constructing propagators for plasma-particle distributions at times shorter than the relaxation time for these distributions. In the approximation of a self-consistent field, the propagator for the density matrix (distribution function in the coordinate representation) describing particles of sort a has the form

$$K_a(2,1) = \left(\frac{m_a}{2\pi\hbar(t_2 - t_1)}\right)^3 \times \exp\left\{\frac{i}{\hbar}(S_0 + \Delta S_p) + \Delta S_{sl}\right\}, \quad (1)$$

where S_0 is the action functional for a particle in a laser field of linear polarization (which is typical of powerful lasers). In this functional, the nonuniformity of the field is taken into account parametrically; that is,

$$S_0 = \frac{m_a}{t_2 - t_1}(\mathbf{r}_2 - \mathbf{r}_1)(\Delta\mathbf{r}_2 - \Delta\mathbf{r}_1) - \frac{Z_a e}{\omega c(t_2 - t_1)}\int_{\varphi_1}^{\varphi_2}\mathbf{A}\,d\varphi$$

1063-7842/05/5010-1323$26.00 © 2005 Pleiades Publishing, Inc.

$$+\frac{Z_a e}{\omega c(t_2-t_1)}\frac{(\mathbf{r}_2-\mathbf{r}_1)}{(t_2-t_1)}\left(-\int\limits_{\varphi_1-\Delta\varphi_1}^{\varphi_1+\Delta\varphi_1}\mathbf{A}d\varphi+\int\limits_{\varphi_2-\Delta\varphi_2}^{\varphi_2+\Delta\varphi_2}\mathbf{A}d\varphi\right)$$
$$-\frac{Z_a^2e^2}{\omega^2 m_a(t_2-t_1)}\int\limits_{\varphi_1}^{\varphi_2}\mathbf{A}d\varphi\left(-\int\limits_{\varphi_1-\Delta\varphi_1}^{\varphi_1+\Delta\varphi_1}\mathbf{A}d\varphi+\int\limits_{\varphi_2-\Delta\varphi_2}^{\varphi_2+\Delta\varphi_2}\mathbf{A}d\varphi\right) \quad (2)$$
$$+\frac{Z_a^2e^2}{2\omega m_a c^2}\left(-\int\limits_{\varphi_1-\Delta\varphi_1}^{\varphi_1+\Delta\varphi_1}\mathbf{A}^2d\varphi+\int\limits_{\varphi_2-\Delta\varphi_2}^{\varphi_2+\Delta\varphi_2}\mathbf{A}^2d\varphi\right),$$

where $\mathbf{A} = \mathbf{A}_0(\mathbf{r}_\perp, \varphi/\omega)\sin\varphi$ is the vector potential of a laser field, with $\mathbf{r}_\perp \perp \mathbf{k}$, $\mathbf{k}$ being the wave vector; $\varphi_{1,2} = \omega t_{1,2} - \mathbf{k}\mathbf{r}_{1,2}$; $\Delta\varphi_{1,2} = -\mathbf{k}\Delta\mathbf{r}/2$; and ω is the laser-field frequency.

In Eq. (1), ΔS_p is the addition that the action functional develops under the effect of the ponderomotive forces that arise owing to the nonuniformity of the laser-field amplitude A_0. The ponderomotive forces were taken into account by perturbation theory, this being legitimate for rather short times within which the displacement of a particle is small in relation to the characteristic size of the nonuniformity of the laser-field amplitude A_0,

$$\Delta S_p = -\frac{Z_a^2e^2}{4m_a c^2}\nabla A_0^2\int\limits_{t_1}^{t_2}\Delta\mathbf{r}_a dt. \quad (3)$$

Here, $\Delta\mathbf{r}_a$ is the trajectory of a particle in a uniform laser field, the boundary conditions being $\Delta\mathbf{r}_a(t_1) = \Delta\mathbf{r}_1$ and $\Delta\mathbf{r}_a(t_2) = \Delta\mathbf{r}_2$. The contribution ΔS_{st} to the action from particle interaction is given by (this contribution is also calculated by perturbation theory)

$$\mathrm{Im}\{\Delta S_{st}\} = \pi\sum_b n_b\int d\mathbf{p}_b f_{1Z}(\mathbf{p}_b, t_1)vp$$
$$\times\int\limits_{t_1}^{t_2}dt\frac{Z_a(\mathbf{r}_1)e^2c^2}{\hbar}\frac{[\Delta\mathbf{r}_{a\perp\mathbf{v}_b}(t)]^2}{-\mathbf{v}_b\Delta\dot{\mathbf{r}}_a(t)}, \quad (4)$$
$$f_{1Z}(\mathbf{p}_b, t_1) = \int drf(\mathbf{r}, \mathbf{p}_b, t_1)Z_b(\mathbf{r});$$
$$\mathrm{Re}\{\Delta S_{st}\} = -\pi\sum_b n_b\int d\mathbf{p}_b f_{2Z}(\mathbf{p}_b, t_1)$$
$$\times\int\limits_{t_1}^{t_2}dt\frac{Z_a^2(\mathbf{r}_1)e^4}{\hbar\mathbf{v}_b}(\Delta\mathbf{r}_{a\perp\mathbf{v}_b}(t))^2, \quad (5)$$
$$f_{2Z}(\mathbf{p}_b, t_1) = \int d\mathbf{r}f(\mathbf{r}, \mathbf{p}_b, t_1)Z_a^2(\mathbf{r}).$$

Here, Z_b, $\mathbf{p}_b$, $\mathbf{v}_b$, and n_b are, respectively, the charge, momentum, velocity, and mean density of plasma particles of sort b. The density matrix $\rho(\mathbf{r} + \Delta\mathbf{r}/2, \mathbf{r} - \Delta\mathbf{r}/2)$ is related to the distribution function by the equation

$$f(\mathbf{r}, \mathbf{p}) = \frac{V}{(2\pi\hbar)^3}\int d\Delta\mathbf{r}\rho(\mathbf{r}, \Delta\mathbf{r})\exp\left(-i\frac{\Delta\mathbf{r}\cdot\mathbf{p}}{\hbar}\right),$$
$$\rho(\mathbf{r}, \Delta\mathbf{r}) = \frac{1}{V}\int d\mathbf{p}f(\mathbf{r}, \mathbf{p})\exp\left(i\frac{\Delta\mathbf{r}\cdot\mathbf{p}}{\hbar}\right), \quad (6)$$

where V is the plasma volume.

If the initial distributions of plasma particles are known, their evolution can be found by repeatedly applying the propagators given by Eqs. (1)–(5) according to the relation

$$\rho_a(\mathbf{r}_2, \Delta\mathbf{r}_2, t_2)$$
$$= \int d\mathbf{r}_1\int d\Delta\mathbf{r}_1 K_a(2, 1)\rho_a(\mathbf{r}_1, \Delta\mathbf{r}_1, t_1). \quad (7)$$

In order to study the generation of fast protons, it is necessary to consider particles of three sorts: electrons, target ions, and admixed hydrogen ions.

GENERATION OF FAST PROTONS UPON THE IRRADIATION OF A THIN ALUMINUM FOIL

Here, we consider the interaction of a linearly polarized laser pulse whose envelope is given by

$$A_{0x} = A_0\exp(-(t - z/c)^2/\tau^2)\exp(-(x^2 + y^2)/\sigma^2), \quad (8)$$

the z and x axes being aligned with, respectively, the wave vector of the laser pulse and the polarization axis. The parameters of the laser pulse are the following: $\tau = 20T$, $\sigma = 7\lambda$, and $\lambda = 0.8$ μm, where T and λ are the laser-pulse period and wavelength, respectively. The maximum intensity reaches the value of $I_0 = 10^{20}$ W/cm^2. The aluminum foil used is shown in Fig. 1. The angle α between the laser-radiation wave vector and the normal to the plane is 22°, as in the experiment reported in [13]. The foil thickness is 3 μm, the initial concentrations of electrons and Al^{+13} ions corresponding to a solid-state density. There are also admixed hydrogen ions.

By and large, the interaction process proceeds in just the same way as in a simulation by the "particles in a cell" method. The large ponderomotive force of a laser pulse expels electrons and accelerates them along the direction of its propagation, generating a strong separation of charges. The distributions of electrons in the (z, p_z) and (y, p_z) phase planes are shown in Figs. 2 and 3, respectively. These distributions are given for a time instant following the completion of laser-pulse interaction with the target. As can be seen from Figs. 2 and 3, the electrons are accelerated to relativistic energies in the direction of pulse propagation. Owing to the development of Weibel instability [35], an electron current is generated in the opposite direction. An averaged description (the characteristic scale is about the wave-

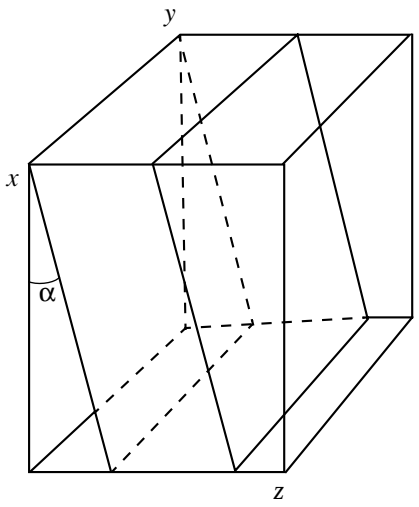

Fig. 1. Three-dimensional representation of a thin aluminum foil.

length) of this instability is given in Fig. 3. Usually, the Weibel instability develops to smaller scales [36].

The electron-density distribution at a time instant following the completion of laser-pulse interaction with the target is displayed in Fig. 4. One can see that there occurs electron detachment at the target center, the electron-density value in the detached parts remaining close to a solid-state value. In a simulation by the "particles in a cell" method, relativistic electrons form a dilute halo around the target (see, for example, [13, 21, 22]). However, a model initial electron concentration that is an order of magnitude lower than a solid-state value was taken in those studies.

The ambipolar electric field formed upon the separation of charges accelerates ions, predominantly admixed protons. The distribution of fast protons with respect to the momentum p_z is displayed in Fig. 5. In the case where the initial concentrations of aluminum ions and protons are equal to each other, the temperature of fast protons is T_{ph} = 4 MeV, while the total number of accelerated protons whose energy is above 1 MeV is approximately 3.5×10^{11} (the accuracy of the calculation is about 20%). These results agree with experimental data from [13], which indicate that T_{ph} = 3.2 ± 0.3 MeV and that the number of accelerated protons is 1.6×10^{11}. The total number of accelerated protons depends strongly on their initial relative concentration in the target, since, at their concentration of 3%, the number of accelerated protons falls down to 0.5×10^{10} (see Fig. 5). The source of the discrepancy between the numbers of accelerated protons is that the initial concentration of the protons in the target is unknown.

From Fig. 6, which shows the distribution of fast protons in the (z, p_z) phase plane, one can see that the bulk of the protons are accelerated in the region around z = 5–6λ, which is close to the z value at which the x = 0 plane intersects the rear boundary of the target. Therefore, the protons are accelerated predominantly in the vicinity of the rear boundary of the target, this being consistent with the results of the simulation performed in [13].

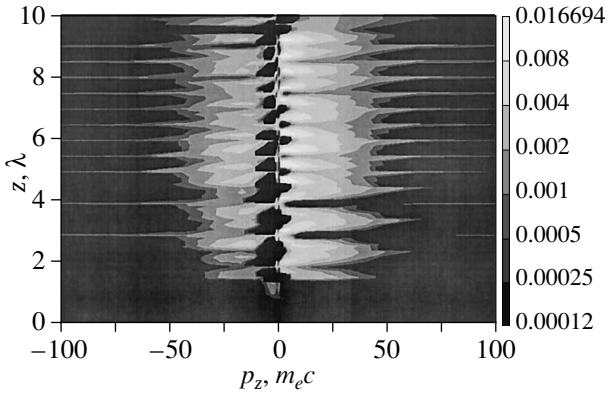

Fig. 2. Distribution of electrons in the (z, p_z) phase plane.

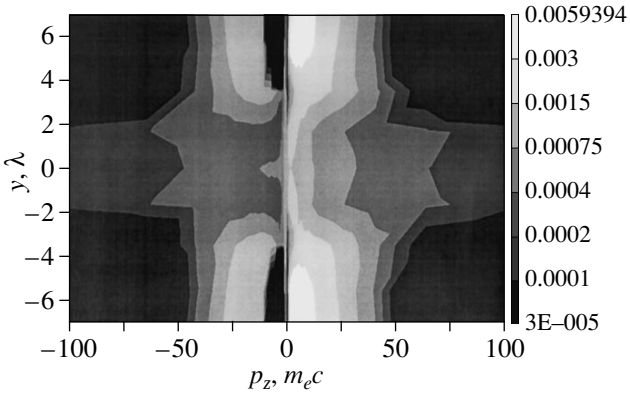

Fig. 3. Distribution of electrons in the (y, p_z) phase plane.

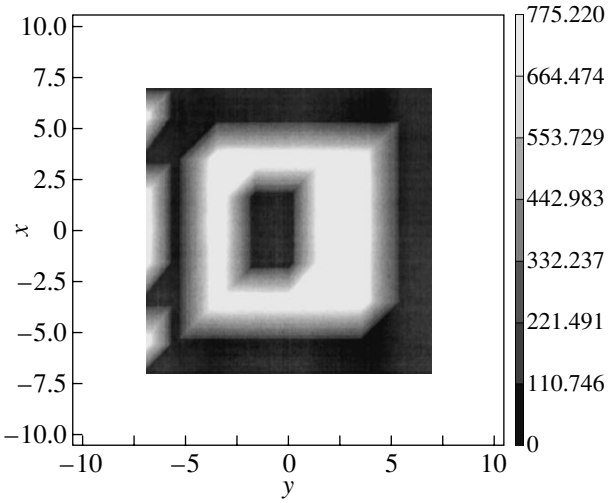

Fig. 4. Three-dimensional representation of the electron density in units of 10^{21} cm^{-3}.

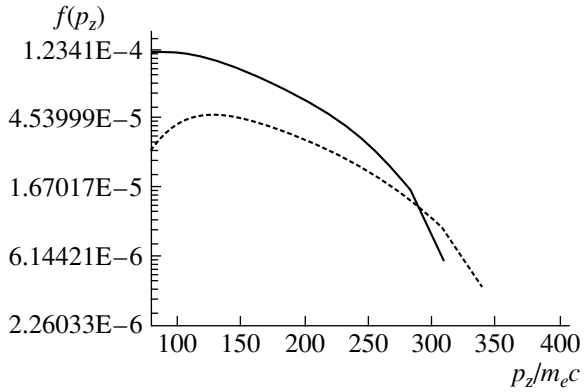

Fig. 5. Distribution of fast protons with respect to the momentum p_z at various concentrations of protons in the aluminum target: (solid curve) result for the proton concentration equal to the concentration of target ions and (dashed curve) result for the relative proton concentration of 3%.

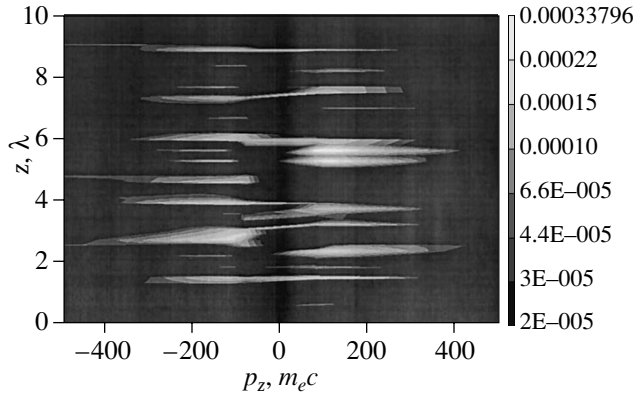

Fig. 6. Distribution of fast protons in (z, p_z) phase plane.

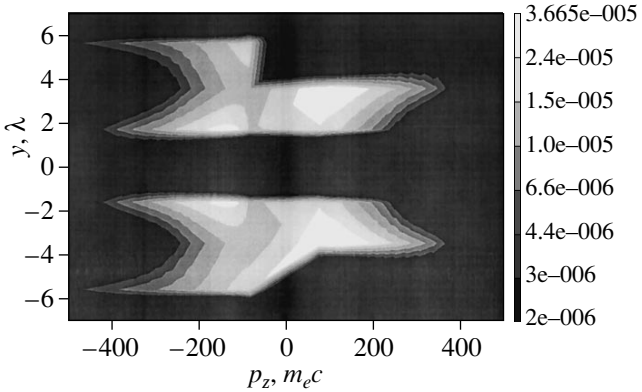

Fig. 7. Distribution of fast protons in the (y, p_z) plane.

The absence of proton acceleration in the target in the vicinity of $y = 0$ (see Fig. 7) is an interesting feature. In all probability, this is associated with the intense inverse current of relativistic electrons in the vicinity of this value of y (see Fig. 3). The calculations were performed by using a Pentium-4 PC.

CONCLUSIONS

The interaction of a femtosecond relativistic ($I = 10^{20}$ W/cm^2) laser pulse with an aluminum foil of thickness 3 μm has been studied on the basis of the previously developed theory of interaction of powerful short laser pulses. The new method used has made it possible to perform a simulation at realistic solid-state densities. By and large, the interaction process follows the same scenario as that observed in a simulation by the conventional "particles in a cell" method at densities much lower than a solid-state value. A strong ponderomotive force leads to the separation of charges and to the acceleration of protons by an ambipolar electric field. At initial solid-state concentrations, however, the electron cloud is ruptured without a sizable decrease in the concentration. The protons are accelerated predominantly in the vicinity of the rear boundary of the target. The momentum distribution of fast protons is of a Maxwellian character and is characterized by the temperature of $T_{ph} = 4$ MeV.

REFERENCES

1. P. G. Kryukov, Kvantovaya Élektron. (Moscow) **31**, 95 (2001).
2. I. Spenser, K. V. D. Ledingham, P. McCanny, *et al.*, Phys. Rev. E **67**, 046402 (2003).
3. A. Maksimchuk, S. Gu, K. Flippo, and D. Umstadler, Phys. Rev. Lett. **84**, 4108 (2000).
4. E. L. Clark, K. Krushelnik, M. Zepf, *et al.*, Phys. Rev. Lett. **85**, 1654 (2000).
5. K. Kruchelnick, E. L. Clark, M. Zepf, *et al.*, Phys. Plasmas **7**, 2055 (2000).
6. A. J. Mackinnon, M. Borghesi, S. Hatchett, *et al.*, Phys. Rev. Lett. **86**, 1769 (2001).
7. Y. Murakami, Y. Kitagawa, Y. Sentoku, *et al.*, Phys. Plasmas **8**, 4138 (2001).
8. S. P. Hatchett, C. G. Brown, T. E. Cowan, *et al.*, Phys. Plasmas **7**, 2076 (2000).
9. T. E. Cowan, M. Roth, J. Johnson, *et al.*, Nucl. Instrum. Methods Phys. Res. A **455**, 130 (2000).
10. M. Roth, T. E. Cowan, C. Brown, *et al.*, Nucl. Instrum. Methods Phys. Res. A **464**, 201 (2001).
11. A. A. Andreev, V. M. Komarov, A. V. Charukhchev, *et al.*, Zh. Éksp. Teor. Fiz. **121**, 266 (2002) [JETP **94**, 222 (2002)].
12. M. Hegelich, S. Karsch, G. Pretzler, *et al.*, Phys. Rev. Lett. **89**, 085002 (2002).
13. A. J. Mackinnon, Y. Sentoku, P. K. Patel, *et al.*, Phys. Rev. Lett. **88**, 215006 (2002).
14. M. Zepf, E. L. Clark, F. N. Beg, *et al.*, Phys. Rev. Lett. **90**, 064801 (2003).
15. H. Habara, R. Kodama, Y. Sentoku, *et al.*, Phys. Plasmas **10**, 3712 (2003).

16. M. Allen, Y. Sentoku, P. Audebert, *et al.*, Phys. Plasmas **10**, 3283 (2003).
17. Y. Setoku, T. V. Liseikina, T. Zh. Esirkepov, *et al.*, Phys. Rev. E **62**, 7271 (2000).
18. S. V. Bulanov, T. Zh. Esirkepov, F. Kalifano, *et al.*, Pis'ma Zh. Éksp. Teor. Fiz. **71**, 593 (2000) [JETP Lett. **71**, 407 (2000)].
19. Y. Ueshima, Y. Sentoku, and Y. Kishimoto, Nucl. Instrum. Methods Phys. Res. A **455**, 181 (2000).
20. W. S. Lawson, P. W. Rambo, and D. J. Larson, Phys. Plasmas **4**, 788 (1997).
21. C. S. Wilks, A. B. Langdon, T. E. Cowan, *et al.*, Phys. Plasmas **8**, 542 (2001).
22. A. Pukhov, Phys. Rev. Lett. **86**, 3562 (2001).
23. A. Zhidkov and M. Uesaka, Phys. Rev. Lett. **89**, 215002 (2002).
24. T. Zh. Esirkepov, S. V. Bulanov, K. Nishihara, *et al.*, Phys. Rev. Lett. **89**, 175003 (2002).
25. S. V. Bulanov, T. Zh. Esirkepov, F. F. Kamenets, *et al.*, Fiz. Plazmy **28**, 1059 (2002) [Plasma Phys. Rep. **28**, 975 (2002)].
26. Q. L. Dong, Z.-M. Sheng, M. y. Yu, and J. Zhang, Phys. Rev. E **68**, 026408 (2003).
27. S. V. Bulanov, T. Zh. Esirkepov, J. Koga, *et al.*, Fiz. Plazmy **30**, 21 (2004) [Plasma Phys. Rep. **30**, 18 (2004)].
28. M. Roth, T. E. Cowan, M. H. Key, *et al.*, Phys. Rev. Lett. **86**, 436 (2001).
29. V. Yu. Bychenkov, V. Rozmus, A. Maksimchuk, *et al.*, Fiz. Plazmy **27**, 1076 (2001) [Plasma Phys. Rep. **27**, 1017 (2001)].
30. M. Borghesi, S. Bulanov, D. H. Campbell, *et al.*, Phys. Rev. Lett. **88**, 135002 (2002).
31. P. K. Patel, A. J. MacKinnon, M. H. Key, *et al.*, Phys. Rev. Lett. **91**, 125004 (2003).
32. Z.-M. Sheng, K. Mita, Y. Sentoku, *et al.*, Phys. Rev. Lett. **88**, 055004 (2002).
33. V. F. Kovalev, V. Yu. Bychenkov, and V. T. Tikhonchuk, Pis'ma Zh. Éksp. Teor. Fiz. **74**, 12 (2001) [JETP Lett. **74**, 10 (2001)].
34. I. N. Kosarev, Zh. Tekh. Fiz. **75** (1), 32 (2005) [Tech. Phys. **50**, 30 (2005)].
35. E. S. Weibel, Phys. Rev. Lett. **2**, 83 (1959).
36. N. V. Elkina and V. D. Levchenko, Vopr. At. Nauki Tekh., No. 4, 124 (2003).

Translated by A. Isaakyan

Technical Physics, Vol. 50, No. 10, 2005, pp. 1328–1334. Translated from Zhurnal Tekhnicheskoĭ Fiziki, Vol. 75, No. 10, 2005, pp. 78–84.

OPTICS, QUANTUM ELECTRONICS

Gas Dynamics in Nuclear-Pumped Laser and Luminescent Cells with Buffer Volumes

A. A. Pikulev

All-Russia Research Institute of Experimental Physics, Russian Federal Research Center, Sarov, Nizhegorodsk Oblast, 607190 Russia

e-mail: pikulev@expd.vniief.ru

Received February 11, 2005

Abstract—A nonstationary gasdynamic model of sealed laser and luminescent cells pumped by uranium fission fragments is developed. This model extends the earlier 1D model of gas dynamics in cells of flat geometry to the case of cells with buffer volumes and allows analysis of gasdynamic processes for the energy deposition step distribution over the laser cell length. © *2005 Pleiades Publishing, Inc.*

INTRODUCTION

Gaining insight into thermal gasdynamic processes taking place in the active medium of gas lasers and luminescent cells pumped by uranium fission fragments [2] is a challenging problem. It covers such issues as the amount and distribution of energy deposition, as well as the velocity, density, temperature, and pressure of the active medium.

The effect of gasdynamic processes is the most pronounced when the energy delivered to the active medium is comparable to its initial inner energy. In this case, gas density redistribution is observed, which drastically changes the energy deposition distribution.

Among the available theoretical models of gas dynamics in nuclear-pumped sealed laser and luminescent cells, two merit attention: the model of low energy deposit [3] and the 1D model of gas dynamics in cells of flat geometry [1].

When the energy deposition is low, the gas flow is potential [3]; therefore, the former model allows 3D analysis of gas dynamics with regard to heat conduction. The essential disadvantage of this model is a severe limitation of the energy deposition.

In the latter model, the energy deposition is related to the Lagrangean coordinate of a fluid particle and a solution to the gasdynamic problem is given in quadratures [1], which is a serious advantage of this model. Its disadvantages are the unfeasibility of adequate inclusion of heat conduction and a low dimension of the problem. The latter factor makes it impossible to take into account the nonuniformity of the energy deposition distribution over the cell length (i.e., along the layers containing the fissioner).

Most experimental cells have spaces of relief: the so-called buffer volumes, where the pump intensity is zero [2, 4]. A specific feature of cells with buffer volumes is forcing the heated gas out of the active volume (where the energy deposition is other than zero) into a buffer during a pump pulse. Obviously, buffered cells may be viewed as the limiting case of cells with energy deposition nonuniform distribution.

This paper presents a gasdynamic model of buffered cells that extends the model developed in [1]. The new model assumes that acoustic pressure oscillations during a pump pulse are negligible, the active volume is bounded by plane-parallel plates with a fissioner, and the plate spacing is much shorter than the active volume length. The last-named assumption allows us to ignore edge effects at the boundary between the active volume and a buffer and, thereby, solve the gasdynamic problem by integrating an ordinary differential equation for the mean pressure to obtain a solution in the form of a quadrature in Lagrangean coordinates.

BASIC EQUATIONS

The set of gasdynamic equations for an ideal nonheat-conducting gas involves the continuity and energy equations (the Navier–Stokes equation in the model is lacking) [5],

$$\begin{cases} \dfrac{\partial \rho}{\partial t} + (\nabla \cdot \rho \mathbf{u}) = 0 \\ \dfrac{\partial}{\partial t}\left\{\dfrac{p}{\gamma - 1} + \dfrac{\rho \mathbf{u}^2}{2}\right\} + \operatorname{div}\left\{\dfrac{\gamma p}{\gamma - 1} + \dfrac{\rho \mathbf{u}^2}{2}\right\} = q, \end{cases} \quad (1)$$

where ρ, $\mathbf{u}$, and p are, respectively, the density, velocity, and pressure of the gas; γ is the adiabatic exponent; and q is the pump power.

It was shown [1] that, if pump pulse duration τ satisfies the inequality $\tau\nu \gg L$, where ν is the sound velocity and L is the cell length, the kinetic energy in the energy equation may be ignored (it is much lower than the potential energy). Below, we disregard the intensity

1063-7842/05/5010-1328$26.00

of pressure waves and assume that the pressure is uniform within the cell. Then, the energy equation simplifies to [3]

$$\frac{1}{\gamma-1}\frac{dP}{dt}+\frac{\gamma P}{\gamma-1}(\nabla\cdot\mathbf{u}) = q, \tag{2}$$

where P is the cell-volume-averaged pressure value.

Consider the idealized representation of a buffered cell (Fig. 1). The cell has the form of a rectangular parallelepiped consisting of active and buffer volumes. A layer of the fissioner is applied on a plate coinciding with the plane $z = 0$ (the fissioner can also be applied on a plate $z = h$) and is in contact with the active volume. The pump intensity is assumed to be uniform (edge effects near the fissioner are ignored), and so the pump intensity in the active volume depends only on coordinate z. In addition, we assume that the length of the active volume far exceeds the spacing between the plates with uranium fuel. This allows us to ignore edge effects at the boundary between the active volume and buffer.

It is easy to check that, with the conditions mentioned above satisfied, the density and gas velocity component w along the $0z$ axis in the active volume will depend on only time and coordinate z, while velocity components u and v along the $0x$ and $0y$ coordinates will be z-independent. This is because the pressure along the $0z$ axis levels off much more rapidly than along the $0x$ and $0y$ axes. Note that the above assumptions were used previously [3] to provide quasi-one-dimensional flow in flat cells.

Eventually, the continuity and energy equations take the form

$$\begin{cases}\dfrac{\partial\rho}{\partial t}+\dfrac{\partial\rho w}{\partial z}+\rho\left\{\dfrac{\partial u}{\partial x}+\dfrac{\partial v}{\partial y}\right\} = 0\\ \dfrac{1}{\gamma-1}\dfrac{dP}{dt}+\dfrac{\gamma P}{\gamma-1}(\nabla\cdot\mathbf{u}) = q.\end{cases} \tag{3}$$

Let us integrate the second equation in set (3) over cell volume V,

$$\frac{1}{\gamma-1}\frac{dP}{dt} = \beta\langle q\rangle,\quad \beta = \frac{V_0}{V}, \tag{4}$$

where V and V_0 are the total and active volumes of the cell, respectively, and $\langle q\rangle$ is the mean pump intensity in the active volume.

Below, the gasdynamic parameters will be considered only in the active volume and $\langle\ldots\rangle$ will mean averaging of a parameter over the active volume. Averaging set (3) over coordinate z and using the no-percolation conditions at the cell walls, we obtain

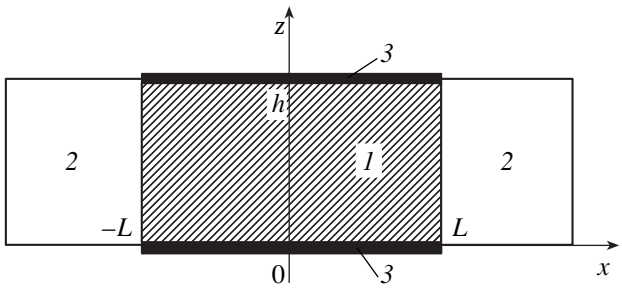

Fig. 1. Sealed cell with buffer volumes: (*1*) active volume, (*2*) buffer volume, and (*3*) plates with the fissioner.

$$\begin{aligned}&\frac{\partial u}{\partial x}+\frac{\partial v}{\partial y} = -\frac{d\ln\langle\rho\rangle}{dt},\\ &\frac{1}{\gamma-1}\frac{dP}{dt}+\frac{\gamma P}{\gamma-1}\left\{\frac{\partial u}{\partial x}+\frac{\partial v}{\partial y}\right\} = \langle q\rangle.\end{aligned} \tag{5}$$

Eliminating mean pump intensity $\langle q\rangle$ in the active volume, we find from (4) and (5) a relationship between the gas density and pressure in the active volume,

$$\langle\rho\rangle P^{\varphi} = \rho_0 P_0^{\varphi},\quad \varphi = \frac{1-\beta}{\gamma\beta}. \tag{6}$$

Formula (6), which was derived in [6], relates the pressure and mean density in the active volume, i.e., has the form of an equation of state with adiabatic exponent φ. In the absence of the buffer volume, $\varphi = 0$ and the mean density in the active volume is constant.

By way of deviation, let us consider the effect of heat conduction on equation of state (6). For a heat-conducting gas, the second equation in set (3) and Eq. (4) take the form

$$\begin{cases}\dfrac{1}{\gamma-1}\dfrac{dP}{dt} = \beta\langle q\rangle-\dfrac{J_S}{V}\\ \dfrac{1}{\gamma-1}\dfrac{dP}{dt}-\dfrac{\gamma P}{\gamma-1}\dfrac{d\ln\langle\rho\rangle}{dt} = \langle q\rangle-\dfrac{J_{S_0}}{V_0},\end{cases} \tag{7}$$

where

$$J_S = \iint_S\lambda\frac{\partial T}{\partial n}dS',\quad J_{S_0} = \iint_{S_0}\lambda\frac{\partial T}{\partial n}dS_0' \tag{8}$$

are the total heat flux toward the cell wall and the heat flux toward the cell wall in the active volume, respectively, and λ is the thermal conductivity.

After eliminating $\langle q\rangle$ from set (7) and integrating over time, we arrive at an equation of state of the gas in

the active volume with allowance for heat removal,

$$\langle \rho \rangle P^{\varphi} = \rho_0 P_0^{\varphi} \exp\left\{ \frac{\gamma - 1}{\gamma V_0} \int_0^t \frac{J_{S-S_0}}{P} dt' \right\}, \quad (9)$$

where $J_{S-S_0} = J_S - J_{S_0}$ is the heat flux toward the cell wall in the buffer volume.

It follows from formula (9) that the accuracy of equation of state (6) depends on the energy the heated gas transfers to the buffer volume walls. The effect of heat conduction on gas dynamics in sealed cells has been comprehensively considered elsewhere [3, 7] and here is omitted.

Let us turn to the expression for mean pump intensity $\langle q \rangle$ in the active volume. It was shown [8] that, if $\langle q \rangle$ is proportional to the energy deposited into the gas by fission fragments, the pump intensity due to a plane-parallel indefinitely long layer with a fissioner is given by the formula

$$q = \bar{\rho} \eta(t) q_0(\langle \bar{\rho} \rangle_z z), \quad \langle \bar{\rho} \rangle_z = \frac{1}{\rho_0 z} \int_0^z \rho(z', t) dz'. \quad (10)$$

Here, η is the relative shape of the pump pulse, $\bar{\rho} = \rho \rho_0^{-1}$ is the relative density of the gas, $\langle \bar{\rho} \rangle_z$ is the mean relative density within the segment $[0, z]$,

$$q_0 = \frac{E_0 L_0 \langle n \rangle}{L_{\text{gas}}} f, \quad (11)$$

is the pump power in the maximum of the reactor pulse for local density $\bar{\rho} = 1$, E_0 is the mean fission energy, L_0 is the range of a mean fission fragment in the fissioner layer, L_{gas} is the range of a fission fragment in the gas of density ρ_0, $\langle n \rangle$ is the number of fission events per unit volume in a unit of time averaged over the uranium layer surface area, and $f = f_0 - f_\delta$ is a dimensionless factor of energy deposition (hereafter, the energy factor).

If fission fragments slow down by a quadratic law and the gas density is uniform, we have the following expressions for the energy factor [8]:

$$\begin{cases} f(\zeta) = h(1-\zeta)\{1 + 2\zeta \ln \zeta - \zeta^2\}/2 \\ \zeta_0 = \dfrac{\delta_{\text{Al}}}{L_{\text{Al}}} + \langle \bar{\rho} \rangle_z \dfrac{z}{L_{\text{gas}}}, \quad \zeta_\delta = \zeta_0 + \dfrac{\delta}{L_0}, \end{cases} \quad (12)$$

where h is the Heaviside function; δ and δ_{Al} are the thicknesses of the uranium layer and protective aluminum film, respectively; and L_{Al} is the range of a fission fragment in aluminum.

As follows from formulas (11) and (12), the energy deposition depends only on relative fragment range ζ calculated in the 0z direction, which is normal to the fissioner layer surface, and has a constant value in the Lagrangean variables.

PASSAGE TO THE LAGRANGEAN VARIABLES

Consider now the gas flow in the active volume. Combining formulas (3) and (5), we obtain

$$\frac{\gamma P}{\gamma - 1} \frac{\partial w}{\partial z} = q - \langle q \rangle, \quad \frac{\partial u}{\partial x} + \frac{\partial v}{\partial y} = -\frac{d \ln \langle \bar{\rho} \rangle}{dt}, \quad (13)$$

where it is assumed that the pressure, gas mean density $\langle \bar{\rho} \rangle$, and mean pump intensity $\langle q \rangle$ in the active volume are known functions of time.

Set (13) will be solved in the Lagrangean variables [9]. The initial coordinates of a fluid particle are (x_0, y_0, z_0), and the relative density equals unity. The law of conservation of mass for the particle in the Lagrangean coordinates has the form $dV_0 = \bar{\rho}\, dV$, and the running coordinates of the particles can be found by integrating the equations

$$x = x_0 + \int_0^t u dt', \quad y = y_0 + \int_0^t v dt', \quad z = z_0 + \int_0^t w dt'. \quad (14)$$

Combining the second equation of set (13) and Eqs. (14), we get

$$\frac{\partial x}{\partial x_0} \frac{\partial y}{\partial y_0} = \frac{1}{\langle \bar{\rho} \rangle}. \quad (15)$$

Also,

$$\begin{cases} \bar{\rho} dz = \langle \bar{\rho} \rangle dz_0 \longrightarrow \langle \bar{\rho} \rangle_z z = \langle \bar{\rho} \rangle z_0 \\ \dfrac{1}{\bar{\rho}} = \dfrac{\partial V}{\partial V_0} = \dfrac{1}{\langle \bar{\rho} \rangle} \left\{ 1 + \displaystyle\int_0^t \frac{\partial w}{\partial z_0} dt' \right\}. \end{cases} \quad (16)$$

From (10) and the first equation of set (16), it follows that the pump intensity in the Lagrangean coordinates has the form

$$q = \bar{\rho} \eta(t) q_0(\langle \bar{\rho} \rangle z_0), \quad (17)$$

and the pump intensity averaged over the active volume is given by

$$\langle q \rangle = \langle \bar{\rho} \rangle \eta(t) \langle q_0(\langle \bar{\rho} \rangle) \rangle, \quad (18)$$

where $\langle q_0(\bar{p}) \rangle = \frac{1}{h} \int_0^h q_0(p z_0) dz_0$ is the active-volume-averaged pump intensity in the pulse maximum for the uniform distribution of density $\langle \bar{\rho} \rangle$.

Substituting relationships (6) and (18) into formula (4) yields a set of equations for gas mean density $\langle \bar{\rho} \rangle$

and pressure in the active volume,

$$\frac{1}{\gamma-1}\frac{dP}{dt} = \beta\langle\bar{\rho}\rangle\eta(t)\langle q_0(\langle\bar{\rho}\rangle)\rangle, \quad \langle\bar{\rho}\rangle P^{\varphi} = P_0^{\varphi}. \quad (19)$$

Equation (19) can be solved numerically, for example, by the Runge–Kutta method or by integration in quadratures using the method of successive approximations [10].

It should be noted that, if, during a pump pulse, the range of a mean fission fragment in the gas does not exceed spacing h between the plates with the fissioner, the mean pump intensity does not depend on the gas density, $\langle q_T\rangle = h(t)\langle q_0\rangle$. In this case, Eq. (19) is easy to integrate,

$$P = P_0 + \beta(\gamma-1)\langle q_0\rangle\int_0^t \eta(t')dt', \quad (20)$$

where P_0 is the initial pressure.

Formula (20) characterizes one of two limiting cases for the pressure shock (for details, see [6]) and coincides with the pressure equation derived in the low energy deposition approximation [3].

SOLUTION IN THE LAGRANGEAN VARIABLES

Consider the solution of set (13) where the gas pressure and mean density $\langle\bar{\rho}\rangle$ are solutions to set (19). Substituting (18) into the first equation of (13) in view of the fact that $\partial z_0/\partial z = \bar{\rho}/\langle\bar{\rho}\rangle$, which follows from the first equation of set (15), we get

$$\frac{\gamma P}{\gamma-1}\frac{\bar{\rho}}{\langle\bar{\rho}\rangle}\frac{\partial w}{\partial z_0} = \eta(t)\{\bar{\rho}q_0(\langle\bar{\rho}\rangle)z_0 - \langle\bar{\rho}\rangle\langle q_0(\langle\bar{\rho}\rangle)\rangle\}. \quad (21)$$

The solution to Eq. (21) under the initial condition $\rho(0, z_0) = \rho_0$ is

$$\left\{\int_0^t \frac{\partial w}{\partial z_0}dt = \int_0^t C(z_0, t')\left(\frac{P(t')}{P(t)}\right)^{1/\beta\gamma}dt' - \left\{1-\left(\frac{P_0}{P(t)}\right)^{1/\beta\gamma}\right\}, \quad (22)$$

where

$$C(z_0, t) = \frac{\gamma-1}{\gamma P(t)}\eta(t)\langle\bar{\rho}\rangle q_0(\langle\bar{\rho}\rangle z_0).$$

In (22), it is convenient to change integration over time to integration over pressure,

$$\int_0^t \frac{\partial w}{\partial z_0}dt = \frac{1}{\theta}\int_1^{\theta}\left\{\frac{q_0(\zeta^{\beta-1}z_0)}{\langle q_0(\zeta^{\beta-1})\rangle} - 1\right\}d\zeta, \quad (23)$$

where

$$\theta = \left\{\frac{P}{P_0}\right\}^{1/\beta\gamma}.$$

From the definition of θ, it follows that $\theta^{\beta-1} = \langle\bar{\rho}\rangle$. Since the time dependence of the pressure is known from the solution to Eq. (19), parameter θ is a given function of time and so the integral on the right of (23) can be taken numerically. From (14), (16), and (23), one can find the density and coordinate z of the fluid particle; namely,

$$\frac{1}{\bar{\rho}} = \frac{1}{\langle\bar{\rho}\rangle}\left\{1 + \int_0^t \frac{\partial w}{\partial z_0}dt'\right\},$$
$$z(z_0, t) = z_0 + \int_0^{z_0}\int_0^t \frac{\partial w}{\partial z_0'}dt'dz_0'. \quad (24)$$

To return to the Eulerian (fixed) coordinates, it is necessary to pass from Lagrangean coordinates (x_0, y_0, z_0, t) to running coordinates (x, y, z, t) in all the formulas derived. To do this requires inversion of set (14), which is a routine numerical procedure if the trajectory of the fluid particle is known.

Expression (23) is an extension of the formula derived in [1] for buffered cells. In the absence of the buffer, the integrand in formula (23) clearly does not depend on the variable of integration; therefore, for the density and Lagrangean coordinate of the particle, we obtain the following relationships:

$$\frac{1}{\bar{\rho}} = 1 + \frac{q_0 - \langle q_0\rangle}{\langle q_0\rangle}\left\{1 - \frac{1}{\theta}\right\},$$
$$z = z_0 + \left\{1 - \frac{1}{\theta}\right\}\int_0^{z_0}\frac{q_0 - \langle q_0\rangle}{\langle q_0\rangle}dz_0'. \quad (25)$$

Formulas (25) coincide with those derived in [1].

COMPUTATIONAL RESULTS

Of special interest in studying the gas dynamics and optics of laser and luminescent cells are optical inhomogeneities and the energy deposition distribution over the cell volume. Accordingly, one must know the density and energy factor. In the model considered, the energy factor is a function of the mean density and Lagrangean coordinate of the fluid particle,

$$f = f(\langle\bar{\rho}\rangle z_0), \quad (26)$$

as is easy to see from (11) and (17).

Using formulas (23) and (25), one can reduce expression (24) for the density in the Lagrangean coor-

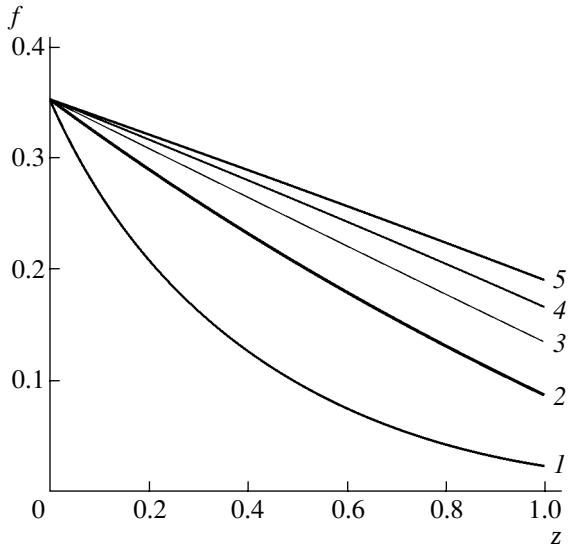

Fig. 2. Energy factor distribution along the 0*z* axis for β = 0.4 (numbers by the curves are the relative pressures).

dinates to the form

$$\frac{1}{\bar{\rho}} = \left\{\frac{P_0}{P}\right\}^{1/\gamma}\left\{\int_1^\theta \frac{f(\zeta^{\beta-1}z_0)}{\langle f(\zeta^{\beta-1})\rangle}d\zeta + 1\right\},$$
$$\langle f(p)\rangle = \frac{1}{h}\int_0^h f(pz_0)dz_0. \qquad (27)$$

As follows from (26) and (27), the energy factor and the density, when expressed in the Lagrangean coordinates, depend only on the gas pressure (and, certainly, on parameter β, adiabatic exponent γ, and the initial distribution of this factor, that is, on the quantities that remain constant during pumping). Since the displacement of fluid particles along the 0*z* axis also depends only on the pressure (see formula (24)), we find that the energy factor and the density depend only on the pressure in the Eulerian coordinates too. The pressure is a thermodynamic parameter that is the easiest to measure experimentally; therefore, the computational results for the density and energy factor are convenient to represent as parametric dependences of pressure. This is not pertinent to the gas velocity components, which, as follows from relationships (13) and (21), depend also on the shape and amplitude of the pump pulse.

By way of illustration, we give the results of model calculations for the pressure dependences of the gas density distribution at β = 1.0, 0.8, 0.6, and 0.4. It was assumed that the cell is filled with an inert gas (γ = 1.67) in which the range of a mean fission fragment is twice as large as the cell transverse dimension ($R_0 = 2h$). At h = 1 cm, this condition is met for helium at an initial pressure of 7 atm, neon (1.8 atm), argon (1.2 atm), and xenon (0.65 atm) [11]. It was also assumed that a 3-μm-thick 235-uranium layer applied on the lower plate (the plane z = 0) is covered by a protective aluminum film 0.038 μm thick (such parameters are typical of fuel elements used in nuclear-pumped laser and luminescent cells). The energy factor was calculated on the assumption that fission fragments slow down by a quadratic law (see formula (12)).

For the uniform gas density, the distribution of the energy factor is shown by curve *1* in Fig. 2. Figure 3 plots the mean density versus pressure in the active volume. The results obtained in the low energy deposition approximation are also shown for comparison. From

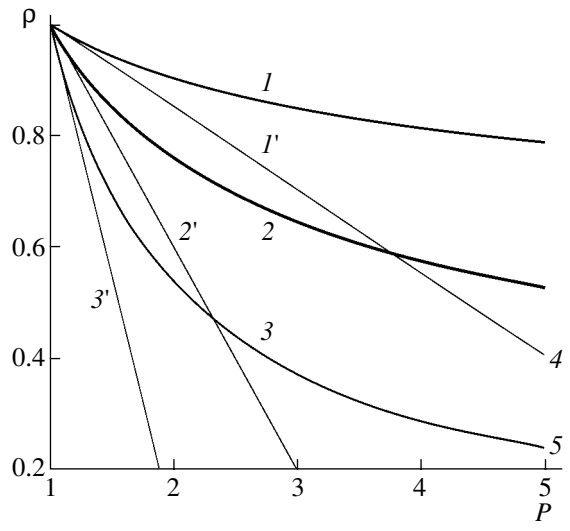

Fig. 3. Mean density in the active volume vs. pressure for β = (*1*, *1*') 0.8, (*2*, *2*') 0.6, and (*3*, *3*') 0.4. The primed curves are constructed in the low energy deposition approximation.

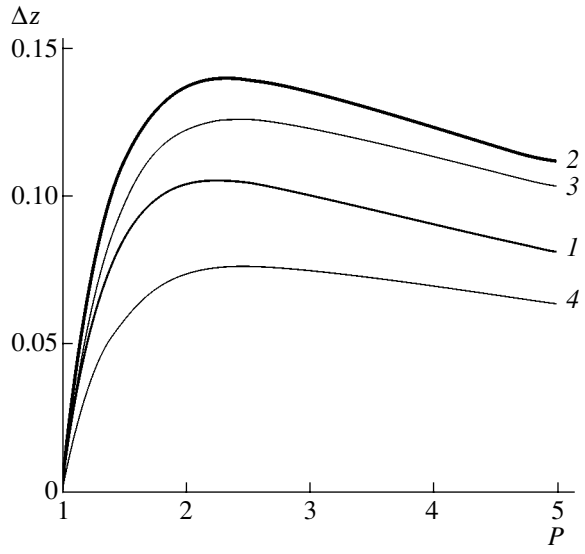

Fig. 4. Fluid particle displacement along the 0*z* axis vs. pressure for β = 0.4. z_0/h = (*1*) 0.2, (*2*) 0.4, (*3*) 0.6, and (*4*) 0.8.

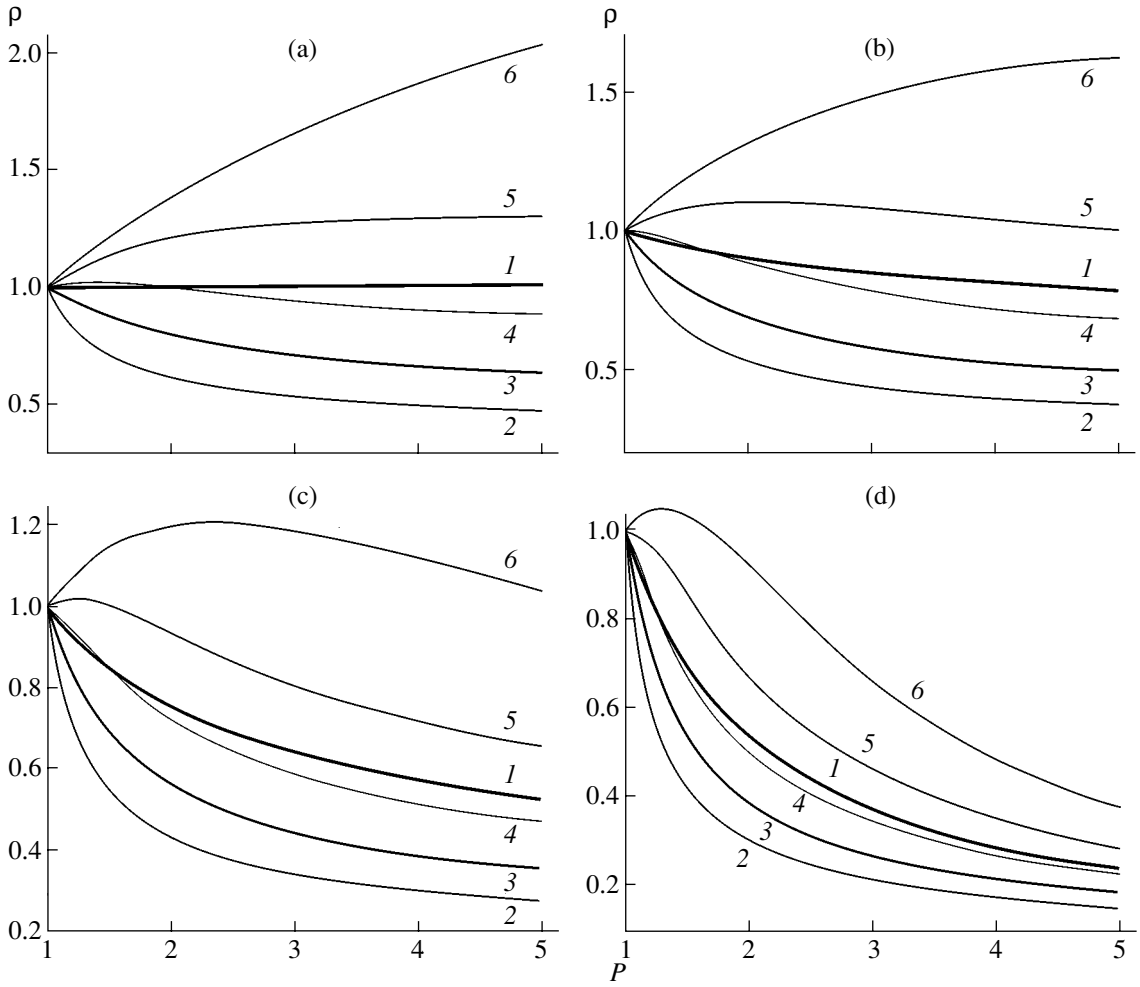

Fig. 5. Relative density of the gas vs. pressure for β = (a) 1.0, (b) 0.8, (c) 0.6, and (d) 0.4.Thick line *1* depicts the mean density in the active volume. *z*/*h* = (*2*) 0, (*3*) 0.25, (*4*) 0.5, (*5*) 0.75, and (*6*) 1.0.

Fig. 3, it follows that the presence of the buffer volume leads to a considerable decrease in the density in the active volume as the pressure grows. In particular, when the pressure grows fivefold, the mean density in the active volume drops roughly by 20% at β = 0.8, twofold at β = 0.6, and more than fourfold at β = 0.4.

Figure 4 shows the displacement of fluid particles in the 0*z* direction as a function of their initial pressure at β = 0.4. As the relative pressure rises up to 2.5, the particles rapidly move away from the plate with the fissioner. With a further increase in the pressure, the particles start moving in the opposite direction, since the energy factor distribution levels off with pressure (Fig. 2).

The relative density versus pressure in the active volume is demonstrated in Fig. 5 for β = 1.0, 0.8, 0.6, and 0.4. Thick curve *1* refers to the mean density in the active volume. It is seen that the interior of the cell may be subdivided into two regions in the 0*z* direction: that where the density is lower than the mean value and that where the density is higher than the mean. The boundary between these regions is roughly coincident with the middle of the cell ($z = 0.5$) and depends on the pressure only slightly (the slight dependence on the pressure is associated with the nonzero shift of the particles). In cells without the buffer volume, the particles stop as the pressure tends to infinity, as follows from (25), and the density distribution in the Lagrangean coordinates becomes inversely proportional to the energy factor distribution [1].

In the presence of the buffer volume, the density distribution is affected by two factors: the decrease in the mean density in the active volume as the gas flows into the buffer and the redistribution of the gas density in the transverse direction (i.e., toward the plates with the fissioner). In the lower (expansion) region of the cell, $0 < z < 0.5$, these processes add up and so the gas density decreases more rapidly than in the case β = 1. In the upper (compression) region, $0.5 < z < 1$, these processes compete: as the pressure grows, the gas first may contract (under certain conditions) and then necessarily expands (Fig. 5).

CONCLUSIONS

Thus, the given study shows that the presence of buffer volumes in nuclear-pumped laser and luminescent cells appreciably affects gas dynamics in the cells. The basic effect is the leakage of the gas from the active volume into the buffer during a pump pulse. Because of this, the mean gas density in the active volume decreases, the distribution of the energy deposition levels off, and its absolute value diminishes.

The model considered in this work is an extension of the 1D model of gas dynamics in cells of flat geometry [1] and applies at any energy deposited into the active volume. Therefore, the model may be helpful in estimating the thermal, gasdynamic, and optical parameters of laser and luminescent cells pumped by uranium fission fragments at a high value of energy deposition.

REFERENCES

1. J. R. Torczynski, J. Fluid Mech. **201**, 167 (1989).
2. A. A. Sinyanskii and S. P. Melnikov, Proc. SPIE **3686**, 43 (1998).
3. V. Yu. Mat'ev, V. V. Borovkov, and S. P. Mel'nikov, Zh. Tekh. Fiz. **71** (1), 79 (2001) [Tech. Phys. **46**, 76 (2001)].
4. V. V. Borovkov, B. V. Lazhintsev, S. P. Mel'nikov, *et al.*, Izv. Akad. Nauk SSSR, Ser. Fiz. **54**, 2009 (1990).
5. L. G. Loitsyanskiy, *Mechanics of Liquids and Gases* (Nauka, Moscow, 1987; Begell House, New York, 1995).
6. A. A. Pikulev, in *Proceedings of the 3rd International Conference "Problems of Nuclear-Pumped Lasers and Pulsed Reactors," Snezhinsk, 2003*, pp. 307–315.
7. V. Yu. Mat'e, in *Proceedings of the 2nd Conference on Nuclear-Excited Plasma and Problems of Nuclear-Pumped Lasers, Arzamas-16, 1995*, Vol. 1, pp. 410–420.
8. V. Yu. Mat'e, in *Proceedings of the Conference on Nuclear-Excited Plasma and Problems of Nuclear-Pumped Lasers, Obninsk, 1993*, Vol. 2, pp. 79–88.
9. L. D. Landau and E. M. Lifshitz, *Course of Theoretical Physics*, Vol. 6: *Fluid Mechanics* (Nauka, Moscow, 1988; Pergamon, New York, 1987).
10. A. A. Samarskiĭ and A. V. Gulin, *Numerical Methods* (Nauka, Moscow, 1989) [in Russian].
11. V. T. Kazazyan, B. A. Litvienko, L. P. Roginets, and I. A. Savushkin, *Use of Fission Fragment Kinetic Energy in Radiation Chemistry: Physical Grounds* (Nauka i Tekhnika, Minsk, 1972) [in Russian].

Translated by V. Isaakyan

Technical Physics, Vol. 50, No. 10, 2005, pp. 1335–1342. Translated from Zhurnal Tekhnicheskoĭ Fiziki, Vol. 75, No. 10, 2005, pp. 85–93.

RADIOPHYSICS

Microwave Up-Converter Based on a Nonlinear Ferroelectric Capacitor

T. B. Samoilova, A. B. Kozyrev, A. V. Tumarkin, A. M. Nikolaenko, and A. G. Gagarin

St. Petersburg State Electrotechnical University, ul. Prof. Popova 5, St. Petersburg, 197376 Russia

e-mail: mcl@eltech.ru

Received December 22, 2004

Abstract—An up-converter in which a capacitor with a nonlinear dielectric film is used as a nonlinear element is analyzed. Relationships between the conversion gain and capacitor parameters, such as loss tangent and the parameters of the *C–V* characteristic, which are of importance in converter design, are given. An up-converter using $Ba_xSr_{1-x}TiO_3$ capacitors is designed and tested. Experimental characteristics of this up-converter raising the frequency from 0.8 to 4.4 GHz are reported. © *2005 Pleiades Publishing, Inc.*

INTRODUCTION

Frequency converters are basic elements of transceiver systems, since heterodyne reception of signals remains the main approach. Development of frequency converters (along with tunable filters, delay lines, and phase shifters [1, 2]) where a thin-film ferroelectric capacitor in paraphase serves as a nonlinear element is among the mainstream areas in microwave application of ferroelectrics. This avenue of inquiry seems to be promising for tackling the challenging problem of designing microwave converters. The feasibility of such converters is apparent from a high-speed (10^{-11} s [3]) dielectric response to an external electric field and a relatively low loss tangent ($\tan\delta = 5 \times 10^{-3}$–$5 \times 10^{-2}$) of ferroelectric films in the paraelectric state at frequencies between 1 and 60 GHz [4], which is of special importance for the upper part of the microwave range. To date, little has been known about the performance of thin-film nonlinear $Ba_xSr_{1-x}TiO_3$ (BSTO) ferroelectrics in frequency converters. Works devoted to frequency conversion in coplanar waveguides made of strontium titanate and $(Ba,Sr)TiO_3$ solid solutions [5–7] have appeared only recently, and generation of harmonics and signals at combination frequencies in a cavity including a ferroelectric capacitor has been considered in [8]. However, reliable data indicating a great potential of using ferroelectrics in microwave converters are still lacking and ways of improving the performance of these devices are not quite clear.

In this work, we report theoretical results concerning optimal operating conditions and achievable parameters of ferroelectric frequency converters, as well as simulate and measure the characteristics of a converter designed for up-conversion from 0.8 to 4.4 GHz that employs thin-film BSTO capacitors.

1. ANALYSIS OF AN UP-CONVERTER WITH A NONLINEAR FERROELECTRIC CAPACITOR

A high-speed response of a thin-film paraelectric capacitor in paraphase to an applied voltage lets us assume that dynamic capacitance $C = dQ/dU$ responds to an instantaneous high-amplitude control microwave signal virtually inertialessly (the pump signal is $u_p = U_p\cos\omega_p t$) according to the small-signal dc *C–V* characteristic.

Experimental *C–V* characteristics of thin-film ferroelectric capacitors are usually described well by the expression [3]

$$C(U) = \frac{C(0)}{K}\left[1 + \frac{K-1}{1+\left(\frac{U}{U_0}\right)^2}\right], \qquad (1)$$

where $C(0)$ is the capacitance at $U = 0$, U_0 is a phenomenological parameter having the dimension of voltage, $K = C(0)/C(\infty)$ is the adjustability factor of the capacitor, and $C(\infty)$ is the high-voltage capacitance ($U \longrightarrow \infty$).

Generally, parameter U_0 depends on the structure and composition of the ferroelectric and is intimately related with the geometry of the capacitor.

The operation of the up-converter was analyzed under the assumption that only the input signal, the signal picked up from the load (output signal), and pump signals (at input frequency f_{in}, output frequency f_{out}, and pump frequency f_p, respectively) may be present in the converter's circuit (this condition is provided by inserting filters in corresponding circuits, see Fig. 1a) and that pump signal amplitude U_p far exceeds the amplitudes of the input, U_{in}, and output, U_{out}, signals. Under this assumption, the nonlinear capacitance may be

1063-7842/05/5010-1335$26.00

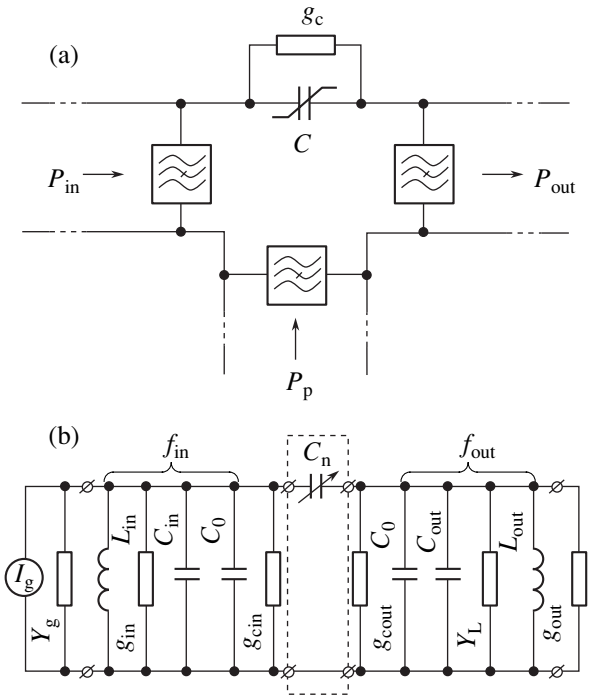

Fig. 1. (a) Basic diagram and (b) equivalent electrical circuit of the frequency converter.

viewed as a parametric capacitance varying in time with frequency f_p according to the *C–V* characteristic. Then, the instantaneous small-signal dynamic capacitance of a ferroelectric capacitor can be expanded into the Fourier series in pump harmonics,

$$C(t) = C_0 + 2\sum_{n=1}^{\infty} C_n \cos(n\omega_p t), \qquad (2)$$

where

$$C_0 = \frac{1}{2\pi}\int_{-\pi}^{\pi} C(t)\,d(\omega_p t)$$

is the constant component of the capacitance and

$$C_n = \frac{1}{2\pi}\int_{-\pi}^{\pi} C(t)\cos(n\omega_p t)\,d(\omega_p t)$$

is the amplitude of an *n*th harmonic of the capacitance at frequency nf_p (this frequency characterizes the conversion of the input signal with frequency f_{in} to the output signal with frequency $f_{out} = nf_p + f_{in}$).

Indeed, if weak input signal $u_{in} = U_{in}\cos(\omega_{in}t + \varphi_{in})$ is applied to the converter with its output short-circuited, the current passing through the capacitor,

$$i = \frac{d}{dt}[C(t)u_{in}(t)] = -\omega_{in}C_0U_{in}\sin(\omega_{in}t + \varphi_{in}) - U_{in}\sum_{n=1}^{\infty}(n\omega_p \pm \omega_{in})C_n\sin[(n\omega_p \pm \omega_{in})t \pm \varphi_{in}] \qquad (3)$$

contains a larger number of components at combination frequencies $(n\omega_p \pm \omega_{in})$, the conversion to which is characterized by coefficient C_n in expansion (2). In the presence of filters in the input and output circuits of the converter, only two terms of the Fourier series with coefficients C_0 and C_n should be taken into consideration. Usually, the conversions at the fundamental ($n = 1$) and the second ($n = 2$) harmonics of the pump signal are of interest. According to (3), for frequencies f_{in} and f_{out}, the constant component of the capacitance at the working point, C_0, as well as linear conductivities $g_{c,in}$ and $g_{c,out}$ characterizing losses in the nonlinear capacitor at frequencies f_{in} and f_{out}, respectively, can be assigned to the respective resonant circuits of the converter. Figure 1b shows the equivalent electrical circuit of the up-converter, where the dashed rectangle outlines the nonlinear two-port network responsible for conversion (the pump circuit in Fig. 1b is omitted). In Fig. 1b, Y_g and Y_L are the conductivities of the pump generator and load, respectively, and g_{in} and g_{out} are the conductivities characterizing losses due to linear inductances and capacitances in the input and output resonant circuits (L_{in}, L_{out}, C_{in}, and C_{out}).

Analytical expressions relating Fourier coefficients C_0 and C_n to the pump voltage and dc bias voltage across the plates of the capacitor, U_b, can be found from theoretical relationship (1) for the *C–V* characteristic. Substituting the instantaneous voltages specifying the working point of the nonlinear capacitor, $u(t) = U_b + U_p\cos(\omega_p t)$, into (1), we find the Fourier coefficient in the form

$$\begin{cases} C_0 = \dfrac{C(0)}{K}[1 + (K-1)F_0(U_b, U_p)], \\ F_0(U_b, U_p) = \dfrac{1}{2\pi}\displaystyle\int_{-\pi}^{\pi}\frac{d(\omega_p t)}{1 + \left(\dfrac{U_b}{U_0} + \dfrac{U_p}{U_0}\cos(\omega_p t)\right)^2}, \end{cases} \qquad (4a)$$

$$\begin{cases} C_n = \dfrac{C(0)}{K}[(K-1)F_n(U_b, U_p)], \\ F_n(U_b, U_p) = \dfrac{1}{2\pi}\displaystyle\int_{-\pi}^{\pi}\frac{\cos(n\omega_p t)d(\omega_p t)}{1 + \left(\dfrac{U_b}{U_0} + \dfrac{U_p}{U_0}\cos(\omega_p t)\right)^2}, \end{cases} \qquad (4b)$$

where F_0 and F_n are dimensionless functions depending on the pump voltage amplitude and dc bias voltage.

Clearly, the higher the absolute value of F_n, the more efficient the conversion. Figure 2 plots functions F_0, F_1, and F_2 versus normalized pump voltage U_p/U_0 with the bias voltage taken as a parameter. It is seen that conversion at the second-harmonic frequency of the pump signal ($f_{out} = 2f_p + f_{in}$) is the most efficient in the absence of the dc bias ($U_b = 0$) at $U_p \cong 2U_0$. In this case, $F_0 \approx 0.45$ and $|F_2| \approx 0.18$. Conversion at the fundamental frequency of the pump signal ($f_{out} = f_p + f_{in}$) is the most efficient at $U_b = (1–3)U_0$ and $U_p = (1–3)U_0$, respectively. In particular, for $U_b = U_p = U_0$, $F_0 \approx 0.55$ and $|F_1| \approx 0.22$.

Conversion gain $G = P_{out}/P_{in}$ (where P_{out} and P_{in} are, respectively, the powers of the output and input signals) is maximal when the nonlinear two-port network is matched to external circuits. For the circuit depicted in Fig. 1b, the expression for the maximal conversion gain has the form

$$\frac{G_{opt}}{G_{MR}} = \frac{\omega_{out}\omega_{in}C_n^2}{(g_{cout}+g_{out})(g_{cin}+g_{in})\left(1+\sqrt{1+\dfrac{\omega_{in}\omega_{out}C_n^2}{(g_{cout}+g_{out})(g_{cin}+g_{in})}}\right)^2} \quad (5)$$

at optimal conductivities of the pump generator, Y_g, and load, Y_L, defined as

$$\left.\begin{aligned} Y_{g,\,opt} &= (g_{cin}+g_{in})\sqrt{1+\frac{\omega_{in}\omega_{out}C_n^2}{(g_{cin}+g_{in})(g_{cout}+g_{out})}} \\ Y_{L,\,opt} &= (g_{cout}+g_{out})\sqrt{1+\frac{\omega_{in}\omega_{out}C_n^2}{(g_{cin}+g_{in})(g_{cout}+g_{out})}}, \end{aligned}\right\} \quad (6)$$

where $G_{MR} = \omega_{out}/\omega_{in}$ is the maximal conversion gain corresponding to a lossless nonlinear-reactance converter (as follows from the Manley–Rowe relationships [9]).

Let us take into account that

$$\left.\begin{aligned} g_{cout} &= \omega_{out}C_0\tan\delta_{out}, \\ g_{out} &= \frac{\omega_{out}(C_0+C_{out})}{Q_{out}}, \quad \xi_{out} = \frac{C_0}{C_0+C_{out}}, \\ g_{cin} &= \omega_{in}C_0\tan\delta_{in}, \\ g_{in} &= \frac{\omega_{in}(C_0+C_{in})}{q_{in}}, \quad \xi_{in} = \frac{C_0}{C_0+C_{in}} \end{aligned}\right\} \quad (7)$$

and introduce the notation

$$\left.\begin{aligned} m &= \frac{C_n}{C_0} = \frac{(K-1)F_n}{1+(K-1)F_0} \\ b &= \tan\delta_{in}\tan\delta_{out}\left(1+\frac{1}{\xi_{in}Q_{in}\tan\delta_{in}}\right)\left(1+\frac{1}{\xi_{out}Q_{out}\tan\delta_{out}}\right), \end{aligned}\right\} \quad (8)$$

where $\tan\delta_{in}$ and $\tan\delta_{out}$ are the loss tangents of the ferroelectric capacitor at the input, f_{in}, and output, f_{out}, frequencies, respectively; Q_{in} and Q_{out} are, respectively, the quality factors of the input and output circuits of the converter without the nonlinear capacitor; and ξ_{in} and ξ_{out} are the coefficients of insertion of the nonlinear capacitor into the input and output resonant circuits, respectively, which are defined as the energy stored in the capacitor divided by the total energy stored in the resonant circuit.

In view of the aforesaid, relationships (5) and (6) can be recast as

$$\left.\begin{aligned} \frac{G_{opt}}{G_{MR}} &= \frac{m^2}{b\left(1+\sqrt{1+\dfrac{m^2}{b}}\right)^2} \\ (Y_{in}Y_L)_{opt} &= \omega_{in}\omega_{out}C_0^2(m^2+b). \end{aligned}\right\} \quad (9)$$

The depth of modulation of the capacitance, m, at frequency nf_p depends on only adjustability factor K and control voltages U_p and U_b. For values of K typical of standard ferroelectric capacitors, K = 1.5–3.0, and

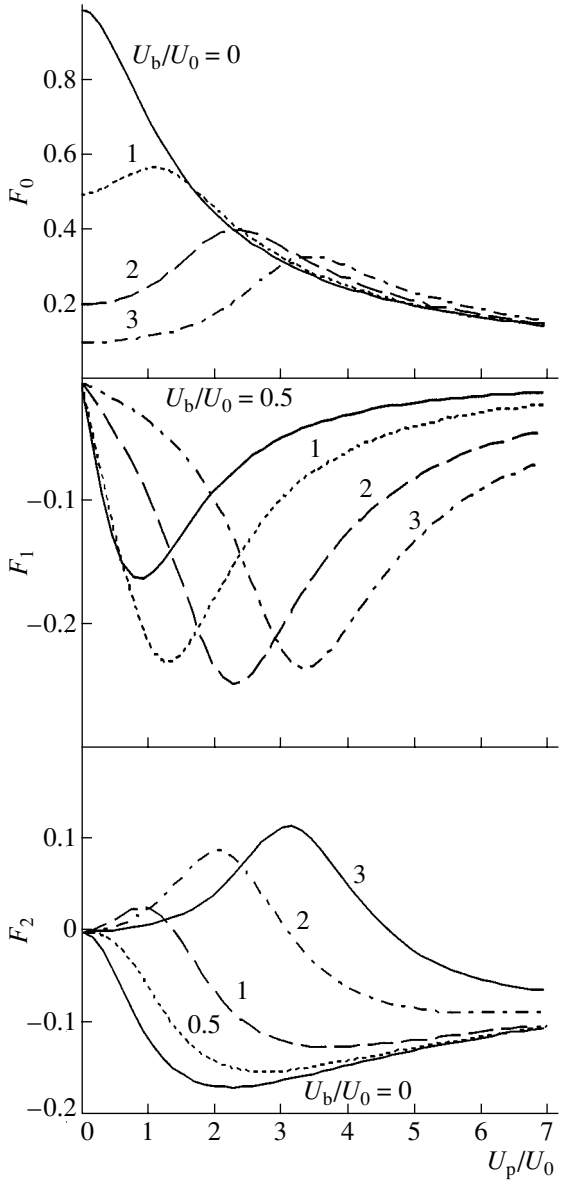

Fig. 2. Functions F_0, F_1, and F_2 vs. pump voltage amplitude U_p across the nonlinear capacitor with bias voltage U_b used as a parameter. The values of U_b and U_p are normalized to parameter U_0 of the *C–V* characteristic.

the values of F_0 and F_n mentioned above, m falls into the range 0.07–0.70 at $n = 1$ and 2. Quantity b characterizes conversion losses due to losses in the ferroelectric capacitor and those in the resonant circuits. If $(K - 1)F_0 \gg 1$, the adjustability factor has a negligible influence on the conversion efficiency. For the inverse inequality, an increase in the adjustability of the capacitor may partially compensate for losses in the converter. Below, we will consider conversion only at the fundamental pump frequency ($n = 1$, $f_{out} = f_{in} + f_p$).

Figures 3 and 4 plot optimal conversion gain G_{opt}/G_{MR} and the product of the optimal conductivities of the pump and load, $(Y_gY_L)_{opt}$, versus adjustability fac-

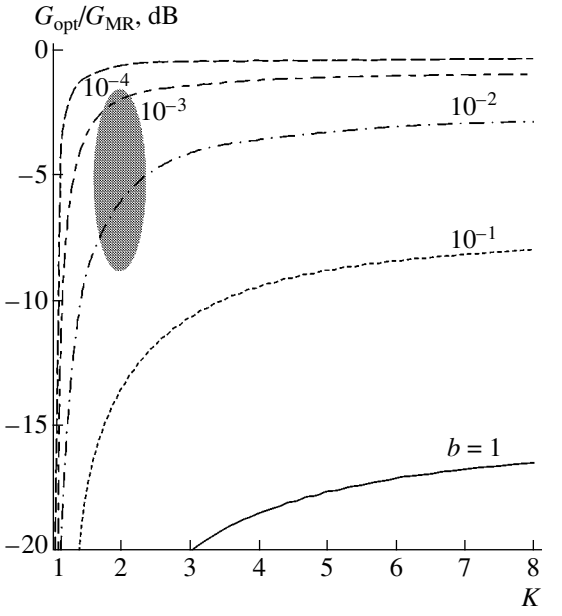

Fig. 3. Optimal conversion gain G_{opt} vs. adjustability factor K of the nonlinear capacitor at different b for conversion at the fundamental frequency ($n = 1$) of the pump ($U_b = U_p = U_0$). The conversion gain is normalized to the gain of a lossless converter. The range of values expected in practice is darkened.

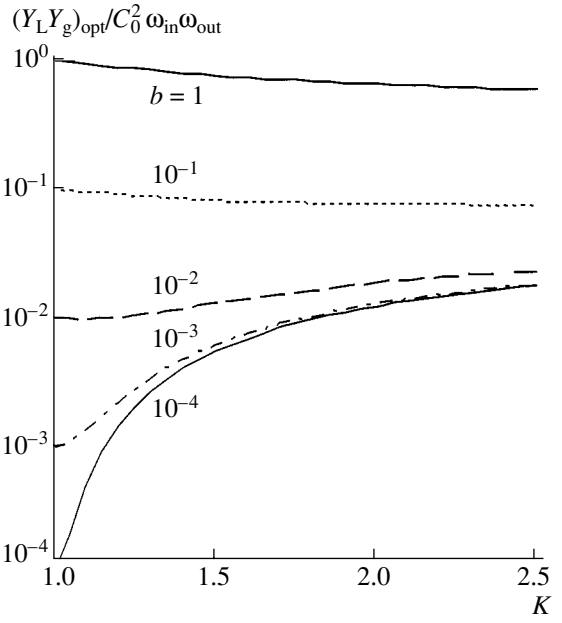

Fig. 4. Product $(Y_gY_L)_{opt}$ of the optimal conductivities of the pump signal generator and load vs. adjustability of the nonlinear capacitor at different b for conversion at the fundamental frequency of the pump ($U_b = U_p = U_0$). The values of $(Y_gY_L)_{opt}$ are normalized to the product of the input and output frequencies and capacitance of the capacitor squared at $U_p = 0$.

tor K of the ferroelectric capacitor for different b at $U_b = U_p = U_0$. Product $(Y_g Y_L)_{opt}$ is normalized to the product of frequencies ω_{in} and ω_{out} and the capacitance of the ferroelectric capacitor squared in the absence of the pump signal. With such plots, the converter can be designed for any frequency. For example, it follows from Fig. 3 that, at $b \le 10^{-4}$, there is no need to use capacitors with K higher than two, since the maximum conversion gain changes by no more than 1 dB at such b, whereas, at $b = 10^{-2}$, an increase in K from 2 to 8 raises conversion gain G_{opt} by 3 dB.

In today's microstrip resonant circuits, quality factors Q and insertion coefficients ξ are typically 10^2 and 0.1–0.3, respectively, at frequencies on the order of 10 GHz. In resonant cavities, Q reaches several thousand at the same frequencies, while the coefficient of insertion of a ferroelectric capacitor into a cavity is low, usually $\xi \sim 10^{-2}$. Taking into account that $\tan\delta$ in ferroelectric capacitors varies between 5×10^{-3} and 5×10^{-2} in the frequency interval 1–60 GHz, one can assume that losses due to the linear elements in the converter's circuit prevail. Then, values of $b \cong (\xi_{in}\xi_{out}Q_{in}Q_{out})^{-1} = 10^{-2}$–$10^{-3}$ apply to both microstrip resonant lines and resonant cavities. Consequently, conversion gain G_{opt} is below the Manley–Rowe value by 2.5–8.0 dB at K = 1.5–2.0 (in Fig. 3, the range of values expected in practice is hatched).

As follows from Fig. 2 and expression (4), at $U_b = U_0$, coefficient C_n reaches a maximum when the pump voltage amplitude approaches U_0. This circumstance specifies a necessary level of pump power P_p. If the converter is matched to the pump circuit at frequency f_p, the power delivered by the pump can be written as

$$P_p = \frac{1}{2}U_p^2(g_p + g_{c,p}),$$

where g_p and $g_{c,p}$ characterize losses due to the linear elements in the pump resonant circuit and nonlinear capacitor at frequency f_p.

Taking into account that $U_p = U_0$ and relationships similar to (7), the pump power providing a maximal conversion gain takes the form

$$P_p = \frac{1}{2}\omega_p C_0 U_0^2 \tan\delta_p\left(1 + \frac{1}{\xi_p Q_p \tan\delta_p}\right), \qquad (10)$$

where Q_p, ξ_p, and $\tan\delta_p$ are, respectively, the quality factor of the pump resonant circuit, coefficient of insertion of nonlinear capacitor in it, and $\tan\delta$ of the capacitor at frequency f_p.

Expression (10) implies that the pump power depends on the parameters of the ferroelectric capacitor (C_0, U_0, and $\tan\delta$) and efficiency of its insertion into the converter's circuit. The pump power dissipated in the active region of the ferroelectric capacitor, $P_{dis} = 0.5 U_p^2 \omega_p C_0 \tan\delta_p$, may cause overheating of the ferroelectric film. The amount of overheating depends on the capacitor's design and to a large extent on parameter U_0. This fact should be taken into account in designing the converters.

From relationship (9) and the run of the normalized conversion gain and external circuit conductivities (Figs. 3 and 4), one can easily estimate the parameters of ferroelectric frequency converters by taking small-signal C–V curves and measuring the loss tangent of a ferroelectric capacitor, the parameters of which (K, U_0, and $\tan\delta$) may be varied (according to the thickness, microstructure, and composition of compound oxide thin-film ferroelectrics) during fabrication of the capacitive structure.

2. UP-CONVERTER DESIGN AND SIMULATION OF ITS CHARACTERISTICS

As nonlinear elements of the converter, we used planar and parallel-plate thin-film BSTO capacitors. Compared with the planar design, parallel-plate capacitors allow one to reduce the capacitance-controlling voltage with ferroelectric films being the same. This fact is of crucial importance for selecting the pump power. The design of the capacitors is schematically shown in the

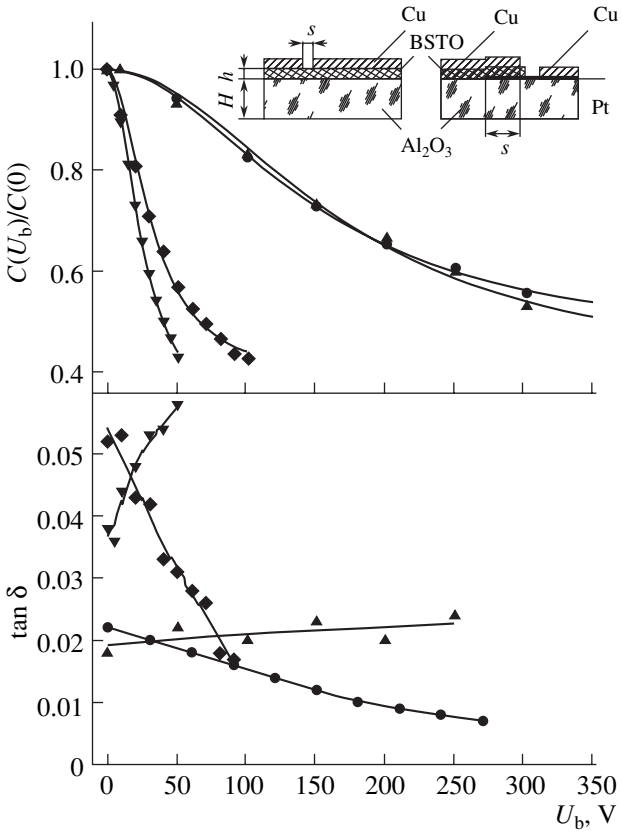

Fig. 5. Capacitance and $\tan\delta$ vs. dc bias voltage at a frequency of 3 GHz for thin-film BSTO capacitors (▲) 1, (●) 2, (◆) 3, and (▼) 4. The inset shows the cross-sectional view of (1–3) planar and (4) parallel-plate capacitors.

Parameters of the $Ba_xSr_{1-x}TiO_3$ capacitors

Capacitor no.	Structure of film	x	h, μm	s, μm	U_0, V	K
1	Ceramic	0.6	8.0	20	150	2.2
2	Polycrystalline	0.3	0.5	5	165	2.5
3	»	0.5	0.5	5	27	2.8
4	»	0.3	0.8	30	25	3.4

inset to Fig. 5. They were formed on a 0.5 × 1.5 × 0.5-mm Polikor (alumina-based ceramics) substrate, and a BSTO film was applied by magnetron sputtering. The length, *t*, and width, *s*, of the gap in the planar capacitors and the electrode surface area, $s \times s$, in the parallel-plate capacitors provided the same rated capacitances (≈6 pF) of the capacitors used in the converters.

Prior to implementing the converter, we took *C–V* curves from and measured tanδ in a large number of capacitors with different geometries where both polycrystalline and ceramic $Ba_xSr_{1-x}TiO_3$ films of different composition *x* and thickness *h* were used. The table lists geometric parameters *h* and *s* of (*1–3*) planar and (*4*) parallel-plate capacitors, composition *x* of the BSTO films, and parameters *K* and U_0 appearing in expression (1) for the *C–V* characteristic of a ferroelectric capacitor.

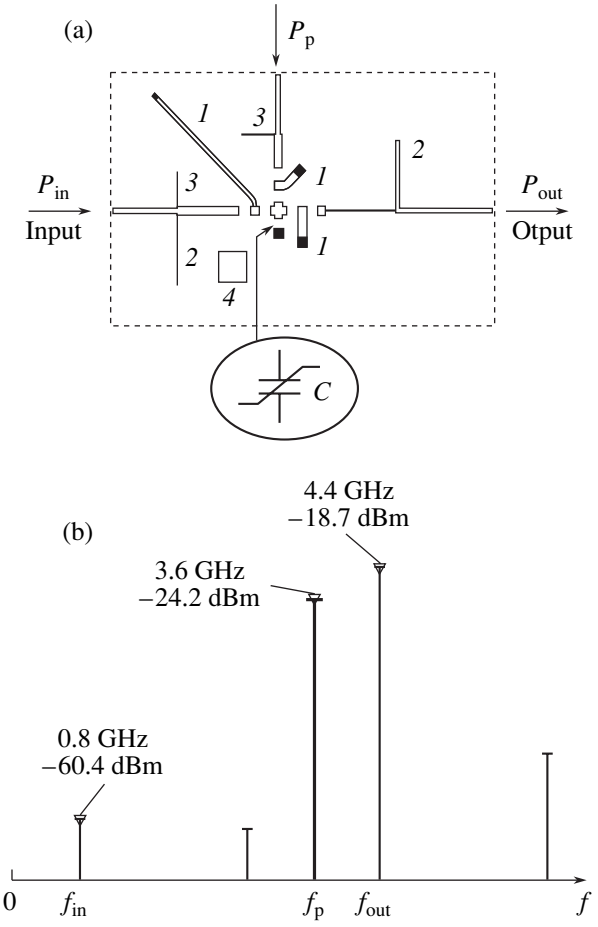

Fig. 6. (a) Layout of the frequency converter and (b) output signal spectrum of the optimized converter for P_p = +30 dBm, P_{in} = –20 dBm, and U_b = 27 V. (*1*) Closed stubs; (*2*, *3*) open stubs serving as rejection filters for signals at frequencies f_p and $2f_p$, respectively; and (*4*) contact pad used to apply the bias voltage to the nonlinear capacitor.

The small-signal capacitance and tanδ of the capacitors as functions of dc bias U_b that were measured at a frequency of 3 GHz are shown in Fig. 5. Two sets of capacitors the *C–V* curves of which differ markedly in parameter U_0 can be distinguished. High U_0 (≈150 V) is observed for planar capacitors based on thick ceramic films with $x = 0.6$ (capacitor *1*) and thin polycrystalline films with a small barium content ($x = 0.3$, capacitor *2*). For planar capacitor *3* ($x = 0.5$) and parallel-plate capacitor *4* ($x = 0.3$), $U_0 \approx 25$ V. It was noted [10] that U_0 in parallel-plate capacitors can be decreased to several volts. Thus, one can vary parameter U_0 and, hence, the pump power of the converter over wide limits by varying the design, composition, and thickness of BSTO films. In spite of elevated values of tanδ for capacitors *3* and *4*, just these capacitors were selected for implementing the converter with the aim of reducing the pump power.

An up-converter (f_{in} = 0.8 GHz, f_{out} = 4.4 GHz) intended for a 50-Ω termination was implemented on a 48 × 30 × 0.64-mm Rogers 3010 substrate with ε = 10.2 and $\tan\delta = 3.5 \times 10^{-3}$. The layout of the converter and the frequency spectrum at the output of its optimized version are shown in Fig. 6. Nonlinear capacitor *C* is connected in series to the capacitive branches of parallel resonant circuits produced by the inductances of closed stubs and capacitances of linear capacitors inserted into the gaps of the microstrip lines. Open λ/2 stubs at the inputs of each of the three converter's circuits serve as rejection filters for signals at fundamental frequency f_p and at second-harmonic frequency $2f_p$ of the pump. The contact pad facilitates application of the bias voltage to the nonlinear capacitor through resistance R = 1 MΩ.

The characteristics of the converter were simulated with computer routines intended for microwave circuit analysis. The input data of simulation were the *C–V* characteristic of planar capacitor *3* and tanδ = 0.05. In simulation, the nonlinear voltage dependence of the capacitance of this capacitor was described by the analytic relationship $C(U) = C_0 + C_2U^2 + C_4U^4 + \ldots + C_{2k}U^{2k} + \ldots$ containing only even powers of voltage. Such a description is valid if hysteresis phenomena at the initial portion of the *C–V* curve are neglected. We leave the first eight terms of the series ($k = 7$).

In simulation, the input signal power was taken to be P_{in} = –20 dBm. The pump power was varied from –20 to +34 dBm and was limited from above by a voltage across the nonlinear capacitor, for which the above

approximation of the C–V curve by a power series is valid.

Figure 7 illustrates the simulated dependence of the output power of the converter on the bias voltage at a pump power of +30 dBm (Fig. 7a) and on the pump power at different biases (Fig. 7b). From Fig. 7a, it follows that, in the pump power range considered, the conversion gain is maximal at $U_b = U_0 = 27$ V. The decrease in the output power of the converter at $U_b \neq U_0$ is associated largely with a mismatch of the converter's circuit and also with a decrease in coefficient C_1 in the expansion of the nonlinear capacitance in the Fourier series (this coefficient is responsible for conversion to frequency f_{out}; see expression (4) and Fig. 2). From Fig. 7b, it is seen that the output power of the converter is directly proportional to the pump power at $P_p <$ +25 dBm for any U_b. The curve $P_{out}(P_p)$ becomes nonlinear at $P_p \geq +25$ dBm and $U_b = 20$–30 V, possibly because the depth of modulation of the capacitance depends on the pump power only slightly near the extremum of function $F_1(U_p)$ (Fig. 2). Another reason is a mismatch of the converter's circuit arising when the constant component of the capacitance changes under the action of the pump power. In practice, the same effect may be due to heating of the BSTO film by the pump signal dissipated power (the heating of the film was disregarded in the converter model used in the simulation).

The spectrum of the output signal from the optimized converter (Fig. 6) was simulated at $U_b = 27$ V and $P_p = +30$ dBm. The latter value provides a pump signal amplitude U_p across the nonlinear capacitor of 26 V. In full accordance with the analytical results (see Sect. 1), that conversion gain $G = P_{out}/P_{in}$ reaches a maximum under the condition $U_b \approx U_p \approx U_0$ and its maximum equals 1.3 dB, which is 6 dB below the value for an idealized lossless converter.

3. EXPERIMENTAL CHARACTERISTICS OF THE UP-CONVERTER

As follows from Fig. 6b, the output spectrum contains the basic signal at fundamental frequency f_{out} and also spurious components at frequencies f_{in}, f_p, and combination frequencies. A narrow-band filter (a bandwidth of 0.9%) with insertion losses of 5 dB was placed at the output of the converter to suppress the spurious components. Below are the characteristics of a developmental version of the converter designed for frequencies $f_{in} = 0.83$ GHz ($S_{11} = -11$ dB), $f_p = 3.57$ GHz ($S_{22} = -12$ dB), and $f_{out} = 4.4$ GHz ($S_{33} = -9$ dB).

The dependences of the output power of the converter on the bias voltage and pump power are shown in Fig. 8. The output power is given in relative units (is divided by a maximal value obtained in experiments with planar capacitors) for conveniently comparing the measured and simulated results with allowance for external losses (in the measuring scheme) and losses inside the converter.

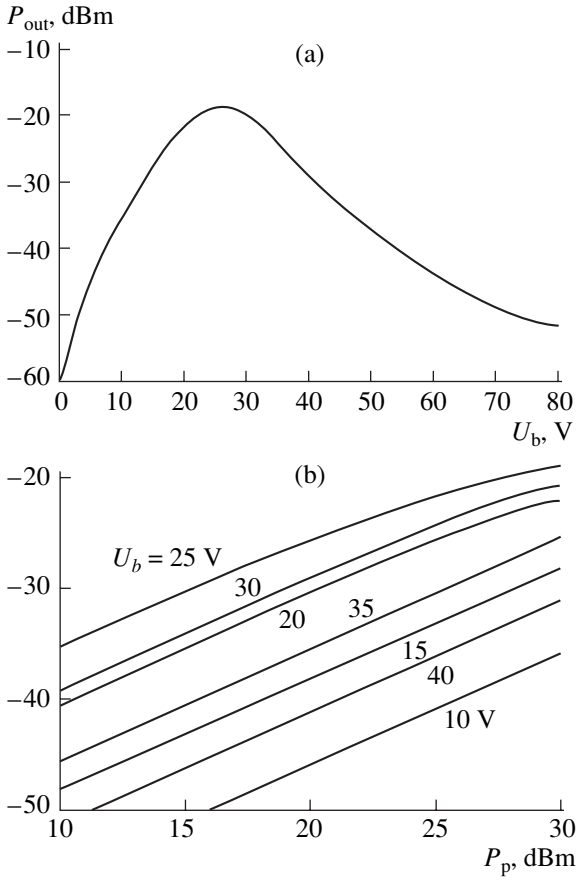

Fig. 7. Simulated dependences of the converter's output power at frequency f_{out} (a) on bias voltage U_b at P_p = +30 dBm and (b) on pump power at different U_b. The input signal power is $P_{in} = -20$ dBm.

The dependence of the output power on the bias voltage for the planar capacitor (Fig. 8) qualitatively agrees with the simulation results (Fig. 7a). However, the maximum of the experimental curve $P_{out}(U_0)$ is broader, presumably because the quality factor of the resonant circuits in the real converter is lower than the model result. For the converter with the parallel-plate capacitor, the dependence $P_{out}(U_0)$ also weakens near $U_b = U_0$ but does not exhibit a maximum as a result of degradation of the capacitor's parameters when U_b exceeds 30 V with the pump signal applied. The maximal value of the conversion gain for the converter with the parallel-plate capacitor is 3–4 dB lower than for the planar-capacitor device.

From Fig. 8, it follows that measured output power P_{out} is directly proportional to pump power P_p at any U_b for P_p up to +30 dBm when the planar capacitor is applied. For the converters with the parallel-plate capacitor, direct proportionality between P_{out} and P_p breaks at $P_p > +26$ dBm. It seems that, in the parallel-plate capacitor, the conversion gain is depressed by heating of its active region due to the dissipated power of the pump.

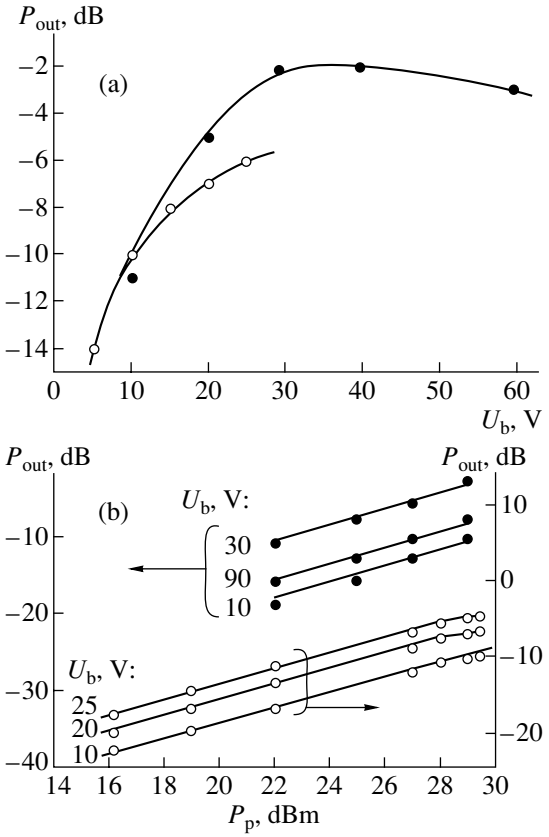

Fig. 8. Experimental dependences of the converter's output power (a) on bias voltage U_b at P_p = +28 dBm and (b) on pump power at different U_b. (●) Planar and (○) parallel-plate capacitor.

We roughly estimated overheating ΔT of the ferroelectric film by removing heat from the BSTO film into the substrate with cylindrical (for the planar capacitor) and spherical (for the parallel-plate capacitor) heat sinks. The back side of the substrate was kept at a constant temperature. For a planar capacitor,

$$\Delta T = T - T_0 = \frac{P_{dis}}{2l\lambda_f}\left[\frac{h}{s} + \frac{2}{\pi}\frac{\lambda_f}{\lambda_{sub}}\ln\left(\frac{\pi H}{s}\right)\right]; \quad (11)$$

for a parallel-plate capacitor,

$$\Delta T = \frac{P_{dis}}{2s\lambda_f}\left[\frac{h}{s} + \frac{\lambda_f}{\lambda_{sub}}\frac{1}{\pi}\left(\sqrt{2\pi} - \frac{s}{H}\right)\right]. \quad (12)$$

Here, λ_f and λ_{sub} are the thermal conductivities of the BSTO film and substrate, respectively; H and h are the thicknesses of the film and substrate, respectively; s is the gap of the planar capacitor and the length of a side of the square electrode in the parallel-plate capacitor; and l is the length of the gap in the planar capacitor.

Taking into account that λ_f = 2 W/(m K) and λ_{sub} = 25 W/(m K) [3], we find that, with the dissipated power being the same, the overheating of the parallel-plate capacitor is roughly 40 times that of the planar capacitor. Thus, overheating may become an obstacle for using parallel-plate capacitors in elevated-power microwave circuits.

CONCLUSIONS

We analyzed the performance of a frequency converter using a thin-film ferroelectric capacitor in paraphase as a nonlinear element. Based on the phenomenological description of the small-signal C–V characteristic of the nonlinear capacitor, the conditions were found under which the conversion gain reaches a maximum. For the best values of tanδ currently available, the feasible conversion gain is expected to be 2.5–8.0 dB lower than the value predicted by the Manley–Rowe relationship.

We simulated and evaluated the performance of up-converters built around planar and parallel-plate BSTO capacitors. The measurements are in good agreement with the simulation results.

In the case of using parallel-plate capacitors, overheating of the ferroelectric film due to pump power dissipation may limit the application of up-converters on their basis.

The results obtained in this work may be helpful in optimizing the circuit design of frequency converters of this class and, specifically, the design of capacitors involved in the device; in refining noise-measuring techniques; and in developing transceiver equipment.

ACKNOWLEDGMENTS

This work was supported by the program "Research of Higher School in Advanced Areas of Science and Technology" of the Ministry of Education and Science of the Russian Federation, subprogram no. 208.

REFERENCES

1. F. W. van Keuls, R. R. Romanofsky, and C. H. Mueller, Integr. Ferroelectr. **34**, 165 (2001).
2. S. Gevorgian, E. Carlsson, E. Wikborg, *et al.*, Integr. Ferroelectr. **22**, 245 (1998).
3. O. G. Vendik, *Ferroelectrics in Microwave Technology* (Sov. Radio, Moscow, 1979) [in Russian].
4. A. B. Kozyrev, M. M. Gaĭdukov, A. G. Gagarin, *et al.*, Pis'ma Zh. Tekh. Fiz. **28** (6), 51 (2002) [Tech. Phys. Lett. **28**, 239 (2002)].
5. A. T. Findikoglu, Q. X. Jia, D. W. Reagor, *et al.*, Electron. Lett. **31**, 1814 (1995).
6. A. T. Findikoglu, Q. X. Jia, and D. W. Reagor, IEEE Trans. Appl. Supercond. **7**, 2925 (1997).
7. T. Samoilova, K. Astafiev, T. Rivkin, and D. Ginley, J. Appl. Phys. **90**, 5703 (2001).
8. A. Kozyrev, A. Ivanov, T. Samoilova, *et al.*, J. Appl. Phys. **88**, 5334 (2000).
9. J. M. Manley and H. E. Rowe, Proc. IRE **44**, 904 (1956).
10. I. P. Koutsaroff, P. Woo, L. McNeil, *et al.*, in *Proceedings of the 13th IEEE International Symposium on Applications of Ferroelectrics, Nara, Japan, 2002*, p. 247.

Translated by V. Isaakyan

Technical Physics, Vol. 50, No. 10, 2005, pp. 1343–1347. Translated from Zhurnal Tekhnicheskoĭ Fiziki, Vol. 75, No. 10, 2005, pp. 94–98.

RADIOPHYSICS

Orientation Dependence of the Incoherent Radiation Yield in Crystals

A. Kh. Khokonov, M. Kh. Khokonov, and K. V. Éfendiev

Kabardino-Balkar State University, ul. Chernyshevskogo 173, Nalchik, 360004 Russia

e-mail: khokon6@mail.ru

Received August 4, 2004

Abstract—The yield of incoherent bremsstrahlung due to 1.2-GeV ultrarelativistic electrons moving near atomic chains in crystals is investigated by numerical simulation. It is shown that the electron distribution over the number of close collisions with crystal atoms deviates significantly from the Poisson distribution. The simulation results are compared with experimental data. © *2005 Pleiades Publishing, Inc.*

The flux peaking effect [1, 2], which is observed when electrons move in the channeling mode, increases the cross section of their interaction (showing up as scattering or bremsstrahlung) with atoms in a crystal compared with in an amorphous target. In particular, the effect of enhanced incoherent bremsstrahlung (IB) of 3-GeV electrons in an oriented tungsten crystal has recently been used to increase the yield of electron–positron pairs from an amorphous target placed behind the crystal [3]. Earlier [4, 5], the enhanced IB of 1.2-GeV electrons was observed in a (110) silicon crystal.

The theory of IB in oriented crystals has been developed by many authors [6–8]. It has been established that the IB cross section in crystals may be represented in the form $\sigma_c(\omega, r) = \sigma_{am}(\omega)P(r)$, where σ_c is the IB cross section in a crystal; $\sigma_{am}(\omega)$ is the IB cross section in the amorphous state; and function $P(r)$, being independent of bremsstrahlung frequency ω, specifies the dependence on distance r between the electron and atomic chain [9, 10]. Such an expression for the cross section implies that a rise in the IB intensity is unrelated to the energy of emitted photons, which is consistent with experimental data. In [9], the IB cross section in a crystal, $\sigma_c(\omega, r)$, calculated by the virtual photon method was carefully compared with the results obtained elsewhere. In this work, we numerically simulate the IB yield in thick silicon crystals with allowance for dechanneling and analyze the orientation dependence of the IB enhancement effect, i.e., its dependence on the angle the electrons make with a given crystallographic axis when entering the crystal.

Simulation of multiple scattering of an electron moving in an oriented crystal has been carried out with regard to each event of its interaction with lattice atoms [10–13]. Such an approach makes it possible to find the electron distribution over the number of scattering events that change transverse electron energy ε (incoherent scattering). The transverse energy is the integral of motion in the field of the continuous potential of an atomic chain [14] (coherent scattering by a continuous potential). The continuous potential raises the cross sections of incoherent scattering and IB by a factor of $S_0/S(\varepsilon)$ compared with an amorphous medium (see, i.e., [15]), where $S_0 = 1/Nd$ is the cross-sectional area per chain, N is the number of atoms per unit volume, and d is the least atomic spacing in the chain. The cross-sectional area accessible for the electron is $S(\varepsilon) = \pi r^2(\varepsilon)$, where $r(\varepsilon)$ is determined from the condition $U(r) = \varepsilon$, where $U(r)$ is the continuous potential of the atomic chain. Factor $S_0/S(\varepsilon)$ arises upon averaging function $P(r)$, which specifies the dependence on the impact parameter, over the accessible area with regard to the uniform electron distribution over transverse coordinates [14]. Function $P(r)$ is assumed to have the Gaussian form, $P(r) \sim \exp(-r^2/u_\perp^2)$. Strictly speaking, it is also necessary to take into account factor $1 - \exp[-r^2(\varepsilon)/u_\perp^2] \approx 1$ [15], since $r(\varepsilon) \gg u_\perp$, where $u_\perp$ is the temperature oscillation amplitude of crystal atoms.

The cross section of incoherent scattering by an atom was calculated using the Moliere potential, which gives realistic values of the cross section in the vicinity of the atom ($r \le a_F$, where a_F is the Thomas–Fermi screening parameter) and has regular asymptotics at $r \longrightarrow 0$. Atomic chain continuous potential $U(r)$ was calculated from the Doyle–Turner atomic potential [16], which is preferable at distances $r \ge a_F$. This circumstance is essential for proper calculation of accessible area $S(\varepsilon)$.

The Moliere atomic potential has the form

$$V(r) = -(Ze^2/r)\sum_{i=1}^{3}\alpha_i \exp(-\beta_i r/a_F), \qquad (1)$$

where $\alpha_i = (0.1, 0.55, 0.35)$, $\beta_i = (6.0, 1.2, 0.3)$, and Z is the atomic number of the material.

1063-7842/05/5010-1343$26.00 © 2005 Pleiades Publishing, Inc.

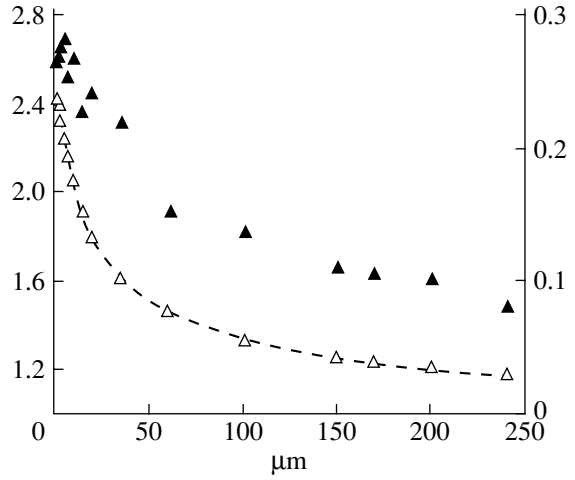

Fig. 1. (▲) Ratio between the numbers of electron–atom close collisions in the (110)Si crystal and in the amorphous target (on the left) and (△) the number of electrons in the channel (on the right). In the abscissa, the target thickness is plotted in micrometers. The electron energy and initial divergence are, respectively, 1.2 GeV and $\pm 0.5\theta_L$.

Calculated in the first Born approximation for potential (1), the differential cross section of electron scattering by angle θ is given by

$$d\sigma = \sigma_0 \theta_a^2 \sum_{i,k=1}^{3} \frac{\alpha_i \alpha_k 2\theta d\theta D(\theta)}{(\theta^2 + \beta_i^2 \theta_a^2)(\theta^2 + \beta_k^2 \theta_a^2)}. \qquad (2)$$

Here, $\theta_a = \hbar c/(Ea_F)$ is the characteristic angle of electron scattering by an atom; $E = \gamma mc^2$ is the electron energy; γ is the Lorentz factor; m is the electron mass at rest; a_F is the Thomas–Fermi screening parameter;

$$D(\theta) = 1 - \exp(-u_\perp^2 \theta^2 / a_F^2 \theta_a^2) \qquad (3)$$

is the Debye–Waller factor; $u_\perp$ is the mean temperature oscillation amplitude of crystal atoms; $\sigma_0 = \pi a_F^2 \eta^2$ is the scattering total cross section calculated for the screened Coulomb potential; $\eta = 2\alpha Z$ is the Bohr parameter [17], which defines the condition of applicability of the Born approximation ($\eta \ll 1$); and $\alpha = 1/137$.

The Debye–Waller factor makes it possible to separate the scattering coherent component, which is associated with scattering by the atomic chain continuous potential. Therefore, one may say that expression (2) describes incoherent scattering of electrons by individual atoms.

According to (2) and (3), the total cross section of scattering by an atom is given by

$$\sigma = \sigma_0 (u_\perp / a_F)^2 \sum_{i,k=1}^{3} f_{ik}, \qquad (4)$$

where

$$f_{ik} = \begin{cases} -\alpha_i^2 x_i, & i = k \\ \alpha_i \alpha_k (\mu_i - \mu_k)^{-1} [\ln(\mu_i/\mu_k) + x_k - x_i], & i \neq k. \end{cases}$$

Here, $x_i = \exp(\mu_i)\mathrm{Ei}(-\mu_i)$, $\mu_i = (u_\perp \beta_i / a_F)^2$, and $\mathrm{Ei}(x)$ is the integral exponent. Expression (4) specifies the free path of quasi-channeled electrons ($\varepsilon > 0$), $l_q = (\sigma N)^{-1}$. For such electrons, the entire cross-sectional area, $S(\varepsilon) = S_0$, is accessible. The free path of an electron with $\varepsilon < 0$ is, accordingly, $S_0/S(\varepsilon)$ times shorter. In silicon, $l_q \approx 1$ μm, which is roughly twice as much as without considering the Debye–Waller factor.

Let $k(z)$ be the mean number of inelastic scattering events for electrons in a target of thickness z. It is worth comparing this value in an oriented crystal and in an amorphous material of the same thickness. Figure 1 (the left-hand vertical axis) plots ratio $\langle k \rangle / \langle k \rangle_{am}$ where $\langle k \rangle$ is the number of inelastic scattering events (close collisions) for 1.2-GeV electrons in an axially oriented (110) silicon crystal and $\langle k \rangle_{am}$ is the number of collisions in the disordered crystal) versus the thickness. In calculations, the initial angular divergence of the electrons, Δθ, was set equal to $\pm 0.5\theta_L$, where $\theta_L = (4Ze^2/dE)^{1/2}$ is the Lindhard critical angle [14]. The number of close collisions in the amorphous material was calculated by the formula $\langle k \rangle_{am} = N\sigma z$ with cross section σ defined by expression (4).

The right-hand vertical axis in Fig. 1 plots the number of electrons at a certain depth in the channel, $N_c(z)$ (the dashed line; cf. [18]). Of practical importance is the effective channeling length [19]

$$z_{eff}(z) = \int_0^z N_c(z')dz'. \qquad (5)$$

In Fig. 1, $z_{eff} \approx 15$ μm at a crystal thickness of 240 μm. At crystal thicknesses of 20 and 1000 μm, the effective channeling depth is 3 and 27 μm, respectively.

Thus, it follows from Fig. 1 that, even in a relatively thick ($z \gg z_{eff}$) crystal, the number of electron–atom close collisions may significantly exceed that in the amorphous material. At large z, ratio $\langle k \rangle / \langle k \rangle_{am}$ declines with increasing z more slowly than by the law $1/z$, which is consistent with the statistical theory developed in [20].

The mean number of close collisions in an oriented crystal, $\langle k(z) \rangle$, does not give adequate insight into the nature of multiple scattering, since the spread in the number of collisions about the mean value in the crystal is much higher than in the amorphous material. Let $P_k(z)$ be the probability that an electron in a target of thickness z experiences k incoherent scattering events.

Then, the mean number of such events will be

$$\langle k(z)\rangle = \sum_{k=0}^{\infty} kP_k(z). \quad (6)$$

It is this value that is plotted on the left of Fig. 1.

In the amorphous medium, quantity $P_k(z)$ obeys the Poisson distribution,

$$P_k(z) = \frac{\langle k(z)\rangle_{\text{am}}^k}{k!}\exp(-\langle k(z)\rangle_{\text{am}}), \quad (7)$$

where $\langle k(z)\rangle_{\text{am}} = N\sigma z$ and σ is given by (4).

Probability $P_k(z)$ that an electron experiences k incoherent scatterings is shown in Figs. 2 and 3 for the 15- and 240-μm-thick crystals, respectively (the dashed lines refer to the oriented crystals), at the same energy and angular divergence of the electrons as in Fig. 1. The continuous curves in Figs. 2 and 3 show Poisson distribution (7) for the amorphous medium. The abscissa axis in Figs. 2 and 3 plots ratio $k/\langle k\rangle_{\text{am}}$; the ordinate axis, distribution P_k multiplied by $\langle k\rangle_{\text{am}}$. Thus, the distributions in Figs. 2 and 3 are normalized to unity. It is seen that distribution $P_k(z)$ in the crystal deviates significantly from Poisson distribution (7) because of factor $S_0/S(\varepsilon)$. Namely, the former has a long tail at a large number of close collisions. At thicknesses $z \sim z_{\text{eff}}$ in the crystal (Fig. 2), the number of collisions decreases sharply for $k/\langle k\rangle_{\text{am}} < 1$. Note that the maximum of the distribution in the oriented crystal exceeds that in the amorphous medium. In thick targets ($z \gg z_{\text{edd}}$, Fig. 3), conversely, the distribution peak in the amorphous target is higher than in the crystal, the tail in the thick crystal being more pronounced than in the thin one.

The number of photons emitted within a given frequency interval per unit length in an amorphous target is given by the Bethe–Heitler formula

$$n_{\text{am}}(u) \equiv \frac{d^2 n_{\text{am}}}{du\,dz} = \frac{4}{3Lu}\left(1 - u + \frac{3}{4}u^2\right), \quad (8)$$

where $1/L = 4\alpha Z^2 r_0^2 N\ln(183Z^{-1/3})$, L is the radiation length, $u = \hbar\omega/E$, and $r_0 = e^2/mc^2$.

The IB cross section for an electron with given transverse energy ε in an oriented crystal is expressed through cross section (8) for an amorphous medium as $n = n_{\text{am}}S_0/S(\varepsilon)$.

Free path z_0 between two successive radiation events is found from the formula for probability W that an electron will emit no photons over length z_0,

$$W(z_0) = \exp\left[-\int_0^{z_0} n(z')dz'\right]. \quad (9)$$

Here, the dependence of the total probability of radiation per unit length, n, on penetration depth z takes into account the fact that this quantity in an oriented crystal is related to the electron transverse energy and this energy changes after multiple scattering.

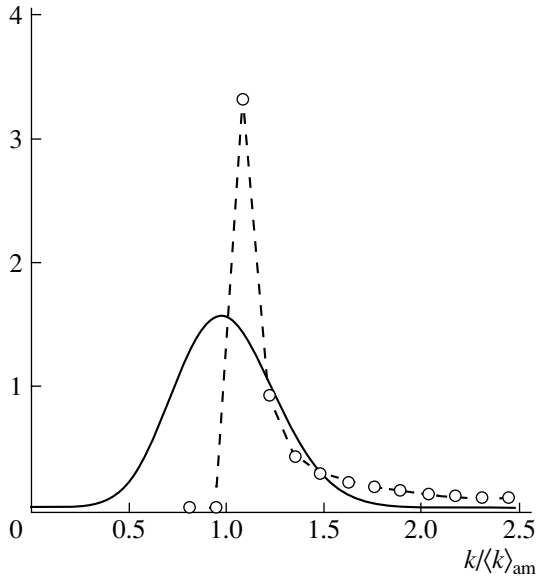

Fig. 2. Probability distribution for the number of close collisions for 1.2-GeV electrons in the 15-μm-thick (110)Si crystal (dashed line). The abscissa plots the number of collisions in terms of their mean value for the amorphous target. The continuous line shows the Poisson distribution in the amorphous target. The initial angular divergence of electrons is $\pm 0.5\theta_{\text{L}}$.

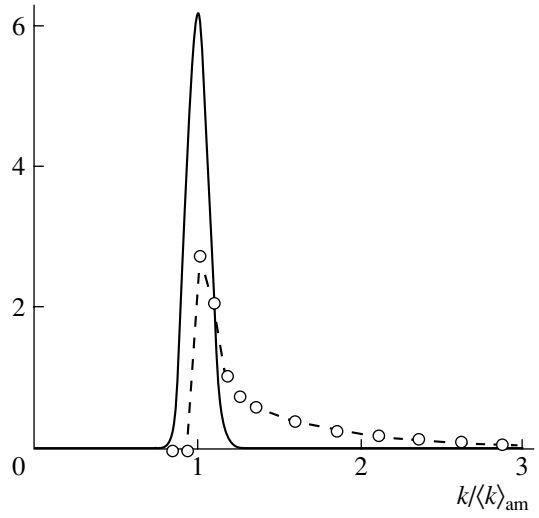

Fig. 3. The same as in Fig. 2 for the 240-μm-thick silicon crystal.

The total probability of radiation per unit length, n, is found by integration of formula (8) over frequencies starting from some minimal frequency u_{min}. In our calculations, u_{min} was set equal to 0.01.

Figure 4 compares the calculated IB yield in the 240-μm-thick (110)Si crystal with experimental data

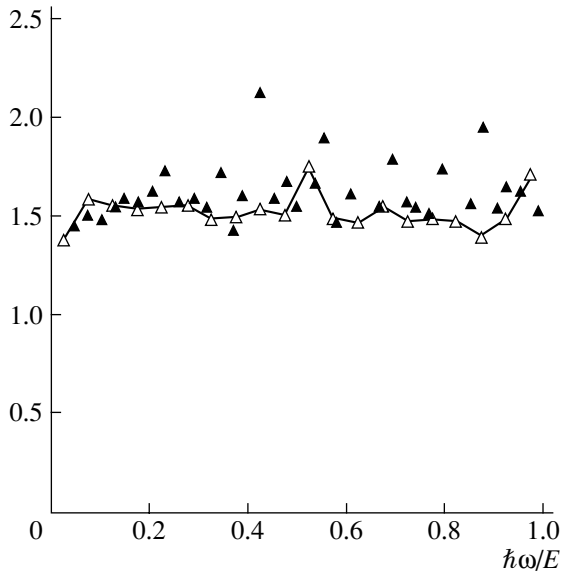

Fig. 4. Ratio between the IB yields for 1.2-GeV electrons in the 240-μm-thick (110)Si crystal and in the amorphous target: (▲) data points [4] and (△) analytical data. The initial angular divergence of electrons is $\pm 0.5\theta_L$.

[4] for electrons with an energy of 1.2 GeV. The filled symbols in Fig. 4 are data points; the empty ones connected by the continuous line refer to the numerical simulation. The ordinate axis plots the ratio between the IB intensities in the crystal and amorphous medium. Note that in the experiments in [4], just the incoherent part of the spectrum was measured. In this work, the IB intensity in the amorphous medium was also calculated by numerical simulation. The 1.5-fold excess of the intensity in the crystal over that in the amorphous material (as demonstrated in Fig. 4) is in exact coincidence with the excess of the number of close collisions in the crystal (z = 240 μm, Fig. 1). Thus, from Fig. 1, one can judge how much the IB intensity in the crystal target exceeds that in the amorphous target at different target thicknesses. For example, in the 15-μm-thick crystal, the IB intensity is roughly 2.4 times higher. Although the data points in Fig. 4 lie somewhat above the analytical values, the calculation and experiment are in fairly good agreement. Hence, the supposition that factor $S_0/S(\varepsilon)$ differentiates the oriented crystal from the amorphous medium is valid.

In [5], IB was measured in 500-μm-thick (110)Si crystals for a widely divergent electron beam ($\sim 1.3\theta_L$) of energy 1.2 GeV. Figure 5 compares our calculation results (empty symbols) with experimental data (filled symbols) when the electron beam axis runs parallel to the ⟨110⟩ direction in the crystal. The high excess of the experimental data over the calculated values in the soft part of the spectrum is due to coherent scattering [21] in the atomic chain continuous potential, which was disregarded in the calculation. It is seen from Fig. 5 that the excess in the case at hand (for photon energy $\hbar\omega >$ 200 MeV) is ≈1.2 times.

Figure 6 illustrates the orientation dependence of the IB yield (the photon energy is 1.05 ± 0.03 GeV) for electrons in the 500-μm-thick silicon crystal (E = 1.2 GeV). The abscissa axis plots the angle (in degrees) between the electron beam and the ⟨110⟩ direction in

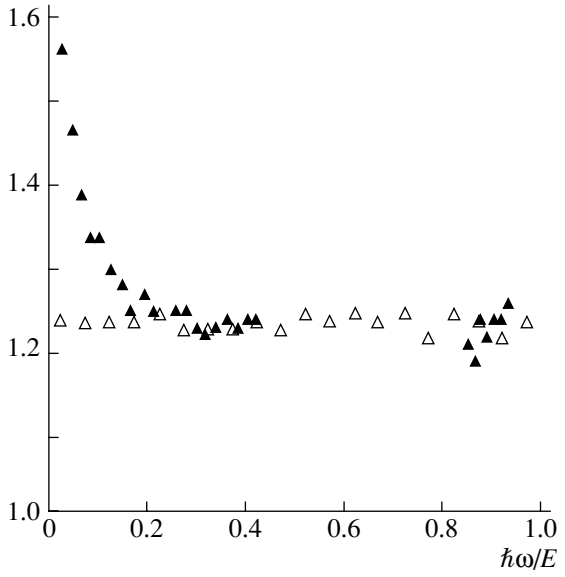

Fig. 5. (△) Analytical and (▲) experimental [5] data on the IB yield for 1.2-GeV electrons in the 500-μm-thick (110)Si crystal. The abscissa axis plots the photon energy; the ordinate axis, the ratio between the IB intensities in the crystal and in the amorphous target. The initial angular divergence of electrons is $\pm 1.3\theta_L$.

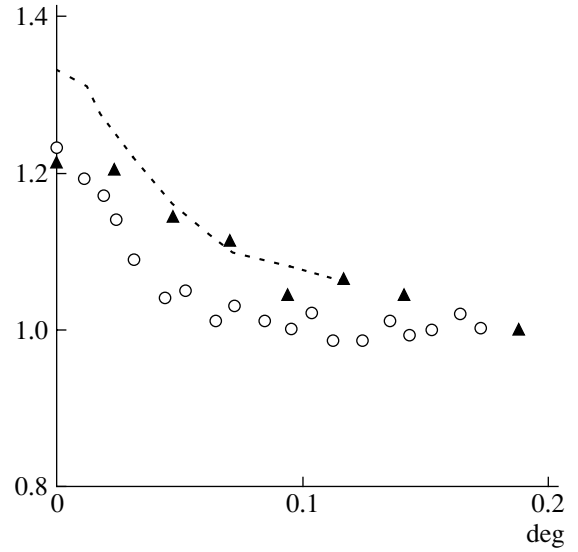

Fig. 6. Orientation dependence of the IB yield for 1.2-GeV electrons in the 500-μm-thick (110)Si crystal: (○) data points [5] and (▲) analytical data. The abscissa axis plots the angle between the electron beam axis and ⟨110⟩ crystallographic direction. The angular divergence of the electron beam is $\pm 1.3\theta_L$. The dashed line is drawn for the divergence $\pm 0.2\theta_L$.

the crystal ($\theta_L = 0.024°$ in this case). Here, the empty symbols are data points [5] and the filled symbols show the results of our calculation. The angular divergence of the electron beam is $\approx 1.3\theta_L$. At small angles, the experiment and calculation are in good agreement, while at angles on the order of several critical channeling angles, the analytical curve goes above the experimental one. The dashed curve in Fig. 6 is drawn for a smaller angular divergence of the electrons, $\approx 0.2\theta_L$. The discrepancy between the analytical and experimental data in the range $(2–3)\theta_L$ is a surprise in view of the good agreement observed for the parallel arrangement of the beam axis and ⟨110⟩ crystallographic axis. This discrepancy cannot be explained by photon collimation, since in [5] the output energy of the electrons was measured. In light of this, one should bear in mind that, in the case of inclined incidence of electrons, high coherent scattering by the atomic chain continuous potential takes place with the transverse energy of the electrons preserved. Then, the electron angular distribution at the exit from the target is no longer azimuth-symmetric [22, 23] and so it remains unclear whether all the electrons in the experiment [5] fell into the detector in the angular range $(2–3)\theta_L$.

REFERENCES

1. V. V. Beloshitskiĭ and M. A. Kumakhov, Zh. Éksp. Teor. Fiz. **82**, 462 (1982) [Sov. Phys. JETP **55**, 265 (1982)].
2. M. A. Kumakhov, Usp. Fiz. Nauk **115**, 427 (1975) [Sov. Phys. Usp. **18**, 203 (1975)].
3. M. Inoue, S. Takenaka, K. Yoshida, *et al.*, Nucl. Instrum. Methods Phys. Res. **173**, 104 (2001).
4. G. L. Bochek, I. A. Grishaev, G. D. Kovalenko, and V. I. Kulibaba, Pis'ma Zh. Éksp. Teor. Fiz. **32**, 380 (1980) [JETP Lett. **32**, 355 (1980)].
5. I. Endo, T. Monaka, A. Sakaguchi, *et al.*, Phys. Lett. A **146**, 150 (1990).
6. V. N. Baier, V. M. Katkov, and V. M. Strakhovenko, Usp. Fiz. Nauk **159**, 455 (1989) [Sov. Phys. Usp. **32**, 972 (1989)].
7. A. I. Akhiezer and N. F. Shulga, *High Energy Electrodynamics in Matter* (Nauka, Moscow, 1993; Gordon and Breach, New York, 1996).
8. V. A. Bazylev and N. K. Zhevago, *Radiation from Fast Particles in Materials and External Fields* (Nauka, Moscow, 1987) [in Russian].
9. H. Nitta, K. Shimizu, and Y. H. Ohtsuki, Radiat. Eff. Defects Solids **122–123**, 383 (1991).
10. A. Sorensen, *Relativistic Channeling*, Ed. by R. A. Carrigan, Jr. and J. A. Ellison (Plenum, New York, 1987), pp. 331–337.
11. M. Kh. Khokonov, Zh. Éksp. Teor. Fiz. **103**, 1723 (1993) [JETP **76**, 849 (1993)].
12. M. Kh. Khokonov and F. K. Tuguz, Nucl. Instrum. Methods Phys. Res. **82**, 46 (1993).
13. M. Kh. Khokonov, Radiat. Eff. Defects Solids **132**, 91 (1994).
14. J. Lindhard, K. Dan. Vidensk. Selsk., Mat.-Fys. Skr. **34** (14), 1 (1965).
15. V. A. Ryabov, *Channeling Effect* (Énergoatomizdat, Moscow, 1994) [in Russian].
16. P. A. Doyle and P. S. Turner, Acta Crystallogr., Sect. A **24**, 390 (1968).
17. N. Bohr, K. Dan. Vidensk. Selsk., Mat.-Fys. Skr. **18** (8), 1 (1948).
18. M. Kh. Khokonov, Zh. Tekh. Fiz. **64**, 181 (1994) [Tech. Phys. **39**, 330 (1994)].
19. M. Kh. Khokonov, Phys. Lett. A **145**, 195 (1990).
20. A. Kh. Khokonov and M. Kh. Khokonov, Pis'ma Zh. Tekh. Fiz. **31** (4), 44 (2005) [Tech. Phys. Lett. **31**, 154 (2005)].
21. M. Kh. Khokonov, Phys. Lett. A **57A**, 17 (1976).
22. V. V. Beloshitskiĭ and M. A. Kumakhov, Fiz. Tverd. Tela (Leningrad) **15**, 1588 (1973) [Sov. Phys. Solid State **15**, 1060 (1973)].
23. J. A. Golovchenko, Phys. Rev. B **13**, 4672 (1976).

Translated by V. Isaakyan

Technical Physics, Vol. 50, No. 10, 2005, pp. 1348–1352. Translated from Zhurnal Tekhnicheskoĭ Fiziki, Vol. 75, No. 10, 2005, pp. 99–103.

ELECTRON AND ION BEAMS, ACCELERATORS

Image Reconstruction by Scanning a Crystal with an Electron-Beam-Produced Grating of Atomic Lens Focuses

A. G. Rezikyan and V. V. Smirnov

Fok Research Institute of Physics (Petrodvorets Branch), St. Petersburg State University, ul. Pervogo Maya 100, Petrodvorets, St. Petersburg, 198504 Russia

e-mail: aram_rn@mail.ru

Received February 11, 2005

Abstract—When atomic rows in a crystal layer are used to focus a beam from an electron microscope, the intensity distribution behind the crystal represents a grating of narrow peaks with diameters from 0.03 to 0.04 nm in the first Fourier plane. A scheme of scanning transmission electron microscopy (STEM) with such a grating is simulated that makes it possible to reconstruct the transmission function of an object from the signal recorded. The reconstruction quality depends on the type and amount of distortions. Distortions due to the following two factors are simulated: random noise imposed on the signal detected in the experiment and the lack of information about the wave incident on the object because of uncertainty involved in the width of the electron beam striking the focusing crystal. The range of distortions within which the object can be reconstructed with a tolerable quality is determined. © *2005 Pleiades Publishing, Inc.*

INTRODUCTION

The idea of an atomic lens in corpuscular optics has been proposed and elaborated upon in [1–14]. The essence of this concept is the formation of narrow crossovers of corpuscular (electron, atomic, etc.) beams focused by various atomic- and nanometer-scale systems, the simplest example of which is an atom. The methods based on this concept hold promise for many applications, including microscopy. For example, it has been theoretically shown [1, 6] that single heavy atoms or columns of atoms in a thin crystal may act as a lens focusing an electron beam into a spot several tens of picometers across. This speculation has been experimentally supported in [2], where one of the schemes described in [6] provided a resolution of 0.06 nm using a transmission electron microscope (TEM) with a resolution of no higher than 0.34 nm.

If the diameter of an electron beam incident on a focusing crystal is wider than the atomic row spacing, the pattern resulting behind the crystal represents a grating of narrow intensity peaks several tens of picometers in size. By scanning such a grating over the object, one may basically reconstruct the image with a resolution comparable to the peak diameter.

In this study, we numerically simulate image reconstruction based on such scanning.

The schematic of the system under study is shown in Fig. 1. The simulation procedure includes three stages: (1) propagation of a TEM beam through a thin crystal layer, (2) propagation of the transmitted beam from the crystal to an object to be visualized (it is supposed that the wave travels in a vacuum at this stage), and (3) image reconstruction from the wave scattered by the object as a result of scanning.

1. PROPAGATION THROUGH A CRYSTAL

Electron beam channeling in a crystal was simulated using Earl J. Kirkland's software package. It utilizes the Cowley–Moodie multislice simulation technique [15], which is widely used for simulation in electron microscopy. For example, beam channeling in a 6-nm-thick gold crystal (15 unit cells along the [100] crystallographic direction) was considered in [4]. In this work, the parameters of the beam are typical of a TEM: the electron energy is 100 keV; angle of convergence, 10 mrad; and the minimal diameter in the crossover, about 0.2 nm.

Calculations made for different shifts of the initial beam axis from a selected column of atoms showed that

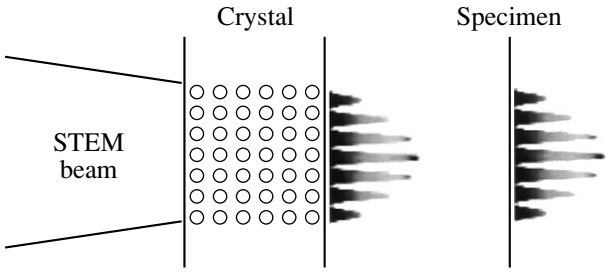

Fig. 1. General picture of the experiment.

1063-7842/05/5010-1348$26.00 © 2005 Pleiades Publishing, Inc.

a narrow (30 pm in diameter) crossover forms behind the crystal with a maximal intensity approximately 0.2 nm distant from the last atom in the column. The output intensity profile is firmly related to the axis of the column and does not change upon shifting the initial beam. When the beam covers a neighboring chain, a satellite focus (intensity peak) appears. The peaks do not broaden upon shifting the beam.

To analyze a grating of focuses, we calculated the transmission of a wider primary beam. Figure 2 compares the intensity profiles over the cross section of a beam leaving the TEM (the energy 300 keV, angle of convergence 0.5 mrad), at the exit surface of a 6-nm-thick gold crystal (15 unit cells along the [100] crystallographic direction), and in the crossover with a minimal diameter of about 1.6 nm. The profiles were calculated by the multislice method.

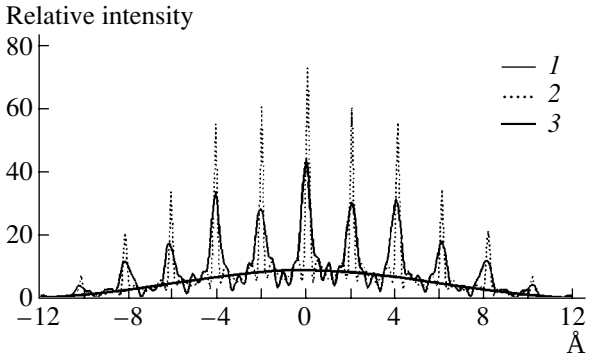

Fig. 2. Intensity distribution (*1*) in the first Fourier plane, (*2*) near the exit crystal surface, and (*3*) over the cross section of the TEM beam.

2. PROPAGATION THROUGH VACUUM

As was mentioned above, the beam leaving the crystal forms a narrow crossover with a maximal intensity located several tenths of a nanometer away from the last crystal atom. Since the surface of a real crystal is rough, scanning at such a close distance to the crystal surface is hardly possible. Practically, the gap between the crystal and crossover depends on the surface roughness; therefore, conditions should generally be provided under which the crossover is as distant from the crystal as possible. A method to overcome these difficulties was suggested in [5]. The Fourier principle of planes, which is well known in wave optics, says that an infinite grating of point coherent sources periodically arranged in a plane (with their spatial intensity distribution described by the delta function) is periodically translated in space (i.e., divergent rays are focused again with a certain spatial period).

However, if the grating is finite and sources are nonpoint (in our case, the peaks have a finite width and height), the signal in each subsequent focusing plane becomes more and more distorted. Hence, it follows that the larger the number of crystal rows covered by the TEM beam, the higher the reproducibility of the beam in the Fourier planes (it can be reproduced even in the zeroth-order plane). On the other hand, when the incident wave carries a large number of peaks, noise, which is inevitable in real experiments, may adversely affect the image reconstruction. Thus, one has to choose an optimal number of peaks that would provide for periodic beam focusing with small distortions, at least in the first focusing plane, and still offer a reasonably high accuracy of image reconstruction.

For point sources, the distance to the Fourier planes can be calculated by the well-known formula [5]

$$R = \frac{na^2}{2\lambda}, \qquad (1)$$

where R is the distance to a Fourier plane, a is the source spacing, n is the number (order) of the plane, and λ is the wavelength.

For a finite grating and nonpoint sources, the Fourier planes turn out to be displaced relative to their positions in the ideal case. Our calculation shows that this displacement is insignificant (at least, for the beam configurations considered here).

Calculation by formula (1) for a 300-keV electron beam striking a gold target with $a = 0.2$ nm yields distance $R = 9.3$ nm to the first Fourier plane. Advanced technologies allow for placing and moving a specimen at such a small distance from the crystal.

After the beam has left the crystal, the wave can be found as a convolution over transverse coordinates $\mathbf{r}$ with a vacuum propagator given by [6]

$$p(\mathbf{r}, z) = \frac{1}{i\lambda z}\exp\left(ik\left(z + \frac{r^2}{2z}\right)\right), \qquad (2)$$

where λ is the wavelength and k is the wavenumber.

This expression is valid as long as the range of longitudinal coordinate z far exceeds the ranges of the transverse coordinates.

Figure 2 shows the intensity profile in the first Fourier plane that was obtained by the convolution of the output wave with vacuum propagator (2).

3. IMAGE RECONSTRUCTION

The image of an object can be obtained by scanning it with electron beam *1* (Fig. 2) produced as described above. However, the specimen visualization quality depends on a number of factors, some of which are considered below. If the specimen is scanned by one narrow peak (ideally, in the form of the delta function), the distortions in the reconstructed image will be minor (the closer the peak's shape to the delta function, the smaller the distortions). However, when the number of focuses (peaks) is large, the images from each of the

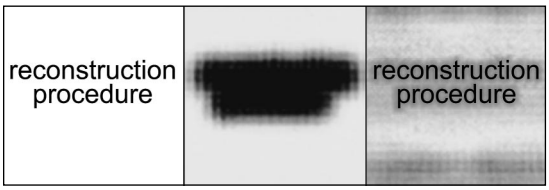

Fig. 3. Initial object (on the left), result of scanning (in the middle), and reconstructed image (on the right).

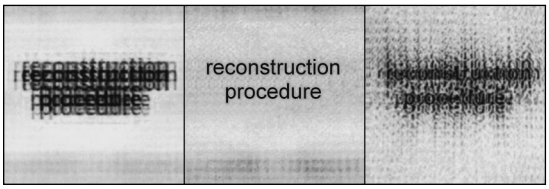

Fig. 4. Reconstructed images of the pattern described by function f (Fig. 3) for $\Delta r_1 = 0.15$ (on the left), 0.25 (in the middle), and 0.30 nm (on the right). Function g is characterized by $\Delta r_1 = 0.25$ nm.

focuses superimpose and the resulting pattern becomes fuzzy.

Let wave $w(x, y)$ strike an object with transmission function $v(x, y)$, where (x, y) are the coordinates in the object plane (i.e., transverse coordinates $\mathbf{r}$ in formula (2) for the vacuum propagator). According to [5], the output wave in the plane behind a thin object (in which diffraction can be neglected) is given the product wv and its intensity can be expressed as $R' = gf$, where $g \equiv |w|^2$ and $f \equiv |v|^2$.

The recorded signal is given by $R = \iint_F R'(x, y)dx\,dy$, where F is the domain occupied by the object. In accordance with [5], $v = \exp(-i\sigma U)$, where $\sigma = m/k$ (m is the electron mass, k is the wavenumber), $U(\mathbf{r}) = \int_{-\infty}^{\infty} V(\mathbf{r}, z)dz$ is the so-called projected potential distribution, and V is the scattered potential. Thus, given $f = \exp(2\sigma \mathrm{Im}(U))$, one can find the imaginary part of the projected potential of the object,

$$\mathrm{Im}(U) = \frac{1}{2}\sigma \ln(f).$$

The imaginary part of the complex scattered potential corresponds to absorption in the object [16]. Thus, the absorptivity of the object is embodied in function f.

Scanning of the object by the incident wave can evidently be represented by the convolution

$$g \otimes f = R. \qquad (3)$$

Here, $R(\Delta x, \Delta y)$ is the function of displacements $(\Delta x, \Delta y)$ associated with scanning.

With g and recorded signal R known, to reconstruct f means to carry out deconvolution in (3). This is done, first, by applying the Fourier transformation to Eq. (3),

$$\left.\begin{aligned} F[g \otimes f] &= F[R] \\ F[g \otimes f] &= F[g]F[f] \end{aligned}\right\} \Rightarrow F[f] = \frac{F[R]}{F[g]} \qquad (4)$$

and then applying the inverse Fourier transformation to resulting equation (4),

$$f = F^{-1}\left[\frac{F[R]}{F[g]}\right].$$

According to (4), any point where the value of function $F[g]$ is small is a singular point of function $F[f]$; thus, the regularization procedure is required, for example, in the form

$$f = F^{-1}[F[R]Q]\begin{cases} Q = \dfrac{1}{reg} \ \text{if} \ |F[g]| < reg \\ Q = \dfrac{1}{F[g]} \ \text{otherwise,} \end{cases} \qquad (5)$$

where reg is the regularization parameter.

Basically, the processes of recording and reconstruction may be simulated using the multislice method, as described in Sect. 1. Such an approach gives a close approximation to a real wave. However, for preliminary qualitative analysis, less elaborate models are preferable.

Model function g was taken in the form of a mesh function in which nodes the Gaussian functions

$$2\pi/\Delta r \exp(-0.5r^2/(\Delta r)^2)$$

(where $r = \sqrt{x^2 + y^2}$) modulated by the Gaussian envelope $\exp(-r^2/(\Delta r_1)^2)$ are set; i.e.,

$$g = \left(\sum_{i=-m}^{m}\sum_{j=-m}^{m} \frac{2\pi}{\Delta r} \times \exp\left(-0.5\frac{[r(x + id; y + jd)]^2}{(\Delta r)^2}\right)\right)\exp\left(-\frac{r^2}{(\Delta r_1)^2}\right).$$

In numerical simulation, we put $\Delta r = 0.04$ nm (the result of multislice simulation of the peaks in the first Fourier plane) and set the node spacing equal to 0.2 nm (which corresponds to the gold crystal). It was assumed that, at the stage of reconstruction, we will use function R determined from a real experiment and distribution g obtained by the multislice method (curve *1* in Fig. 2). The envelope width used in the simulation, $\Delta r_1 = 0.25$ nm, corresponds to a 0.5-nm-wide primary beam that forms a grating of nine intense peaks and many weak peaks.

Model transmission function f is shown on the left of Fig. 3. Such a test pattern is easily discernible and has

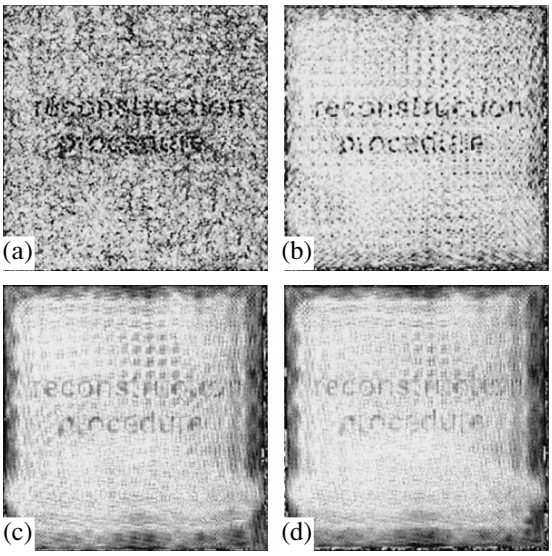

Fig. 5. Reconstruction of the noisy image. The noise parameters are ε = (a) 0.03, (b) 0.05, (c) 0.09, and (d) 0.11 nm and β = (a) 0.5, (b) 2.0, (c) 5.0, and (d) 6.0%.

a typical feature size of 0.6 nm, which is comparable in order of magnitude to the probe width, $\Delta r = 0.04$ nm. The pattern to be reconstructed is of no concern for or the simulation process. The simulated area is 4×4 nm.

The need for image construction from the detected signal follows from Fig. 3, which shows a result of scanning.

When simulating, we also revealed factors that limit the scope of visualization.

Since the width of the TEM beam intensity distribution can never be known exactly, width g of the grating envelope cannot be determined accurately. For this reason, the intensity distribution in the wave incident on the object is simulated by another grating g', the envelope width of which differs from the true value. It therefore makes sense to see how the reconstruction quality depends on the difference between the envelope width used in reconstruction and its true value, as well as to determine the associated range of discrepancy (between the true envelope width and the envelope width of grating g') that allows visualization with a desired quality.

Table

ε, nm	β, %
0.03	0.5
0.05	2.0
0.09	5.0
0.11	6.0

In real experiments, there invariably exist factors distorting the signal recorded. These may be vibration due to scanning, foreign particles in the detector, a drift of the TEM beam, pollution of the scanning chamber or specimen, thermal drift, damage to the specimen, etc. It is therefore important to determine the amount of distortions that makes visualization with a desired quality possible. A tolerable amount of distortions can be found only experimentally. As a simple source of distortions, we consider random noise superposed on the signal.

First, we studied the reconstruction quality versus the regularization parameter (see formula (5)). The highest quality was obtained for a regularization parameter of the order of 10^{-3}. This value was used in the following calculations.

To simulate uncertainty in specifying wave g, the recorded signal was found by formula (3) and, at the stage of reconstruction, function g in (5) was substituted for by function g', which differs from g in the value of parameter Δr_1. The results are shown in Fig. 4.

When the effect of noise was simulated, recorded signal (3) was mixed with random noise components having various spatial frequencies (or periods ε) and amplitudes β. The corresponding numerical results are given in Fig. 5, where noise amplitude β is expressed in percentage of maximum signal R.

CONCLUSIONS

In this work, we found the STEM parameter ranges that provide a tolerable accuracy of image reconstruction by scanning an electron-beam-produced grating of atomic lens focuses. In particular, the width of the envelope of the incident wave intensity distribution peaks must fall into the range $\Delta r_1 = 0.15$–0.30 nm (the true width is $\Delta r_1 = 0.25$ nm). Maximum noise amplitudes β that allow a reasonable visualization quality are listed in the table for various spatial frequencies ε^{-1} of noise.

The results obtained may serve as tentative data in design of experiments.

REFERENCES

1. V. V. Smirnov, J. Phys. D **31**, 1548 (1998).
2. J. M. Cowley, Phys. Rev. Lett. **84**, 3618 (2000).
3. V. V. Smirnov and J. M. Cowley, Phys. Rev. B **65**, 064109 (2002).
4. J. M. Cowley and J. B. Hudis, Microsc. Microanal. **5**, 429 (2000).
5. R. E. Dunin-Borkowski and J. M. Cowley, Acta Crystallogr., Sect. A **55**, 119 (1999).
6. J. M. Cowley, J. C. H. Spence, and V. V. Smirnov, Ultramicroscopy **68**, 135 (1997).
7. V. V. Smirnov, Zh. Tekh. Fiz. **71** (7), 92 (2001) [Tech. Phys. **46**, 877 (2001)].
8. A. A. Mityureva, V. V. Smirnov, and O. A. Vorobiev, J. Phys. D **34**, L65 (2001).

9. V. V. Smirnov, O. A. Vorob'ev, A. A. Mityureva, and T. E. Primagina, Vestn. St-Peterb. Univ., Ser. 4: Fiz., Khim., No. 3 (20), 23 (2003).
10. V. V. Smirnov, O. A. Vorob'ev, A. A. Mityureva, and T. E. Primagina, Izv. Vyssh. Uchebn. Zaved., Élektronik., No. 2, 3 (2003).
11. M. Sanchez and J. M. Cowley, Ultramicroscopy **72**, 214 (1998).
12. J. M. Cowley, R. E. Dunin-Borkowski, and Hayward Michele, Ultramicroscopy **72**, 223 (1998).
13. J. M. Cowley, N. Ooi, and R. E. Dunin-Borkowski, Acta Crystallogr., Sect. A **55**, 533 (1999).
14. J. M. Cowley, Ultramicroscopy **81**, 47 (2000).
15. D. van Dyck, Adv. Electron. Electron Phys. **65**, 295 (1985).
16. L. D. Landau and E. M. Lifshitz, *Course of Theoretical Physics*, Vol. 3: *Quantum Mechanics: Non-Relativistic Theory* (Nauka, Moscow, 1989; Pergamon, New York, 1977).

Translated by A. Sidorova

Technical Physics, Vol. 50, No. 10, 2005, pp. 1353–1359. Translated from Zhurnal Tekhnicheskoĭ Fiziki, Vol. 75, No. 10, 2005, pp. 104–110.

SURFACE, ELECTRON AND ION EMISSION

Hysteresis of Pulsed Characteristics of Field Emission from Nanocarbon Films

A. V. Arkhipov, M. V. Mishin, G. G. Sominski, and I. V. Parygin

St. Petersburg State Polytechnical University, Politekhnicheskaya ul. 29, St. Petersburg, 195251 Russia

e-mail: arkhipov@rphf.spbstu.ru

Received January 18, 2005

Abstract—The dynamic characteristics of field emission from nanocarbon films subjected to microsecond electric field pulses are studied. The emission curves exhibit hysteresis the parameters of which are complicated functions of the pulse amplitude, length, and shape. The experimental results are explained based on a phenomenological model that assumes two-stage emission involving shallow acceptor levels localized near the emitting surface. © *2005 Pleiades Publishing, Inc.*

INTRODUCTION

The recent progress in fabrication of effective cold cathodes is mainly related to the use of nanodisperse carbon films (such as nanotubes, fulleroids, nanodiamonds, nanographites, etc.) serving as distributed field emitters of electrons [1–8]. According to the published data, the mean emission current density in such systems may exceed 1 A/cm^2, with emission becoming appreciable (e.g., 1 μA/cm^2) even in electric fields under 1 kV/mm (without regard to its enhancement due to the surface microrelief). The reasons for such a high emissivity of carbon materials are not yet fully understood. They are the clearest in the case of carbon nanotubes, where the decisive factor is considerable "geometric" enhancement of the field. The existing models explain not only the high values of the emission current from nanotubes but also fine effects, such as the deviation of the emission characteristics from the Fowler–Nordheim law at high currents [9]. At the same time, to gain insight into emission from nanocarbon films, whose surface structure cannot tangibly enhance the field, is a great challenge. The work function of carbon films is rather high (4.0–4.5 eV), and so their high emissivity has not yet found sound explanation. Nor have mechanisms underlying a number of phenomena typical of carbon films, such as hysteresis of the emission characteristics [10–13] and a rise in the emissivity upon thermal–field treatment [14], been understood.

Below, we present the results of experiments performed under typical operating conditions of advanced field-emission cathodes. The electric field was generated in a wide emission gap by applying a constant and/or pulsed potential difference up to 50 kV. The emitted electrons were taken out of the gap into a field-free region. During the measurements, the residual gas pressure was kept at a level of $(3–10) \times 10^{-7}$ Torr.

EXPERIMENTAL

The field-emission cathodes under study were made from two types of nanocarbon materials: (1) nanoporous carbon obtained by chemical extraction of silicon from silicon carbide at the Prikladnaya Khimiya Federal State Unitary Enterprise [14] and (2) powder of astralenes (heavy fulleroids with particles about 100 nm across) prepared by Astrin Holding Co.) [15].

The powders were fixed on the cathodes by electrophoresis, sintering in a ceramic matrix, or using a binder. After a chamber with the sample had been evacuated, the sample was annealed at 200–300°C and then subjected to thermal–field activation (for details, see [14]).

The setup used to measure the pulsed emission characteristics of distributed field-emission cathodes is schematically shown in Fig. 1. Emitter *1* with heater-activating emitter *2* is fixed behind a hole of diameter 3.3 mm in thin-walled (0.2 mm) protective electrode *3*. The surfaces of the emitter and protective electrode form the cathode of a quasi-plane emission gap. The

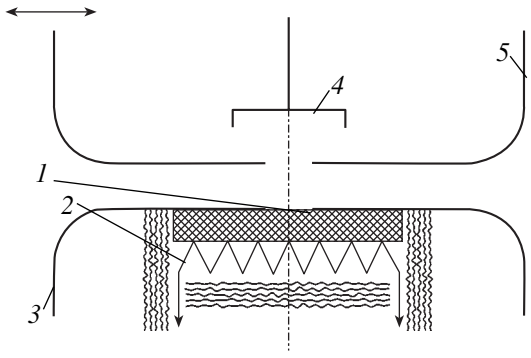

Fig. 1. Experimental setup for taking pulsed emission curves.

1063-7842/05/5010-1353$26.00

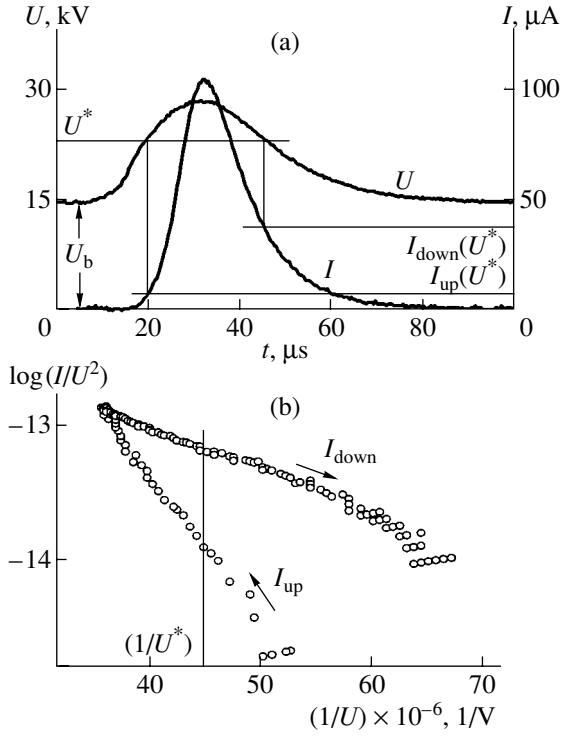

Fig. 2. (a) Typical waveforms of the voltage across the emission gap and of the emission current and (b) corresponding emission curve $I(U)$ plotted in the Fowler–Nordheim coordinates. The emitter is a nanoporous carbon film.

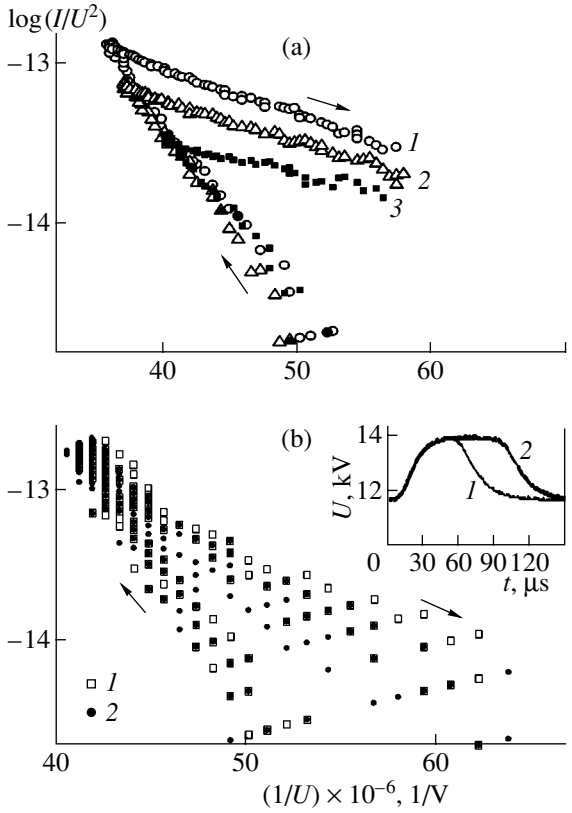

Fig. 3. Variation of the emission curves with the applied voltage parameters. (a) Curve *1*, which is the curve plotted in Fig. 2, vs. curves *2* and *3* obtained at the same amplitude and shape of the voltage pulsed component but lower values of voltage constant component U_b and (b) emission curves taken for voltage pulses with differing widths of their flat top. The waveforms of the pulses are shown in the inset. The emitter is a nanoporous carbon film.

gap width can be varied from 1.5 to 5.0 mm. Emission current collector *4* is placed inside anode *5* behind a hole 2.5 mm in diameter. Such an arrangement of the probing electrode eliminates the contribution of the emission from the protective electrode and considerably suppresses the contribution of capacitive crosstalk to the pulsed current signal recorded. The remaining portion of the capacitive current (crosstalk) was subtracted from the recorded signal at the stage of data processing.

HYSTERESIS OF THE EMISSION CHARACTERISTICS IN THE CASE OF "SMOOTH" VOLTAGE PULSES

Typical waveforms $U(t)$ of the voltage across the emission gap and of the current of collector *4*, $I(t)$, in the case of smooth bell-shaped applied voltage pulses are shown in Fig. 2a. A pair of such waveforms allows one to construct two *I–V* characteristics for the cases when the voltage rises and drops. We will call them the forward and backward branches of the emission curve and denote them as $I_{up}(U)$ and $I_{down}(U)$, respectively. The data taken of the nanocarbon films under study show a considerable divergence of these branches (hysteresis of the emission curve).

Figure 2b demonstrates the emission curve for the above pair of waveforms that is plotted in the Fowler–Nordheim coordinates. The straight lines $I_{up}(U)$ and $I_{down}(U)$ count in favor of the field mechanism of emission. According to the theory, the difference in their slopes may be viewed as evidence of a rapid change in the emission center parameters (work function *W*, effective emitting area, and/or field enhancement coefficient β) at the instant the rise in the field switches to its decrease. For any fixed voltage U^*, ratio $I_{down}(U^*)/I_{up}(U^*) > 1$, which indicates emitter activation during the pulse.

The experiments showed that the amount of hysteresis (which can be evaluated, e.g., through ratio $I_{down}(U^*)/I_{up}(U^*)$) depends on both the emitter properties and measurement conditions. Figure 3a illustrates the variation of the emission curve with constant bias voltage U_b. As U_b, as well as the maximal voltage and current (over the pulse), increases, the backward branch of the emission curve shifts almost parallel to itself toward the high current range. Since the forward branch remains virtually the same, one can state that the amount of hysteresis grows with the applied field and extracted current.

Such an increase in the emissivity of the samples during the pulse could be related, e.g., to a rise in the temperature of emission centers, reconfiguration of these centers under the action of the field, or desorption of gases from the surface. In any of these cases, one can expect that the activated state of the emitter will persist for a certain time after the current has been terminated and the amount of hysteresis will grow with the pulse width. However, experiments did not support these assumptions. Figure 3b illustrates that the emission curves taken for an extended voltage pulse (extended plateau where $U(t) \approx$ const) remain invariable. To measure the time within which the emission centers remain in the activated state, we carried out experiments using a pair of identical voltage pulses of duration $\tau = 3$ μs with delay Δt between them ranging from 10 to 500 μs (Fig. 4a). It turned out that, as the delay decreases to $\Delta t = \tau$, the initial section of the emission curve due to the latter pulse remains unchanged; i.e., the emitter becomes deactivated immediately after the current has been switched off. Figure 4b shows the case $\Delta t < \tau$, when both voltage pulses merge into a single pulse with two maxima. These plots make it possible to estimate the time interval within which the emitter passes into the inactive state (i.e., to the forward branch of the characteristic) after the voltage again starts rising from the dip between the peaks. This time does not exceed 5 μs, which is much shorter than the time taken to maintain the elevated emitter activity at a monotonic decay of the voltage at the end of the pulse. Thus, the characteristic time for which the system "memorizes" its state cannot be determined unambiguously. This time could be identified with the time of emitter cooling, time of recovery of its initial structure, time of deposition of a gas monolayer, etc. However, none of these speculations can explain the phenomenon of fast recovery of the emitter into the initial inactive state when the current is terminated or the applied voltage is increased. It seems that the emission mechanism described below might be helpful in theoretical comprehension of the experimental data obtained.

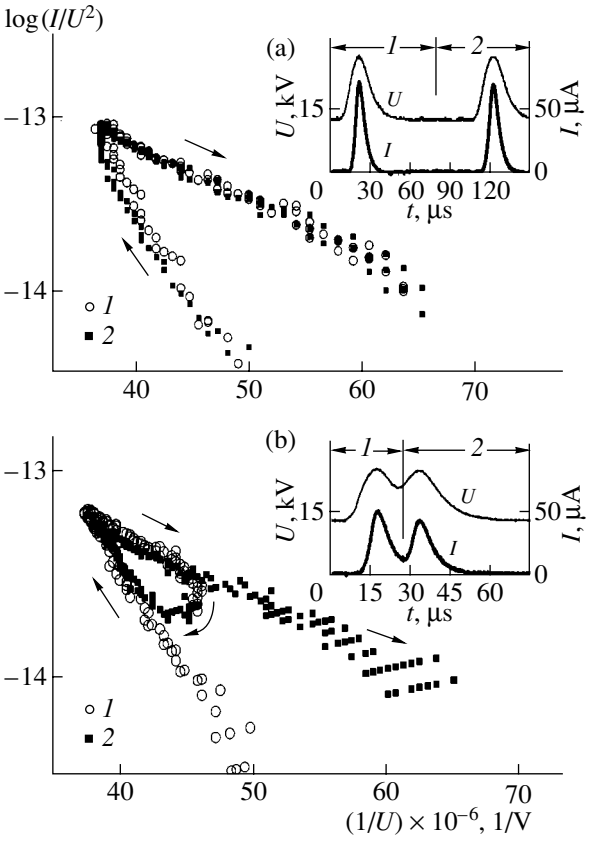

Fig. 4. Emission curves taken of the nanoporous carbon film using a pair of voltage pulses *1* and *2*. The delay between the pulses is Δt = (a) 100 and (b) 20 μs.

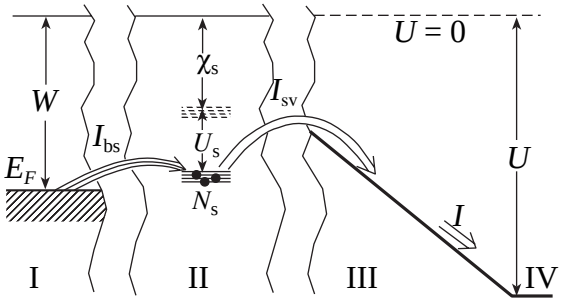

Fig. 5. To the model of emission mechanism: I, emitter volume; II, acceptor energy levels in the surface layer of the emitter; III, vacuum; and IV, anode. In the absence of voltage across the emission gap (dashed line), $U = 0$, $U_s = 0$, and $N_s = 0$.

TWO-STAGE MECHANISM OF EMISSION FROM CARBON FILMS

Let us suppose that the most effective mechanism of field emission from the films under study is indirect electron transfer from the conduction band of the emitter to a vacuum through intermediate states localized near the surface. Energy levels χ_s corresponding to these (initially vacant) surface acceptor states lie between the Fermi level and the level of a vacuum, $0 < \chi_s < W$ (Fig. 5). Their physical origin here is of no importance: they may be, e.g., surface electron states of graphite particles, levels in the conduction band of diamond or amorphous inclusions, etc. [3, 11, 16]. We assume that the emission current from these surface states into a vacuum is described by a formula similar to the Fowler–Nordheim formula,

$$I = I_{sv} = AN_s U^2 \exp(-a\chi_s^{3/2}/U), \qquad (1)$$

where a and A (as well as b, B, c, and C used below) are constants and N_s is the number of intermediate states occupied by electrons.

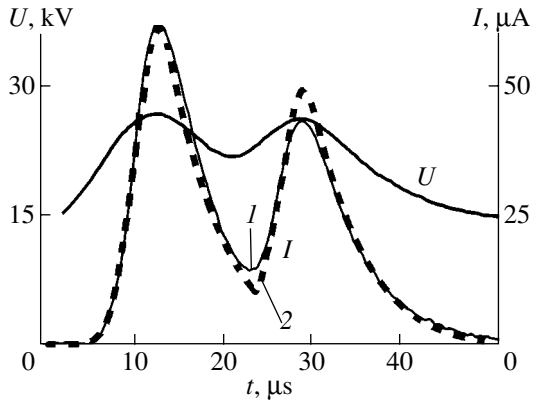

Fig. 6. (*1*) Emission current pulse measured in the experiment with a real voltage pulse (Fig. 4b) vs. (*2*) the result of numerical solution of Eqs. (1)–(4).

Quantity N_s can be determined from the difference between the currents from the bulk to the surface, I_{bs}, and from the surface to a vacuum, I_{sv},

$$N_s = \frac{1}{e}\int (I_{bs} - I_{sv})dt. \quad (2)$$

Electron transfer between the volume and surface states will be described by an asymmetrical (e.g., exponential) *I–V* characteristic,

$$I_{bs} = B(\exp(bU_s) - 1). \quad (3)$$

Quantity U_s has the dimension of voltage and can be viewed as a measure of variation of the energy position of the intermediate levels relative to the Fermi level in the emitter volume. This variation depends on two factors: penetration of the external electric field into the emitting film and charging of the film surface upon filling the acceptor levels. Accordingly,

$$U_s = U/c - eN_s/C. \quad (4)$$

With the constants chosen appropriately, solutions to the system of Eqs. (1)–(4) simulate the emission dynamics with a reasonable accuracy, including the case when voltage pulses are of an intricate shape (Fig. 6).

Based on the simulation results, one can describe the hysteresis observed experimentally in the following way. The emission current grows with the voltage applied to the emission gap (forward branch $I_{up}(U)$ of the emission curve), because the surface barrier becomes more transparent and also because the surface levels are filled with electrons (N_s rises) when the energy positions of these levels change. By contrast, when the current drops, backward branch $I_{down}(U)$, N_s remains nearly constant. If the voltage declines at a sufficiently high rate, electron escape into a vacuum cannot be regarded as an effective mechanism of electron emission from the intermediate states, since the emission current decreases with decreasing applied field. The curve $I_{bs}(U_s)$ is asymmetric by virtue of Eq. (3); therefore, electron transfer to the emitter volume is also ineffective. Thus, the elevated emissivity of the samples at the trailing edge of the voltage pulse can be explained by high population N_s of the intermediate states. Its value depends on the history, i.e., on the current and voltage attained during the pulse. The electrons may stay on the intermediate levels only if $U_s < 0$ (Eq. (3)). According to (4), this condition is provided by the action of the self-field of the excess (for a given external field) surface charge. When the voltage grows again, the condition $U_s < 0$ is quickly violated and electron exchange between the intermediate states and volume is regained (the volume–surface transition "opens"). In other words, we return to the forward branch of emission curve $I(U)$.

EMISSION ACTIVATION BY A RAPIDLY DAMPED ELECTRIC FIELD

From comparison of the experimental data and simulation results, we can conclude that the model proposed adequately describes the situation in a wide range of voltage pulse widths and amplitudes. The discrepancy between the model and experiment arises when the rate of change of the field exceeds a certain limiting value. In this case, the shape of the pulsed emission characteristics changes dramatically. Figure 7a compares the data obtained for voltages pulses *1* and *2* with almost identical amplitudes and widths, which differ in that voltage *2* applied to the gap decreases starting with a shallow but abrupt drop (the dashed areas in the waveform and emission characteristic). During this short time period and in several microseconds after it, the emission current continues to grow with decreasing voltage. The delay between the voltage and current maxima for the given pulse is about 8 μs. In the Fowler–Nordheim coordinates, this interval corresponds to that portion of the characteristic running roughly parallel to the line I = const (a shift to the right and upward). This portion is absent in the characteristic obtained for "smooth" pulse *1*. The discrepancy between these two characteristics that has been accumulated for this relatively short time period persists up to the applied voltage pulses are switched off. Thus, we can state that the interval of the fast electric field damping has a long-term activating effect on the emission from the samples. In this case, the hysteresis of the pulsed emission characteristic becomes more pronounced, but its main features (such as the dependence of the amount of hysteresis $I_{down}(U^*)/I_{up}(U^*)$ on the maximal current and voltage values during the pulse and the stability of the slope of the backward branch (Fig. 7b)) are retained. In terms of phenomenological model (1)–(4), the observed parallel shift of the emission curve backward branch should be related to a further increase in intermediate electron states population N_s rather than with the variation of the emission centers properties (which specify the slope of the backward branch). In terms of our model, this phenomenon can be

explained of the inhomogeneity of the emitter surface is taken into account.

Equations (1)–(4) are written on the assumption that electrons are emitted from a single emission center or from an ensemble of emission centers with similar characteristics. Actually, the surface of the film emitters under study is formed by nanoparticles of different shape and electronic structure [14]. However, both these statements do not necessarily contradict to each other. Let us assume that a major part of the emission current flows through active emission centers that are nanoparticles or their complexes. We also suppose that the shape and arrangement of the particles (complexes) provide a highest geometric amplification of the applied electric field, while the electronic structure of the centers involves the highest surface acceptor levels (which are characterized by lowest electron affinity χ_s), which serve as intermediate electronic states for field emission. For particles with deeper acceptor levels, emission, at the same electric field amplification, will be weaker because of a lower transparency of the energy barrier between the intermediate levels and vacuum. However, occupation of such nonemitting centers by electrons from deeper acceptor states in the bulk may begin at a lower strength of the applied field and result in the accumulation of a larger number of electrons on these centers. For a stationary or slowly varying electric field, these electrons insignificantly contribute to the emission. The electric field component parallel to the emitter surface acts on the electrons in the surface layer and collects them at the sites of field enhancement (at protrusions on the emitter), thereby separating these sites from each other. However, when the field abruptly decreases, the efficiency of such a separation drops and Coulomb repulsion of the electrons accumulated on the surface states in certain emitter regions (primarily, at the nonemitting sites of field enhancement) may cause their redistribution in favor of the emitting centers. In our opinion, it is such a redistribution of the electrons over the inhomogeneous nanocarbon film surface under the action of a nonstationary electric field that caused a long-term rise in the emissivity after the voltage across the gap had been drastically decreased [13].

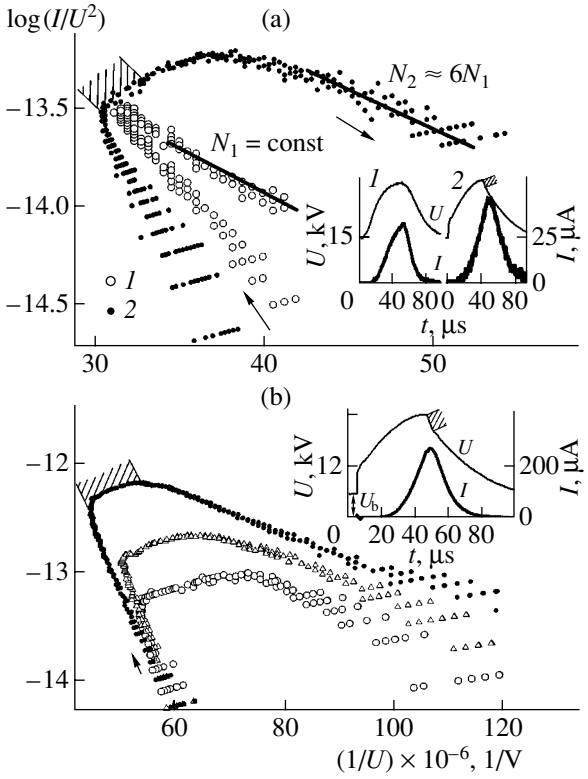

Fig. 7. (a) Emission curves taken of the nanoporous carbon film for (*1*) a smooth bell-shaped voltage pulse and (*2*) a voltage pulse containing a rapidly descending portion immediately after the maximum (dashed area by the waveform and emission curve). (b) Emission curves obtained for different constant bias U_b with the shape and amplitude of the pulsed component of the voltage remaining the same. The waveforms in the inset correspond to the pulse with the largest value of U_b. The source of emission is a small amount of astralenes appearing on the surface of the protective electrode (stainless steel) as a result of diffusion from the sample.

EFFECT OF THE VOLTAGE PULSE SHAPE ON EMISSION CHARACTERISTICS

The model dependences of the emission characteristics on the parameters of voltage pulses applied to the emission gap were verified in experiments with a number of carbon films.

According to formula (1), if the rate of fall of the voltage suffices to fulfill the condition $N_s \approx$ const, the slope of the backward branch of the emission curve plotted in the Fowler–Nordheim coordinates is bound to depend on only the emitter properties and to be independent of the parameters of the pulse. Figure 8 compares the results obtained for one of the samples when voltage pulses of different amplitude (Fig. 8a) and width (Fig. 8b) were applied to the gap. In spite of different rates of voltage variation, the slope of the backward branches in the two curves is the same. The situation with the forward branch is much more complicated. For instance, if the leading edge of the pulse is 5 μs wide (Fig. 8b), the rectilinear portion of the forward branch remains almost unresolved, since the emission current is detectable only near the maximum of the voltage (and increases approximately by a factor of 8 within the following 5 μs of voltage drop).

At a slow variation of the voltage, when electrons are not trapped by the acceptor levels and the condition $N_s \approx$ const does not hold, hysteresis of the emission characteristics is absent (see, e.g., the initial portion of the trailing edge of the pulse in Fig. 3b).

When the emitter properties change, the slope of the backward branch of the pulsed emission curve changes in a regular fashion. Figure 8c compares the data mea-

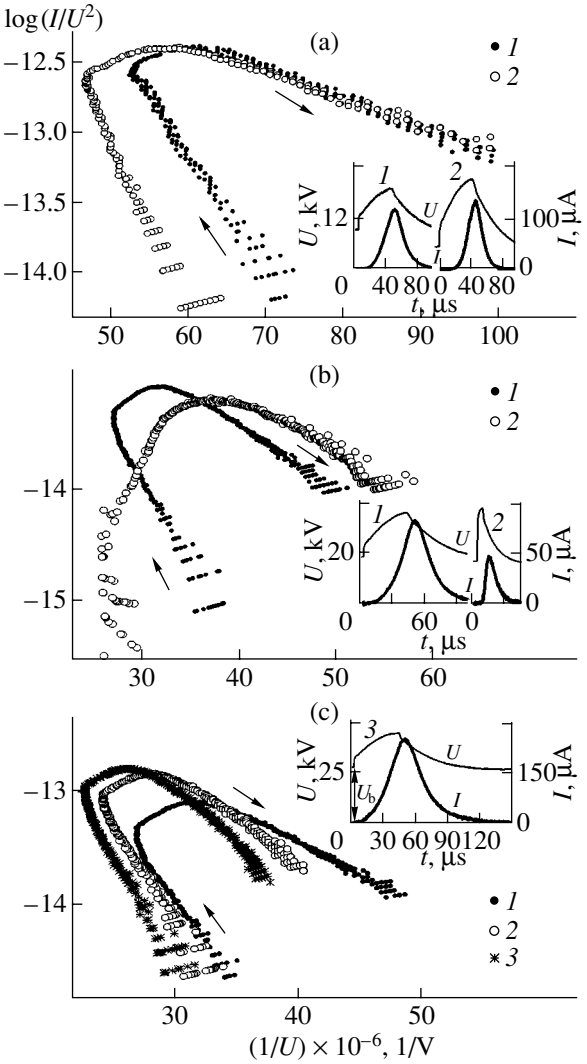

Fig. 8. (a) Emission curves taken at voltage pulses of different amplitude. The voltage and current waveforms are given in the inset; the emitter is the same as in Fig. 7b. (b) Emission curves taken at voltage pulses of different length; the emitter is a trace amount of nanoporous carbon on the surface of niobium foil. (c) Emission curves taken of the same surface during its degradation due to multiple breakdowns of the emission gap. Curve *1* corresponds to the "as-prepared" emitter. The measurements were carried out with the shape and amplitude of the voltage pulsed component remaining the same and with constant bias U_b gradually increasing (to compensate for the degradation of the sample's emissivity).

sured during the degradation of one of the samples. A general decrease in its emissivity is accompanied by a noticeable (severalfold) increase in the backward branch slope. The slope of the forward branch changes little, which may be explained by different current distributions among the emission centers for the intervals of voltage rise and fall. During the leading edge of the pulse, a lower transparency of the surface barrier for the centers with deep intermediate levels may be compensated for by a higher rate of occupation of these levels, as a result of which the emission current is distributed fairly uniformly among the centers. During the trailing edge of the pulse, the occupation of the intermediate layers evens out (e.g., due to the redistribution of the electrons under the action of the nonstationary field) and the emission concentrates at the centers with lowest χ_s. Probably, it is these centers that collapse first during the degradation of the film, which the form of the pulsed emission curves indicates.

CONCLUSIONS

Thus, our results indicate that field emission from heterogeneous carbon films is a complex process. To explain the hysteresis of the emission curves observed in the experiments, a model of indirect electron transfer to a vacuum is suggested that assumes the participation of intermediate acceptor-type electron states. The phenomenon of activation of emission from the carbon films under the action of a nonstationary field, which was revealed in the experiments, may explain the difficulties arising in fabrication of field film emitters intended for high-current operating mode and be helpful for development of new types of such emitters with improved performance.

ACKNOWLEDGMENTS

The authors are grateful to the Prikladnaya Khimiya Federal State Unitary Enterprise, Astrin Holding Co., and the Central Research Institute of Robotics and Technical Cybernetics for submitting nanocarbon samples, as well as to L.M. Baskin, P.G. Gabdulin, and B.A. Kriegel for encouragement, assistance, and valuable discussion.

The work was supported by the Russian Foundation for Basic Research, grant no. 05-02-17206.

REFERENCES

1. J.-M. Bonard, J.-P. Salvetat, T. Stockli, *et al.*, Appl. Phys. A **69**, 245 (1999).
2. A. A. Talin, K. A. Dean, and J. E. Jaskie, Solid-State Electron. **45**, 963 (2001).
3. A. N. Obraztsov, I. Yu. Pavlovskiĭ, and A. P. Volkov, Zh. Tekh. Fiz. **71** (11), 89 (2001) [Tech. Phys. **46**, 1437 (2001)].
4. N. S. Xu, Y. Chen, S. Z. Deng, *et al.*, J. Phys. D **34**, 1597 (2001).
5. J.-M. Bonard, M. Croci, C. Klinke, *et al.*, Carbon **40**, 1715 (2002).
6. G. Pirio, P. Legagneux, D. Pribat, *et al.*, Nanotechnology **13**, 1 (2002).
7. A. N. Obraztsov, A. P. Volkov, K. S. Nagovitsyn, *et al.*, J. Phys. D **35**, 357 (2002).
8. Yu. V. Gulyaev, Vestn. RAN **73**, 389 (2003).
9. J. Chen, H. Y. Chen, S. Z. Deng, *et al.*, in *Proceedings of the 49th International Field Emission Symposium (IFES'04), Seggau Castle, 2004*, p. 76.

10. A. V. Okotrub, L. G. Bulusheva, A. V. Gusel'nilov, *et al.*, Carbon **42**, 1099 (2004).
11. V. Konov, in *Proceedings of the 6th Biennial International Workshop on Fullerenes and Atomic Clusters (IWFAC'2003), St. Petersburg, 2003*, p. 10.
12. A. Arkhipov, M. Mishin, G. Sominski, and I. Parygin, in *Proceedings of the 10th ITG-Conference on Displays and Vacuum Electronics, Garmisch-Partenkirchen, 2004*, pp. 121–124.
13. A. V. Arkhipov, M. V. Mishin, G. G. Sominski, *et al.*, in *Proceedings of the 49th International Field Emission Symposium (IFES'04), Seggau Castle, 2004*, p. 102.
14. V. B. Bondarenko, P. G. Gabdullin, N. M. Gnuchev, *et al.*, Zh. Tekh. Fiz. **74** (10), 113 (2004) [Tech. Phys. **49**, 1360 (2004)].
15. V. A. Ponomarev, V. A. Nikitin, D. G. Letenko, *et al.*, in *Proceedings of the 6th Biennial International Workshop on Fullerenes and Atomic Clusters (IWFAC'2003), St. Petersburg, 2003*, p. 293.
16. S. A. Pshenichnyuk and Yu. M. Yumaguzin, Zh. Tekh. Fiz. **74** (5), 105 (2004) [Tech. Phys. **49**, 623 (2004)].

Translated by M. Lebedev

Technical Physics, Vol. 50, No. 10, 2005, pp. 1360–1362. Translated from Zhurnal Tekhnicheskoĭ Fiziki, Vol. 75, No. 10, 2005, pp. 111–114.

**SURFACE,
ELECTRON AND ION EMISSION**

High-Current Electron Gun with a Field-Emission Cathode and Diamond Grid

N. N. Dzbanovskiĭ, P. V. Minakov, A. A. Pilevskiĭ, A. T. Rakhimov, B. V. Seleznev, N. V. Suetin, and A. Yu. Yur'ev

Skobel'tsyn Research Institute of Nuclear Physics, Moscow State University, Vorob'evy Gory, Moscow, 119992 Russia

e-mail: Yuriev@dnph.phys.msu.su

Received January 28, 2005

Abstract—Control grids used in high-current devices with field emission cathodes should be made of an appropriate, "grid-grade" material. Such a material must offer a high mechanical strength, thermal conductivity, and electric conductivity. In addition, grids as thin as several microns must be available. As a grid material, boron-doped diamond is tested. © *2005 Pleiades Publishing, Inc.*

INTRODUCTION

Electron guns with field emission cathodes have a number of advantages over their thermionic counterparts, specifically, a much lower power consumption, a much higher speed of response, and a narrower energy spectrum of electrons emitted. It is of no less importance that field-emission electron sources operate at low (room) temperatures and, therefore, occupy the niche where thermionic emitters fail [1].

Along with the cathode, any device of this sort must incorporate elements providing independent control of the current and energy of the electron beam. The most popular control element is a grid. In thermionic electron guns, a modulating (control) grid usually blocks the electrons (it has a negative potential with respect to the cathode). In field emission devices, conversely, the first grid serves to extract the electrons and, thereby, to raise the field at the cathode surface to the point where electron emission starts. It is clear that the parameters of the cathode–grid assembly considerably depend on the physical characteristics of the field-emission cathode. In this study, an electron gun made of nanocrystalline carbon films [2, 3] is investigated for feasibility of its effective control.

The basic mechanism of electron emission in cold cathodes is tunneling through a potential surface barrier in a strong electric field. The probability of such a tunneling is specified by the fundamental properties of a material. In the best case, emission currents needed in practice are provided by extremely high electric fields (on the order of 10 MV/cm) on the emitter surface. The only way of generating such high electric fields is application of tip-shaped emitters. Then, even if an applied electric field is not too high, its value at the tips will be higher by several orders of magnitude because of geometrical enhancement. Many recent studies have shown that the most promising material for cold cathodes is films consisting of carbon nanoplatelets several nanometers in thickness and several microns in length and height that are oriented normally to the cathode surface [2, 3].

Let us note some problems associated with grid control in devices with field emission cathodes. To decrease the control voltage, it is necessary to decrease the cathode–grid distance down to several tens of microns (basically, this distance can be decreased to a fraction of a micron [4] by applying microelectronic technologies; however, the cost of the device inevitably increases in this case). At the same time, for a high uniformity of emission from the cathode surface and transparency of the grid for the current to be kept at a desired level, it is necessary to shrink a grid mesh and to increase its geometrical transparency. In this case, the mechanical strength and thermal conductivity of the grid decreases. The grid exceedingly heats up, sags, and eventually shorts the cathode.

Similar problems appear in modern high-power microwave tubes with a thermionic cathode operating in the high grid current regime. Therefore, in the majority of these devices, grids are made of refractory metals, such as W, Mo, Hf, Zr, and Ta. However, since the control grid is located near the cathode (which is especially true for microwave tubes), its temperature deformation (sagging) may change the grid–cathode gap and, thereby, the device performance. In this connection, the search for more appropriate grid materials intended for use in high-power electron vacuum devices is being actively pursued today. Pyrolytic graphite offering good thermal properties is one of the most promising materials. However, this material is extremely brittle and anisotropic; therefore, it is necessary to deposit it on a metallic substrate, which is a technological challenge. Moreover, thermal stresses arising at the points where the graphite grid is in contact with the metallic

1063-7842/05/5010-1360$26.00

holder cause its failure. Other disadvantages of grids made of pyrolytic graphite are their rough surface, giving rise to secondary electron emission from the grid, and a poor high-voltage resistance. The roughness may be due to stuck graphite particles and also to the sharp irregular edges of holes after laser drilling. In the latter case, the carbon condensing near the holes forms granules on or near the edges. In general, formation of carbon particles (or particles of another sort) upon material recrystallization is typical not only of laser cutting but of any (ion, electron-beam, spark, mechanical, and electromechanical) cutting method. To remove these particles, graphite grids are annealed in a chemically active atmosphere (air, oxygen, or an oxygen–nitrogen mixture) at lower pressures and temperatures of 900–1000°C. This all complicates the preparation and use of grids made of pyrolytic graphite.

Thus, to eliminate the problems discussed above, it is necessary to use a grid made of a material with a high mechanical strength, low thermal expansion coefficient, and high thermal conductivity. In addition, the material of choice must be well conducting in order to avoid charging effects. Based on the aforesaid, we proposed that control and focusing grids be made of a doped diamond film, which is known to offer unique thermal and mechanical properties and a high isotropic strength. Such a film heteroepitaxially grown on an iridium film (related growth techniques have been recently developed) may be both single- and polycrystalline.

A thin (2–5 μm) diamond grid placed near the cathode (at a distance of about 10 μm) would make it possible to reduce the control voltage and time of flight of electrons in the cathode–grid gap. This is central to using the grid in microwave (operating at frequencies above 2 GHz) devices (for comparison, the distance between a thermionic cathode and a control metal grid in electron vacuum devices is usually greater than 100 μm).

DIAMOND GRIDS

Diamond is well known as a material featuring a high thermal conductivity, mechanical strength, and corrosion stability, together with other remarkable properties, which makes it promising for a wide range of applications. Moreover, pure diamond has an extremely low electrical conductivity. For diamond to acquire *p*-type conductivity, it is doped by boron, which is easily activated even at room temperature [5].

Electron-beam-controlling grids may be plane, cylindrical, or of any other geometry depending on the type of device. A diamond grid may be obtained either by etching a continuous diamond membrane or by selective CVD. Doped diamond films were deposited in a reactor with a microwave-discharge-excited active medium (the frequency is 2.45 GHz; the power delivered to the discharge, 1 kW). For details concerning the reactor and deposition method, see [6].

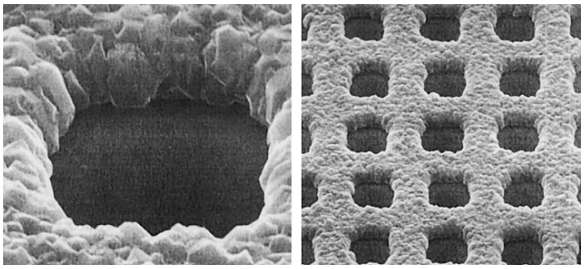

Fig. 1. Diamond grid visualized with an electron microscope. The transparency is about 50%.

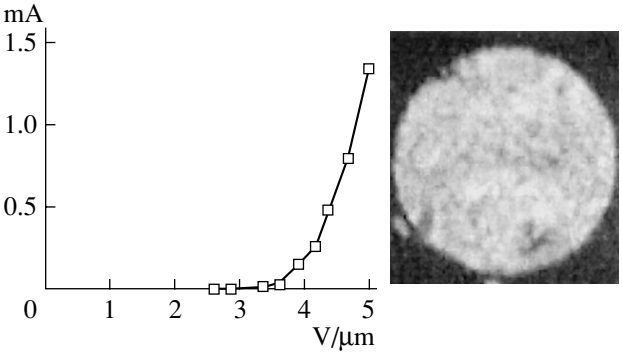

Fig. 2. Emission characteristic for the diode scheme with a phosphor screen.

A typical example of a grid thus produced is shown in Fig. 1. It is seen that the grid is fairly homogeneous and has a rather high transparency. Raman spectroscopy and X-ray diffraction examinations of the films showed that the grids consist of high-quality diamond with a low content of nondiamond phases.

FIELD-EMISSION TRIODE WITH A DIAMOND GRID

In this case, we used a field-emission cathode similar to that described in [2]. The diameter of the emission spot was 2.3 mm ($S = 0.04$ cm^2). The emission characteristics of this cathode were preliminary investigated in a diode scheme with a phosphor screen. The results of measurements are presented in Fig. 2. As is seen, the emission current distribution is uniform and the density of emission centers is high. This cathode was subsequently used in a triode scheme with a diamond grid.

The gap between the cathode and diamond grid was equal to 40 μm. Such a gap, on the one hand, provided the uniform distribution of the electric field intensity over the cathode and, on the other hand, made it possible to control the electron beam by applying low potentials to the grid.

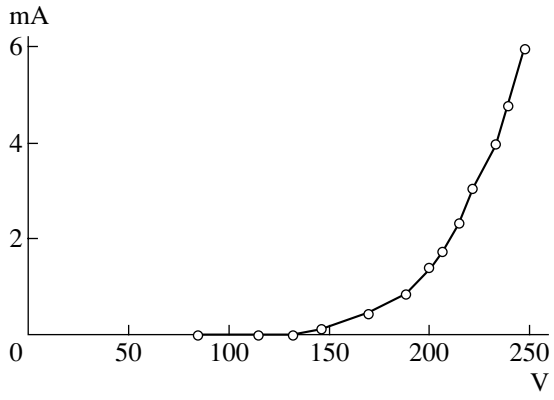

Fig. 3. *I–V* characteristic for the 40-μm gap.

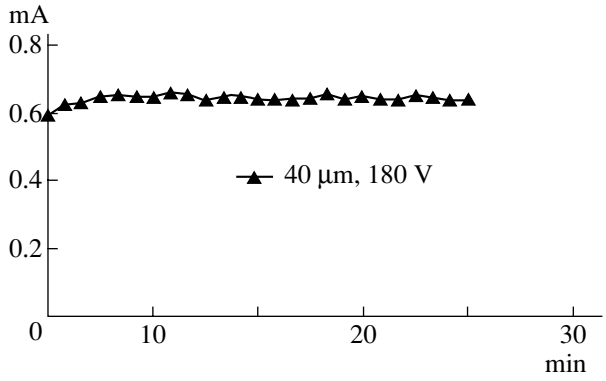

Fig. 4. Aging in the dc regime for the 40-μm gap.

The experiments were performed in both the continuous and pulsed regimes. In the latter case, negative pulses with a duration of 340 μs and a frequency of 50 Hz were applied to the cathode. Note that the results obtained for the diamond grid in both regimes were virtually the same (in contrast to metallic grids), which indicates a high stability of diamond grids. A typical *I–V* characteristics taken for one of the grids in the pulsed regime is depicted in Fig. 3. As follows from Figs. 2 and 3, the *I–V* characteristics in the diode and triode schemes nearly coincide, which suggests a high uniformity of the electric field over the cathode surface.

In a number of applications, of primary importance is the modulating voltage amplitude rather than the total cathode–grid potential difference. In our case, the current could be modulated starting from only the ascending portion of the curve, for example, from 3 V/μm. As is seen from Fig. 3, in the case of the 40-μm gap, a current of 6 mA can be completely modulated by voltage difference $\Delta U = 120$ V (Fig. 3). This value corresponds to a current density at the cathode of 150 mA/cm^2 and a power density at the grid of about 0.3 W/cm^2.

Our measurements showed that the transparency of the grid for electrons is 50%, which exactly coincides with the geometric transparency. The grid withstood a pulsed current density from the cathode of 1 A/cm^2 at a voltage of 1.5 kV. None of the many metallic grids investigated made a close approach to such values.

The operating stability of the diamond grid was investigated in the dc regime for a gap of 40 μm. The measurements of the long-term current stability are presented in Fig. 4. It is seen that the current is stable: no marked oscillations (including in the pulsed regime) are observed. Note that similar experiments with metallic grids invariably showed the presence of mechanical vibration of a grid due to its thermal expansion and sagging in a strong electric field.

CONCLUSIONS

Doped CVD-grown diamond grids are proposed to be used as extracting grids of field-emission cathodes. Comparative analysis of diamond and metallic grids is presented.

From our measurements, it follows that the diamond grid withstands a pulsed current density from the cathode of 1 A/cm^2 at a voltage of 1.5 kV. None of the metallic grids investigated made a close approach to such values.

The possibility of controlling the field-emission current up to 150 mA/cm^2 with a modulation voltage of no higher than 120 V is demonstrated.

ACKNOWLEDGMENTS

This work was supported by "Program of the President of the Russian Federation in Support of Leading Scientific Schools," grant no. NSh-1713.2003.2.

REFERENCES

1. H. H. Busta, J. M. Chem, Z. Shen, *et al.*, J. Vac. Sci. Technol. B **21**, 344 (2003).
2. A. A. Bliablin, A. V. Pilevsky, A. N. Rakhimov, *et al.*, in *Proceedings of the IEEE International Vacuum Electron Sources Conference, Orlando, 2000*, p. 44.
3. H. H. Busta, R. J. Espinosa, A. T. Rakhimov, *et al.*, Solid-State Electron. **45**, 1039 (2001).
4. H. H. Busta, D. Furst, S. Samorodov, *et al.*, Appl. Phys. Lett. **78**, 3418 (2001).
5. F. Fontaine, E. Gheeraert, and A. Deneuville, Diamond Relat. Mater. **5**, 753 (1996).
6. V. V. Dvorkin, N. N. Dzbanovskiĭ, P. V. Minakov, *et al.*, Fiz. Plazmy **29**, 851 (2003) [Plasma Phys. Rep. **29**, 789 (2003)].

Translated by Yu. Vishnyakov

Technical Physics, Vol. 50, No. 10, 2005, pp. 1363–1365. Translated from Zhurnal Tekhnicheskoĭ Fiziki, Vol. 75, No. 10, 2005, pp. 115–117.

SHORT COMMUNICATIONS

Electro- and Magnetostatic Fields in Media with a Nonuniform Velocity

N. N. Rozanov and G. B. Sochilin

Research Institute of Laser Physics, St. Petersburg, 199034 Russia

e-mail: rosanov@ilph.spb.su

Received December 2, 2003

Abstract—A motion-induced magnetic or electric field is calculated by the integral method in the first order of smallness in the ratio of the motion velocity to the speed of light for homogenous media with an arbitrary stationary velocity distribution that are placed in static electric or magnetic fields. For the case of rotation of a sphere, the validity of the results is corroborated by comparing with a solution obtained by joining the fields in the moving and quiescent parts of the medium. Estimates suggest the feasibility of experimentally observing this effect of continuum electrodynamics. © *2005 Pleiades Publishing, Inc.*

The electrodynamics of moving media, which is based on the Maxwell equations and Minkowski material equations [1–3], basically allows solving a wide number of problems [4, 5]. However, the medium–medium interface is, as a rule, considered plane, cylindrical, or spherical [3–5], because using continuity conditions at the interface in the general case poses great difficulty.

Generally speaking, continuity conditions at the interface are not independent of the Maxwell equations. On the contrary, they are consequences of the Maxwell equations. These conditions are dropped out if we introduce a smooth transition range between the parameters of the media and then shrink this range down to zero. Using such an approach, we have recently considered the relativistic scattering (diffraction) of electromagnetic radiation by nonuniformities of the velocity of a dielectric medium [6]. We assumed that the medium is homogenous and isotropic but part of the medium rotates with some angular velocity. A solution to wave equations of the retarded potential type that was obtained in the first order of smallness in the ratio between the velocity of the medium and speed of light allowed us to find, in the integral form, the scattered field for an arbitrary distribution of the velocity. In [6], we also estimated the maximum velocity at which relativistic effects dominate over those caused by the mechanical deformation of a body (dynamooptical effects [3]).

The aim of this paper is to demonstrate the possibility of using a similar integral approach (without invoking continuity conditions at the interface) for determination of the static electric and magnetic field intensities in the case of an arbitrary (to some extent) distribution of the velocity of a homogenous medium. To be specific, we shall consider the case of the stationary (time-independent) velocity distribution, which occurs, for example, when part of an axisymmetric body rotates about a symmetry axis. In this case, the electric and/or magnetic field remains stationary in the moving medium too. As in [6], the permittivities and permeabilities of the moving and quiescent parts are assumed to be the same and effects of the first order of smallness in the ratio between the velocity of the medium and the speed of light are analyzed. Attendant effects associated with mechanical stresses due to rotation are neglected (for the conditions when they can be neglected, see [6]). We will show that, in the case at hand (a rotating sphere), for which a solution can also be found by the standard method using continuity conditions at the interface between the moving and quiescent parts of the medium [3], both approaches yield consistent results.

For static fields, the "differential" Maxwell equations have the form

$$\mathrm{div}\mathbf{B} = 0, \quad \mathrm{curl}\mathbf{E} = 0, \quad \mathrm{div}\mathbf{D} = 0, \quad \mathrm{curl}\mathbf{H} = 0. \tag{1}$$

Here, **E** and **H** are the electric and magnetic fields and **D** and **B** are the electric and magnetic inductions. The Minkowski material equations are used in the approximation form, i.e., in the first order of smallness in small parameter **v**/*c*, where **v** is the velocity of the medium (hereafter velocity) and *c* is the speed of light in vacuum,

$$\mathbf{D} = \varepsilon\mathbf{E} + \frac{\varepsilon\mu - 1}{c}[\mathbf{v}\times\mathbf{H}], \ \mathbf{B} = \mu\mathbf{H} + \frac{\varepsilon\mu - 1}{c}[\mathbf{E}\times\mathbf{v}]. \tag{2}$$

Permittivity ε and permeability μ are constant and correspond to the quiescent medium. In such a definition of the problem, relativistic effects show up most vividly.

Let us consider the case when the medium moves with a coordinate-dependent velocity in a uniform

1063-7842/05/5010-1363$26.00

static electric field with intensity E_0 = const. In the zeroth order of smallness in v/c, the electric field coincides with $\mathbf{E}_0$ and the magnetic field is $\mathbf{H}_0 = 0$. In the first order of smallness in v/c, material equations (2) take the form

$$\mathbf{D}_1 = \varepsilon\mathbf{E}_1, \quad \mathbf{B}_1 = \mu\mathbf{H}_1 + \frac{\varepsilon\mu - 1}{c}[\mathbf{E}_0 \times \mathbf{v}]. \tag{3}$$

Then, from Maxwell equations (1) it follows that

$$\mathrm{div}\mathbf{H}_1 = -\frac{\varepsilon\mu - 1}{\mu c}\mathrm{div}[\mathbf{E}_0 \times \mathbf{v}]. \tag{4}$$

By virtue of the second equation in (1), the magnetic field is irrotational and has the potential

$$\mathbf{H}_1 = -\mathrm{grad}\Psi. \tag{5}$$

In view of (4), the potential has the form

$$\begin{aligned}\Psi(\mathbf{r}) &= -\frac{1}{4\pi}\int\frac{\mathrm{div}\mathbf{H}_1(\mathbf{r}')}{R}d\mathbf{r}' \\ &= \frac{\varepsilon\mu - 1}{4\pi\mu c}\int\frac{\mathrm{div}[\mathbf{E}_0 \times \mathbf{v}(\mathbf{r}')]}{R}d\mathbf{r}',\end{aligned} \tag{6}$$

where $R = |\mathbf{r} - \mathbf{r}'|$ is the distance between point $\mathbf{r}$ at which the field is calculated and vector of variable of integration $\mathbf{r}'$.

Since for uniform electric field $\mathbf{E}_0$ we have

$$\mathrm{div}[\mathbf{E}_0 \times \mathbf{v}] = -(\mathbf{E}_0 \cdot \mathrm{curl}\mathbf{v}), \tag{7}$$

Eq. (6) can be recast as

$$\Psi(\mathbf{r}) = -\frac{\varepsilon\mu - 1}{4\pi\mu c}\int\frac{(\mathbf{E}_0 \cdot \mathrm{curl}\mathbf{v}(\mathbf{r}'))}{R}d\mathbf{r}'. \tag{8}$$

Equations (6) and (8) are the general solution to the problem for an arbitrary distribution of the velocity. In the case of rotation of an axisymmetric body, the velocity experiences a jump at the boundary,

$$\mathbf{v} = \mathbf{u}(\mathbf{r})\Phi(\mathbf{r}), \quad \Phi(\mathbf{r}) = \begin{cases}1 & \mathbf{r} \in V, \\ 0 & \mathbf{r} \notin V.\end{cases} \tag{9}$$

Since

$$\begin{aligned}\mathrm{curl}(\Phi(\mathbf{r})\mathbf{u}(\mathbf{r})) &= \Phi\mathrm{curl}\mathbf{u} + [\mathrm{grad}\Phi \times \mathbf{u}], \\ \mathrm{grad}\Phi &= -\mathbf{n}\frac{d\Phi}{dl} = -\mathbf{n}\delta(l - l_s),\end{aligned} \tag{10}$$

where l is the coordinate along the normal to the surface, l_s is its value on the surface, and $\mathbf{n}$ is the unit vector normal to the surface, the integral on the right of Eq. (8) reduces to a sum of two integrals, one of which is taken over the volume of the rotating part and the other over the surface of this part,

$$\Psi = \frac{\varepsilon\mu - 1}{4\pi\mu c}\left\{\int_V dV\frac{(\mathbf{E}_0 \cdot \mathrm{curl}\mathbf{u})}{R} - \int_S dS\frac{(\mathbf{E}_0 \cdot [\mathbf{n} \times \mathbf{u}])}{R}\right\}. \tag{11}$$

Let us apply the above results to the case of a sphere of radius a rotating with angular velocity Ω directed along the z axis; i.e., $\Omega = (0, 0, \Omega)$. We assume that the external electric field is also directed along the z axis, $\mathbf{E}_0 = (0, 0, E_0)$. Then, the linear velocity is $\mathbf{u} = [\Omega \times \mathbf{r}]$, $(\mathbf{E}_0 \cdot \mathrm{curl}\mathbf{u}) = 2E_0\Omega$, and $(\mathbf{E}_0 \cdot [\mathbf{n} \times \mathbf{u}]) = E_0\Omega(n_x x + n_y y)$. In view of axial symmetry of the problem, the integrals in Eq. (11) can be reduced to the one-dimensional form. Eventually, the magnetic potential outside the sphere will have the form

$$\Psi = -\frac{4}{15}\frac{\varepsilon\mu - 1}{\mu c}E_0\Omega\frac{a^5}{r^3}\left(1 - 3\frac{z^2}{r^2}\right). \tag{12}$$

Here, r is the distance from the center of the sphere. Similarly, for a dielectric sphere rotating in a constant magnetic field with intensity H_0 directed along the axis of rotation, we obtain electric potential Φ outside the sphere in the form

$$\Phi = \frac{4}{15}\frac{\varepsilon\mu - 1}{\varepsilon c}H_0\Omega\frac{a^5}{r^3}\left(1 - 3\frac{z^2}{r^2}\right). \tag{13}$$

For comparison with the conventional approach, which is based on joining the solutions at the interface between the moving and quiescent media, it is necessary to generalize the solution of the problem obtained in [3], where a sphere rotated in a vacuum (i.e., it was assumed that $\varepsilon^{(e)} = 1$ and $\mu^{(e)} = 1$ outside the rotating sphere). For an external magnetic field with intensity $\mathbf{H}_0$ and arbitrary values of $\varepsilon^{(e)}$ and $\mu^{(e)}$ of the environment, electric field potential Φ outside the sphere can be expressed by

$$\Phi = \frac{1}{2}\sum_{i,k=1}^{3} D_{ik}\frac{n_i n_k}{r^3}, \tag{14}$$

where

$$\begin{aligned}D_{ik} &= -\frac{a^5}{c}\frac{3(\varepsilon^i\mu^i - 1)\mu^e}{(3\varepsilon^{(e)} + 2\varepsilon^{(i)})(2\mu^{(e)} + \mu^{(i)})} \\ &\times\left\{H_{0i}\Omega_k + H_{0k}\Omega_i - \frac{2}{3}\delta_{ik}(\mathbf{H}_0, \Omega)\right\}.\end{aligned} \tag{15}$$

When the permittivities of the environment and rotating sphere are equal to each other, Eq. (15) takes the form

$$\begin{aligned}D_{ik} &= -\frac{a^5}{c}\frac{(\varepsilon\mu - 1)}{5\varepsilon} \\ &\times\left\{H_{0i}\Omega_k + H_{0k}\Omega_i - \frac{2}{3}\delta_{ik}(\mathbf{H}_0, \Omega)\right\}.\end{aligned} \tag{16}$$

Similarly, for a sphere rotating in a uniform electric field, the magnetic field potential outside the sphere is given by

$$\Psi = \frac{1}{2}\sum_{i,k=1}^{3} B_{ik}\frac{n_i n_k}{r^3}, \tag{17}$$

where

$$B_{ik} = \frac{a^5}{c}\frac{3(\varepsilon^{(i)}\mu^{(i)}-1)\varepsilon^{(e)}}{(3\mu^{(e)}+2\mu^{(i)})(2\varepsilon^{(e)}+\varepsilon^{(i)})} \times\left\{E_{0i}\Omega_k + E_{0k}\Omega_i - \frac{2}{3}\delta_{ik}(\mathbf{E}_0, \Omega)\right\}. \quad (18)$$

When the permeabilities inside and outside the sphere are the same, we have

$$B_{ik} = \frac{a}{c}\frac{(\varepsilon\mu-1)}{5\mu}\left\{E_{0i}\Omega_k + E_{0k}\Omega_i - \frac{2}{3}\delta_{ik}(\mathbf{E}_0, \Omega)\right\}. \quad (19)$$

It is easy to show that, when the axis of rotation is aligned with the constant field direction on the outside, the integrals corresponding to Eqs. (16) and (19) turn into Eqs. (12) and (13), respectively, which confirms the validity of the integral approach.

As one more example, we give the magnetic potential at the axis of rotation of a circular cylinder with base radius a and length $2h$ that was calculated at a point z distant from the center of inertia of the cylinder. Integrating over the surface and volume of the cylinder in Eq. (11) yields

$$\Psi_c = E_0\Omega\{(z+h)\sqrt{(z+h)^2+a^2} + (z-h)\sqrt{(z-h)^2+a^2} - 4zh\}. \quad (20)$$

Let us compare the magnetic potentials of the sphere, Ψ_{sp}, and cylinder, Ψ_c, at the axis of rotation for a point z distant from the center of inertia, $z \gg a, h$. From Eqs. (12) and (20), we obtain

$$\Psi_{sp}(0, 0, z) = \frac{2}{5\pi}\frac{(\varepsilon\mu-1)}{\mu c}\frac{a^2 V_{sp}}{z^3}E_0\Omega, \quad (21)$$

$$\Psi_c(0, 0, z) = \frac{1}{8\pi}\frac{(\varepsilon\mu-1)}{\mu c}\frac{a^2 V_c}{z^3}E_0\Omega, \quad (22)$$

where V_{sp} and V_c are the volumes of the sphere and cylinder, respectively.

Thus, the integral approach allows one to determine the electro- and magnetostatic fields for media with a fairly nonuniform velocity distribution. The use of the perturbation theory here is justified by the smallness of the velocity relative to the speed of light. For a sphere rotating in a uniform magnetic or electric field applied to such media, the integral approach is in agreement with the conventional one, which is based on joining solutions inside the moving and quiescent media.

Note that experiments of such a type concerning the electrodynamics of moving media are of undeniable importance, since relevant experimental data are sparse and a number of theoretical issues call for further discussion (see, e.g., different approaches by Minkowski and Abragam stated in monograph [1]). The results of earlier investigations [7–9], as well as our estimates [6, 10], indicate that the above effect concerned with the electrodynamics of moving media can be verified experimentally. In fact, the intensity of the static electric field under rotation of a sphere (cylinder) in the magnetic field and that of the static magnetic field for a sphere (cylinder) rotating in the electric field are determined through the gradients of the corresponding potentials. Their maximal values are estimated as $(u/c)H_0$ and $(u/c)E_0$, where $u = \Omega a$ is the maximum linear velocity on the spherical (cylindrical) surface. The results of a more rigorous calculation are the following. The static permittivity, for example, of glass varies from 5.5 to 11 (depending on its type) [11], and its permeability is close to unity. Then, for $u \sim 10^3$ cm/s, the electric field intensity due to rotation of a sphere in the magnetic field is $\sim 10^{-7}H_0$, while for a sphere rotating in a uniform electric field, the induced magnetic field intensity is $\sim 10^{-6}E_0$ (compare the denominators of the first fractions in (12) and (13)). It seems that such intensities can be detected experimentally.

ACKNOWLEDGMENTS

The authors thank L.S. Dolin for encouraging discussions.

This work was supported by the Russian Foundation for Basic Research, grant no. 05-02-16342.

REFERENCES

1. W. Pauli, *The Theory of Relativity* (Pergamon, Oxford, 1958; Gostekhizdat, Moscow, 1983).
2. I. E. Tamm, *Foundations of the Theory of the Electricity* (Nauka, Moscow, 1989) [in Russian].
3. L. D. Landau and E. M. Lifshitz, *Course of Theoretical Physics*, Vol. 8: *Electrodynamics of Continuous Media* (Nauka, Moscow, 2001; Pergamon, New York, 1984).
4. B. M. Bolotovskiĭ and S. N. Stolyarov, in *Einstein Studies 1974* (Nauka, Moscow, 1976), pp. 179–275 [in Russian]; Usp. Fiz. Nauk **114**, 569 (1974).
5. S. N. Stolyarov, in *Einstein Studies 1975–1976* (Nauka, Moscow, 1978), pp. 152–215 [in Russian].
6. N. N. Rozanov and G. B. Sochilin, Opt. Spektrosk. **94**, 624 (2003) [Opt. Spectrosc. **94**, 569 (2003)].
7. A. M. Glutsyuk, Zh. Tekh. Fiz. **36**, 413 (1966) [Sov. Phys. Tech. Phys. **11**, 305 (1966)].
8. Ya. B. Zel'dovich, Zh. Éksp. Teor. Fiz. **62**, 2076 (1972) [Sov. Phys. JETP **35**, 1085 (1972)].
9. J. van Bladel, *Relativity and Engineering* (Springer, Berlin, 1984).
10. N. N. Rozanov and G. B. Sochilin, *Problems of Coherent Nonlinear Optics* (ITMO, St. Petersburg, 2004), pp. 118–153 [in Russian].
11. *Tables of Physical Quantities*, Ed. by I. K. Kikoin (Atomizdat, Moscow, 1976) [in Russian].

Translated by M. Astrov

Technical Physics, Vol. 50, No. 10, 2005, pp. 1366–1369. Translated from Zhurnal Tekhnicheskoĭ Fiziki, Vol. 75, No. 10, 2005, pp. 118–121.

SHORT COMMUNICATIONS

Electromagnetic Field of a Dipole in an Anisotropic Medium

A. O. Savchenko* and O. Ya. Savchenko**

** Institute of Computational Mathematics and Mathematical Geophysics, Siberian Division, Russian Academy of Sciences, Novosibirsk, 630090 Russia*

*** Novosibirsk State University, ul. Pirogova 2, Novosibirsk, 630090 Russia*

e-mail: savch@ommafaol.sscc.ru

Received July 22, 2004

Abstract—The harmonically varying field of point electric and magnetic dipoles in an anisotropic medium with an anisotropic axis is found for the first time. © *2005 Pleiades Publishing, Inc.*

In this work, we for the first time give a complete and, more importantly, exact solution to the Maxwell equations for the radiation of point electric and magnetic dipoles in a homogeneous anisotropic medium where the conductivity and permittivity along the anisotropy axis differ from those in the transverse directions. The solution is found for any orientation of the dipole relative to the anisotropy axis. When finding the electromagnetic field of the dipole, which varies by a harmonic law, we apply two approaches, one of which is suggested in [1]. Here, the basic Maxwell equations, where displacement currents are ignored, are reduced to equations for vector potential that allow determination of these currents. The second approach [2–4] consists in converting the basic set of Maxwell equations (reduced at any point of the domain) to an equation for the electric field strength and applying the Fourier transformation to this equation. In this case, finding of the transforms of the electric field components is reduced to solving a set of linear algebraic equations and the field components themselves can be determined by applying the inverse Fourier transformation to their transforms. However, the creators of such an approach, also ignoring displacement currents, restricted the analysis to finding the transforms of only two electric field components and one magnetic field component [3], not explaining how it was obtained. In this work, we for the first time derive an exact solution to the Maxwell equation for electric and magnetic dipoles in an anisotropic medium, which allows for displacement currents, contrary to works [1–4]. To solve the problem, we chose the second approach. First, it is more general and does not require the presence of the anisotropy axis. Second, studying the electromagnetic field near the dipole is unnecessary in this approach.

Let a homogeneous anisotropic medium contain a point dipole in which the density of extraneous electric, $\mathbf{j}^E$, and magnetic, $\mathbf{j}^H$, currents varies by a harmonic law, $\exp(-i\omega t)$. We choose a rectangular coordinate system with the origin at the site of the dipole and assume that the conductivity and permittivity components in the tangential x and z directions are the same (γ_t and ε_t, respectively) and the respective components in the normal y direction are γ_n and ε_n. Note at once that the choice of direction where the conductivity differs is of no significance, since an otherwise stated problem is reduced to that under consideration merely by coordinate transformation. Let the electromagnetic field of the dipole also vary by a harmonic law, $\exp(-i\omega t)$. Then, according to the Maxwell equations, the amplitudes of the electric, $\mathbf{E}$, and magnetic, $\mathbf{H}$, fields of the dipole satisfy the equation [5]

$$\operatorname{curl}\mathbf{H} = \hat{\sigma}E + \mathbf{j}^E - i\omega\hat{\varepsilon}\mathbf{E}, \quad (1)$$

$$\operatorname{curl}\mathbf{E} = i\omega\mu\mathbf{H} - \mathbf{j}^H. \quad (2)$$

Here, $\hat{\sigma}$, $\hat{\varepsilon}$, and μ are the conductivity tensor, permittivity tensor, and permeability of the medium, respectively. Matrices $\hat{\sigma}$ and $\hat{\varepsilon}$ have the diagonal form

$$(\sigma)_{11} = (\sigma)_{33} = \gamma_t, \quad (\sigma)_{22} = \gamma_n,$$
$$(\sigma)_{kl} = 0 \quad (k \neq l),$$

$$(\varepsilon)_{11} = (\varepsilon)_{33} = \varepsilon_t, \quad (\varepsilon)_{22} = \varepsilon_n,$$
$$(\varepsilon)_{kl} = 0 \quad (k \neq l).$$

Applying the curl operator to both sides of Eq. (2), we obtain

$$\operatorname{curl}\operatorname{curl}\mathbf{E} - i\omega\mu\hat{\sigma}\mathbf{E} - \omega^2\mu\hat{\varepsilon}\mathbf{E} = i\omega\mu\mathbf{j}^E - \operatorname{curl}\mathbf{j}^H. \quad (3)$$

The direct and inverse Fourier transformations of function $f(x, y, z)$ in coordinates x, y, and z look as follows:

$$f^+(\xi, \eta, m)$$
$$= \int_{-\infty}^{\infty}\int\int f(x, y, z)\exp(-i\xi x - i\eta y - imz)\,dx\,dy\,dz,$$

1063-7842/05/5010-1366$26.00 © 2005 Pleiades Publishing, Inc.

$$f(x, y, z) = \frac{1}{(2\pi)^3}$$

$$\times \int_{-\infty}^{\infty}\int\int f^{+}(\xi, \eta, m)\exp(i\xi x + i\eta y + imz)d\xi d\eta dm.$$

Let us recast Eq. (3) componentwise by applying the Fourier transformation to both sides of the resulting set of equations. Eventually, we arrive at a set of linear algebraic equations for the electric field component transforms,

$$\begin{pmatrix} \eta^2 + m^2 + k_t^2 & -\xi\eta & -\xi m \\ -\xi\eta & \xi^2 + m^2 + k_n^2 & -\eta m \\ -\xi m & -\eta m & \xi^2 + \eta^2 + k_t^2 \end{pmatrix} \begin{pmatrix} E_x^+ \\ E_y^+ \\ E_z^+ \end{pmatrix} = \begin{pmatrix} F_x \\ F_y \\ F_z \end{pmatrix}, \quad (4)$$

where

$$F_l = \int_{-\infty}^{\infty}\int\int (i\omega j_l^E - \mathrm{curl}_l \mathbf{j}^H)$$

$$\times \exp(-i\xi x - i\eta y - imz)dxdydz,$$

$$k_t^2 = -i\omega\mu\gamma_t', \quad k_n^2 = -i\omega\mu\gamma_n',$$

$$\mathrm{Re}k_t > 0, \quad \mathrm{Re}k_n > 0,$$

$$\gamma_t' = \gamma_t - i\omega\varepsilon_t, \quad \gamma_n' = \gamma_n - i\omega\varepsilon_n.$$

Having found the electric field component transforms from a solution to set (4), we then find the desired field components by applying the inverse Fourier transformation to the transforms of these components. The magnetic field components can be derived from (2).

Let us write the electromagnetic field components when magnetic and electric dipoles are oriented along one of the coordinate axes. To do this, we introduce the following notation:

$$\lambda^2 = \gamma_t'/\gamma_n', \quad r^2 = x^2 + z^2,$$

$$R^2 = r^2 + y^2, \quad \bar{R}^2 = r^2 + \lambda^2 y^2.$$

1. MAGNETIC DIPOLE

(i) Orientation along the *y* axis. In this case, only one component of the extraneous magnetic current is nonzero,

$$j_y^H = -i\omega\mu M\delta(x)\delta(y)\delta(z),$$

where M is the moment of the magnetic dipole.

The electromagnetic field components are given by

$$E_x = \frac{i\omega\mu Mz}{4\pi}\exp(-k_t R)\left(\frac{k_t}{R^2} + \frac{1}{R^3}\right),$$

$$E_y = 0,$$

$$E_z = -\frac{i\omega\mu Mx}{4\pi}\exp(-k_t R)\left(\frac{k_t}{R^2} + \frac{1}{R^3}\right),$$

$$H_x = \frac{Mxy}{4\pi}\exp(-k_t R)\left(\frac{k_t^2}{R^3} + \frac{3k_t}{R^4} + \frac{3}{R^5}\right),$$

$$H_y = \frac{M}{4\pi}\exp(-k_t R)\left[-\frac{k_t^2}{R} - \frac{k_t}{R^2} - \frac{1}{R^3} + y^2\left(\frac{k_t^2}{R^3} + \frac{3k_t}{R^4} + \frac{3}{R^5}\right)\right],$$

$$H_z = \frac{Myz}{4\pi}\exp(-k_t R)\left(\frac{k_t^2}{R^3} + \frac{3k_t}{R^4} + \frac{3}{R^5}\right).$$

(ii) Orientation along the *x* axis. Only one component of the extraneous magnetic current is nonzero,

$$j_x^H = -i\omega\mu M\delta(x)\delta(y)\delta(z).$$

The electromagnetic field components are given by

$$E_x = \frac{i\omega\mu Mxyz}{4\pi}\left\{\exp(-k_1 R)\left(\frac{k_t}{r^2R^2} + \frac{1}{r^2R^3} + \frac{2}{r^4R}\right) - \lambda\exp(-k_n\bar{R})\left(\frac{k_n}{r^2\bar{R}^2} + \frac{1}{r^2\bar{R}^3} + \frac{2}{r^4\bar{R}}\right)\right\},$$

$$E_y = \frac{i\omega\mu M\lambda z}{4\pi}\exp(-k_n\bar{R})\left(\frac{k_n}{\bar{R}^2} + \frac{1}{\bar{R}^3}\right),$$

$$E_z = -\frac{i\omega\mu My}{4\pi}\left\{\exp(-k_t R)\left[\frac{k_t}{R^2} + \frac{1}{r^2R} + \frac{1}{R^3} - z^2\left(\frac{k_t}{r^2R^2} + \frac{1}{r^2R^3} + \frac{2}{r^4R}\right)\right]\right\} - \frac{i\omega\mu My\lambda}{4\pi}$$

$$\times\left\{\exp(-k_n\bar{R})\left[-\frac{1}{r^2\bar{R}} + z^2\left(\frac{k_n}{r^2\bar{R}^2} + \frac{1}{r^2\bar{R}^3} + \frac{2}{r^4\bar{R}}\right)\right]\right\},$$

$$H_x = \frac{M}{4\pi}\left\{\exp(-k_t R)\left[\frac{k_t}{R^2}+\frac{1}{R^3}-\frac{k_t}{r^2}\right.\right.$$

$$\left.\left.+x^2\left(\frac{2k_t}{r^4}+\frac{k_t^2}{r^2R}-\frac{k_t^2}{R^3}-\frac{3k_t}{R^4}-\frac{3}{R^5}\right)\right]\right\}$$

$$+\frac{Mk_t}{4\pi}\left\{\exp(-k_n\bar{R})\left[\frac{k_n}{\bar{R}}+\frac{1}{r^2}-x^2\left(\frac{k_n}{r^2\bar{R}}+\frac{2}{r^4}\right)\right]\right\},$$

$$H_y = -\frac{Mxy}{4\pi R^3}\exp(-k_t R)\left(k_t^2+\frac{3k_t}{R}+\frac{3}{R^2}\right),$$

$$H_z = \frac{Mxz}{4\pi}\left\{\exp(-k_t R)\left(\frac{2k_t}{r^4}+\frac{k_t^2}{r^2R}-\frac{k_t^2}{R^3}-\frac{3k_t}{R^4}-\frac{3}{R^5}\right)\right.$$

$$\left.-k_t\exp(-k_n\bar{R})\left(\frac{2}{r^4}+\frac{k_n}{r^2\bar{R}}\right)\right\}.$$

(iii) Orientation along the *z* axis. Only one component of the extraneous magnetic current is nonzero,

$$j_z^H = -i\omega\mu M\delta(x)\delta(y)\delta(z).$$

All the electromagnetic field components are found from the previous case by substituting z for x, x for z, and $-\mu$ for μ.

2. ELECTRIC DIPOLE

(i) Orientation along the *y* axis. In this case, only one component of the extraneous electric current is nonzero,

$$j_y^E = I\delta(x)\delta(y)\delta(z),$$

where I is the moment of the electric dipole.

The electromagnetic field components are given by

$$E_x = -\frac{i\omega\mu I\lambda xy}{4\pi k_n^2\bar{R}^3}\exp(-k_n\bar{R})\left(k_n^2+\frac{3k_n}{\bar{R}}+\frac{3}{\bar{R}^2}\right),$$

$$E_y = -\frac{i\omega\mu I\lambda}{4\pi k_n^2 R^2}$$

$$\times\exp(-k_n\bar{R})\left\{2k_n+\frac{2}{\bar{R}}-r^2\left(\frac{k_n^2}{\bar{R}}+\frac{3k_n}{\bar{R}^2}+\frac{3}{\bar{R}^3}\right)\right\},$$

$$E_z = -\frac{i\omega\mu I\lambda yz}{4\pi k_n^2\bar{R}^3}\exp(-k_n\bar{R})\left(k_n^2+\frac{3k_n}{\bar{R}}+\frac{3}{\bar{R}^2}\right),$$

$$H_x = \frac{I\lambda z}{4\pi\bar{R}^2}\exp(-k_n\bar{R})\left(k_n+\frac{1}{\bar{R}}\right),$$

$$H_0 = 0,$$

$$H_z = -\frac{I\lambda x}{4\pi\bar{R}^2}\exp(-k_n\bar{R})\left(k_n+\frac{1}{\bar{R}}\right).$$

(ii) Orientation along the *x* axis. Only one component of the extraneous electric current is nonzero,

$$j_x^E = I\delta(x)\delta(y)\delta(z).$$

The electromagnetic field components are given by

$$E_x = \frac{i\omega\mu I}{4\pi k_t}\left\{\exp(-k_t R)\left[\frac{k_t}{R}+\frac{1}{r^2}-x^2\left(\frac{k_t}{r^2R}+\frac{2}{r^4}\right)\right]\right\}$$

$$+\frac{i\omega\mu I\lambda}{4\pi k_t^2}\left\{\exp(-k_n\bar{R})\left[\frac{k_n}{\bar{R}^2}+\frac{1}{\bar{R}^3}-\frac{k_n}{r^2}\right.\right.$$

$$\left.\left.+x^2\left(\frac{k_n^2}{r^2\bar{R}}-\frac{k_n^2}{\bar{R}^3}+\frac{2k_n}{r^4}-\frac{3k_n}{\bar{R}^4}-\frac{3}{\bar{R}^5}\right)\right]\right\},$$

$$E_y = -\frac{i\omega\mu I\lambda xy}{4\pi k_n^2\bar{R}^3}\exp(-k_n\bar{R})\left(k_n^2+\frac{3k_n}{\bar{R}}+\frac{3}{\bar{R}^2}\right),$$

$$E_z = -\frac{i\omega\mu Ixz}{4\pi k_t^2}\left\{\exp(-k_t R)\left(\frac{k_t^2}{r^2R}+\frac{2k_t}{r^4}\right)\right.$$

$$\left.+\lambda\exp(-k_n\bar{R})\left(-\frac{k_n^2}{r^2\bar{R}}+\frac{k_n^2}{\bar{R}^3}-\frac{2k_n}{r^4}+\frac{3k_n}{\bar{R}^4}+\frac{3}{\bar{R}^5}\right)\right\},$$

$$H_x = \frac{Ixyz}{4\pi r^2}\left\{\exp(-k_t R)\left(\frac{k_t}{R^2}+\frac{2}{r^2R}+\frac{1}{R^3}\right)\right.$$

$$\left.-\lambda\exp(-k_n\bar{R})\left(\frac{k_n}{\bar{R}^2}+\frac{2}{r^2\bar{R}}+\frac{1}{\bar{R}^3}\right)\right\},$$

$$H_y = -\frac{Iz}{4\pi R^2}\exp(-k_t R)\left(k_t+\frac{1}{R}\right),$$

$$H_z = -\frac{Iy}{4\pi}\left\{\exp(-k_t R)\left[\frac{1}{r^2R}\right.\right.$$

$$\left.\left.-z^2\left(\frac{k_t}{r^2R^2}+\frac{2}{r^4R}+\frac{1}{r^2R^3}\right)\right]\right\}+\frac{Iy\lambda}{4\pi}\{\exp(-k_n\bar{R})$$

$$\times\left[\frac{k_n}{\bar{R}^2}+\frac{1}{r^2\bar{R}}+\frac{1}{\bar{R}^3}-z^2\left(\frac{k_n}{r^2\bar{R}^2}+\frac{2}{r^4\bar{R}}+\frac{1}{r^2\bar{R}^3}\right)\right]\right\}.$$

(iii) Orientation along the *z* axis. Only one component of the extraneous electric current is nonzero,

$$j_z^E = I\delta(x)\delta(y)\delta(z).$$

All the electromagnetic field components are found from the previous case by substituting z for x, x for z, $-\mu$ for μ, and $-I$ for I.

Below, magnetic and electric dipoles were oriented along one of the coordinate axes. The field of an arbitrary oriented dipole is found as a superposition of the field projections onto the coordinate axes.

APPENDIX

It should be noted that not all the field components can be found by direct integration of the transforms; specifically, we omitted from consideration the orientation along the axis $r = 0$. The field components along this axis are found by passing to the limit $r \longrightarrow 0$. Below, we give only those field components along the axis $r = 0$ which appear nontrivial.

Magnetic dipole oriented along the *x* axis, *r* = 0.

$$E_x = 0,$$

$$E_z = -\frac{i\omega\mu My}{4\pi}\exp(-k_t|y|)\left\{\frac{k_t}{2y^2}\left(1+\frac{1}{\lambda^2}\right)+\frac{1}{|y|^3}\right\},$$

$$H_z = \frac{M}{4\pi}\exp(-k_t|y|)\left\{\frac{k_t^2}{2|y|}\left(1+\frac{1}{\lambda^2}\right)+\frac{k_t}{y^2}+\frac{1}{|y|^3}\right\},$$

$$H_z = 0.$$

The components of the magnetic dipole oriented along the z axis are found by making an appropriate change of variables (see Sect. 1(iii)).

Electric dipole oriented along the *x* axis, *r* = 0.

$$E_x = \frac{i\omega\mu I}{4\pi k_t^2}\exp(-k_t|y|)\left(\frac{k_t^2}{2|y|}+\frac{k_t}{\lambda^2 y^2}+\frac{1}{\lambda^2|y|^3}+\frac{k_t^2}{2\lambda^2|y|}\right),$$

$$E_z = 0,$$

$$H_x = 0,$$

$$H_z = \frac{Iy}{4\pi}\exp(-k_t|y|)\left(\frac{k_t}{2y^2}+\frac{k_t}{2\lambda^2 y^2}+\frac{1}{\lambda^2|y|^3}\right).$$

REFERENCES

1. A. A. Kaufman and A. M. Kaganskiĭ, *The Inductive Method of Studying Transverse Resistance in Wells* (Nauka, Novosibirsk, 1972) [in Russian].
2. L. A. Tabarovskiĭ, A. M. Kaganskiĭ, and M. I. Épov, Geol. Geofiz., No. 3, 94 (1976).
3. L. A. Tabarovskiĭ and M. I. Épov, in *Electromagnetic Methods in Well Studies* (Nauka, Novosibirsk, 1979) [in Russian].
4. M. I. Épov, in *Electromagnetic Methods in Well Studies* (Nauka, Novosibirsk, 1979) [in Russian].
5. G. T. Markov and A. F. Chaplin, *Excitation of Electromagnetic Waves* (Radio i Svyaz', Moscow, 1983) [in Russian].

Translated by V. Isaakyan

Technical Physics, Vol. 50, No. 10, 2005, pp. 1370–1373. Translated from Zhurnal Tekhnicheskoĭ Fiziki, Vol. 75, No. 10, 2005, pp. 122–125.

SHORT COMMUNICATIONS

On the Possibility of Developing Thermoelectric Sensors Based on Multielement Higher Manganese Silicide Film Structures

T. S. Kamilov, D. K. Kabilov, I. S. Samiev, and Kh. Kh. Khusnutdinova

State Aviation Institute, Tashkent, 700047 Uzbekistan

e-mail: tdai_kts@mail.ru

Received November 24, 2004

Abstract—The possibility of designing thermoelectric sensors based on multielement structures of higher manganese silicide (HMS) polycrystalline films is considered. Test structures with various configurations are developed for studying electrical and thermoelectric parameters of polycrystalline HMS films. The geometrical sizes of the elements of test structures are chosen to match the grain size in polycrystalline HMS films. The test structures are prepared using the planar silicon technology. In these structures, the current-voltage characteristics, Hall constant, charge carrier concentration, and mobility are measured. The thermopower (α) and electrical conductivity (σ) are studied in a temperature range of T = 77–600 K, where $\alpha > 250$ μV/K and electrical conductivity $\sigma \sim 20$ $(\Omega\ \text{cm})^{-1}$. It is shown that the sensitivity and thermopowers increase upon a decrease in the cross-sectional area of the elements. © *2005 Pleiades Publishing, Inc.*

INTRODUCTION

Thin and thick films of transient metal silicides attract considerable attention due to their unique photo- and thermoelectric properties, high-temperature stability, and compatibility with silicon technology. It is well known from the literature [1] that the higher manganese silicide (HMS) $MnSi_{1.71–1.75}$ is one of the most promising thermoelectric materials among silicides since bulk HMS samples exhibit a thermoelectric effectiveness $Z = 0.7 \times 10^{-3}$ K^{-1} in the temperature range 300–1000 K. Intense studies aimed at obtaining thin and ultrathin HMS films have been carried out in Germany, China, and Japan [2–5]. However, film-type thermoelectric elements based on the HMS $MnSi_{1.71–1.75}$ have not been developed so far.

The possibility of obtaining continuous polycrystalline HMS films by reactive diffusion of manganese vapor atoms directly into a silicon substrate was demonstrated by us earlier [6]. The features of the crystalline structure of HMS films grown from silicon were studied in [7], where it was found that the films prepared at a substrate temperature of 1040–1070°C and then annealed at 350–800°C consist of HMS crystallites with a preferred orientation of the *c* axis along the normal to the substrate. Subsequently, the possibility of designing nonselective sensors based on HMS films was demonstrated [8]. The present study is devoted to the development of multielement test structures of thermoelectric sensors based on HMS film and to analysis of their electrophysical properties.

EXPERIMENTAL TECHNIQUE

Film-type thermocouples and thermopiles are developed on the basis of the standard planar technology, where thin films of silicon dioxide SiO_2 are widely used as the main protecting and separating layer for active elements. In our earlier publications [9, 10], we demonstrated that a SiO_2 surface layer grown during silicide formation serves as a mask preventing the formation of silicide on the surface of a silicon substrate. This allowed us to develop a technology for obtaining test structures based on HMS films on the silicon surface in the form of thermopiles of various configurations. The geometrical sizes of the elements of test structures were chosen depending on the grain size of polycrystalline HMS films.

In developing the technology for preparing test structures, we chose special designs and worked out sketch versions of photomasks, in which the details of individual units of test structures were envisaged. We developed three types of test structures; the model sets of these structures are shown in Fig. 1. The first type of test structure is a continuous HMS film on a Si substrate with four Ni or Al contacts for measuring the Hall effect using the van der Pauw method and strip contacts across the sample for measuring the thermal emf and the sensitivity coefficient (Figs. 1a and 1b). The second type has the form of continuous HMS strips separated by insulating SiO_2 layers and Al contacts for measuring electrophysical parameters (Fig. 1c). Test structures of the third type are similar to the second type, but with

1063-7842/05/5010-1370$26.00

additional lateral contacts for studying separately the current transport in the grains proper (Fig. 1d).

Test structures of the second and third types contained several identical elements being measured of various thicknesses (10, 20, 100, 200, 400, 800, and 1000 μm) of the same length (7000 μm) and thickness (8–10 μm). This enabled us to perform a number of measurements of electrical parameters of test structures under the same conditions, which made it possible to obtain averaged data on the measured quantities and estimate the spread in the parameters of the elements of test structures. Metallization of test structures was carried out by vacuum sputtering of a 1.5-μm-thick Al or Ni film followed by vacuum annealing at temperatures of 300–350°C.

For each chip with a size of 9.5 × 9.5 mm, special packages of metallized glass fiber plastic were prepared, on which contact area elements with leads were obtained photolithographically. Chips were fixed to the packages by a special adhesive. After mounting a crystal into the package, the contact area was connected to the leads of the package with the help of ultrasonic welding. One of the test structures is shown in Fig. 2.

For first-type test structures, we measured the thermopower, electrical conductivity, and Hall coefficient by the van der Pauw method. The Hall emf of HMS films was measured in a constant magnetic field of 0.1 T for two directions of the current.

The longitudinal and transverse thermal emf emerging in polycrystalline HMS films were measured in accordance with the technique described in [11]. The sample under investigation was placed on a copper table, and copper probes of a configuration corresponding to the contacts with built-in thermocouples were pressed against the metallic contacts of the sample (see Fig. 1). An electric heater producing a temperature gradient was wound on one of the probes, while the other probe had the same temperature as the copper table. The temperature drop between the probes did not exceed ΔT = 5–10 K. The thermal emf produced in the film was measured by a Shch-300 microvoltmeter. Passage from the longitudinal to transverse thermal emf measurements and vice versa was made by rotating the sample through 90° in the horizontal plane, which made it possible to determine the anisotropy in the thermoelectric (Seebeck) coefficient.

To detect the anisotropic thermal emf, a pulse laser radiation with wavelengths λ = 1.06 and 10.6 μm was supplied to the middle of the sample, which produced a temperature gradient across the film thickness. The incident beam diameter d was much smaller than the distance l between the contacts (i.e., $d \ll l$). We measured thermal emf ε_α emerging at the contacts and its dependence on the incident radiation power P. The conversion factor (sensitivity) S in this case was

$$S = \frac{\varepsilon_\alpha}{P}.$$

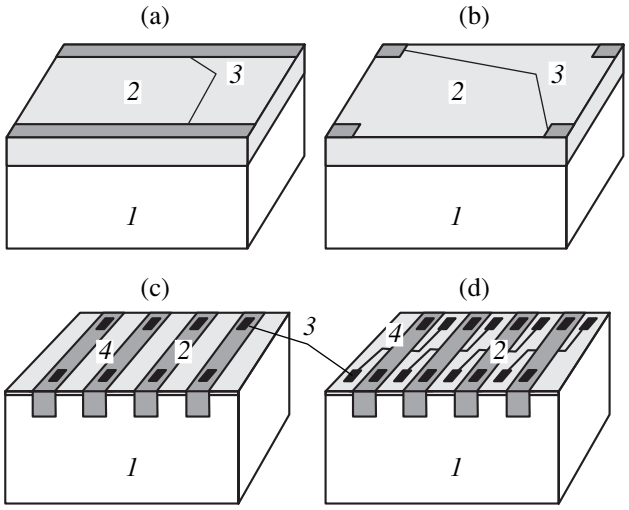

Fig. 1. Model form of test structures: first type (a, b), second type (c), and third type (d) (*1*—Si substrate, *2*—HMS layer, *3*—Al ohmic contacts, and *4*—SiO_2 layer).

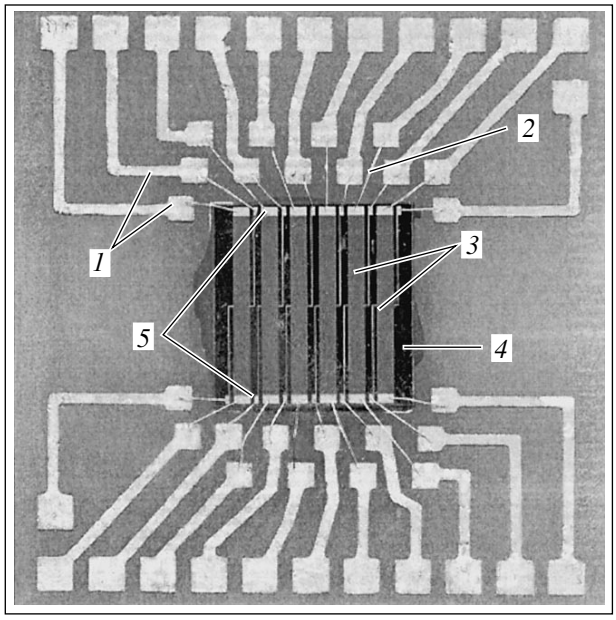

Fig. 2. Photograph of a test structure: *1*—copper contacts, *2*—Al leads, *3*—silicide strips, *4*—Si substrate, and *5*—Al ohmic contacts.

The anisotropy of thermal emf was determined by rotating the sample through 90° in the horizontal plane.

To study sensitivity S and time constant τ, the prepared test structures were placed in a screened package and the thermal emf emerging at the contacts upon irradiation of the structure was fed to the input of an oscilloscope. The values of S and τ were measured at radiation wavelengths λ = 1.06 μm for pulse durations 40–200 ns and λ = 10.6 μm for radiation modulated with a frequency of 10^2–10^4 Hz for pulse durations 0.1–1.5

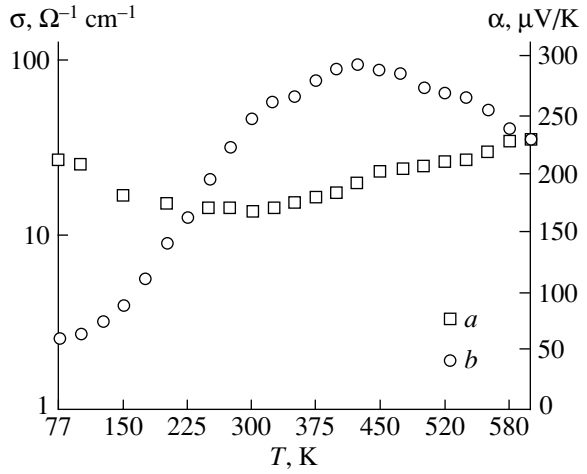

Fig. 3. Temperature dependences of (*a*) conductivity and (*b*) thermopower of HMS films.

ms. To take into account the contribution from the photoelectromotive force, measurements were made for the same radiation flux with different laser wavelengths.

RESULTS AND DISCUSSION

The kinetic parameters investigated for the test structures of HMS films had the following values at T = 300 K: electrical conductivity $\sigma = 11–25\ \Omega^{-1}\ cm^{-1}$; Hall coefficient $R_x = 0.058–0.065\ C^{-1}\ cm^{-3}$ (the corresponding hole concentration was $p \approx 10^{19}–10^{20}\ cm^{-3}$), charge carrier mobility $\mu_p = 0.6–2\ cm^2/V\ s$, and thermopower $\alpha = +250–280\ \mu V/K$. In addition, the temperature dependences of the thermopower and electrical conductivity were studied in the temperature range T = 77–600 K (Fig. 3). It can be seen from the figure that the thermopower of HMS films has values exceeding those attained in bulk HMS single crystals by a factor of 1.5–2 [1]. This is probably associated with the emergence of potential barriers at grain boundaries of polycrystalline HMS films.

The first-type test samples with HMS films grown with a columnar structure tilted relative to the normal to the substrate exhibit anisotropic thermoelectric effect [8]. This was confirmed by the measurement of the longitudinal and transverse thermal emfs, the difference between which was $\Delta\alpha = 50–70\ \mu V/K$. The sensitivity of the anisotropic effect on such samples was S = 0.5–1.0 mV/W and the time constant was $\tau \sim 10^{-6}$ s.

The anisotropic effect was not observed in samples with HMS films grown with a columnar structure oriented so that one of the crystallographic axes (*c* axis in our case) was perpendicular to the surface of the Si substrate and was not deflected from the normal to the substrate. However, the longitudinal thermoelectric effect was predominant in such samples: the signs of the registered dc thermal emf and the ac phase were reversed as the thermal probe moved from the region of one contact to the other contact. In such test structures, radiation was incident in contact regions. The volt-watt sensitivity was S = 0.1 V/W, and the time constant was $\tau \sim 10^{-6}$ s. The sensitivity and the time constant of the films exceeded the values attained in bulk monocrystalline HMS samples by one and three orders of magnitude, respectively [12].

We measured the current-voltage characteristics (*I–V* curves) in three types of structures under bias voltages ranging from 10 mV to 10 V in the dc mode as well as in the ac mode with a frequency up to 10 kHz. The results showed that the *I–V* characteristics were linear in all test structures. Such a behavior of the transport current in the structures indicates that the contacts are of the ohmic type.

For test structures of the second and third types, we measured the resistances of each element of the test structure and compared them with calculated values depending on their widths. The comparison shows that for widths of the elements smaller than 100 μm, the experimental values of the resistance are much larger than the calculated values. This is probably due to a smaller number of contacts between grain boundaries in the transverse direction relative to the current, while grain boundaries along the current naturally form additional potential barriers, which facilitate an increase in the resistance of the elements.

Analysis of thermoelectric parameters in the structures of the second and third types revealed that the thermopower and the sensitivity increased with decreasing width of the elements of the test structures (800, 600, and 400 μm). In all probability, this is due to a decrease in the surface dissipation of heat across the elements with small cross-sectional areas. When such elements were connected in series, the thermopower attained values exceeding 500 μV/K and the values of S were on the order of 0.2–0.3 V/W.

CONCLUSIONS

Test structures with elements having various geometrical sizes were developed using planar technology based on HMS films.

Analysis of kinetic parameters of the test structures shows that values of thermopower $\alpha \geq 500\ \mu V/K$ and sensitivity $S \sim 0.2–0.3$ V/W can be attained by varying the width of the structure elements. The results suggest that thermoelectric sensors can be prepared on the basis of multielement structures of HMS films.

ACKNOWLEDGMENTS

This study was supported by the Center of Science and Technology of the Republic of Uzbekistan, grant no. GNTP-10-20.

REFERENCES

1. V. K. Zaitsev, in *CRC Handbook of Thermoelectrics*, Ed. by D. M. Rowe (CRC, New York, 1995), pp. 299–309.
2. A. Mogilatenko, M. Falke, S. Teichert, *et al.*, Microelectron. Eng. **60**, 247 (2002).
3. Q. Zhang, M. Takeguchi, M. Tanaka, *et al.*, J. Cryst. Growth **237–239**, 1956 (2002).
4. J. Yang, N. F. Chen, Z. Liu, *et al.*, J. Cryst. Growth **226**, 517 (2001).
5. Y. Souno, Y. Maeda, H. Tatsuoka, and H. Kuwabara, J. Cryst. Growth **229**, 527 (2001).
6. S. I. Adasheva, I. Abdullaev, E. L. Vyaz'mina, *et al.*, Izv. Ross. Akad. Nauk, Ser. Fiz. **57**, 133 (1993).
7. V. V. Klechkovskaya, T. S. Kamilov, S. I. Adasheva, *et al.*, Kristallografiya **39**, 894 (1994) [Crystallogr. Rep. **39**, 815 (1994)].
8. T. S. Kamilov, A. Zh. Khusanov, M. Bakhadyrkhanov, and D. K. Kobilov, Pis'ma Zh. Tekh. Fiz. **28** (22), 11 (2002) [Tech. Phys. Lett. **28**, 929 (2002)].
9. T. S. Kamilov, D. K. Kabilov, A. A. Uzokov, *et al.*, in *Proceedings of the 8th Interstate Seminar "Thermoelectrics and Their Application," St. Petersburg, 2002*, pp. 255–259.
10. T. S. Kamilov, A. A. Uzokov, D. K. Kabilov, *et al.*, in *Proceedings of the 22nd International Conference on Thermoelectrics, Herault, 2003*, IEEE Catalog No. 03TH8726, pp. 388–390.
11. T. S. Gudkin, Z. M. Dashevskiĭ, and I. V. Sgibnev, Zavod. Lab. **42**, 820 (1976).
12. S. V. Ordin, T. S. Kamilov, D. K. Kabilov, *et al.*, in *Proceedings of the 8th Interstate Seminar "Thermoelectrics and Their Application," St. Petersburg, 2002*, pp. 249–254.

Translated by N. Wadhwa

Technical Physics, Vol. 50, No. 10, 2005, pp. 1374–1375. Translated from Zhurnal Tekhnicheskoĭ Fiziki, Vol. 75, No. 10, 2005, pp. 126–127.

SHORT COMMUNICATIONS

Experimental Study of the Stability of the Interface between a Liquid Electrolyte and the Glow Discharge Plasma

D. V. Vyalykh, A. E. Dubinov, K. E. Mikheev, Yu. N. Lashmanov, I. L. L'vov, S. A. Sadovoĭ, and V. D. Selemir

All-Russia Research Institute of Experimental Physics, Russian Federal Nuclear Center, Sarov, Nizhegorodsk Oblast, 607190 Russia

e-mail: dubinov@ntc.vniief.ru

Received February 8, 2005

Abstract—The stability of the interface between a liquid electrolyte and the plasma of a contracted low-pressure dc glow discharge in air is investigated by means of digital photography. Water solutions of potassium permanganate and copper sulfate were used as electrolytes. It is found that, in the case of potassium permanganate, the instability of the interface leads to ejection of the electrolyte into the plasma and extinction of the discharge. Discharge modes with different types of quasi-steady interface are observed for copper sulfate at different values of the discharge current: a smooth interface, a solitary wave perturbation, regular ripples, and a churning foamed turbulent mixing zone. © *2005 Pleiades Publishing, Inc.*

The gas discharge over the electrolyte surface is one of the most interesting objects of study in applied plasma chemistry [1–3]. The aim of the present work is the visual and photographic investigation of the interface between a liquid electrolyte and the plasma of a low-pressure dc glow discharge.

The experiments were conducted in a vertical glass discharge tube 200 mm in length and 30 mm in diameter. A stainless-steel cathode and anode were located at the lower and upper ends of the tube, respectively.

The tube was filled with a liquid electrolyte up to a 130-mm height. Red-brown 0.2% water solutions of potassium permanganate ($KMnO_4$) and blue 10% water solutions of copper sulfate ($CuSO_4$) were used as electrolytes.

The air pressure in the remaining part of the tube was set at 40–60 Torr. A further decrease in the pressure led to intense boiling of the electrolyte at room temperature. At a pressure just above the boiling threshold, the

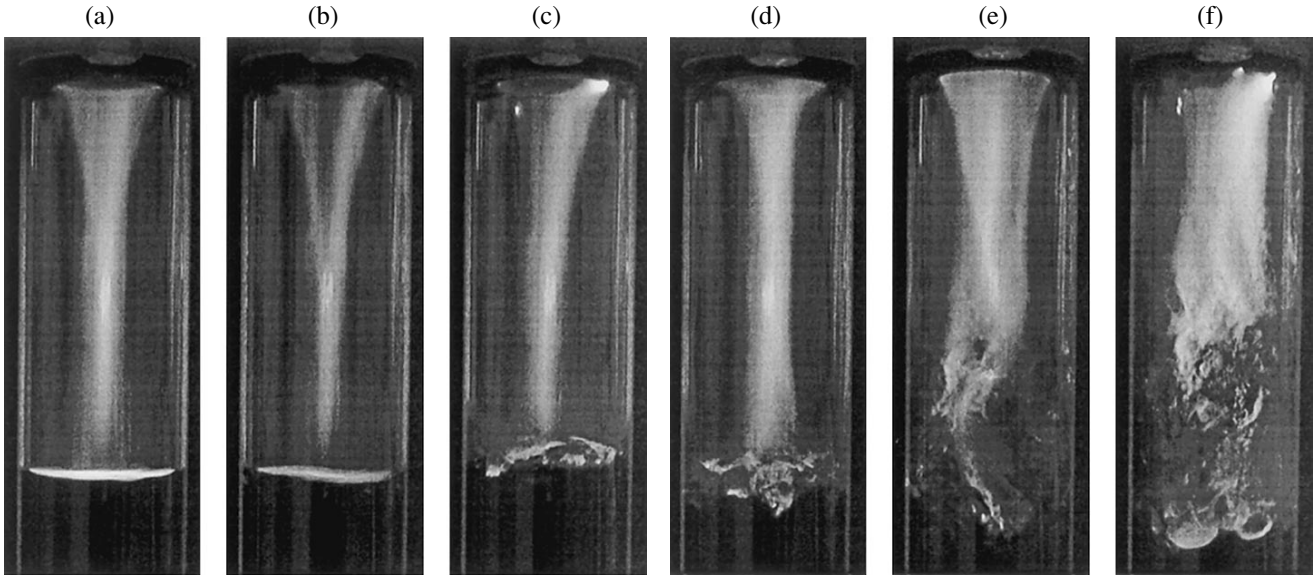

Fig. 1. Dynamics of a glow discharge over a potassium permanganate solution: (a) smooth surface, (b) warped surface, (c) wave perturbation of the surface, (d) growing perturbation, (e) turbulent ejection of the plasma–electrolyte mixture into the discharge zone, and (f) another turbulent ejection of the plasma–electrolyte mixture into the discharge zone.

1063-7842/05/5010-1374$26.00 © 2005 Pleiades Publishing, Inc.

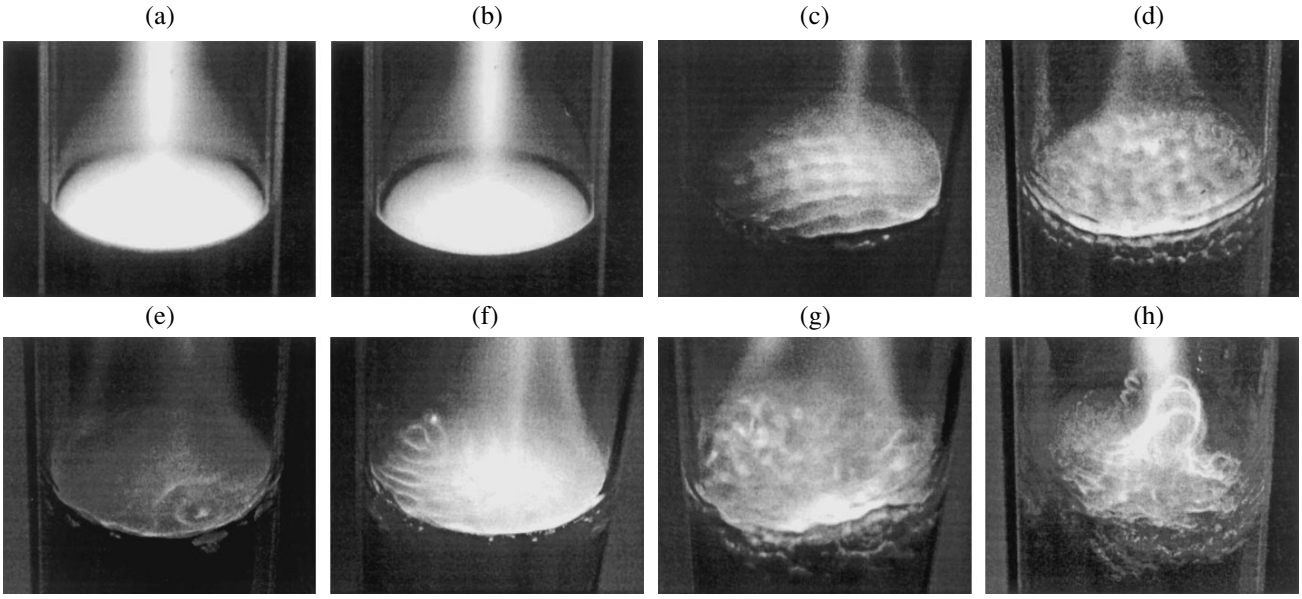

Fig. 2. Modes of a glow discharge over a copper sulfate solution: (a, b) smooth surface, (c, d) solitary wave perturbation, (e, f) regular ripples, and (g, h) churning foamed turbulent mixing zone.

discharge gap was appreciably saturated with electrolyte vapor.

The discharge was powered from a dc power supply. The discharge current flowing through the electrolyte was carried by ions, and, in the glow discharge plasma, it was carried by electrons. The change of the current carriers at the plasma–electrolyte interface is a rather complicated kinetic process. Besides kinetic processes, the surface is also affected by intense acoustic oscillations excited by the current flowing through the electrolyte. Therefore, investigation of the plasma–electrolyte interface is of great importance for understanding the processes occurring in the discharge.

The discharge was observed visually and was photographed with an Olimpus C-40ZOOM digital camera. This allowed us to obtain high-quality color photographs of the discharge in different stages of the process and to study the discharge dynamics by means of short-term (over a few seconds) digital video recording.

At pressures of 40–60 Torr, dc glow discharge is contracted for both types of solution. The dynamics of the plasma–electrolyte interface for these two solutions is, however, different.

A 250-mA discharge over a potassium permanganate solution operated over 3–5 s and passed through several stages. Initially, it was a contracted discharge over a smooth plasma–electrolyte interface. A surface glow was also observed in this stage. Further on, the interface warped, intense surface waves were excited, the electrolyte and plasma underwent turbulent mixing, and the mixture produced was ejected into the discharge zone. After the ejected mixture reached the upper electrode, the discharge was extinguished. Figure 1 shows photographs of six successive stages of this dynamic process.

In the case of a copper sulfate solution, the situation is quite different: the discharge is quieter and can occur in different quasi-steady modes, which differ in the structure of perturbations of the plasma–electrolyte interface. The following modes were observed as the discharge current was increased from 50 to 150 mA: a smooth surface, a solitary wave perturbation, regular ripples (Faraday waves), and a churning foamed turbulent mixing zone (see Fig. 2).

Thus, in this study, we have observed for the first time glow discharges over an electrolyte surface that are quite different in their dynamics and structure.

ACKNOWLEDGMENTS

This study was supported by the Netherlands Organization for Scientific Research (NWO), grant no. 047-016-020.

REFERENCES

1. F. M. Gaĭsin and É. E. Son, in *Plasma Chemistry*, Ed. by B. M. Smirnov (Énergoatomizdat, Moscow, 1990), No. 16, pp. 120–156 [in Russian].
2. S. Kuzmin, R. Vaculik, and J. Janča, in *Proceedings of the International Congress on Plasma Physics and 25th EPS Conference on Controlled Fusion and Plasma Physics (ICPP&25thEPS), Prague, 1998*, Vol. 22C, pp. 2651–2654.
3. A. M. Kutepov, A. G. Zakharov, and A. I. Maksimov, *Vacuum–Plasma and Plasma–Solution Modification of Polymers* (Nauka, Moscow, 2004) [in Russian].

Translated by B. Chernyavskiĭ

Technical Physics, Vol. 50, No. 10, 2005, pp. 1376–1378. Translated from Zhurnal Tekhnicheskoĭ Fiziki, Vol. 75, No. 10, 2005, pp. 128–130.

SHORT COMMUNICATIONS

Magnetooptic Setup for Investigating the Dynamic Properties of Domain Walls in Thin Ferromagnetic Films

A. V. Semirov, B. V. Gavrilyuk, A. A. Rudenko, V. O. Kudryavcev, and N. P. Kovaleva

Irkutsk State Pedagogical University, Irkutsk, 664011 Russia

e-mail: semirov@isttu.irk.ru

Received February 9, 2005

Abstract—A magnetooptic Kerr setup is designed for investigating the dynamic properties of domain walls in thin ferromagnetic films subjected to an external magnetic field in the temperature range 20–150°C. With this setup, the method of interrupted magnetization is implemented and the magnetic (domain) structure is visualized based on the meridional Kerr effect. The domain structure is displayed on a PC monitor using a Nikon DXM 1200 high-resolution digital video camera. A dedicated software makes it possible to automatize measurements and data processing. © *2005 Pleiades Publishing, Inc.*

Study of magnetization reversal in ferromagnets occupies a prominent place in solid-state physics. Comprehensive insight into the physics of transient processes can be gained only by directly observing the magnetic structure of a sample and tracing its variation upon magnetization reversal. Bulk magnetic materials are difficult to study, since it is impossible to visualize their internal magnetic structure. In thin ferromagnetic films, the domain structure occupies the entire sample; therefore, pulsed processes in them occur under conditions more favorable to analysis than those in bulk materials. Being largely a vacuum condensate, thin ferromagnetic films have a specular reflecting surface, which makes observation of the domain structure dynamics by applying the magnetooptic Kerr effect basically possible. The advantage of magnetooptic observation over other methods is that it has no effect on the magnetization reversal process in the films and on the domain wall (DW) structure.

To investigate the DW dynamics in thin ferromagnetic films, we designed a setup schematically shown in Fig. 1. Its optics consists of light source *1* (halogen lamp); lenses *2* and *3* and polarizing filter *4*, which form a parallel plane-polarized light beam; Polaroid analyzer *5*; and microscope *6* interfaced with digital video camera *7*.

Since the angle of rotation of plane of polarization depends on the orientation of the magnetization vector relative to the plane of incidence of the light beam, analyzer *5* can be adjusted in such a way that the image received by video camera *7* will consist of dark and bright regions corresponding to different orientations of the magnetization in the sample (Fig. 2).

The magnification of the optics is varied in steps from ×10 to ×100. The digital video camera makes it possible to visualize an area of interest with a resolution of 3840 × 3072 pix. The exposure time varies between 80 μs and 700 s.

When the light reflects from the surface of a thin ferromagnetic film, the rotation of plane of polarization is small and so the image formed by the video camera is of low contrast. The contrast was raised by digital image processing.

In our setup, the DW dynamics was investigated by the method of interrupted magnetization [1, 2]. In this method, the sample is exposed either to single rectangular pulses or to a periodic train of pulses of a magnetic field. The time between pulses is much longer than the DW relaxation time. The DW average velocity

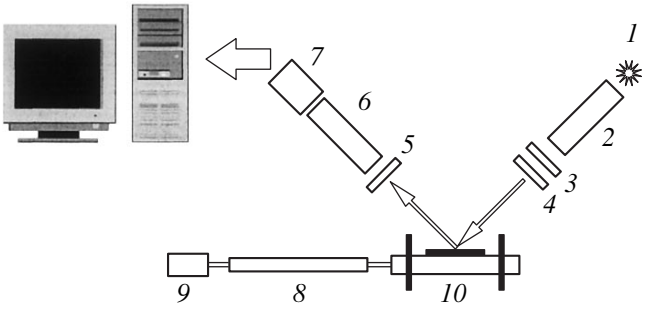

Fig. 1. Block diagram of the pulsed magnetooptic setup: (*1*) light source, (*2*) lens system, (*3*) diaphragm, (*4*) polarizer, (*5*) analyzer, (*6*) microscope, (*7*) Nikon DXM 1200 digital video camera, (*8*) tube with heater, (9) air compressor, and (*10*) magnetization-reversing rings.

1063-7842/05/5010-1376$26.00 © 2005 Pleiades Publishing, Inc.

here is defined as the distance the wall travels during magnetization reversal divided by the total time of reversal. In addition, the following conditions must be fulfilled: the rise time and fall time of the (rectangular) magnetization-reversing pulses should be much shorter than the pulse duration and the top of the rectangular pulses must be flat.

Since magnetization reversal in our work was accomplished with low-inductance low-resistance Helmholtz rings, rectangular current pulses of amplitude as high as 100 A were necessary to generate magnetic fields of desired intensity. Such rectangular magnetization-reversing pulses were produced by a generator with the discharge circuit in the form of a coaxial cable [1]. A thyratron with an ionization time of 10–15 ns was used as a switch. The rise and fall times of the rectangular pulse in the aggregate did not exceed 50 ns for a pulse duration of more than 0.5 μs. Thyratron-igniting pulses were generated by a square-wave hand-operated one-shot generator.

The duration of the current pulses was controlled by the length of the storage cable; their amplitude, by the charging voltage of the cable.

Rectangularity of a magnetization-reversing pulse is a key issue in the method of interrupted magnetization. To control the pulse shape, we used a trigger-mode oscilloscope synchronized with the igniting-pulse generator.

The reversing-pulse generator terminates in double-coil Helmholtz rings *1* (Fig. 3). In combination with the generator, these low-inductance magnetization-reversing rings generate rectangular magnetic pulses with a duration from 500 ns to 10 μs and an amplitude from 80 A/m to 4 kA/m. Constructively, the double-coil Helmholtz rings are a part of the reversing device, which can apply, along with pulsed magnetic fields, mutually orthogonal uniform magnetic fields to the sample (Fig. 3).

The reversing device (Fig. 3) consists of three pairs of Helmholtz rings and a hollow ceramic sample holder on a mica substrate. Rings *4* and *5* generate mutually orthogonal uniform magnetic fields of intensity up to 16 kA/m and are fed by regulated current sources (Fig. 3).

To exclude the effect of external magnetic fields (of both natural and technogenic origin), the device was placed in compensating Helmholtz rings generating orthogonal triaxial magnetic fields (not shown in Figs. 1–3).

To study the DW dynamics in a temperature range, the reversing device was equipped with a specially designed thermal attachment (Fig. 1) consisting of air compressor *9* and a copper tube with heating element *8*. The air from the compressor passes through the copper tube with the heater and then enters the interior of the sample holder, where it warms the mica substrate with the sample. The sample temperature can be varied between 20 and 150°C by varying the voltage applied to the heater.

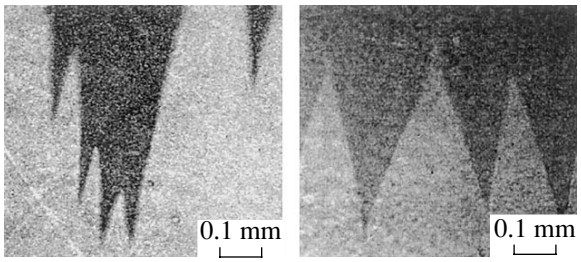

Fig. 2. Domain walls visualized by using the meridional Kerr effect.

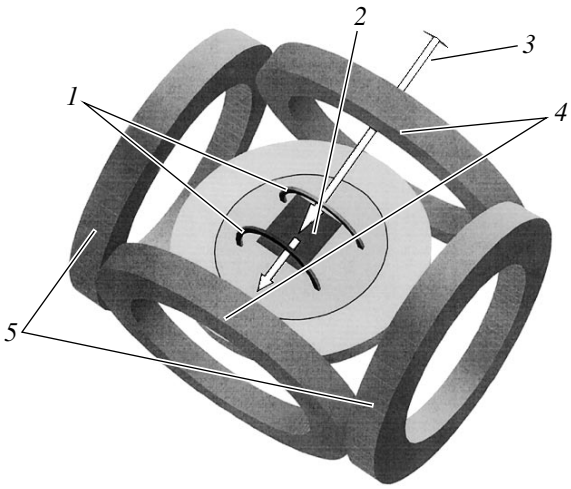

Fig. 3. External view of the magnetization-reversing device (not to scale). (*1*) Double-coil reversing rings, (*2*) sample holder on mica substrate, (*3*) beam propagation direction, and (*4*, *5*) pairs of Helmholtz rings generating mutually orthogonal magnetic fields.

The temperature was measured with a thermocouple mounted in the magnetization-reversing device and a digital voltmeter with an accuracy of 2%.

To automatize measurements, we developed a software package making it possible to measure the DW displacement and automatically generate data lists.

The DW displacement along the hard and easy magnetization axes is found by a change in the coordinates of a cursor, which indicates the initial and final positions of the wall on the monitor. Three reference points of the domain wall can be fixed simultaneously.

Along with DW displacements, the data list also contains the name of the sample, its temperature, the number of magnetization-reversing pulses, and the values of acting magnetic fields.

To improve the reliability of experimental results, the program allows for statistical treatment of the

results obtained under identical experimental conditions.

Thus, the digital image processing techniques combined with data acquisition and processing software tools enable one to effectively study the DW dynamics using the setup based on the magnetooptic Kerr apparatus.

ACKNOWLEDGMENTS

This work was supported by a program in support of scientific instrumentation development at the Ministry of Education and Science of the Russian Federation.

REFERENCES

1. O. S. Kolotov, V. A. Pogozhev, and R. V. Telesnin, *Methods and Equipment for Investigation into the Pulsed Properties of Thin Magnetic Films* (Mosk. Gos. Univ., Moscow, 1970) [in Russian].
2. A. V. Semirov and A. V. Gavrilyuk, Fiz. Met. Metalloved. **87** (2), 44 (1999).

Translated by Yu. Vishnyakov

Technical Physics, Vol. 50, No. 10, 2005, pp. 1379–1382. Translated from Zhurnal Tekhnicheskoĭ Fiziki, Vol. 75, No. 10, 2005, pp. 131–134.

SHORT COMMUNICATIONS

Relaxation of the Volume and Shear Viscosities in Diethyl Siloxane and Ethyloctyl Siloxane

V. V. Surnychev, V. I. Kovalenko, A. S. Lagunov, and V. V. Belyaev

Moscow State Regional University,
ul. Radio 10a, Moscow, 107005 Russia

e-mail: conrad@nm.ru

Received February 10, 2005

Abstract—The variable distance pulsed phase-locked method is applied to study the temperature and frequency dependences of the rate and coefficient of ultrasound absorption in diethyl siloxane and ethyloctyl siloxane in the frequency range 4–63 MHz at temperatures from 293 to 348 K. Based on experimental data, the frequency dependence of the volume and shear viscosities is derived. The values of the shear and volume viscosity coefficients, as well as the relaxation times of processes discovered, are found. © *2005 Pleiades Publishing, Inc.*

Organosiloxanes belong to the class of substances whose molecules contain the main siloxane chain with Si–O main-chain links and organic substitutes in silicon [1, 2]. Some of the properties of organosiloxanes are as yet little understood. Of special interest is investigation into the relaxation of their viscoelastic properties by the acoustic spectroscopy method. Data for the rate and coefficient of ultrasound absorption are of great value both for applications and for clarifying the domain of applicability of the phenomenological theories of viscoelastic media. Compression and shear strains due to elastic wave propagation change the arrangement of molecules and their associated complexes, i.e., cause restructuring modifying the structure-sensitive properties, which are of relaxation character. According to [3],

$$\frac{\alpha}{f^2} = \frac{2\pi^2}{\rho c_0^3}\left(\frac{4}{3}\eta_s + \eta_v\right), \quad (1)$$

where η_s and η_v are the shear and volume viscosities, respectively.

At $\eta_v = 0$, we obtain the relationship

$$\left(\frac{\alpha}{f^2}\right)_s = \frac{2\pi^2}{\rho c_0^3}\frac{4}{3}\eta_s, \quad (2)$$

which describes losses due to shear viscosity (Stokes absorption). Quantity $(\alpha/f^2) - (\alpha/f^2)_S$ is called the super-Stokes absorption. This absorption and, hence, volume viscosity η_v may be attributed to both structural and thermal relaxation [3–5].

The objects of investigation in this work were diethyl siloxane (DES) and ethyloctyl siloxane (EOS) (the general formula $(C_2H_5)_3SiO[(C_2H_5)_2SiO]_4Si(C_2H_5)_3$ and $(C_2H_5)_3SiO[C_2H_5C_8H_{17}SiO]_{18}Si(C_2H_5)_3$, respectively) with triethyl siloxane terminal links. The samples were prepared at the State Research Institute of Chemistry and Technology of Organoelemental Compounds (Moscow). Such compounds are used as lubricants and biological liquids. The molar weights of DES and EOS are 0.65 and 3.5 kg/mol, respectively.

The rate and coefficient of ultrasound absorption were measured by the variable distance pulsed phase-locked method [6, 7]. The thermal physical properties of DES were studied in [8]. The measurements are plotted in Fig. 1 together with calculated values. At certain temperatures, Stokes absorption $(\alpha/f^2)_S$ are seen to exceed experimental values of (α/f^2) (domain II in the temperature dependences plotted in Fig. 2). Similar results were obtained for high-viscosity liquids [9, 10]. This fact testifies that the volume and shear viscosities relax at low temperatures in the given compounds. Furthermore, at all temperatures, the frequency dependences of the absorption coefficient decrease monotonically without clear-cut inflections, the presence of which would indicate a set of widely spaced discrete relaxation times. Thus, in DES and EOS, processes related to volume and shear viscosity relaxation superimpose.

According to the relaxation theory, specifically, in terms of the single-process model, the frequency dependence of the absorption coefficient is given by

$$\frac{\alpha}{f^2} = \frac{A}{1 + \omega^2\tau^2} + B. \quad (3)$$

1063-7842/05/5010-1379$26.00

Table 1. Relaxation parameters of DES and EOS

t, °C	*A*	*B*	A_s	B_s	τ_α	τ_s	τ_α/τ_s	$(\alpha/f^2)s$	$B/(\alpha/f^2)s$
	$\times10^{12}$, m^{-1} s^2				$\times10^9$, s			$\times10^{12}$, m^{-1} s^2	
DES									
0	0.28	0.61	0.37	0.58	8.2	6.4	1.28	1.02	0.60
5	0.27	0.59	0.28	0.58	7.9	6.1	1.30	0.90	9.65
10	0.25	0.57	0.25	0.56	7.5	5.7	1.31	0.80	0.71
15	0.24	0.55	0.2	0.55	7.1	5.3	1.35	0.72	0.77
25	0.22	0.51	0.14	0.52	5.7	4.2	1.35	0.58	0.87
45	0.18	0.43			4.3			0.4	1.00
60	0.15	0.37			3.4			0.4	1.02
75	0.13	0.30			2.7			0.3	0.95
EOS									
0	1.81	1.16	2.2	0.9	12.2	6.9	1.77	3.0	0.39
5	1.60	1.07	1.72	0.87	10.6	6.4	1.67	2.6	0.41
10	1.45	0.98	1.5	0.83	9.4	6.1	1.53	2.3	0.43
15	1.28	0.90	1.15	0.79	8.4	5.5	1.53	2.0	0.45
30	0.91	0.68	0.75	0.64	6.2	4.1	1.51	1.4	0.50
45	0.66	0.53			4.0			1.0	0.55
60	0.50	0.41			3.7			0.7	0.58
75	0.40	0.36			2.8			0.5	0.66

Using these relationship, one can find relaxation parameters *A*, *B*, τ_α (relaxation time), and $B/(\alpha/f^2)_S$ (Table 1).

The dependences of τ_α were assumed to obey the Arrhenius law with activation energies ΔE_α listed in Table 2.

The ultrasound velocity in both substances varies considerably depending on frequency and temperature. In the frequency range 4.2–63 MHz at a temperature of 303 K, it falls into the interval 1214–1219 m/s in DES and into the interval 1309–1330 m/s in EOS; at T = 348 K, it varies from 1078 to 1102 m/s in DES and from 1180 to 1240 m/s in EOS. Within the limits of measurement error, the ultrasound velocity is a linear function of temperature throughout the temperature interval studied.

Knowing the relevant parameters, one can find volume viscosity η_v by the formula

$$\eta_v = \frac{\rho c^3}{2\pi^2}\left[\left(\frac{\alpha}{f^2}\right) - B\right]. \quad (4)$$

The values of η_v for several temperatures and frequencies are listed in Table 3.

Since in domain II in Fig. 2 $\eta_v = 0$, the ultrasound absorption depends only on η_s; that is, quantity $(\alpha/f^2)_s$ becomes frequency-dependent. Taking into account the values of (α/f^2) in domain II and assuming that $A_s + B_s = (\alpha/f^2)_s$, one can find with (2) parameters A_s, B_s, and τ characterizing the relaxation of absorption in the classical sense (Table 1), as well as activation energy ΔE_s (Table 2). Then, using the resulting values, one finds η_s

Table 2. Activation energies for DES and EOS in kJ/mol

ΔE_α	ΔE_s	ΔE_η	ΔE_α	ΔE_s	ΔE_η
DES			EOS		
13.1	11.8	17.8	15.3	16.6	24.6

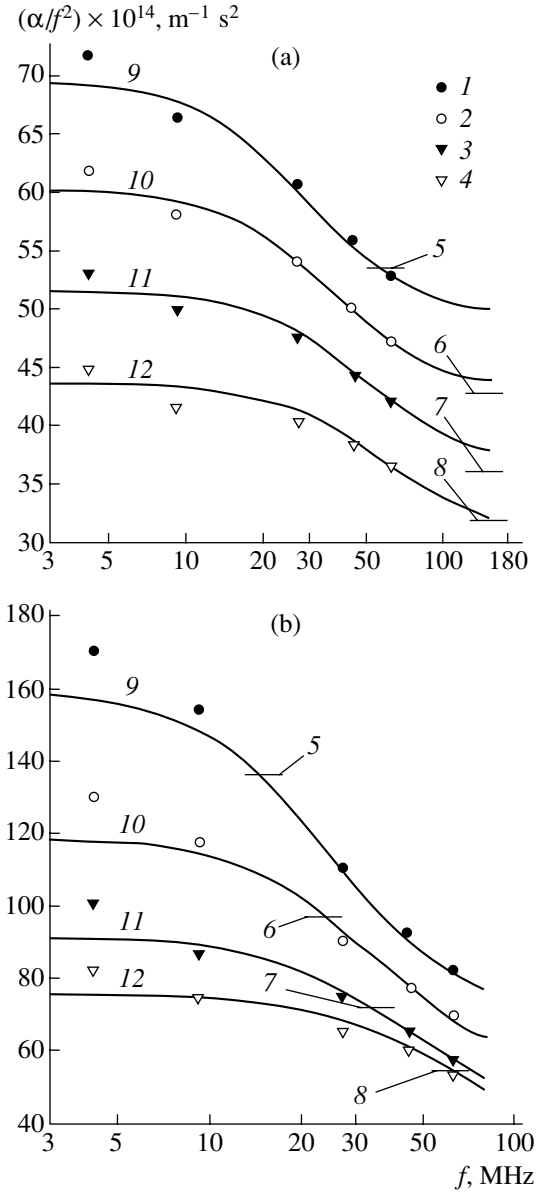

Fig. 1. Frequency dependences of (*1–4*) measured absorption coefficient α/f^2 vs. (*9–12*) its values calculated by (3) and (*5–8*) absorption coefficient $(\alpha/f^2)_s$ calculated by (2) for (a) DES and (b) EOS. T = (*1, 5, 9*) 30, (*2, 6, 10*) 45, (*3, 7, 11*) 60, and (*4, 8, 12*) 75°C.

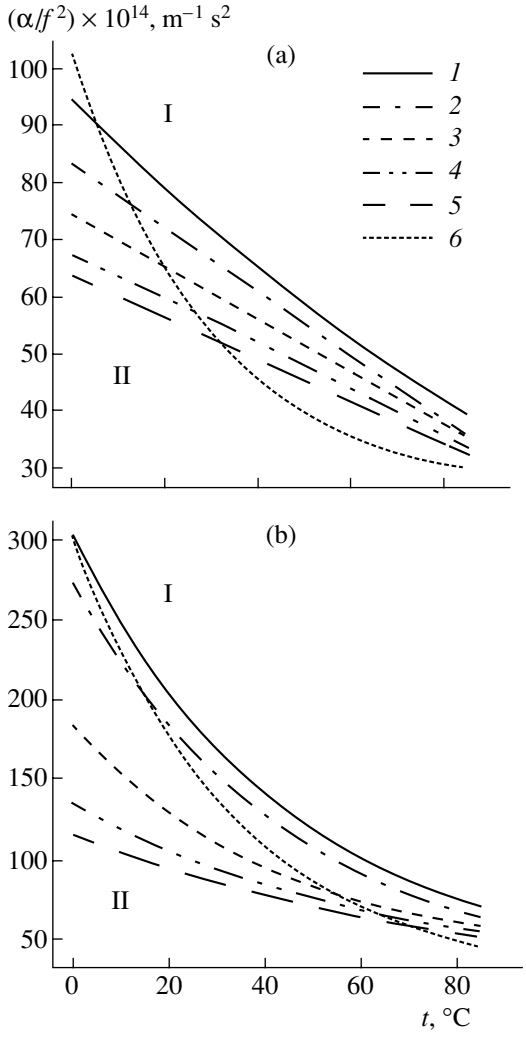

Fig. 2. Temperature dependences of ultrasound absorption coefficient α/f^2 at frequency f = (*1*) 4.2, (*2*) 9.6, (*3*) 27.3, (*4*) 45, and (*5*) 63 MHz vs. (*6*) absorption coefficient $(\alpha/f^2)_s$ calculated by (2) for (a) DES and (b) EOS. I and II, domains where $\alpha/f^2 > (\alpha/f^2)_s$ and $\alpha/f^2 < (\alpha/f^2)_s$, respectively.

at different temperatures and frequencies (Table 3),

$$\eta_s = \frac{3\rho c^3}{8\pi^2}\left[\left(\frac{\alpha}{f^2}\right) - B_s\right]. \quad (5)$$

Table 3 lists ratios η_v/η_s for various temperatures and frequencies, and Table 1 gives ratios τ_α/τ_s at different temperatures. In both materials, $\eta_v/\eta_s < 1$ and $\tau_\alpha/\tau_s = 1.3$–1.7. Both ratios depend on temperature only slightly. Therefore, we can infer that both materials exhibit structural relaxation. The fact that the relaxation times of volume and shear viscosities differ insignificantly and activation energies ΔE_α, ΔE_s, and ΔE_η (the activation energy of viscous flow, which was obtained from the temperature dependence of the shear viscosity) are fairly close to each other (Table 2) lets us suppose that mechanisms underlying shear and volume viscosities are of similar nature.

The data for the relaxation behavior and viscosity of DES and EOS suggest that the ultrasound absorption coefficient, both viscosities η_v and η_s, and activation energy ΔE_η are of greater importance for EOS, which has longer-chain and more ridgelike molecules.

Table 3. Values of η_v,η_s, and η_v/η_s for DES and EOS at different temperatures and frequencies

t, °C	$\eta_v \times 10^2$, Pa s					$\eta_s \times 10^2$, Pa s					η_v/η_s				
	f, MHz														
	4.2	9.2	27.3	45	63	4.2	9.2	27.3	45	63	4.2	9.2	27.3	45	63
DES															
0	3.5	2.3	1.2	0.6	0.2	10	9.1	8.2	7.4	7.0	0.34	0.25	0.15	0.080	0.028
5	3.2	2.2	1.2	0.6	0.2	9.5	8.4	7.6	6.9	6.5	0.34	0.25	0.16	0.087	0.034
10	2.9	2	1.2	0.6	0.2	8.0	7.8	7.0	6.4	6.0	0.36	0.26	0.16	0.095	0.041
15	2.65	1.9	1.1	0.6	0.3	6.9	6.9	6.4	5.9	5.6	0.39	0.28	0.17	0.104	0.048
20	2.4	1.7	1.1	0.6	0.3	5.9	5.9	5.9	5.4	5.1	0.41	0.30	0.18	0.111	0.057
25	2.2	1.6	1.0	0.6	0.3	5.1	5.1	5.1	5.0	4.7	0.43	0.32	0.20	0.120	0.065
EOS															
0	22	19	8.1	2.4	0.8	30	27	18	13	11	0.74	0.69	0.45	0.18	0.07
5	20	17	7.3	2.5	1.2	25	23	16	12	10	0.79	0.71	0.46	0.21	0.12
10	17	15	6.5	2.6	1.4	21	20	14	11	10	0.82	0.71	0.47	0.24	0.15
15	16	13	5.8	2.6	1.5	18	16	12	10	9	0.88	0.79	0.47	0.27	0.17
20	14	11	5.3	2.7	1.5	15	14	11	8.9	8.0	0.92	0.80	0.49	0.30	0.18
25	12	10	4.7	2.6	1.6	13	12	10	8.1	7.4	0.95	0.86	0.48	0.32	0.22
30	11	8.9	4.4	2.7	1.9	11	11	8.6	7.4	6.8	0.99	0.85	0.51	0.37	0.28
35	9.3	7.8	4.0	2.7	2.0	9.1	10	7.7	6.7	6.2	1.02	0.82	0.52	0.40	0.32

REFERENCES

1. K. A. Andrianov, *Methods of Organoelemental Chemistry (Silicon)* (Nauka, Moscow, 1968) [in Russian].
2. M. V. Sobolevskiĭ, I. I. Skorokhodov, and K. P. Grinevich, *Organic Siloxanes: Properties, Production, and Applications* (Khimiya, Moscow, 1985) [in Russian].
3. M. V. Mikhaĭlov, V. A. Solov'ev, and Yu. S. Syrnikov, *Fundamentals of Molecular Acoustics* (Nauka, Moscow, 1964) [in Russian].
4. L. S. Kagramanyan and A. L. Badalyan, in *Ultrasound and Thermodynamic Properties of Materials* (Kursk. Gos. Pedagog. Univ., Kursk, 1981), pp. 131–138 [in Russian].
5. V. F. Yakovlev, Candidate's Dissertation (Moscow, 1952).
6. T. Litovitz and C. Davis, in *Physical Acoustics: Principles and Methods*, Ed. by W. P. Mason (Academic, New York, 1968; Mir, Moscow, 1973), Vol. 2A, pp. 298–370.
7. J. Lamb, in *Physical Acoustics: Principles and Methods*, Ed. by W. P. Mason (Academic, New York, 1968; Mir, Moscow, 1973), Vol. 2A, pp. 222–297.
8. V. S. Kononenko, Doctoral Dissertation (Tashkent, 1995).
9. V. N. Khudaĭberdyev, Z. N. Amanov, M. K. Karabaev, *et al.*, Izv. Akad. Nauk Uzb. SSR, Ser. Fiz. Mat. Nauk, No. 1, 53 (1979).
10. I. G. Mikhaĭlov and L. I. Savina, in *Application of Ultrasonics for Material Studies* (MOPI, Moscow, 1957), pp. 85–93 [in Russian].

Translated by V. Isaakyan

Technical Physics, Vol. 50, No. 10, 2005, pp. 1383–1385. Translated from Zhurnal Tekhnicheskoĭ Fiziki, Vol. 75, No. 10, 2005, pp. 135–138.

SHORT COMMUNICATIONS

On the Feasibility of Using X-ray Faster-than-Light Spots to Check the Isotropy of the Speed of Light

G. B. Malykin

Institute of Applied Physics, Russian Academy of Sciences,
ul. Ul'yanova 46, Nizhni Novgorod, 603950 Russia
e-mail: malykin@mail.nnov.ru

Received February 21, 2005

Abstract—An experimental method for checking the isotropy of the speed of light is proposed. It is based on excitation of Cherenkov radiation by a virtual electric charge moving with a faster-than-light velocity. © *2005 Pleiades Publishing, Inc.*

The motion of a light spot from a rotating projector on a screen was considered in classical works [1, 2] (see also [3–5]). If projector–screen distance R is large, i.e., satisfies the condition $v_{\text{proj}} = R\Omega > c$ (where v_{proj} is the linear velocity of the spot on the screen, Ω is the angular velocity of the projector, and c is the speed of light in free space), the spot on the screen may take a faster-than-light phase velocity (v_{proj}). In [6], we proposed faster-than-light spots of different nature (for example, from a rotating electron beam) satisfying the condition $v_{\text{proj}} = R\Omega \gg c$ that can be used for synchronization of space-separated clocks with the aim to check the equality of the speeds of light in the forward and backward directions and, thereby, to strengthen the validity of the second postulate of special relativity [7].

In [2] (see also [8]), faster-than-light spots of electromagnetic nature were investigated for feasibility of generating Cherenkov radiation. Indeed, such a spot moving over the inner surface of a cylindrical metallic screen for a moment produces the nonuniform charge distribution on the metal surface or, which is much more efficient for generating Cherenkov radiation, knocks out electrons from the metal (in the latter case, the screen virtually serves as a cathode). This gives rise to a virtual electric charge moving with a velocity $v_{\text{proj}} > c$. However, to overcome the potential barrier (electron work function), an electromagnetic radiation with a wavelength much shorter than that of visible light is required. Such an experiment with X rays has been recently carried out to advantage in [9] (however, under conditions somewhat different from those suggested in [2, 8]).

The aim of this study is to experimentally verify the isotropy of the speed of light by generating Cherenkov radiation with a virtual electric charge [2, 8, 9] moving with a faster-than-light velocity.

First, recall that special relativity assumes the speed of light to be isotropic; therefore, an experimental support of this assumption would be a direct proof of the validity of special relativity or, more precisely, of its second postulate. Anisotropy of the speed of light is asserted, for example, in the theory of luminiferous ether. This outdated but unfortunately still persisting theory states that, in a certain hypothetical inertial frame of references (IFR) in which the ether is at rest, the speed of light is isotropic and equals c, while in any other IFR, the speed of light is the sum of speed c the direction of which coincides with that of the source and ether velocity $\mathbf{v}_{\text{eth}}$. Without loss in generality, the ether velocity may be directed along the X axis. Then, the light from a source oriented at angle φ to the X axis has the velocity

$$V(\varphi) = c\sqrt{1 + \frac{2v_{\text{eth}}}{c}\cos\varphi + \frac{v_{\text{eth}}^2}{c^2}} \quad (v_{\text{eth}} \ll c),$$

and propagates at the angle

$$\psi(\varphi) = \arctan\frac{c\sin\varphi}{c\cos\varphi + v_{\text{eth}}}$$

to this axis.

Note that, if $v_{\text{eth}} = 0$, $V = c$ and $\psi = \varphi$. Straightforward while cumbersome calculations show that, if the source placed at the center of a cylindrical screen rotates with angular velocity Ω, the spot moves on the screen with the linear velocity

$$v_{\text{proj}} = R\Omega\frac{\left(1 + \frac{v_{\text{eth}}}{c}\cos\Omega t\right)\sqrt{1 + 2\frac{v_{\text{eth}}}{c}\cos\Omega t + \frac{v^2}{c^2}}}{1 + 2\frac{v_{\text{eth}}}{c}\cos\Omega t + R\Omega\frac{v_{\text{eth}}}{c^2}\sin\Omega t + \frac{v^2}{c^2}}, \quad (1)$$

where t is the time.

1063-7842/05/5010-1383$26.00

This expression may be considerably simplified by omitting small quantities v_{eth}/c and $v_{eth}^2/c^2 \ll R\Omega/c$,

$$v_{proj} \simeq \frac{R\Omega}{1 + R\Omega\frac{v_{eth}}{c^2}\sin\Omega t}. \quad (2)$$

Since the velocity of the spot is periodic in time and, hence, so is the velocity of the virtual charge, the parameters of Cherenkov radiation (the apex angle and the radiation frequency) will vary in a similar way. Moreover, when radius R is so large that

$$R\Omega v_{eth} > c^2, \quad (3)$$

even the direction of motion of the spot on the screen is bound to periodically vary in time[1] with the velocity of the spot tending to infinity at certain instants. Such variations are basically detectable, and their absence would be direct evidence for the validity of the second postulate. In the opinion of adherents of the theory of luminiferous ether, velocity v_{eth} lies in the range from 30 (the orbital velocity of the Earth) to 360 km/s (the velocity of the Solar System with respect to the IFR where the relic background is isotropic [13]). Thus, condition (3) is met with $v_{proj} = R\Omega$ falling into the range $(10^3–10^4)c$.

Let us now consider how to make a virtual charge move with a faster-than-light velocity on the surface of a cylindrical screen using rotating continuous X-ray radiation (see [2, 8]). One obvious way is to rotate the X-ray source, as was done in [14] for detection of the Sagnac effect. However, to impart a sufficiently high angular velocity to the source seems unrealistic because of its considerable weight. Another way is to make use of the transient radiation (predicted as early as in 1946 [15]), which arises when an electron beam crosses the interface between two insulators with different permittivities. Currently, portable sources of transient X-ray radiation based on multilayer periodic nanostructures are being developed [16]. Finally, one can use X rays reflected from a rotating X-ray mirror, for example, from a silicon single crystal serving as a diffraction grating with the source remaining quiescent [14].

However, rotation of an X-ray source (or beam) is not a necessary condition for creating a faster-than-light spot. Instead, one may use a short widely divergent X-ray pulse and a specially configured screen. This idea was implemented in [9].[2] A short (0.3–0.5 ns) pulsed beam with a diameter of ≈1 mm from a high-power optical laser (λ = 1.315 μm) was incident on a planar gold target, inducing a short (0.6–1.0 ns) X-ray pulse with a spherical wave front. Striking an aluminum cathode, this pulse knocked out electrons toward a grid anode, which was under a voltage of several tens of kilovolts. The anode, being transparent to X rays and electrons, accelerated the electron flow and, thus, greatly enhanced the Cherenkov radiation power. The presence of the anode has a negligible effect on the relativistic effects concerned. If the cathode (screen) were cylindrical, all parts of the incident X-ray pulse with a spherical wave front would reach the cathode surface simultaneously, which corresponds to $v_{proj} = \infty$. It is known, however, that a virtual charge moving over a screen (cathode) with an infinite velocity does not induce Cherenkov radiation. Therefore, the cathode used in [9] was made in the form of an 850-mm-long plane-parallel plate placed 340 mm from the target, i.e., from a point X-ray source. The distance from the source to the near and far ends of the plate was 400 and 1100 mm, respectively. The angle of incidence on the cathode surface ranged from 70° to 25°. In this case, velocity v_{proj} of the virtual charge on the cathode was not constant: under the assumption that the speed of light is isotropic and equal to c, it varied from $1.3c$ to $1.05c$ at the near and far ends of the plate, respectively. These values are in agreement with the parameters of Cherenkov radiation measured in [9]. Thus, the results of [9] suggest that the anisotropy of the speed of light does not exceed 25–30% for angles near 40°; otherwise, Cherenkov radiation from certain regions of the cathode would be absent. Since measurements in [9] were taken at various times of the astronomical day, that is, at different orientations of the experimental setup with respect to outer space, this conclusion is valid for a wider range of angles.

Although the accuracy of estimating the isotropy of the speed of light in [9] is not high, this does not mean that such an approach to verifying the basic postulates of special relativity should be disregarded. Recall that the pioneering experiments of Michelson [18] also featured a very low accuracy; moreover, it was even overestimated by a factor of 2, as indicated by Lorentz [19]. In the subsequent experiments by Michelson and Morley [20], the accuracy was appreciably higher, and to date it has been improved by several orders of magnitude [21, 22]. Note that experiments similar to those of Michelson and Morley may only indicate that the average speed of reciprocating light is the same in all directions (for details, see [6]). Study [9] was the first to demonstrate the feasibility of experimentally checking the isotropy of one-way speed of light; in this respect, its significance for special relativity can hardly be overstated.

The upper estimate of the anisotropy can be determined with a much higher accuracy by using the cathode of a special shape. Specifically, if the cathode represents a fragment of the Archimedean spiral [23], the virtual charge will move with constant velocity v_{proj}, naturally, provided that the speed of light is isotropic. Under this condition, the equality $v_{proj} = Kc$ (where K is the excess velocity factor) is satisfied when distance R

[1] Such a conjecture is difficult to recognize: nobody has observed a change in the direction of motion of light spots from pulsars [1, 2, 10] or from a diffraction grating [11, 12]; the absence of such observations is indirect evidence for the isotropy of the speed of light.

[2] A comprehensive theoretical consideration of experiments [9] can be found in [17].

between a point X-ray source and the cathode depends on angle φ as

$$R(\varphi) = R_0\left(1 + \frac{\varphi c}{v_{\text{proj}}}\right) = R_0\left(1 + \frac{\varphi}{K}\right), \qquad (4)$$

where R_0 is the minimal source–cathode distance.

For $v_{\text{proj}} = 10^3\,c$, $R_0 = 1000$ mm, and angle φ varying by 40° along the cathode, it follows from formula (4) that the far end of the cathode is 1000.4 mm distant from the X-ray source. Such an accuracy of manufacturing and installing the cathode is practically feasible. Let the speed of light be anisotropic and the anisotropy be greater than 10^{-3} of its mean value c (in terms of the opponents of special relativity, this corresponds to the condition $v_{\text{eth}} > 300$ km/s). Then, it is easy to check that the projection of a spherical wave (spot) onto a screen (cathode) in the form of the Archimedean spiral would periodically change the direction of motion, as in the case of a rotating X-ray beam and cylindrical screen (see formulas (2) and (3)). The absence of such an unusual behavior of the spot would serve as a direct proof of the second postulate. Clearly, the deviation of the X-ray wave front from ideal sphericity has to be substantially smaller than 0.4 mm and a large number of sensors should be located over the cathode surface to detect the Cherenkov radiation (in [9], three sensors were used). Another important factor in the case at hand is the X-ray pulse duration: if the pulse is too long, all parts of the wave front almost simultaneously reach the cathode surface and the size of the spot becomes comparable to that of the cathode. In our conditions, the spot will be sufficiently small if the X-ray pulse duration is much shorter than 1 ps. The larger the value of K (the excess velocity factor), the smaller should be the step of the Archimedean spiral and, accordingly, the shorter should be the X-ray pulse.

The main result of this study is that the isotropy of the one-way speed of light is confirmed by the characteristics of the Cherenkov radiation induced by the spot of an X-ray beam moving with a faster-than-light speed over the screen (cathode). The spot may be produced both by a rotating source of continuous X-ray radiation (then, a cylindrical screen should be used [2, 8]) and by a pulsed X-ray beam with a spherical wave front (the screen in this case should be plane [9] or have the form of a segment of the Archimedean spiral.

ACKNOWLEDGMENTS

The author is grateful to S.P. Martynenko for the helpful discussion of the results obtained in [9], V.I. Pozdnyakova for assistance, A.M. Sergeev for the valuable remark, and O.V. Chebotarenko for discussion of issues concerning the motion of a rotating beam in the presence of speed-of-light anisotropy.

This work was supported in part by the "Program of the President of the Russian Federation in Support of Leading Scientific Schools," grant no. NSh-1622.2003.2.

REFERENCES

1. V. L. Ginzburg, Zh. Éksp. Teor. Fiz. **62**, 173 (1972) [Sov. Phys. JETP **35**, 92 (1972)].
2. B. M. Bolotovskiĭ and V. L. Ginzburg, Usp. Fiz. Nauk **106**, 577 (1972) [Sov. Phys. Usp. **15**, 184 (1972)].
3. B. M. Bolotovskiĭ and V. L. Ginzburg, in *Einstein Studies 1972* (Nauka, Moscow, 1974), pp. 212–236 [in Russian].
4. V. L. Ginzburg, *Physics and Astrophysics: A Selection of Key Problems* (Nauka, Moscow, 1987; Pergamon, Oxford, 1985), pp. 211–228.
5. V. L. Ginzburg, *On the Theory of Relativity* (Nauka, Moscow, 1979), pp. 212–236 [in Russian].
6. G. B. Malykin, Usp. Fiz. Nauk **174**, 801 (2004) [Phys. Usp. **47**, 739 (2004)].
7. A. Einshtein, *To the Electrodynamics of Moving Bodies*, in *Collection of Scientific Works* (Nauka, Moscow, 1965), Vol. 1, pp. 7–35 [in Russian]; A. Einstein, Ann. Phys. (Leipzig) **17**, 891 (1905).
8. V. Ya. Éĭdman, Izv. Vyssh. Uchebn. Zaved., Radiofiz. **15**, 634 (1972).
9. V. A. Bessarab, A. A. Gorbunov, S. P. Martynenko, and N. A. Prudkoy, IEEE Trans. Plasma Sci. **32** (3), 1 (2004).
10. V. L. Ginzburg, Usp. Fiz. Nauk **103**, 393 (1971) [Sov. Phys. Usp. **14**, 83 (1971)].
11. N. B. Baranova, M. O. Scully, and B. Ya. Zel'dovich, Zh. Éksp. Teor. Fiz. **105**, 469 (1994) [JETP **78**, 249 (1994)].
12. B. Ya. Zel'dovich, N. D. Kundikova, F. V. Podgornov, and L. F. Rogacheva, Kvantovaya Élektron. (Moscow) **23**, 1128 (1996).
13. G. F. Smoot, M. V. Gorenstein, and R. A. Muller, Phys. Rev. Lett. **39**, 898 (1977).
14. V. I. Vysotskiĭ, V. I. Vorontsov, R. N. Kuz'min, *et al.*, Usp. Fiz. Nauk **164**, 309 (1994) [Phys. Usp. **37**, 298 (1994)].
15. V. L. Ginzburg and I. M. Frank, Zh. Éksp. Teor. Fiz. **16**, 15 (1946).
16. A. E. Kaplan, C. T. Law, and P. L. Shkolnikov, Phys. Rev. E **52**, 6795 (1995).
17. Yu. N. Lazarev, P. V. Petrov, and Yu. G. Syrtsova, Zh. Tekh. Fiz. **74** (11), 83 (2004) [Tech. Phys. **49**, 1477 (2004)].
18. A. A. Michelson, Am. J. Sci., Ser. III **22** (128), 120 (1881); *Creators of Physical Optics*, Ed. by U. I. Frankfurt (Nauka, Moscow, 1973), pp. 223–235 [in Russian].
19. H. A. Lorentz, Arch. Neerl. **21**, 103 (1886); H. A. Lorentz, *Collected Papers* (Nijhoff, Hague, 1936), Vol. 4, p. 153.
20. A. A. Michelson and E. W. Morley, Am. J. Sci., Ser. III **34** (203), 333 (1887).
21. C. Braxmaier, H. Müller, O. Pradl, *et al.*, Phys. Rev. Lett. **88**, 010401 (2002).
22. H. Müller, S. Herrmann, C. Braxmaier, *et al.*, Phys. Rev. Lett. **91**, 020401 (2003).
23. I. N. Bronshtein and A. S. Semendyayev, *Handbook of Mathematics* (Nauka, Moscow, 1986; Springer, New York, 1997).

Translated by A. Sidorova

Technical Physics, Vol. 50, No. 10, 2005, pp. 1386–1389. Translated from Zhurnal Tekhnicheskoĭ Fiziki, Vol. 75, No. 10, 2005, pp. 139–142.

SHORT COMMUNICATIONS

On the Effect of Structural Organization on Magnetic Moment Relaxation of Disperse Particles in a Magnetic Fluid

D. V. Gladkikh*, Yu. I. Dikansky*, K. A. Balabanov, and A. V. Radionov*****

** Stavropol State University, Stavropol, 355009 Russia*

e-mail: genphys@stavsu.ru

*** Zhukovsky Air Force Engineering Academy, Stavropol Branch, Stavropol, 355003 Russia*

**** Ferrogidrodinamika Research and Production Enterprise, Nikolaev, 54030 Ukraine*

Received March 14, 2005

Abstract—The complex susceptibility of a magnetic fluid based on vacuum oil, which is used in engineering as a magnetosealing liquid, is investigated. Features of magnetic moment relaxation of disperse particles, which are associated with their structural organization under the action of external factors, are determined from analysis of the results. © *2005 Pleiades Publishing, Inc.*

INTRODUCTION

Magnetic and structural properties of magnetic fluids (MFs) have been studied by many authors [1, 2]. Kerosene-based MFs are the most abundant and well-studied objects. However, fluids based on more viscous substances, such as mineral oils and organosilicon materials, have found applications in practice. The effects of interaction of particles in such MFs and their structural properties have not been studied extensively as yet. This work is devoted to experimental study of the effect of structural organization on magnetic moment relaxation of disperse particles in a magnetic fluid based on vacuum oil.

EXPERIMENTAL TECHNIQUE AND OBJECT OF INVESTIGATION

As the initial sample, we used a magnetic fluid with magnetite particles based on vacuum oil with a volume concentration of $\varphi = 8.6\%$ and a saturation magnetization of 4.3 kA/m. The sample was a homogeneous magnetic fluid, which was stable to phase separation upon a change in temperature and under the action of magnetic fields. The initial sample was used to obtain a concentration series of magnetic fluids consisting of 14 samples by diluting with a carrier fluid; the concentration of the most dilute sample was $\varphi = 0.67\%$. The magnetic susceptibility was measured by the bridge method. The real (χ') and imaginary (χ'') parts of the complex magnetic susceptibility were calculated from the change in the inductance and *Q*-factor of the solenoid upon introduction of the sample into it. Measurements were made using an LCR-817 immittance meter; the error in determining the effective value did not exceed 0.1% for the real part χ' of magnetic susceptibility and 0.3% for its imaginary part χ''. Frequency dependences of the susceptibility were studied in the absence and in the presence of a constant uniform external magnetic field.

EXPERIMENTAL RESULTS AND DISCUSSION

It was found that the initial segment of the concentration dependence of the magnetic susceptibility differs from linearity only slightly up to a concentration of ~4% (curve *1* in Fig. 1).

The action of a constant external magnetic field leads to "smoothing" of the $\chi'(\theta)$ curve so that it

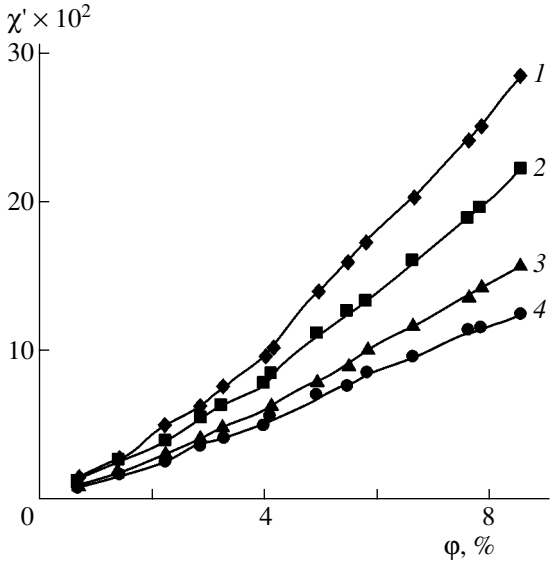

Fig. 1. Dependence of the magnetic susceptibility on the concentration of disperse particles under the action of a constant magnetic field *H*, kA/m: 0 (*1*), 2.15 (*2*), 4.3 (*3*), and 5.8 (*4*).

1063-7842/05/5010-1386$26.00 © 2005 Pleiades Publishing, Inc.

becomes almost linear in the entire concentration range for large values of the constant magnetic field (curves *2–4* in Fig. 1).

Optical microscope observations revealed that structure formation processes begin in a magnetic fluid upon a change in its concentration by diluting the initial homogeneous sample in a concentration range corresponding to 4%. The largest number of aggregates are observed in samples with a disperse phase concentration of 3–3.5%; this is also confirmed by the results of analysis of light scattering from thin layers of the samples (curve *1* in Fig. 2 was obtained in zero magnetic field, while curve *2* was obtained under the action of a magnetic field = 4.6 kA/m directed along the plane of an MF layer). Here, I_0 is the intensity of light incident on the sample and I is the intensity of scattered light.

We can assume that dilution of an initially homogeneous MF leads to the formation of aggregates with partly closed magnetic moments of single-domain disperse particles due to the emerging deficit of a surface-active substance. The presence of such aggregates may be responsible for the linearity of the initial segment of the concentration dependence. Under the action of a constant external magnetic field, the aggregates are combined into chains aligned along the direction of the field, which results in the experimentally observed enhancement of anisotropic light scattering under the action of the field.

It was found that the frequency dependences of the imaginary part of the complex magnetic susceptibility obtained in zero field and under the action of a constant external magnetic field are different for all samples studied here. In zero external field, susceptibility χ'' increases monotonically (curve *1* in Fig. 3) with the measuring field frequency. After the application of a magnetic field, the frequency dependence $\chi''(f)$ of the imaginary part acquires a peak at a certain frequency depending on the value of the constant magnetic field (curves *2–7* in Fig. 3). As the magnetic field increases from 0 to ~1.6 kA/m, the frequency corresponding to the peak of χ'' slightly decreases, while a further increase in the magnetic field leads to its increase. Calculating the effective magnetic moment relaxation time of disperse particles using the peak frequency ($\tau = 1/f_p$), we were able to plot the dependence of τ on the external magnetic field, which is shown in Fig. 4 (Figs. 3 and 4 show the dependences obtained for a sample with concentration φ = 8.6%; the dependences obtained for remaining samples are analogous). Our experiments also led to the dependence of the relaxation time on the disperse phase concentration φ for various values of the magnetic field (Fig. 5).

The observed features of magnetic moment relaxation are apparently associated with the emergence of structural organization in the system of disperse particles under the action of a magnetic field, which was theoretically investigated earlier in [3–6]. In particular, the time variation of relaxation upon the formation of chain aggregates in magnetic fluids is considered in [3].

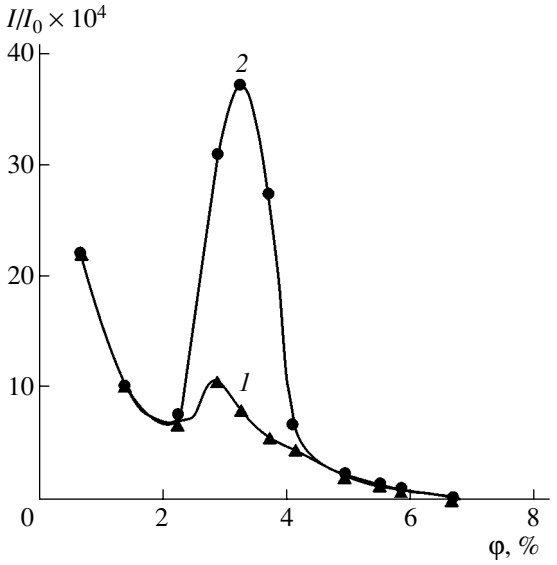

Fig. 2. Dependence of the relative intensity of light scattering on the concentration of disperse particles.

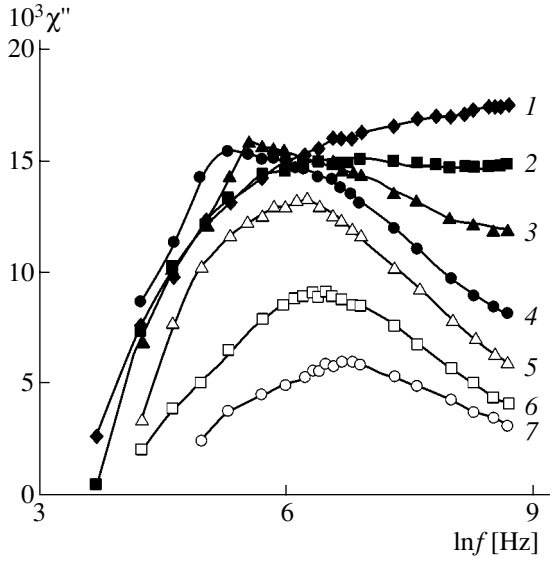

Fig. 3. Frequency dependence of the imaginary part of the complex magnetic susceptibility under the action of a constant magnetic field H, kA/m: 0 (*1*), 0.4 (*2*), 0.8 (*3*), 1.75 (*4*), 3.26 (*5*), 6.45 (*6*), and 9.67 (*7*).

The qualitative agreement between our results and the conclusions drawn in [3] suggests that the observed features of the magnetic properties of the MF samples studied here are associated with the formation of chain aggregates under the action of a constant external magnetic field. The chain parameters depend on the disperse phase concentration, the initial structural state of the sample, and the magnetic field strength.

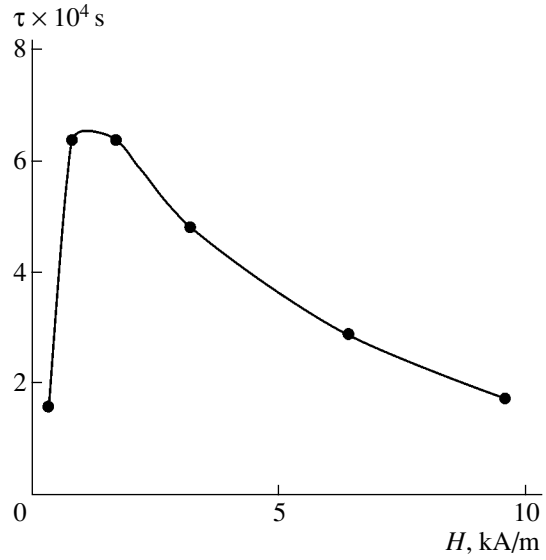

Fig. 4. Dependence of the relaxation time on the constant magnetic field.

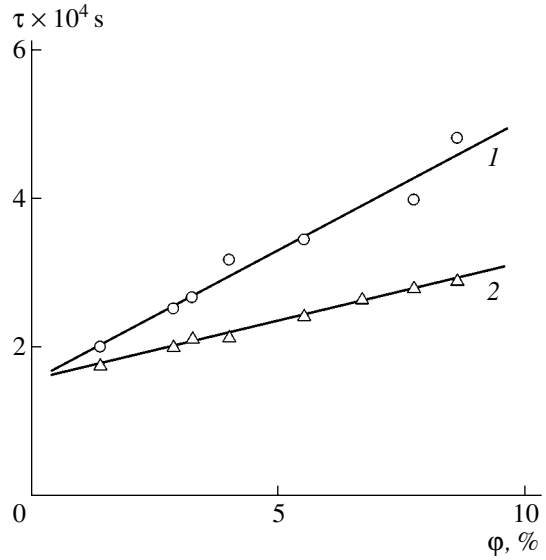

Fig. 5. Dependence of the relaxation time on the concentration of disperse particles under the action of a constant magnetic field (*1*) H = 3.26 and (*2*) 6.45 kA/m.

It should be noted that, in actual practice, a spread of particle size is observed in a magnetic fluid. For this reason, a magnetic fluid cannot be described by a discrete set of relaxation times: it is characterized by a set of relaxation times τ with a weight $c(\tau)$. Function $c(\tau)$ is introduced in such a way that quantity $c(\tau)d\tau$ is a part of the equilibrium differential magnetic susceptibility dM/dH with a relaxation time varying from τ to $\tau + d\tau$. In this case, we can write

$$\chi'(\omega) = \int_0^\infty \frac{c(\tau)d\tau}{1+\omega^2\tau^2}, \quad \chi''(\omega) = \int_0^\infty \frac{\omega c(\tau)d\tau}{1+\omega^2\tau^2}, \qquad (1)$$

for the complex magnetic susceptibility components, where $\omega = 2\pi f$.

The relaxation time distribution function $c(\tau)$ in formulas (1) can be calculated from the experimentally obtained dependences $\chi'(\omega)$ and $\chi''(\omega)$. This problem was solved in [7], where it was found that the behaviour of magnetization for low frequencies can be described by a single effective relaxation time τ_{ef}:

$$\tau_{ef} = \frac{1}{\kappa}\int_0^\infty c^*(\xi)d\tau, \quad \kappa = \int_0^\infty c(\tau)d\tau. \qquad (2)$$

Here, function $c^*(\xi)$ is introduced as a result of substitution of variables ($\tau = \exp(\beta\xi)$, $c(\tau) = c^*(\xi)\exp(-\beta\xi)$, $\beta = \ln 10$) so that the relation $c^*(\xi)d\xi = c(\tau)d\tau$ holds.

The largest contribution to the effective relaxation time comes from values of time τ corresponding to the largest value of c^*. However, the contribution of particles to the magnetic susceptibility of a fluid is proportional to the square of their volume. Consequently, large particles considerably affect the magnetic properties of the liquid in spite of their small number.

In a constant magnetic field, the particle relaxation time decreases in an increasing field. The field dependence of the relaxation time is determined by the Langevin parameter $M_S VH/kT$ [8]. For coarse particles, the Langevin parameter becomes large even in weak fields. As a result, function $c^*(\xi)$ decreases sharply. For the same value of field, coarse particles are closer to saturation than small particles. Consequently, the contribution of coarse particles to the susceptibility decreases with increasing field more rapidly than the contribution from small particles. As a result, the relaxation time decreases. Aggregation processes occurring in an MF under the action of a magnetic field enhance the effect of the above processes on the relaxation time.

We can assume that it is these processes that are responsible for the features of magnetization relaxation observed by us here. The application of a constant external magnetic field to an initially homogeneous MF initiates the formation of chain aggregates. This leads to an increase in the relaxation time (Fig. 4). Upon a further increase in the magnetic field, the chain growth continues, but the decisive role is this case is played by the growth of aggregates, which leads to a decrease in relaxation time τ.

It should also be noted in conclusion that the high serviceability of the sample under investigation in MF sealing is apparently associated with the emergence of structural ordering under the action of a constant magnetic field.

ACKNOWLEDGMENTS

This study was supported financially by the Russian Foundation for Basic Research, project no. 04-02-16901.

REFERENCES

1. V. E. Fertman, *Magnetic Fluids Guidebook: Properties and Applications* (Hemisphere, New York, 1990; Vysheĭshaya Shkola, Minsk, 1988).
2. E. Blums, A. Cebers, and M. Maiorov, *Magnetic Fluids* (Zinatne, Riga, 1986; Walter de Gryuter, Berlin, 1997).
3. L. Yu. Iskakova and A. Yu. Zubarev, J. Magn. Magn. Mater. **252**, 74 (2002).
4. S. Taketomi, Phys. Rev. E **57**, 3073 (1998).
5. N. F. Patsegon, Magn. Gidrodin., No. 3, 10 (1991).
6. N. F. Patsegon, Magn. Gidrodin., No. 4, 40 (1991).
7. É. M. Agabekyan, A. G. Ivanov, V. V. Kiryushin, *et al.*, Magn. Gidrodin., No. 2, 65 (1986).
8. M. A. Martsenyuk, Yu. L. Raĭkher, and M. I. Shliomis, Zh. Éksp. Teor. Fiz. **65**, 834 (1973) [Sov. Phys. JETP **38**, 413 (1973)].

Translated by N. Wadhwa